IMPROVED SEARCH FOR $\mathcal{CP}$-VIOLATION IN ORTHO-POSITRONIUM DECAY

By

Tom-Erik Haugen

A DISSERTATION

Submitted to
Michigan State University
in partial fulfillment of the requirements
for the degree of

Physics—Doctor of Philosophy

2024

ABSTRACT

The observed baryon asymmetry of the universe requires charge parity ($\mathcal{CP}$) violation, likely more than the Standard Model contains. Simultaneously, the scarcity of antimatter makes direct tests of $\mathcal{CP}$-violation difficult to perform in a laboratory, and many tests search for time-reversal violation ($\mathcal{T}$) and use combined $\mathcal{CPT}$-symmetry to equate this with $\mathcal{CP}$-violation. Direct searches involving matter and antimatter are robust and insensitive to false signals like final state interactions.

Positronium is a bound state of an electron and a positron, and can be copiously produced in a laboratory. This motivates the design and construction of a dedicated detector array to search for $\mathcal{CP}$-violation in the 3-γ decay of ortho-positronium, with a target sensitivity of 10^{-5} for a count asymmetry, a factor of 10 improvement on current limits.

The experiment will require tensor polarized positronium, which can be achieved by utilizing a magnetic field. The sensitivity target will require high statistics and large detector acceptances. To these ends the array will feature three rings of γ-detectors with 16 crystals in each ring. The detector array and all readout electronics will be constructed to fit within the warm bore of the FRIB Positron Polarimeter magnet. Detector geometry and placement were optimized in Monte-Carlo simulations in order to optimize the array for this specific experiment. This allowed optimization of detector size, shape, array geometry, and energy and multiplicity cuts.

Extensive tests of the crystal shape and geometry were performed, these characterized and removed a geometric light collection distortion. A test stand for optimization of positronium formation was constructed. Tests of multiple powders showed that using chunks of silica-aerogel could achieve a lifetime of 135 ns, and up to 40% formation fraction. This was then placed in a 3 crystal demonstrator to prototype the online DAQ. The three crystal and start detector combination was able to remove backgrounds and extract the continuous 2-D energy distribution of ortho-positronium decay.

The direct comparison of measured count asymmetries with theory motivated observables (Lagrangian parameters, mixing coefficients, etc.) is non-trivial, and cannot be done in a model-independent way. A detailed discussion of removal of detector acceptances and efficiencies is

presented in the context of a specific model. This further required extension of the theory analysis to incorporate the effects of a static magnetic field, which induces non-trivial time dynamics of the different angular distributions. This clarifies some inconsistencies in the literature on the time dependence of the asymmetry in a magnetic field. The detector array is under construction and will be able to reach the target sensitivity with 35 days of continuous runtime.

ACKNOWLEDGEMENTS

This will be updated in a future version of the document.

TABLE OF CONTENTS

LIST OF ABBREVIATIONS viii

CHAPTER 1 PHYSICS OF $\mathcal{CP}$-VIOLATION 1
- 1.1 Overview 1
- 1.2 Discrete spacetime symmetries 1
- 1.3 Observed discrete symmetry violations 4
- 1.4 Cosmological considerations 5
- 1.5 Experimental evidence and searches for $\mathcal{CP}$-violation 6

CHAPTER 2 POSITRONIUM AND SEARCHES FOR $\mathcal{CP}$-VIOLATION THEREIN . 8
- 2.1 Overview of positronium physics and history 8
- 2.2 Positronium discovery 10
- 2.3 Overview of 3-photon kinematics 12
- 2.4 Searches for fundamental symmetery violations in positronium 14
- 2.5 University of Michigan $\mathcal{CP}$-violation search 15
- 2.6 University of Tokyo search 17
- 2.7 Theoretical description 18
- 2.8 Spin-1 positronium mixed state 19
- 2.9 3-γ phase space 20
- 2.10 Optimal B-field for tensor polarization 23
- 2.11 Open question about time evolution of signal 29
- 2.12 Our experiment 31

CHAPTER 3 INITIAL DESIGN AND SIMULATIONS 33
- 3.1 Basics 33
- 3.2 Extracting the symmetry violating term 33
- 3.3 Planned experiment 34
- 3.4 Basic geometry 35
- 3.5 Initial positronium event generator 36
- 3.6 Geometric Optimization 38
- 3.7 Summary 43

CHAPTER 4 γ-DETECTOR PROTOTYPING 44
- 4.1 Overview 44
- 4.2 Scintillation detectors 44
- 4.3 Initial tests 47
- 4.4 Single crystal design and simulation 50
- 4.5 First prototype and observed distortion 54
- 4.6 Final crystal results 58

CHAPTER 5 POSITRONIUM FORMATION 60
- 5.1 Overview 60
- 5.2 Ps formation and Positron Annihiliation Lifetime Spectroscopy 60
- 5.3 Ps test stand construction and testing 61

5.4 Time spectrum model . . . 63
5.5 Initial results . . . 64
5.6 Extracting lifetime and formation fraction . . . 66
5.7 Powder tests . . . 74

CHAPTER 6 DESIGN AND SIMULATION OF INNER MODULE . . . 78
6.1 Overview . . . 78
6.2 Start detector and powder formation . . . 78
6.3 Simulation and tracking . . . 80
6.4 β-primary generator . . . 80
6.5 Specification of geometry . . . 81
6.6 Stopping fraction and stopping position . . . 84
6.7 Estimation of pseudo-triplet lifetime . . . 87
6.8 Results for three designs . . . 89

CHAPTER 7 SIMULATION OF γ-DETECTOR ARRAY . . . 94
7.1 Primary event generator . . . 94
7.2 Detector array and configurations . . . 96
7.3 Outline of analysis . . . 100
7.4 Coincidence cuts . . . 101
7.5 Optimization of geometric sensitivity . . . 105
7.6 Estimation of final statistical sensitivity . . . 109
7.7 Spreading of the source, finite energy resolution, and 2-γ backgrounds . . . 110
7.8 Inter-ring Shielding . . . 117

CHAPTER 8 FIRST PROTOTYPE TESTING . . . 123
8.1 Overview . . . 123
8.2 Gamma array support structure . . . 123
8.3 Start detector support structure . . . 125
8.4 Demonstrator . . . 126
8.5 Timing properties . . . 129
8.6 Crystal coincidences . . . 130
8.7 Triple coincidences . . . 135
8.8 ^{22}Na vs. ^{68}Ga . . . 136
8.9 Simulation . . . 139

CHAPTER 9 ANGULAR CORRELATIONS IN 3-γ DECAY OF POSITRONIUM . . . 142
9.1 Form factors in ortho-positronium decay . . . 142
9.2 Detector acceptance and phase space cuts . . . 144
9.3 Extraction of count asymmetry terms . . . 145
9.4 Count asymmetry versus expectation value . . . 147
9.5 Application to our analysis . . . 149

CHAPTER 10 TIME DEPENDENCE IN A MAGNETIC FIELD . . . 160
10.1 Detector efficiencies inducing false asymmetries . . . 161

10.2 Decaying systems 162
10.3 Combined spin-0 and spin-1 Hilbert Space 163
10.4 Time evolution for unpolarized positronium 166
10.5 Including pseudo-triplet events 168
10.6 Energy cuts and 2-γ dilution 169
10.7 Intrinsic detection efficiency 172

CHAPTER 11 SUMMARY AND FUTURE WORK 175

BIBLIOGRAPHY 177

APPENDIX A FULL DESCRIPTION OF PS SPIN STATE FOR SPIN-0 AND SPIN-1 186

APPENDIX B MATRIX ELEMENT AND 3-γ PHASE SPACE 193

LIST OF ABBREVIATIONS

MSU	Michigan State University
FRIB	Facility for Rare Isotope Beams
PMT	Photomultiplier Tube
ADCu	Analog to Digital Converter units
PET	Positron Emission Tomography
SiPM	Silicon Photomultiplier
DAQ	Data Acquisition System
FASTER	Fast Acquisition System for nuclEar Research
WU	Wittenberg University
LPC	Labratoire de Physique Corpusculaire

CHAPTER 1

PHYSICS OF $\mathcal{CP}$-VIOLATION

1.1 Overview

In this chapter we give an overview of discrete spacetime symmetries and their relation to antimatter, fundamentally connected through the $\mathcal{CPT}$-theorem of relativistic quantum field theories. This includes a brief review of the cosmological observations that lead to the widely held belief that there must be more $\mathcal{CP}$-violation than currently accomadated in the Standard Model. Following this is an overview of the history and observation of discrete symmetry violations, culminating in a discussion of $\mathcal{CP}$-violation. Finally motivating neutral mixed matter-antimatter systems as particularly clean systems to search for $\mathcal{CP}$-violation.

As the positron and positronium are both historically important for the conceptual development of quantum field theory, and early precision tests of Quantum Electrodynamics (QED), the discussion begins with a general conceptual overview of antimatter and its natural connection to spacetime symmetries. This will follow the discussions in Refs. [1, 2] but highlighting the role of discrete symmetries.

1.2 Discrete spacetime symmetries

The current most precise framework to describe particle interactions is using relativistic quantum field theory. This describes the interactions of quantized fields in a flat spacetime. The structure of spacetime is taken to be flat Minkowski space following from special relativity. The finiteness of the speed of light means that for any event $(\mathbf{x}, t)$ the whole of spacetime can factor into 5 distinct regions, illustrated in Figure 1.1. These are the timelike future, timelike past, lightlike future, lightlike past, and spacelike separation. Since no signal can travel faster than the speed of light, no two events that are spacelike separated can affect each other.

The five regions of spacetime are invariant under rotations and boosts. This means all inertial reference frames agree on the time order of events that are timelike separated. The concept of cause and effect ("causality") can be applied within the past and future lightcones. However, any

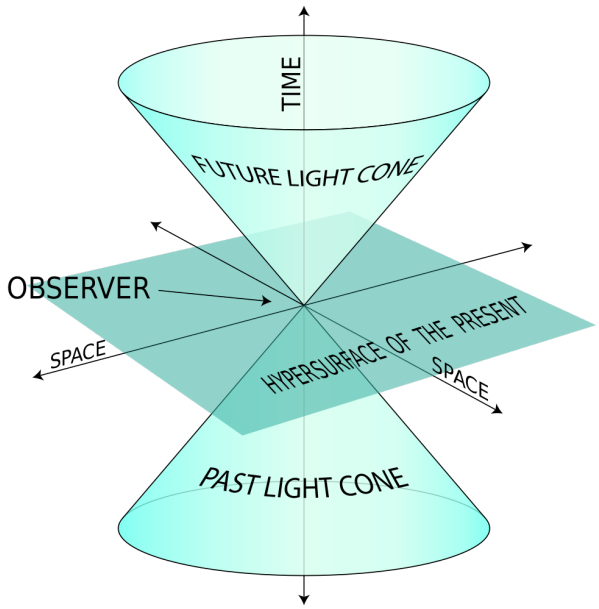

Figure 1.1 Decomposition of Minkowski spacetime into past and future lightcones, and spacelike separated region. Image from Ref. [3]

signal that can reach a spacelike separated event (and therefore travel faster than light) will violate causality. Different observers can disagree on which event was first and which was second (or which was the cause and which was the effect).

Beyond rotations and boosts there are two more spacetime transformations that warrant consideration. The three spatial axes have an intrinsic handedness (right or left), a right handed spacetime cannot be mapped into a left handed through any rotations or boosts, but instead requires a discrete transformation termed "Parity" or $\mathcal{P}$. Similarly, the future and past light cone are individually Lorentz invariant, but they can be mapped between each other through "time-reversal" or $\mathcal{T}$.

Now consider a particle state defined on Minkowski space, it is specified by an energy, momentum, helicity (or chirality), and internal quantum numbers. A state of a single particle of species a can be considered as $|a, \mathbf{p}, \sigma\rangle$, where $\mathbf{p}$ is the momentum and σ is chirality or helicity. Further, consider that this particle has a conserved quantum number, like electric charge, $\hat{Q}\,|a, \mathbf{p}, \sigma\rangle = q_a\,|a, \mathbf{p}, \sigma\rangle$.

Study of the causal structure of relativistic single particle quantum mechanics quickly runs into trouble. The "propagator" gives the amplitude for a particle to travel from position x_i to x_f in time

$t_f - t_i$,

$$K(x_f, t_f; x_i, t_i) = \langle x_f, t_f | x_i, t_i \rangle = \langle x_f | e^{-iH(t_f - t_i)/\hbar} | x_i \rangle \tag{1.1}$$

For the single particle theory to respect causality this should vanish at spacelike separations (ensuring no particle can travel faster than light). Direct computation using the relativistic energy momentum dispersion relations $E = +\sqrt{\mathbf{p}^2 + m^2}$ gives a non-vanishing amplitude at spacelike separations, $\Delta x^2 - c^2 \Delta t^2 > 0$. Instead the propagator falls off like $e^{-\Delta x/\lambda_C}$ for $\Delta x >> c\Delta t$, where λ_C is the Compton wavelength for the particle [1, 2]. This means that relativistic single particle quantum mechanics cannot respect causality on the scale of the Compton wavelength of the particle.

For spacelike separations the order of the two events is dependent on the reference frame of the observer. Instead of abandoning quantum mechanics or special relativity, the solution comes from abandoning a single particle description and instead considering only systems where the particle number can change. So it is in-fact inappropriate, for spacelike separations, to only consider a particle traveling from $(x_i, t_i) \rightarrow (x_f, t_f)$, without also considering a separate particle traveling from $(x_f, t_f) \rightarrow (x_i, t_i)$.

This gives an exact cancellation for propagation across the lightcone when we restrict to only considering observables constructed out of sums of creation operators that create a particle of charge q and helicity σ with destruction operators that annihilates a particle of charge $-q$ and helicity $-\sigma$. This operator is called a "quantum field".

In effect this construction requires that a particle with charge and helicity (q, σ) propagating from $(\Delta x, \Delta t)$ must have a partner with charge and helicity $(-q, -\sigma)$ such that it interferes when travelling from $(-\Delta x, -\Delta t)$ across the lightcone. This partner is called the antimatter partner for the original particle. This construction demonstrates the connection between spacetime symmetries and charge conjugation. The two spacetime intervals, $(\Delta x, \Delta t)$ and $(-\Delta x, -\Delta t)$, are related by a combined parity-time reversal operation $\mathcal{PT}$. Antimatter conceptually arises as a method to ensure causality in a relativistic quantum theory [1, 4, 5], at least in the context of a particle interpretation. It requires most generally that there is a symmetric particle state with opposite charge and opposite helicity. The mapping between these states is anti-unitary and termed Θ [4]. If the theory admits

an operator $\mathcal{P}$ and $\mathcal{T}$, then Θ can be considered as a combined $\mathcal{CPT}$-transformation of the particle state. But this should really be taken as defining the operator $\mathcal{C}$ for the theories that admit a $\mathcal{P}$ and $\mathcal{T}$.

This construction highlights the deep connection between antimatter and spacetime geometry, which appears accidental when presenting each discrete operation individually. It also highlights $\mathcal{CPT}$ as a deep underpinning of the conceptual framework for describing modern physics.

1.3 Observed discrete symmetry violations

All three discrete symmetries $\mathcal{C}$, $\mathcal{P}$, and $\mathcal{T}$ were assumed to be individually respected, and indeed are respected in electromagnetism and strong interactions. Increasingly precise studies of particle properties in the 1950's called these ideas into question. In response to the "θ-τ" puzzle, Lee and Yang proposed that parity may be violated in weak interactions [6]. They formulated an extension of the Fermi theory of weak interactions that allowed for the violation of parity.

This was discovered in the famous Madame Wu experiment in 1957 [7], by the observation that β particles were preferentially emitted opposite to the direction of the spin of a ^{60}Co nucleus. This demonstrated that $\mathcal{P}$ was violated in weak interactions [8].

These experiments did not provide information on possible combined charge-parity symmetry, shortened to $\mathcal{CP}$. Such a test in nuclei would require measuring the angular distribution of β particles from a ^{60}Co nucleus and compare with the angular distribution of β^+ particles from an anti-^{60}Co nucleus [4]. Direct tests of $\mathcal{CP}$-violation prove difficult due to the lack of availability of antimatter.

Nevertheless, $\mathcal{CP}$-violation has been observed in neutral meson physics, first by Fitch and Cronin in neutral kaons in 1964 [9]. The $\mathcal{CP}$-violation in the current Standard Model is very small, entirely contained in the 3x3 Cabibbo-Kobayashi-Maskawa (CKM) quark mixing matrix [10], although there is increasing evidence of a similar mechanism in the neutrino mixing matrix as well [11]. There is good reason to expect that there are as of yet unobserved sources of $\mathcal{CP}$-violation.

1.4 Cosmological considerations

The observed Baryon Assymetry of the universe quantifies the imbalance between matter and antimatter at cosmological scales. It is defined as,

$$\eta = \frac{n_B - \bar{n}_B}{n_\gamma} \tag{1.2}$$

where n_B is the Baryon density, $\bar{n}_B$ is the anti-baryon density, and n_γ is the photon density. Current measurements show this number to be very small $\eta = 10^{-10}$ [12]. In 1967 Andrei Sakharov identified a set of 3 conditions that are sufficient (though not strictly necessary) to generate a baryon asymmetry [12, 13],

1. thermal inequilibrium
2. baryon number violation
3. $C\mathcal{P}$-violation

the first two ingredients are mostly straightforward, the universe must not be in equilibrium, or else as many particles would be becoming antiparticles as the other way around. Similarly, for a net change in baryon number, baryon number must be violated. Understanding the necessity of $C\mathcal{P}$-violation is more nuanced.

It might seem that C-violation alone is enough to generate an imbalance in matter versus antimatter, however this is not the case. Consider a particle X that decays to qq, and its antiparticle $\bar{X}$ that decays to $\bar{q}\bar{q}$, the statement of C-symmetry is that $\Gamma(X \to qq) = \Gamma(\bar{X} \to \bar{q}\bar{q})$. If the universe starts with an equal number of X and $\bar{X}$, then the rate of change of baryon number,

$$\frac{\mathrm{d}B}{\mathrm{d}t} \propto \Gamma(X \to qq) - \Gamma(\bar{X} \to \bar{q}\bar{q}) \tag{1.3}$$

is equal to zero unless C-symmetry is violated. Consider the fact that particles with spin come with a handedness, and that left handed particles are transformed into right handed particles under parity. Now under $C\mathcal{P}$ the particles are mapped such that $X \to \bar{X}$, $q_L \to \bar{q}_R$, $q_R \to \bar{q}_L$, etc. C-violation means that $\Gamma(X \to q_L q_L) \neq \Gamma(\bar{X} \to \bar{q}_L \bar{q}_L)$. However, $C\mathcal{P}$-symmetry means that

$\Gamma(X \to q_L q_L) = \Gamma(\bar{X} \to \bar{q}_R \bar{q}_R)$ and $\Gamma(X \to q_R q_R) = \Gamma(\bar{X} \to \bar{q}_L \bar{q}_L)$. Now if the universe starts with the same amount of X and $\bar{X}$, it can generate a net change in baryon number proportional to,

$$\frac{\mathrm{d}B}{\mathrm{d}t} \propto \Big(\Gamma(X \to q_L q_L) + \Gamma(X \to q_R q_R)\Big) - \Big(\Gamma(\bar{X} \to \bar{q}_L \bar{q}_L) + \Gamma(\bar{X} \to \bar{q}_R \bar{q}_R)\Big) \tag{1.4}$$

which is only non-zero with full $\mathcal{CP}$-violation, not just C-violation. If all X decay to qq and all $\bar{X}$ decay to $\bar{q}\bar{q}$, then once all X and $\bar{X}$'s have decayed the baryon number would return to zero. Further, $\mathcal{CPT}$ requires that the lifetimes of X and $\bar{X}$ must be equal, so there must be competing decay channels as well, $\Gamma(X \to Y)$ and $\Gamma(\bar{X} \to \bar{Y})$. So long as Y has a different baryon number than qq, then a non-zero baryon number can be generated [12, 14].

1.5 Experimental evidence and searches for $\mathcal{CP}$-violation

$\mathcal{CP}$-violation was discovered in the neutral kaon system in which the kaon and anti-kaon mix, further studies have shown $\mathcal{CP}$-violation in B-mesons beyond 5σ as well [10]. These are directly induced by the complex phase of the CKM matrix, and indeed the third generation of quarks was predicted by Koboyashi and Maskawa to explain the $\mathcal{CP}$-violation observed in kaons [15].

Permanent electric dipole moments (EDMs) are highly sensitive to $\mathcal{CP}$-violating physics. Decades of searches for neutron EDMs have tightly constrained possible values of θ_{QCD} [10]. Similar searches for electron EDMs have constrained the possible electric dipole moment of the electron to 10^{-29} $e$cm [16].

There is a distinction between two families of $\mathcal{CP}$-violation searches. One searches for $\mathcal{T}$-odd properties and through $\mathcal{CPT}$-symmetry relates this to $\mathcal{CP}$-violation. This includes EDM searches, and the D-coefficient in β-decay. $\mathcal{T}$-violation can be mimicked in decaying systems by processes that respect $\mathcal{T}$ [17, 18]. In this way, equating $\mathcal{CP}$-violation with signatures of $\mathcal{T}$-violation are technically model dependent interpretations (even when requiring strict $\mathcal{CPT}$-conservation).

Searches for $\mathcal{CP}$-violation that use neutral systems such as kaons, B-mesons, or Z-bosons are termed as "clean signals" of $\mathcal{CP}$-violation, in that they cannot be mimicked in a theory that respects $\mathcal{CP}$. This means that such signals cannot be induced by higher order radiative corrections, or absorptive processes like final state interactions, unless those processes also violate $\mathcal{CP}$-symmetry

[18, 19, 20]. While the interpretation of such signals is very clean, the experiments are hard to perform because of the rarity of such systems limiting the statistical reach of such experiments.

This motivates the use of mixed matter-antimatter bound state searches that utilize systems that can be produced in large quantities, and have moderately long lifetimes. Positronium is one such system.

CHAPTER 2

POSITRONIUM AND SEARCHES FOR $\mathcal{CP}$-VIOLATION THEREIN

In this chapter we give a brief historical overview of the discovery of the positron, and of the bound state positronium. This includes a discussion of some early experimental work that utilized magnetic fields to study the different spin states of positronium. We focus on two previous searches for $\mathcal{CP}$-violation in the angular distribution of the photons from positronium decay, and give a detailed overview of the theoretical description of these searches.

2.1 Overview of positronium physics and history

Antimatter is a generic prediction of relativistic quantum mechanics, historically motivated by the "negative energy" solutions to the Dirac equation. These solutions could not be discarded without sacrificing a Hilbert space interpretation of the solutions. The details of the discussions and theories, along with the resolution are given in Ref. [21].

Dirac's theory generically predicted "positive electrons" or positrons. The positron was quickly discovered in 1932 by Anderson, though it is interesting that positron tracks had been appearing in many cloud chambers for the better part of a decade by this point, but were not identified as such [21]. Figure 2.1 shows one of the cloud chamber images from Anderson's studies. There was a reluctance to equate these positive electrons with the positron from Dirac's theory. The Dirac theory of electrons and positrons was not widely accepted until absorption lengths of the 2.6 MeV γ-ray from ^{208}Tl could not be reproduced without including the pair creation that high energy γ's undergo in matter [21]. In the 1930's this was the highest energy γ source available, and pair creation, which begins to dominate over photo-absorption at higher energies [22], is not even possible below 1 MeV.

As the positron is simply an electron but with positive charge, there is a Coulomb attraction between the two particles. This allows for possible bound states between the two in analogy with the Hydrogen atom. Wheeler proposed that there could be an electron-positron bound state [24]. He coined the term "polyelectrons", and worked out some atomic and molecular properties of the system. A similar proposal by Ruark [25] coined the term "positronium". These initial works

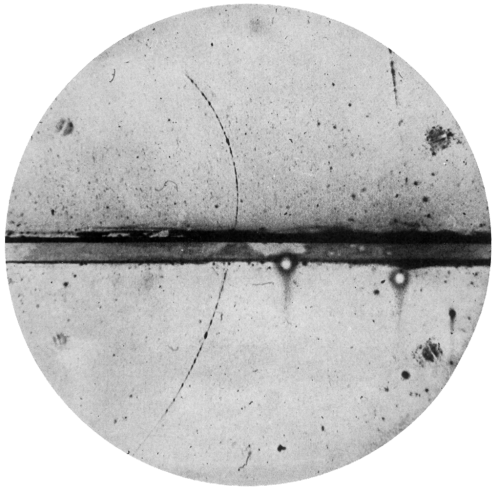

Figure 2.1 Image of positron track in a cloud chamber from Ref. [23].

suggested looking at stellar spectra for the spectral lines that would correspond to positronium, and not the method of directly producing it in the laboratory. Wheeler's work estimated speeds of positron thermalization, and lifetimes of spin-0 ground state positronium. In 1939 Ore and Powell calculated the lifetime of spin-1 positronium and the energy distribution of the photons from unpolarized spin-1 positronium decay [26].

2.1.1 Symmetry properties of positronium and decay selection rules

Positronium has well defined behavior under C and $\mathcal{P}$. Its eigenvalues correspond to $C = (-1)^{L+S}$, and $\mathcal{P} = (-1)^{L+1}$, where L is the orbital momentum, and S is the spin of the bound state [1, 27]. The eigenvalue of the charge conjugation operator is well defined for positronium. As this bound state is mixed matter-antimatter it is mapped back to itself under charge conjugation, unlike charged particles like electrons or protons. In-fact the charge conjugation eigenvalue is only a well defined measurable quantity for neutral particles with no internal conserved quantum numbers [4].

The photon also has a well defined charge conjugation eigenvalue of -1. This follows from Maxwell's equations [27]. This gives the selection rule that dominates the positronium lifetimes. When C is a good symmetry, spin-0 positronium can only decay to an even number of photons and spin-1 can only decay to an odd number.

Positronium has two nearly degenerate ground states separated by an 841 μeV hyperfine interval. The ground state spin-0 positronium is referred to as singlet positronium or "para-positronium"

(p-Ps). Due to the selection rules above it can only decay to an even number of photons, primarily 2. It has a lifetime of 125 ps. Spin-1 positronium is referred to as triplet positronium, or "ortho-positronium" (o-Ps). Due to the C-selection rules it must decay to an odd number of photons, primarily 3. This increases the lifetime of ortho-positronium to 142 ns, over one thousand times longer than para-positronium. Quite generally a spin-1 boson cannot decay to two photons due to the Bose-statistics of the photons [28, 29]. This means that ortho-positronium in general cannot decay to two photons in vacuum for any theory that conserves angular momentum.

2.2 Positronium discovery

Positronium was discovered by Martin Duetsch at MIT in 1951 [30]. The group was studying positron thermalization and annihilation times in different gasses. They had containers filled with gasses (O_2 and N_2), and would bombard them with positrons. They observed a clear drop in time of the amount of annihilation events, not matching the expected 100 ns lifetime of thermalized positrons in gasses. There was a factor of twice as much quenching in Oxygen compared to Nitrogen as well. After multiple experiments Deutsch realized that if some electrons form positronium in the gasses, then that positronium scatters off a gas molecule in such a way that there is a spin flip, the atom would be in a short lifetime state and decay. Then if N_2 and O_2 had similar formation rates, the discrepancy in observed time spectra would be explained by the increased interaction strength between positronium and O_2 causing more spin flips. To test this he added nitric oxide gas and measured the subsequent proportional quenching of the longer lifetime state [30, 31, 32].

2.2.1 Early studies of positronium in a magnetic field

After discovering positronium the MIT group performed further studies of the system. Deutsch performed the calculations of the magnetic mixing of ortho- and para-positronium states that occur in a magnetic field. Since the electron and positron have opposite magnetic moments, the $|s = 1, m = 1\rangle$ and $|s = 1, m = -1\rangle$ states have no net magnetic moment, whereas both $m = 0$ states do have net magnetic moments. This means in a B-field the $|s = 0, m = 0\rangle$ and $|s = 1, m = 0\rangle$ states mix. We call the resulting states "pseudo-singlet" and "pseudo-triplet" states, corresponding to shorter and longer lifetimes respectively [33].

This results in a quenched "pseudo-triplet" state with a lifetime between the long and short lifetimes. Deutsch and Dulit performed coincidence measurements with detectors arranged in a plane perpendicular to the magnetic field and indeed observed a quenching in the counts. They assigned a large uncertainty of 15% to the quoted value.

The lifetime of triplet positronium as calculated by Ore and Powell followed the standard procedure of averaging the initial spin states, and summing over final states. Drisko later observed that this loses some experimentally testable predictions. In particular the observation that the angular distribution of final state photons depends on the initial spin state of the positronium. This intuitively follows from conservation of angular momentum, if the initial positronium carries angular momentum along some axis, the final state of three photons must as well, and therefore likely has a non-trivial angular distribution.

Drisko calculated the angular distortions that occur in QED [34]. This gave the prediction that in the plane perpendicular to the quantization axis, 1/2 of the decays occur from the $m = 0$ state, as opposed to 1/3 as expected by counting statistics.

This led to experiments by Wheatley and Halliday to measure the possible angular dependence to the quenching of counts in a magnetic field [35]. The group measured the coincidence counts for two of the three photons from ortho-positronium decay. The authors utilized a permanent magnet and adjusted the field strength by changing the position. A similar experiment was performed by Hughes, Marder, and Wu [36]. They recorded single counts in the plane perpendicular to the magnetic field axis. They applied a tuneable field using an electromagnet that they powered with two submarine batteries. Both experiments saw a clear quenching that matched the predictions by Drisko. The results from Ref. [36] are shown in Figure 2.2, and show that the data only agrees with the theoretical curve after correcting for the angular dependence.

This non-trivial effect was neglected in the initial Ps experiments in magnetic fields, but was smaller than their large uncertainty estimates. Further experiments that studied the angular distribution of photons from positronium decay searched for more complex distributions. This requires a more thorough discussion of ortho-positronium decay kinematics.

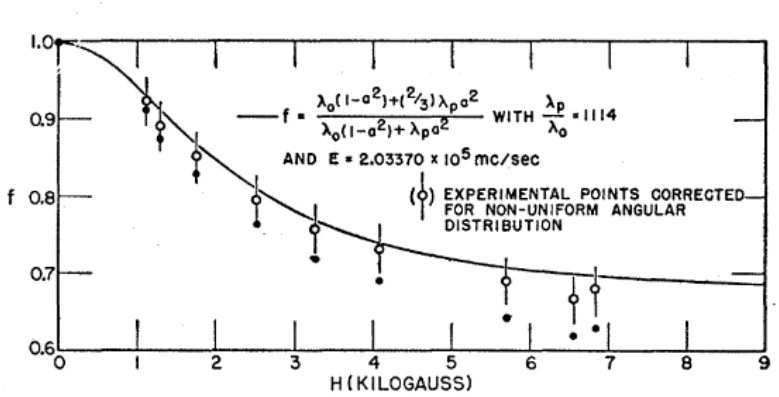

Figure 2.2 Observed quenching of counts in the plane perpendicular to the magnetic field. Experimental data does not agree with the theoretical prediction unless corrected for the angular distribution that occurs in a magnetic-field. From Ref. [36].

2.3 Overview of 3-photon kinematics

The three photons from positronium decay have a continuous energy distribution given by the Ore-Powell distribution [26]. This distribution is shown in Figure **??**. The photons are ordered by their energies, $\omega_1 > \omega_2 > \omega_3$, where $\omega_a = |\mathbf{k}_a|$ is the energy of photon a. The kinetic energy of the positronium is negligible compared to the energies of the photons, so it is safe to assume $\mathbf{k}_1+\mathbf{k}_2+\mathbf{k}_3 \approx \mathbf{0}$. Momentum conservation requires that the three photons are co-planar. Further the event can be fully describe by only observing two of the photons, as the third is entirely constrained kinematically. Figure 2.3c informs the needed detector placement. For instance, measuring $\hat{\mathbf{k}}_1$ and $\hat{\mathbf{k}}_2$ in coincidence requires an angle between the two detectors of $120° - 180°$. The distribution peaks around $160°$.

Figure 2.4 shows the geometry of a decay event. The two photon momenta are confined to a plane. The normal to the decay plane is determined by these momenta, and taken to be $\hat{\mathbf{n}} = \hat{\mathbf{k}}_1 \times \hat{\mathbf{k}}_2$ or any cyclic permutation of indices. Figure 2.4 also includes some axis defined by the positronium state, either the vector polarization or (a component of) the tensor polarization. It is represented with $\hat{\mathbf{s}}$ to match existing literature.

If the vector polarization and tensor polarization lie on the same axis then their values are given by the state populations as,

$$s_z = \frac{N_+ - N_-}{N_+ + N_0 + N_-} \tag{2.1}$$

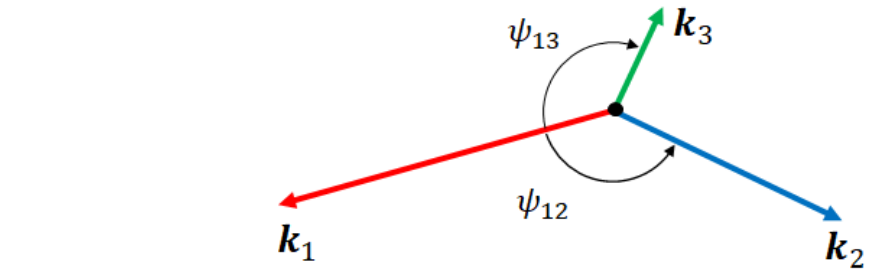

(a)

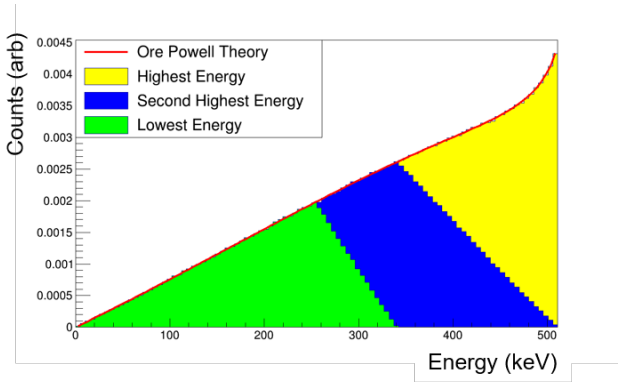

(b)

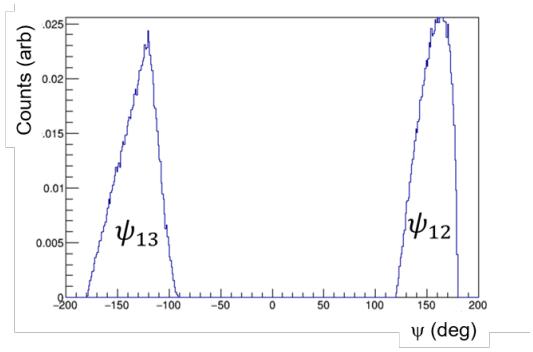

(c)

Figure 2.3 (a) Three photons ordered by their energies $|\mathbf{k}_1| > |\mathbf{k}_2| > |\mathbf{k}_3|$, and respective angles between the photons. (b) Energy distribution of events for each photon, and summed together reproducing the Ore-Powell distribution. (c) Distribution of angles between photons, ψ_{12} shows the optimal detector placement to see the two photons in coincidence.

$$P_2 = \frac{N_+ - 2N_0 + N_-}{N_+ + N_0 + N_-} \tag{2.2}$$

where N_i is the population of the state with $m = i$ along the axis. We call these the polarization and the aligment of the state. We reserve "unpolarized positronium" to refer to a positronium state with neither vector nor tensor polarization.

The charge conjugation properties of the decay are completely fixed by the positronium initial state and the 3-γ final state. This means the observation of parity violation in spin-1 positronium decaying to 3-γ immediately indicates combined $\mathcal{CP}$-violation.

Similar arguments have been applied to argue that an observation of a $\mathcal{P}$-even "$\mathcal{T}$-odd" angular correlation would therefore imply full $\mathcal{CPT}$-violation. This claim is incorrect [19], because $\mathcal{T}$-violation can be mimicked in decaying systems by absorptive processes such as final state interactions [4, 17] Such interactions cannot induce a $\mathcal{CP}$-violating signature in this decay unless

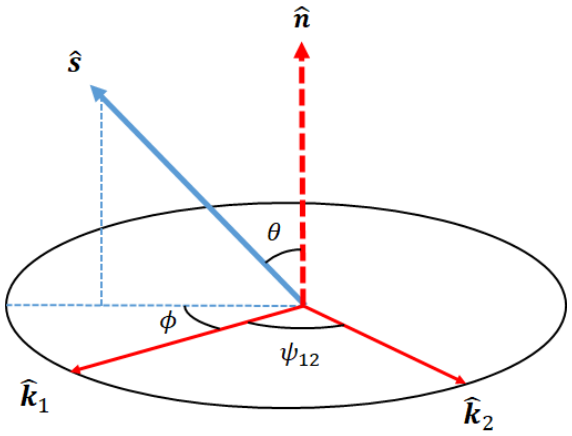

Figure 2.4 $\hat{\mathbf{k}}_1$, $\hat{\mathbf{k}}_2$, and $\hat{\mathbf{k}}_3$ are the 3 linearly independent vectors describing the 3-γ final state. $\hat{\mathbf{s}}$ is the "quantization axis" for the positronium atom, indicative of some axis defined by the positronium state, either by a spin polarization or a tensor polarization.

they also violate $C\mathcal{P}$-symmetry themselves [18].

2.4 Searches for fundamental symmetery violations in positronium

Further studies of positronium were performed in the 80's and 90's by a group at University of Michigan. This group proposed a set of measurements in positronium that would be sensitive to new physics. In Ref. [37] Arbic, Hatamian, Skalsey, Van House, and Zheng proposed and performed a search for an asymmetry in events with the 3-γ decay plane aligned with the initial positronium polarization, or anti-aligned. This would not be induced in the Standard Model except at higher orders due to photon-photon scattering. They performed this search with two sets of NaI detectors read out in coincidence. They utilized parity violation in nuclear β-decay to have polarized positrons that form polarized positronium. They could change the direction of the decay plane by switching which pair of detectors they read out. Utilizing this simple setup they demonstrated the feasibility of such studies. They state that such an asymmetry would be induced by a term in the angular distribution of the form $C_{CPT}\hat{\mathbf{s}} \cdot (\hat{\mathbf{k}}_1 \times \hat{\mathbf{k}}_2)$, coining the term C_{CPT} as the "coefficient" of the "angular correlation" $\hat{\mathbf{s}} \cdot \hat{\mathbf{n}}$. This language matches similar studies in nuclear β-decay, and was suggested by Natchmann. At the end of this work they identify a few other angular distributions that would be indicative of symmetry violations. Of interest for this current work is the "correlation", $(\hat{\mathbf{s}} \cdot \hat{\mathbf{k}}_1)\hat{\mathbf{s}} \cdot (\hat{\mathbf{k}}_1 \times \hat{\mathbf{k}}_2)$ which is odd under parity and would be indicative of $C\mathcal{P}$-violation. They

stated that since $\hat{\mathbf{s}}$ enters this correlation twice it would require tensor polarized positronium in-lieu of vector polarized positronium [37].

In conjunction with this work Bernreuther, Löw, Ma, and Natchmann worked through the general theory of 3-γ decay of spin-1 positronium [19]. They performed a general tensor decomposition to represent the possible angular distributions by irreducible tensors constructed from kinematic vectors each multiplied by a form factor. They then analyzed term by term what symmetries each form factor would respect or violate. They identified four terms that could only be induced by $\mathcal{CP}$ violation, two requiring vector polarized positronium, and two requiring tensor polarized positronium, one of which corresponds to the term referred to as $(\hat{\mathbf{s}} \cdot \hat{\mathbf{k}}_1)\hat{\mathbf{s}} \cdot (\hat{\mathbf{k}}_1 \times \hat{\mathbf{k}}_2)$ above. This is written as $s_{ij}(\kappa_{1i}n_j + \kappa_{1j}n_i)$ in Ref. [19], which highlights the tensorial nature of this quantity, and avoids the possible misconception of equating the vector polarization squared with the tensor polarization, as the two are independent quantities.

To simplify the discussion throughout this work we will use the following notation when discussing unit vectors,

$$\hat{\mathbf{k}}_a = \kappa_{ax}\hat{\mathbf{x}} + \kappa_{ay}\hat{\mathbf{y}} + \kappa_{az}\hat{\mathbf{z}} \tag{2.3}$$

$$\mathbf{n} = \hat{\mathbf{n}} = n_x\hat{\mathbf{x}} + n_y\hat{\mathbf{y}} + n_z\hat{\mathbf{z}} \tag{2.4}$$

where $a = 1, 2, 3$. We take $\mathbf{n}$ to always be a normalized unit vector, otherwize we write $(\hat{\mathbf{k}}_1 \times \hat{\mathbf{k}}_2)$.

For a tensor polarization along the $\hat{z}$-axis this correlation can be reweritten as $\kappa_{1z}n_z$ which is an unambiguous analogue of $(\hat{\mathbf{s}} \cdot \hat{\mathbf{k}}_1)\hat{\mathbf{s}} \cdot (\hat{\mathbf{k}}_1 \times \hat{\mathbf{k}}_2)$, although the two differ by the magnitude of $\hat{\mathbf{k}}_1 \times \hat{\mathbf{k}}_2$. To date there have been two searches for this tensor term that would indicate $\mathcal{CP}$-violation.

2.5 University of Michigan $\mathcal{CP}$-violation search

The first search for the quantity $(\hat{\mathbf{s}} \cdot \hat{\mathbf{k}}_1)\hat{\mathbf{s}} \cdot (\hat{\mathbf{k}}_1 \times \hat{\mathbf{k}}_2)$ was performed at the University of Michigan in 1991 [38]. They utilized the same gamma detector setup used in their previous search for the correlation $\hat{\mathbf{s}} \cdot \hat{\mathbf{n}}$ [37]. Their setup is shown in Figure 2.5. It featured the following components:

1. ^{68}Ga positron emitting β source,

2. Plastic scintillator to detect β emission,

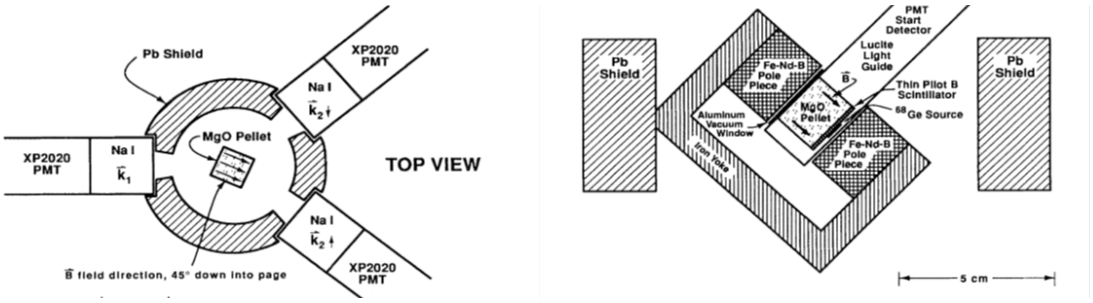

(a) (b)

Figure 2.5 Diagram of the detector setup used for the University of Michigan measurement [38].

3. Magnesium Oxide (MgO) powder for positronium formation,

4. Permanent magnet centered on the positronium source,

5. Three NaI γ-detectors.

They had 9.5% FWHM energy resolution at 511 keV, and 3.9 ns FWHM time resolution between two NaI detectors (for 511-511 coincidences). Their setup featured a dedicated highest energy photon detector, and two second highest energy detectors at 145° from the highest energy detector. These were placed such that the quantity $(\hat{\mathbf{s}} \cdot \hat{\mathbf{k}}_1)\hat{\mathbf{s}} \cdot (\hat{\mathbf{k}}_1 \times \hat{\mathbf{k}}_2)$ is positive for one pair of detectors, and negative for the other pair. They formed a count asymmetry between the two pairs of detectors.

For further control of the systematics they measured in two time windows. The addition of a magnetic field reduces the lifetime of the $m = 0$ state, meaning more $m = 0$ states decay at an earlier time. They state that the alignment of the decaying atoms within a time window will flip sign, the early window is mostly negative from the $m = 0$ decays, and the late window is mostly positive from the $m = \pm 1$ decays. The authors state that they can change the sign of the signal both geometrically, and between two time windows.

They measured a count asymmetry of $A_{Mich} = -0.0004 \pm 0.0010$. They coined the name C_{CP} for the $C\mathcal{P}$-violating coefficient. In effect this is saying that there is a term $C_{CP}(\hat{\mathbf{s}} \cdot \hat{\mathbf{k}}_1)\hat{\mathbf{s}} \cdot (\hat{\mathbf{k}}_1 \times \hat{\mathbf{k}}_2)$, they defined an “analyzing power" as $A = C_{CP}/S_{an}$. This gives their analyzing power as $S_{an} = \frac{1}{2}P_2\langle\cos(2\theta)\sin(\psi_{12})\cos(\phi)\rangle$, where P_2 is the alignment, and θ, ψ, and ϕ are given in Figure

2.4. They estimated their analyzing power as $S_{an} = 0.072 \pm 0.015$, giving a final value for $C_{CP} = -0.0056 \pm 0.0015$.

2.6 University of Tokyo search

A subsequent search was performed at University of Tokyo in 2010 [39]. They used a similar mechanism to form positronium, induce an aligment, and measure a count asymmetry between pairs. They state that the number of events can be written as,

$$N = N_0[1 + C_{CP}(\hat{\mathbf{s}} \cdot \hat{\mathbf{k}}_1)\hat{\mathbf{s}} \cdot (\hat{\mathbf{k}}_1 \times \hat{\mathbf{k}}_2)]e^{-t/\tau} \tag{2.5}$$

where we have slightly changed the notation of unit vectors to match the rest of this discussion. They had two sets of detectors (each with two possible pairings), and placed these detectors on a turntable as shown in Figure 2.6.

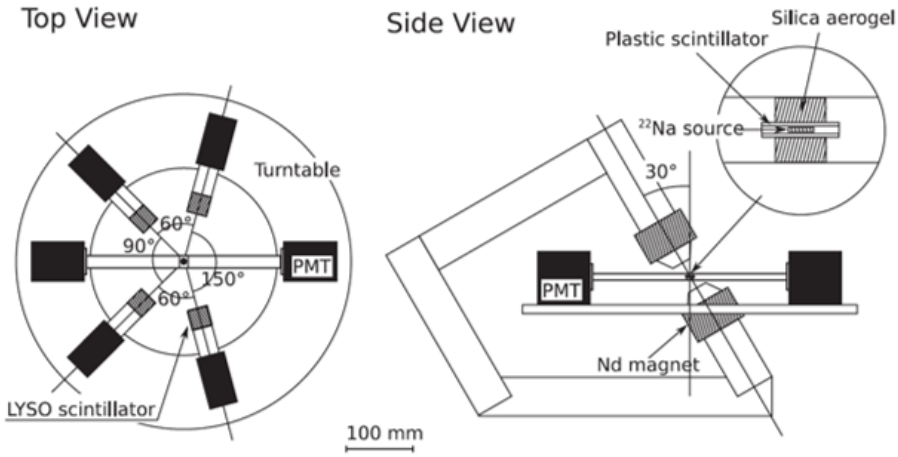

Figure 2.6 Setup for the University of Tokyo search [39].

They formed positronium in silica aerogel, and used a 1 MBq ^{22}Na source for their β^+. Their γ-detectors were LYSO crystals with 11.7% energy resolution FWHM at 511 keV, and 1.2 ns timing resolution FWHM for two 511 keV photons.

If there was a term $(\hat{\mathbf{s}}\cdot\hat{\mathbf{k}}_1)\hat{\mathbf{s}}\cdot(\hat{\mathbf{k}}_1 \times \hat{\mathbf{k}}_2)$ it would create a modulation of counts that goes as $\cos(\phi)$, where ϕ is given in Figure 2.4, which also corresponds to the angle their turntable has rotated. They observed no signal and quote a final value of $C_{CP} = 0.0013 \pm 0.0021(\text{stat}) \pm 0.0006(\text{syst})$. They did not measure in two time windows with flipping alignment, instead they used a 0.49 T

permanent magnet and selected events between 50-130 ns after the β-detection. The experiment collected data for six months and was statistically limited. Their major systematic uncertainties were from the stepper motor that rotated the setup.

2.7 Theoretical description

The authors of Ref. [19] investigated the general form of the 3-γ final state distribution from spin-1 ortho-positronium. For the discussion in this chapter there is no implied summation over repeated indices. They call the mapping of the ortho-positronium state to the 3-γ distribution the "decay matrix". They performed a tensor decomposition on this matrix and identified the 9 independent terms, and what their discrete symmetry properties are. Before summarizing this work we will take one step back to highlight the connection between the decay matrix elements and the time evolution of the positronium states. This will be key to clarifying future discussions in this work.

Start with a pure quantum state $|i\rangle$, this can decay to a variety of final states (for example states with a different number of photons, or different angular distributions of photons). The partial decay rate for this state to a given final state $|f_a\rangle$ is given as $\Gamma_{i\to f_a} = \langle i|\,\mathscr{T}\,|f_a\rangle\,\langle f_a|\,\mathscr{T}\,|i\rangle$, where $\mathscr{T}$ is the "transition matrix", or more standardly the S-matrix [1]. The decay width of the state is given by the sum of the partial decays to all final states, $\Gamma_i = \sum_{f_a}\Gamma_{i\to f_a}$. Assuming the initial state diagonalizes the Hamiltonian then the state will have the following time evolution,

$$|i;t\rangle = \sqrt{N_i}e^{-it\omega_i-\frac{1}{2}t\Gamma_i}\,|i;t=0\rangle \tag{2.6}$$

which reproduces the exponential decay expected for the total number, $N_i(t) = \langle i,t|i,t\rangle = N_i e^{-t\Gamma_i}$. Also consider the population of the final state f_a as $N_{f_a}(t)$. The decay rate of state i, and the rate of population of state f_a as,

$$\dot{N}_i(t) = -N_i\Gamma_i e^{-t\Gamma_i} \tag{2.7}$$

$$\dot{N}_{f_a}(t) = N_i\Gamma_{i\to f_a}e^{-t\Gamma_i} \tag{2.8}$$

Note that $\sum_{f_a}\dot{N}_{f_a}(t) = -\dot{N}_i(t)$, meaning all decaying states decay to some final state. Now consider the rate for some statistical mixture of initial states, for instance in spin-1 $m = +1, 0, -1$, we have

initial populations N_+, N_0, N_-. The final state distribution is,

$$\dot{N}_{f_a}(t) = N_+\Gamma_{+1\to f_a}e^{-t\Gamma_+} + N_0\Gamma_{0\to f_a}e^{-t\Gamma_0} + N_-\Gamma_{-1\to f_a}e^{-t\Gamma_-} \tag{2.9}$$

$$\dot{N}_{f_a}(t) = N_+BR_{+1\to f_a}\Gamma_+e^{-t\Gamma_+} + N_0BR_{0\to f_a}\Gamma_0e^{-t\Gamma_0} + N_-BR_{-1\to f_a}\Gamma_-e^{-t\Gamma_-} \tag{2.10}$$

where $BR_{i\to f_a} = \Gamma_{i\to f_a}/\Gamma$. This can be simplified by invoking rotational invariance, which requires $\Gamma_+ = \Gamma_0 = \Gamma_- = \Gamma$. It does not imply that partial decay rates are equal only the summed final rate [4]. Now consider the final state as a 3 photon state with momenta $(\mathbf{k}_1, \mathbf{k}_2, \mathbf{k}_3)$,

$$\dot{N}(\mathbf{k}_1, \mathbf{k}_2, \mathbf{k}_3) = (N_+R_{++}(\mathbf{k}_1, \mathbf{k}_2, \mathbf{k}_3) + N_{00}R_{00}(\mathbf{k}_1, \mathbf{k}_2, \mathbf{k}_3) + N_-R_{--}(\mathbf{k}_1, \mathbf{k}_2, \mathbf{k}_3))\,\Gamma e^{-t\Gamma} \tag{2.11}$$

where we have introduced $R_{ii}(\mathbf{k}_1, \mathbf{k}_2, \mathbf{k}_3) = \Gamma^{-1}|\langle 3\gamma(\mathbf{k}_1, \mathbf{k}_2, \mathbf{k}_3)|\,\mathscr{T}\,|Ps, i\rangle\,|^2 = BR_i(\mathbf{k}_1, \mathbf{k}_2, \mathbf{k}_3)$. This illustrates that the initial positronium state can be mapped into a distribution of final state photons, and to do so it is useful to introduce some sort of "normalized partial decay rate" that is really just the branching ratio for that initial state to that final state. Following Ref. [19] we refer to this as "the decay matrix". The state populations can be represented in terms of a polarization and an alignment,

$$\dot{N}(\mathbf{k}_1, \mathbf{k}_2, \mathbf{k}_3) = (A(\mathbf{k}_1, \mathbf{k}_2, \mathbf{k}_3) + s_zB_z(\mathbf{k}_1, \mathbf{k}_2, \mathbf{k}_3) + P_2C_{00}(\mathbf{k}_1, \mathbf{k}_2, \mathbf{k}_3))\,\Gamma e^{-t\Gamma} \tag{2.12}$$

where $A = R_{++} + R_{00} + R_{--}$, $B_z = R_{++} - R_{--}$, and $C_{00} = R_{++} - 2R_{00} + R_{--}$. This highlights the dependence of the angular distribution on the polarization (and alignment) of the initial positronium atom. As described here, the formalism is too limiting and cannot accommodate many states of practical importance. To do so we need to use the density matrix as a description of a "mixed" quantum state.

2.8 Spin-1 positronium mixed state

A spin-1 system requires 8 independent numbers to be fully described. These can be taken as the 3 components of the vector polarization, and the 5 components of the tensor polarization (a symmetric traceless tensor) [40]. In the cartesian basis the density matrix takes the simple form,

$$\rho_{ij} = \frac{1}{3}\delta_{ij} + \frac{1}{2i}\sum_k \epsilon_{ijk}s_k - s_{ij} \tag{2.13}$$

where s_i is the ith component of the vector polarization and s_{ij} is the ijth component of the tensor polarization. This is described in more detail in Appendix A.

2.9 3-γ phase space

The final state is described by the massless 3-body Lorentz-invariant phase space for 3 identical particles. In Ref. [19] this is written as $\mathrm{d}\Gamma_f$, but to avoid confusion in future discussions, we will call this $\mathrm{d}f^{3\gamma}$. The form of the 3-body phase space is worked out in detail in many standard texts, for example Ref. [2]. In the center of momentum frame the phase space measure takes the following form,

$$\mathrm{d}f^{3\gamma} = \prod_{j=1}^{3} \frac{\mathrm{d}^3 k_j}{2\omega_j} \frac{\theta(\omega_1 - \omega_2)\theta(\omega_2 - \omega_3)}{(2\pi)^5} \delta\left(\sum_{i=1}^{3} \omega_i - m_{Ps}\right) \delta^{(3)}\left(\sum_{i=1}^{3} \mathbf{k}_i\right) \tag{2.14}$$

where m_{Ps} is the rest mass of the initial positronium, $\omega_j = |\mathbf{k}_i|$ is the energy of the photon, and $\theta(x - y)$ is the Heaviside step function that imposes the energy ordering $\omega_1 > \omega_2 > \omega_3$. The ordering of the photons is a restriction of the phase space so we do not overcount final states. This is ultimately a convention. This is discussed more in Appendix B.

In general any 3-body decay is described by 5 variables. This follows from the 4-momenta of each particle, minus the energy-momentum relation for each particle, total momentum conservation, and total energy conservation. This gets $12 - 3 - 3 - 1 = 5$ independent variables. We can choose these to be the energies of two photons, ω_1 and ω_2, the direction of the normal to the decay plane $\hat{\mathbf{n}}(\theta_n, \phi_n)$, and an azimuthal rotation of $\hat{\mathbf{k}}_1$ within the decay plane, ϕ. The angle between $\hat{\mathbf{k}}_1$ and $\hat{\mathbf{k}}_2$ is fixed by their energies, $\psi_{12}(\omega_1, \omega_2)$.

2.9.1 Tensor decomposition of the decay matrix

The transition matrix maps an initial pure positronium state into a 3-photon final state. Shorten the notation for the state from $|3\gamma; \mathbf{k}_1, \boldsymbol{\epsilon}_1; \mathbf{k}_2, \boldsymbol{\epsilon}_2; \mathbf{k}_3, \boldsymbol{\epsilon}_3\rangle = |3\gamma(\mathbf{k}, \boldsymbol{\epsilon})\rangle$ to match their notation. Take an element of the transition matrix to be $\langle 3\gamma(\mathbf{k}, \boldsymbol{\epsilon})| \mathcal{T} |Ps, i\rangle$. The distribution of final photons for a mixed initial state is given by the decay matrix, which is summed over photon polarizations as those are not measured,

$$R_{ij}(\mathbf{k}_1, \mathbf{k}_2, \mathbf{k}_3) = \Gamma_{o-Ps}^{-1} \sum_{\epsilon} \langle 3\gamma(\mathbf{k}, \boldsymbol{\epsilon})| \mathcal{T} |Ps, i\rangle^* \langle 3\gamma(\mathbf{k}, \boldsymbol{\epsilon})| \mathcal{T} |Ps, j\rangle \tag{2.15}$$

where Γ_{o-Ps} is the vacuum lifetime for ortho-positronium. This is normalized so that,

$$\frac{1}{3}\int \mathrm{d}f^{3\gamma} \sum_i R_{ii}(\mathbf{k}_1, \mathbf{k}_2, \mathbf{k}_3) = 1 \tag{2.16}$$

This contains all measurable information about angular distributions of the photon momenta from an arbitrary mixed $J = 1$ positronium state, assuming photon polarizations are not measured. For an observable defined on the final state the expectation value can be calculated as,

$$\left\langle \hat{O}(\mathbf{k}_1, \mathbf{k}_2, \mathbf{k}_3) \right\rangle_\rho = \hat{O}(\mathbf{k}_1, \mathbf{k}_2, \mathbf{k}_3) \sum_{ij} R_{ij}(\mathbf{k}_1, \mathbf{k}_2, \mathbf{k}_3)\rho_{ij} \tag{2.17}$$

Now perform a tensor decomposition of the decay matrix. As a 3x3 hermitian matrix acting on the spin-1 Hilbert space it can be decomposed into 9 form factors, one scalar, three vector, and five tensor. These can be constructed from the three linearly independent vectors $\hat{\mathbf{k}}_1$, $\hat{\mathbf{k}}_2$, and $\hat{\mathbf{n}}$,

$$R_{ij} = \delta_{ij} a(\omega_1, \omega_2) + \frac{1}{i}\sum_l \epsilon_{ijl} \mathbf{B}_l(\mathbf{k}_1, \mathbf{k}_2, \mathbf{k}_3) - C_{ij}(\mathbf{k}_1, \mathbf{k}_2, \mathbf{k}_3), \tag{2.18}$$

where,

$$\mathbf{B} = \hat{\mathbf{k}}_1 b_1(\omega_1, \omega_2) + \hat{\mathbf{k}}_2 b_2(\omega_1, \omega_2) + \hat{\mathbf{n}} b_3(\omega_1, \omega_2), \tag{2.19}$$

and,

$$\begin{aligned} C_{ij} =& (\kappa_{1i}\kappa_{1j} - \frac{1}{3}\delta_{ij}) c_1(\omega_1, \omega_2) \\ &+ (\kappa_{2i}\kappa_{2j} - \frac{1}{3}\delta_{ij}) c_2(\omega_1, \omega_2) \\ &+ \left(\kappa_{1i}\kappa_{2j} + \kappa_{1j}\kappa_{2i} - \frac{2}{3}(\hat{\mathbf{k}}_1 \cdot \hat{\mathbf{k}}_2)\delta_{ij}\right) c_3(\omega_1, \omega_2) \\ &+ (\kappa_{1i} n_j + n_i \kappa_{1j}) c_4(\omega_1, \omega_2) \\ &+ (\kappa_{2i} n_j + n_i \kappa_{2j}) c_5(\omega_1, \omega_2) \end{aligned} \tag{2.20}$$

Finally, for some observable A on the 3-γ final state, the expectation value is,

$$\langle A \rangle_\rho = \int \mathrm{d}f^{3\gamma} A(\mathbf{k}_1, \mathbf{k}_2, \mathbf{k}_3) \left\{ a(\omega_1, \omega_2) + \hat{\mathbf{s}} \cdot \mathbf{B}(\mathbf{k}_1, \mathbf{k}_2, \mathbf{k}_3) + \sum_{ij} s_{ij} C_{ij}(\mathbf{k}_1, \mathbf{k}_2, \mathbf{k}_3) \right\}. \tag{2.21}$$

where $\hat{\mathbf{s}}$ is the vector polarization, and s_{ij} is the full tensor polarization. This follows from $\langle A \rangle_\rho = \int \mathrm{d}f^{3\gamma} \mathrm{Tr}(AR\rho)$

The authors of Ref. [19] identified the symmetry properties of each form factor and what expectation values it would induce. We shorten these here, so for instance $\langle \hat{\mathbf{k}}_a \rangle_\rho$ means "if this form factor is nonzero then there is a positronium state ρ that would produce a non-zero expectation value for one or more of the components $\langle \kappa_{ai} \rangle$ of photon a". Similarly the tensor terms are shortened, so the term $\langle \hat{\mathbf{k}}_a \hat{\mathbf{k}}_b \rangle_\rho$ really means, "if this form factor is nonzero there is a state ρ that would produce a non-zero value for $\langle \kappa_{ai}\kappa_{bj} + \kappa_{aj}\kappa_{bi} - \frac{2}{3}\hat{\mathbf{k}}_a \cdot \hat{\mathbf{k}}_b \delta_{ij} \rangle$". This is quoted below,

1. $a(\omega_1, \omega_2)$ – The stardard Ore-Powell distribution for unpolarized ortho-positronium decay

2. $b_1(\omega_1, \omega_2)$, $b_2(\omega_1, \omega_2)$ – $\mathcal{CP}$-violating form factors. These would induce non-zero expectation value for $\langle \hat{\mathbf{k}}_a \rangle_\rho$ for any photon k_a. These terms have never been searched for.

3. $b_3(\omega_1, \omega_2)$ – This form factor has been searched for 5 times [37, 41, 42, 43, 44], however it has erroneously been claimed in those searches to be indicative of $\mathcal{CPT}$-violation. A non-zero value would be indicative of new physics, but would give no indication of the symmetry properties of that physics [19]. This term would induce a non-zero value for $\langle \hat{\mathbf{n}} \rangle_\rho$.

4. $c_1(\omega_1, \omega_2)$, $c_2(\omega_1, \omega_2)$, $c_3(\omega_1, \omega_2)$ – These form factors are non-zero in QED, and are precisely the terms measured in the early QED angular anisotropy experiments [35, 36]. These are similar in structure to a "quadrupole deformation" of the distribution of $\hat{\mathbf{k}}_1$, $\hat{\mathbf{k}}_2$, and $\hat{\mathbf{n}}$ respectively. They generate non-zero values for $\langle \hat{\mathbf{k}}_a \hat{\mathbf{k}}_a \rangle_\rho$, $\langle \hat{\mathbf{k}}_a \hat{\mathbf{k}}_b \rangle_\rho$, and $\langle \hat{\mathbf{n}}\hat{\mathbf{n}} \rangle_\rho$

5. $c_4(\omega_1, \omega_2)$, $c_5(\omega_1, \omega_2)$ – These are indicative of $\mathcal{CP}$-violation. They would generate a non-zero expectation value for $\langle \hat{\mathbf{k}}_\alpha \hat{\mathbf{n}} \rangle_\rho$

These functions are given explicitly in Ref. [19], and reproduced here in Appendix B. The authors calculated a, c_1, c_2, and c_3 from QED, and b_1, b_2, c_4, and c_5 in the context of a $\mathcal{CP}$-violating mixing of n^3S_1 and 2^1P_1 states. Though not explicitly stated in Ref. [19] these terms are not completely independent. Within each item above the functions are related due to photon indistinguishability. The relationships are the following,

$$a(\omega_1, \omega_2) = a(\omega_2, \omega_1) \tag{2.22}$$

$$b_1(\omega_1, \omega_2) = b_2(\omega_2, \omega_1) \tag{2.23}$$

$$b_3(\omega_1, \omega_2) = -b_3(\omega_2, \omega_1) \tag{2.24}$$

$$c_1(\omega_1, \omega_2) = c_2(\omega_2, \omega_1) \tag{2.25}$$

$$c_4(\omega_1, \omega_2) = -c_5(\omega_2, \omega_1) \tag{2.26}$$

this is shown for the scalar, vector, and $\mathcal{CP}$-odd tensor terms in Appendix B. c_3 is also related with c_1 and c_2 although it is not transparent in this choice of coordinates.

The $\mathcal{CP}$-violating quantity that has been searched for in Refs. [38, 39] is induced by a nonzero $c_4(\omega_1, \omega_2)$ and $c_5(\omega_1, \omega_2)$. It is important to note that there are actually two terms, and both must be present together due to photon indistinguishability (as shown in Appendix B).

Perhaps most importantly is that no singular number quantifying $\mathcal{CP}$-violation has appeared, like the proposed C_{CP} in Refs. [38, 39]. Instead some model dependent functions of energies, $c_4(\omega_1, \omega_2)$ and $c_5(\omega_1, \omega_2)$, carry the information. It is possible that the terms C_{CPT} and C_{CP} were introduced as a rough characteristic of the scale of the sensitivity. These quantities are inherently model dependent. The structure of the form factors that contribute (a combination of both c_4 and c_5) also eludes any simple factorization into a purely geometric factor multiplied by a purely energy dependent factor.

For this reason we find the terminology "coefficients of angular correlations" to be unclear, as they are functions whose contributions are entwined with the detector placement and energy cuts used in each search.

2.10 Optimal B-field for tensor polarization

Throughout this work Γ_{p-Ps} exclusively refers to the para-positronium lifetime in vacuum, and Γ_{o-Ps} to refer to ortho-positronium lifetime in vacuum. A magnetic field can induce a time dependent alignment in positronium. Denote the relative spin states of the electron and positron as $\left|s_z^p, s_z^e\right\rangle$. These can be combined into states of definite spin in the following combinations,

$$|S = 0, m = 0\rangle = \frac{1}{\sqrt{2}}(|\uparrow\downarrow\rangle - |\downarrow\uparrow\rangle) \tag{2.27}$$

$$|S=1, m=1\rangle = |\uparrow\uparrow\rangle \tag{2.28}$$

$$|S=1, m=0\rangle = \frac{1}{\sqrt{2}}(|\uparrow\downarrow\rangle + |\downarrow\uparrow\rangle \tag{2.29}$$

$$|S=1, m=-1\rangle = |\downarrow\downarrow\rangle \tag{2.30}$$

The introduction of an external B-field breaks overall rotational symmetry, but maintains azimuthal rotational symmetry. This means in general there can be mixing between states with the same m different J, and level splitting between states with different m, but no mixing of states with different m. $\mathcal{CPT}$-symmetry requires that two states related by a $\mathcal{CPT}$-transformation have the same mass and lifetime [4]. The addition of a B-field does not break $\mathcal{CPT}$ symmetry. Under $\mathcal{CPT}$ the $m = \pm 1$ states transform as $\Theta\,|Ps, +m\rangle \rightarrow \zeta_\Theta\,|Ps, -m\rangle$, where ζ_Θ is a phase. This means that in the Standard Model (and most extensions that respect $\mathcal{CPT}$) there is no level splitting between $|Ps, m\rangle$ and $|Ps, -m\rangle$ in a magnetic field to all orders. A more common argument is that $\mathcal{CPT}$ requires the electron and positron have opposite magnetic moments and therefore the net magnetic moment of positronium cancels when the two are spins are parallel. This is a less general argument and does not rule out complicated positronium structure effects, possible higher order interactions, or effects of renormalization of the magnetic moment in the bound state.

Purely by symmetry arguments, positronium in a B-field can only have mixing between states with the same m, and level shifts between states with different $|m|$. The leading order interaction of a positronium atom with a magnetic field is determined by the magnetic moments of the electron and positron. The $|J=1, m=\pm 1\rangle$ are unaffected by the field and can be disregarded in this discussion. In the subspace of $\{|J=0, m=0\rangle, |J=1, m=1\rangle\}$ the Hamiltonian takes the form,

$$H^{ij}_{m=0} = E_0\delta^{ij} - 2\mu B_z\sigma^{ij}_1 - \Delta_{hfs}\sigma^{ij}_3 \tag{2.31}$$

where μ is the magnetic moment of the electron and Δ_{hfs} is the hyperfine splitting of positronium. Define $x = \frac{2\mu}{\Delta_{hfs}}|B| = \frac{|B|}{3.63T}$ the stationary states are [45],

$$|\psi_{pS}\rangle = \cos(\theta)|S=0, m=0\rangle - \sin(\theta)|S=1, m=0\rangle$$

$$|\psi_{pT}\rangle = \sin(\theta)|S=0, m=0\rangle + \cos(\theta)|S=1, m=0\rangle$$

$$E_{pS} = E_0 - \frac{1}{2}\Delta_{hfs}(1 + \sqrt{1+x^2}) \tag{2.32}$$

$$E_{pT} = E_0 + \frac{1}{2}\Delta_{hfs}(1 + \sqrt{1+x^2}) \tag{2.33}$$

$$\cos(\theta) = \frac{1}{\sqrt{2}}\sqrt{1 + \frac{1}{\sqrt{1+x^2}}} \tag{2.34}$$

where pS is short for "pseudo-singlet" and pT is short of "pseudo-triplet". Finally, the singlet and triplet states have relative lifetimes $\tau_{p-Ps} = 124$ ps and $\tau_{o-Ps} = 142$ ns. This results in the new mixed lifetimes,

$$\Gamma_{pS} = \cos^2(\theta)\Gamma_{p-Ps} + \sin^2(\theta)\Gamma_{o-Ps} \tag{2.35}$$

$$\Gamma_{pT} = \sin^2(\theta)\Gamma_{p-Ps} + \cos^2(\theta)\Gamma_{o-Ps} \tag{2.36}$$

even at modest field values of the order of 1 Tesla, there is only a small amount of mixing but a large quenching of the lifetime. This is shown in Figure 2.7, which shows the ortho-positronium decay rate in vacuum and in a magnetic field. This follows from the factor of 10^3 difference in the lifetimes of singlet and triplet positronium. This induces a time evolution of the effective $m = 0$ state relative to the $m = \pm 1$ states, allowing for separation of the different spin states of the resulting positronium (by careful selection of time cuts).

The instantaneous alignment for a decay event is,

$$P_2(t) = \frac{n_T(t) - 2n_{pT}(t)}{n_T(t) + n_{pT}(t)} \tag{2.37}$$

where $n_i(T) = N_i/\tau_i e^{-t/\tau_i}$ is the instantaneous rate of decays from that state, and N_i is the initial population of that state. Averaging over a time window, not all events have the same alignment. The average needs to be weighted by the number of decays with that alignment,

$$\langle P_2 \rangle_\rho = \frac{\int P_2(n)\mathrm{d}n}{\int \mathrm{d}n} = \frac{\int P_2(t)\frac{\mathrm{d}n}{\mathrm{d}t}\mathrm{d}t}{\int \frac{\mathrm{d}n}{\mathrm{d}t}\mathrm{d}t} \tag{2.38}$$

with the number of decays being the infinitesimal times the rate,

$$\langle P_2 \rangle_\rho = \frac{\int \mathrm{d}t \left(\frac{n_T(t) - 2n_{pT}(t)}{n_T(t) + n_{pT}(t)}\big(n_T(t) + n_{pT}(t)\big)\right)}{\int \mathrm{d}t \big(n_T(t) + n_{pT}(t)\big)}$$

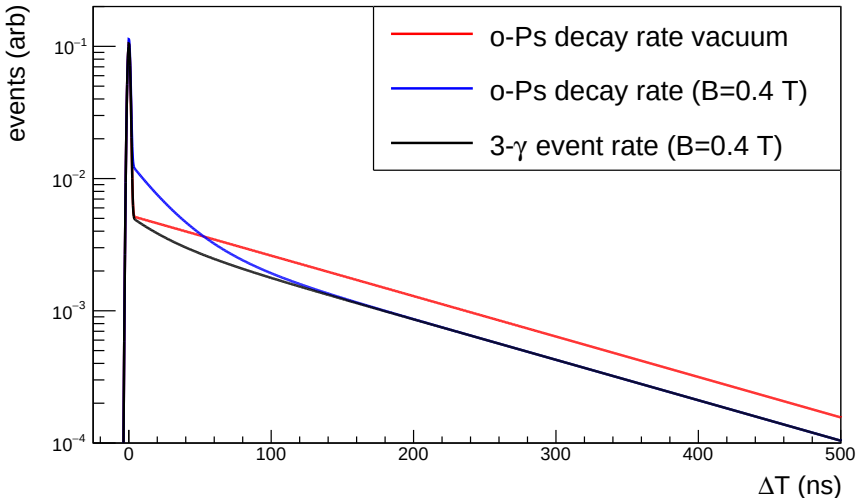

Figure 2.7 Time spectrum for positronium decay. The time spectrum for positronium in vacuum is shown in red. The addition of a B-field shifts one lifetime component to be shorter, shown in blue. At the same time, the B-field shortens the lifetime by opening up a decay channel to 2γ, so the actual number of 3-γ events for this component is greatly reduced (black).

$$= \frac{\left(N_T e^{-t/\tau_T} - 2N_{pT} e^{-t/\tau_{pT}}\right)\Big|_{t_2}^{t_1}}{\left(N_T e^{-t/\tau_T} + N_{pT} e^{-t/\tau_{pT}}\right)\Big|_{t_2}^{t_1}} \tag{2.39}$$

for the time window $[t_1, t_2]$.

However, this has not included the changing branching ratios. This new pseudo-triplet state has some probability to decay to 2-photons and some to 3-photons. Figure 2.7 shows the ortho-positronium decay rate in a magnetic field, and the rate of 3-γ decays. There is a net quenching of 3-γ decays at early times (from the pseudo-triplet). This means increasing the field value also decreases the statistics. The relationship is given as

$$BR(\text{o-Ps} \rightarrow 3\gamma) = BR_{3\gamma} = \tau_{pT}/\tau_{o-Ps} \tag{2.40}$$

The alignment increases for larger B, but the counts decrease. To identify an optimal field value it is necessary to define a "Figure of Merit". Consider the statistical sensitivity, doubling the tensor polarization doubles the size of the asymmetry; but doubling the branching ratio only increases the statistical sensitivity by a factor of $\sqrt{2}$. Take the Figure of Merit as,

$$FoM = \langle P_2(B) \rangle_\rho \sqrt{N(B)} \tag{2.41}$$

Returning to Equation 2.39 shows that the Figure of Merit is defined for some time window. To match the Michigan experiment we identify 2 time windows with opposite tensor polarizations, a start window of 10 ns, and a stop of 500 ns. This determines the time cut between the two windows. The result of optimal time cut versus lifetime for these time windows is plotted in Figure 2.8.

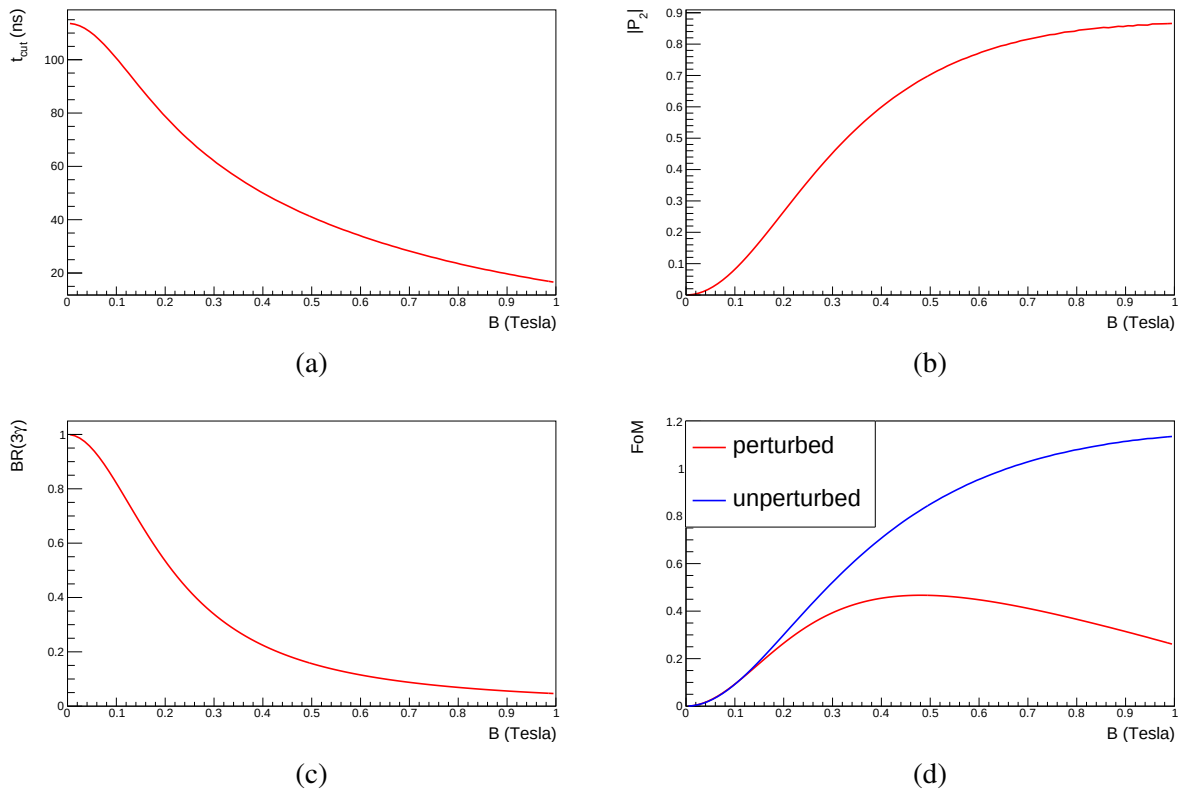

Figure 2.8 The effect of a magnetic field on positronium. (a) The optimal timing cut between two time windows to form populations with opposite tensor polarization (given an initial time start at 10 ns and final at 500 ns. (b) The instantaneous alignment for the population. (c) The tradeoff with increasing tensor polarization is the decreasing branching ratio decreasing statistics. (c) The Figure of Merit, tensor polarization weighted by square root of the counts. For the perturbed time window there is a clear optimal value between 0.4-0.5 Tesla. For unperturbed the optimal choice is as large a field as possible (kill the pseudo-triplet and only take triplet events with complete tensor polarization).

The Figure of Merit versus the B-field is shown in Figure 2.8d. This shows a value around 0.45 Tesla optimizes the statistical sensitivity. This is in agreement with the field values used in the previous experiments. The time spectroscopy related quantities from Refs. [38, 39] are tabulated in Table 2.1. This includes our attempt to reproduce the quoted alignment values using Equation 2.39.

We do not expect a perfect reproduction of their quoted values because they include corrections for systematic effects. However we are not able to reproduce the quantities quoted in both texts.

Group	τ_{pT} (ns)	τ_T (ns)	t_0 (ns)	t_1 (ns)	Calculated $\langle P_2 \rangle$	Quoted $\langle P_2 \rangle$
Michigan						0.37
	30	124	10.3	64.6	−0.43	negative
	30	124	65	270	0.68	positive
Tokyo	22.5	126	50	130	0.57	0.87

Table 2.1 Summary of time-spectroscopy related quantities for Refs. [38, 39], and our attempt to use Equation 2.39 to reproduce their quoted alignments. Our estimation does not include any systematic corrections they may have applied.

There is one systematic effect that is particularly important for this discussion and that is "the 2-γ dilution". The quenching of the $m = 0$ triplet state is performed by mixing with singlet state, allowing decay to 2-γ. As the vacuum decay strength for para-positronium to 2-γ is a factor of one thousand times greater than ortho-positronium to 3-γ, a small mixing induces a large branching ratio to 2-γ for the pseudo-triplet state. This means that the relative 2-γ and 3-γ branching ratios are different for the different spin states.

The University of Michigan group considered the 2-γ dilution in terms of how many 2-γ events could mimick a true 3-γ decay (by Compton scattering in such a way that they passed the energy cuts). They determined that 12.8% of the events in the first time window were due to 2-γ events, and 3.8% for the second time window. Indeed taking our calculated $\langle P_2 \rangle$ for the first time window and correcting by a 12.8% dilution recovers an averaged alignment of -0.37. It has little to no change on the second time window.

We can recover the University of Tokyo group's value by applying the 2-γ quenching correction to the pseudo-triplet's contribution to the signal. They calculate the alignment as,

$$\left\langle P_2' \right\rangle_\rho = \frac{\left(N_T e^{-t/\tau_T} - 2N_{pT} BR_{3\gamma} e^{-t/\tau_{pT}} \right) \Big|_{t_2}^{t_1}}{\left(N_T e^{-t/\tau_T} + N_{pT} BR_{3\gamma} e^{-t/\tau_{pT}} \right) \Big|_{t_2}^{t_1}} \tag{2.42}$$

where the dilution is included in terms of the state that it relates to. Our estimation produces a value of 0.91 using this definition.

Ultimately it is not immediately clear how the alignments were calculated, or how 2-γ dilutions were accounted for. It does seem that these were treated by mutually exclusive methods by both groups.

2.11 Open question about time evolution of signal

According to the theoretical analysis in Ref. [19] the angular anisotropies are proportional to the tensor polarization, both the QED anisotropy (due to the form factors c_1, c_2, and c_3) and the possible $\mathcal{CP}$-odd anisotropy (due to c_4 and c_5). The QED anisotropy was measured by the groups of Wheatley and Hallidy, and Hughes, Marder, and Wu in Refs. [35, 36]. These groups used a magnetic field to quench the $m = 0$ state. Similarly, the University of Michigan group used a magnet to quench the $m = 0$ state and searched for the $\mathcal{CP}$-odd tensor form factor. In this experiment the authors induced a time dependence and state that the signal changes sign between two time windows due to the flipping of the alignment (more $m = 0$ decay at early times, and more $m = \pm 1$ at late times). These three 3 claims are irreconcilable.

Firstly, at any given time the number of 3-γ events in a B-field will always be less than in a vacuum. This can be seen quite generally as follows, take a state A with partial width Γ_{AB} to state B. Now suppose we can turn on a new final state C with partial width Γ_{AC}. This decreases the lifetime, so it might seem like more B states will get populated early, but in-fact decreasing the lifetime by opening new channels will always decrease the instantaneous rate of decay to the existing channels as well. This can be explicitly shown as follow, take the difference between the two rates of decays to the state B,

$$\begin{aligned}
\Delta\Gamma_{AB}(t) &= \left((\Gamma_{AB}+\Gamma_{AC})BR_{A\to B}e^{-(\Gamma_{AB}+\Gamma_{AC})t} - \Gamma_{AB}e^{-\Gamma_{AB}t}\right) \\
&= \left((\Gamma_{AB}+\Gamma_{AC})\frac{\Gamma_{AB}}{\Gamma_{AB}+\Gamma_{AC}}e^{-(\Gamma_{AB}+\Gamma_{AC})t} - \Gamma_{AB}e^{-\Gamma_{AB}t}\right) \\
&= \Gamma_{AB}e^{-\Gamma_{AB}t}\left(e^{-\Gamma_{AC}t} - 1\right) \qquad (2.43)
\end{aligned}$$

$$\Delta\Gamma_{AB}(t) < 0 \qquad (2.44)$$

The takeaway being that, the 3-γ rate will always be decreased at all times in the presence of a magnetic field.

According to the tensor decomposition into irreducible form factors in Ref. [19], the QED anisotropy and the $C\mathcal{P}$-odd tensor correlation must have the same dependence on the positronium state ρ, which in Ref. [19] is parameterized by the tensor polarization. But as argued in Equation 2.39, starting with an even state population in a B-field the decaying positronium will have a tensor polarization of changing sign that averages to zero (in the end all the states decay and we started with a uniform state population). But this is at odds with the experimental results from the early QED anisotropy measurements. In Ref. [36], they placed their positronium in a magnetic field and measured the reduction of counts in the plane perpendicular to the B-field axis. However they did not measure a time spectrum, they did not trigger on the β-emission and record a time difference between Ps formation and decay. This means they were only sensitive to a net anisotropy. They observed that in a B-field the net angular distribution of 3-γ decays was anisotropic, it did not distort in a positive way at early times then flip to a negative distortion at later times such that the total decay distribution was isotropic.

The entire line of symmetry violating angular distribution searches in positronium decay was started by the pioneering studies at University of Michigan, they identified the correlation $\langle n_z \rangle$ as a correlation that would indicate new physics, and as it is a vector correlation would require polarized positronium. At the end of Ref. [37] they identified the tensor correlation $\langle \kappa_{1z} n_z \rangle$ as being indicative of $C\mathcal{P}$-violation, and as it is a tensor correlation it would require tensor polarized positronium. This statement is unequivocally true.

The authors of Ref. [19] worked out the general theory of angular correlations in 3-γ decay of ortho-positronium. They worked out that the tensor terms in the angular distribution would be driven by the tensor polarization in the positronium, which would imply for these experiments a signal that integrates to zero over the full time spectrum. The inconsistency between the Michigan treatment and the early QED anisotropy tests comes from the assumption of rotational invariance in the theoretical treatment. The authors of Ref. [19] equated the tensor term in the positronium state with the tensor term in the final state photon distribution, however the addition of a B-field has broken rotational invariance, total angular momentum and tensor polarization are no longer

conserved quantities in the positronium time evolution and decay. Indeed a direct consequence of rotational invariance is that all m states have the same lifetime and energy [4] which is certainly not the case for Ps in a B-field. This further means that this analysis evades a simple rate-like equation like that given in Equations 2.5 and 2.12. Any such equation cannot be correct as the positronium state is a combination of different lifetime components. Indeed when we illustrated the time dependence of the various angular distributions in Equations 2.9 through 2.12 we had to invoke rotational invariance to factor out the overall exponential and re-write the time dependence of the angular correlation in terms of the alignment.

The analysis of Ref. [19] is directly applicable to tensor polarized positronium without an external field. This can only be produced by impinging polarized positrons on polarized electrons (this is calculated in Appendix A). A proper accounting of the angular correlations including the induced time-dependence will require further in-depth analysis and will be the main focus of Chapter 10.

For the majority of this work it is sufficient to assume that we have a tensor polarized positronium source without entering into the details of the pseudo-triplet state and 2-γ branching ratio. We could realize this experimentally by using the B-field to quench the pseudo-triplet and choosing a time window after the pseudo-triplet has decayed. This of course still has the broken rotational invariance, however there is no level splitting between the $|S = 1, m = \pm 1\rangle$ states in a magnetic field, and so at late times the B-field is having no effect on the dynamics. The system can be treated as if it had a maximal positive tensor polarization. This is how we will interpret the analysis for most of this work. Throughout we will treat the direction of alignment, and the axis of the B-field as intechangeable concepts, at least insofar as their effect on our observable.

2.12 Our experiment

We intend to measure the $C\mathcal{P}$-odd tensor form factors $c_4(\omega_1, \omega_2)$ and $c_5(\omega_1, \omega_2)$ and to achieve a 10-fold improvement in sensitivity over previous experiments. Our planned experiment is structurally similar to the Michigan experiment, with the addition of greatly increased solid angle coverage, and replacing the permanent magnets with an electromagnet. This requires designing

and constructing a dedicated detector array from scratch.

CHAPTER 3

INITIAL DESIGN AND SIMULATIONS

This Section covers the general design work in close contact with the analytic structure of the Ps decay distribution. First we discuss extracting the signal by taking an asymmetry. This is followed by a brief discussion of our superconducting magnet, that serves as the main geometric constraint for the experiment. Next we outline the basics of the geometry forming "configurations" between sets detector pairs. We identify both a cylindrical array and spherical array geometry. These have tradeoffs between solid angle, analyzing power, and detector efficiency (by varying possible detector sizes). Further investigation requires defining a "Figure of Merit" to weight sensitivity of different designs.

3.1 Basics

The experiment follows the basic structure of the University of Michigan measurement [38]. They had a triplet of detectors, one for highest energy, two for second highest, centered on a positronium source. This is illustrated in Figure 3.1a. They oriented the detectors such that the signal is positive or negative between the two pairs of detectors.

Now as we need very high statistics we must fit as many sets of detectors in the array as possible, with the constraint that the magnetic field is horizontal. This leads to the conceptual design shown in Figure 3.1b, circular rings of detectors following the cylindrical geometry of the magnet. This will allow many detector combinations between the rings, and leads to a dramatic increase in the number of possible detector pairs.

3.2 Extracting the symmetry violating term

The previous measurements utilized an "asymmetry" to extract the symmetry violating term [38, 39]. They took two pairs of detectors that see some number of decay events. Call these UP and DOWN. The coincidence counts go as,

$$N_U = N(1 + P_2 \alpha G_{an}) \tag{3.1}$$

$$N_D = N(1 + P_2 \alpha (-G_{an})) \tag{3.2}$$

(a) (b)

Figure 3.1 (a) A single "configuration", a set of three detectors taken in two pairs, sharing a highest energy detector. (b) Rotating the configuration around the B-field allows many sets of detectors to be placed in a ring.

where N is the total normalization, P_2 is the alignment, G_{an} is the "geometric analyzing power" and purely dependent on the geometry of the event, and α is the symmetry violating term. They defined their analyzing power as $G_{an} = \kappa_{1z}(\hat{k}_1 \times \hat{k}_2)_z$ and we will mirror this analysis until Chapter 9, whose main purpose is to define an analyzing power in the context of the theoretical analysis of Ref. [19]. The detectors were arranged so that G_{an} changes sign between the two configurations. α could then be extracted by taking an asymmetry,

$$\alpha = \frac{1}{P_2 G_{an}} \left(\frac{N_U - N_D}{N_U + N_D} \right) \tag{3.3}$$

This cancels the total normalization, and the background cannot induce a false signal. An additive background does increase the denominator, and therefore reduces the sensitivity.

3.3 Planned experiment

Our planned setup will closely mirror the University of Michigan setup, and is described in Ref. [46]. Both previous experiments were sensitive to possible asymmetries induced by γ's scattering on their iron magnets. We will remove this effect by designing the entire experiment to fit inside the Positron Polarimeter magnet, a superconducting magnet with maximum field value of 2 Tesla at FRIB.

This will be the primary geometric constraint for the experiment, the diameter of the warm

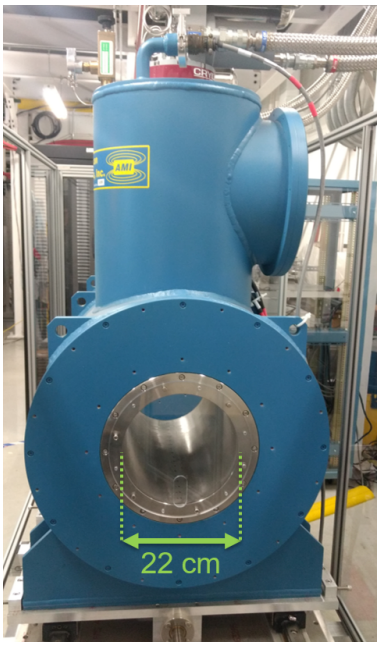

Figure 3.2 One of the two FRIB Positron Polarimeter magnets. Our detector array will be placed in the warm bore of the magnet.

bore is 22 cm. We will utilize the same general principle for positronium formation as the previous experiments. The primary goal will be to fit as many γ-detector sets in the magnet as possible to achieve a large increase in statistical sensitivity. This will require relatively small scintillators ideally read out directly in the magnet, mounted onto an array with many sets aimed at the central source.

3.4 Basic geometry

Fix the B-field direction along the $\hat{z}$-axis. Following Ref. [39], define the "geometric analyzing power" for an event as the $\hat{z}$ component of $\hat{\mathbf{k}}_1$ multiplied by the $\hat{z}$ component of the normal to the decay plane, $G_{an} = \kappa_{1z}(\hat{\mathbf{k}}_1 \times \hat{\mathbf{k}}_2)_z$. The larger this quantity the better the sensitivity. Here we discuss the purely analytic information that can be gleaned for this design. Parameterize the detector pairs as shown in Figure 3.3a. Hold the cylindrical radius constant, and plot G_{an} versus the position along z. Define the unitless position of the ring that detects the higher energy photon as $\chi_1 = \rho_1/z_1$, and the ring that detects the second highest energy photon as $\chi = -\rho_2/z_2$. This

gives the geometric analyzing power as,

$$G_{an} = \frac{\chi_1 \sin(\Phi)}{(1+\chi_1^2)\sqrt{1+\chi_2^2}} \tag{3.4}$$

Plotting this for fixed $\Phi = 90°$ gives the distribution shown in Figure 3.3b. This alone does not determine the optimal detector placement as it includes no actual information about the positronium decay. Kinematically the opening angle is constrained between 120° and 180°, as shown in Figure 2.3c. To investigate this we must simulate the distribution of 3 photon events and create a Figure of Merit, weighting the geometric sensitivity by the statistical sensitivity.

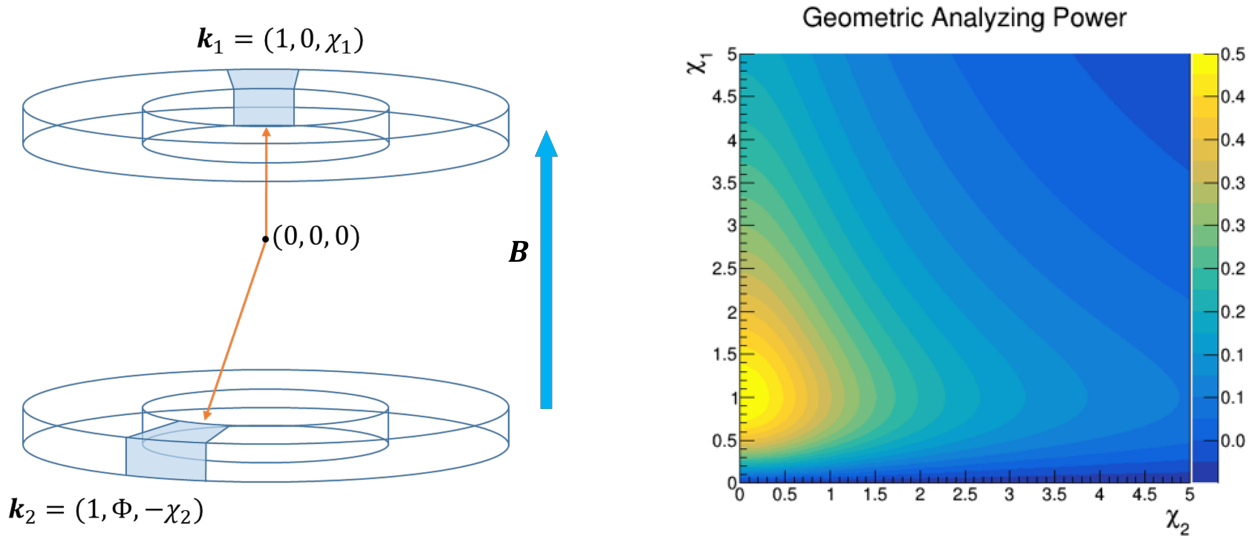

(a) (b)

Figure 3.3 (a) The coordinate system for the cylindrical ring geometry, where $\chi_1 = z_1/\rho_1$, and $\chi_2 = -z_2/\rho_2$. (b) The geometric analyzing power for that ring placement (plotted for $\Phi = \pi/2$). This does not account for kinematics and includes non-physical regions

3.5 Initial positronium event generator

The phase space for a three-body decay to zero mass particles is flat in ω_1 vs ω_2. The angles between the photons is entirely determined by their energies and is given as,

$$\cos(\psi_{ij}) = 1 - 2m_e \frac{\omega_i + \omega_j - m_e}{\omega_i \omega_j} \tag{3.5}$$

The energy distribution for unpolarized ortho-positronium decay follows the Ore-Powell distribution [26],

$$\propto \frac{1}{\omega_1\omega_2\omega_3}\{(1-\cos(\psi_{12}))^2 + (\text{cycl. perm.})\} \tag{3.6}$$

This is taken as a probability distribution function, and two energies are sampled from it. Start with $\hat{\mathbf{k}}_1$ along the $\hat{x}$-axis, and $\hat{\mathbf{n}}$ along the $\hat{z}$-axis. With these specified, the direction of $\hat{\mathbf{k}}_2$ is fully determined, since the angle between $\hat{\mathbf{k}}_1$ and $\hat{\mathbf{k}}_2$ is dependent on the energies $\psi_{12}(\omega_1, \omega_2)$. Now generate a random angle ϕ and rotate both $\hat{\mathbf{k}}_1$ and $\hat{\mathbf{k}}_2$ around $\hat{\mathbf{n}}$ by the angle ϕ. Finally a random direction is thrown, and the decay plane is rotated so that the normal points in this direction.

Note that the angular distribution and energy distribution are fundamentally intertwined. Specifying an opening angle between detectors inherently determines an energy range for 3 photon events, as shown in Figure 3.4. In practice this means when we place a pair of detectors we are selecting this wedge of phase space. Finite detector solid angle will make the wedge wider. For this reason we must investigate the angular distribution and energy distribution in parallel. Detector placement and energy dependent effects (cuts, resolution, efficiency) are considered in a combined way.

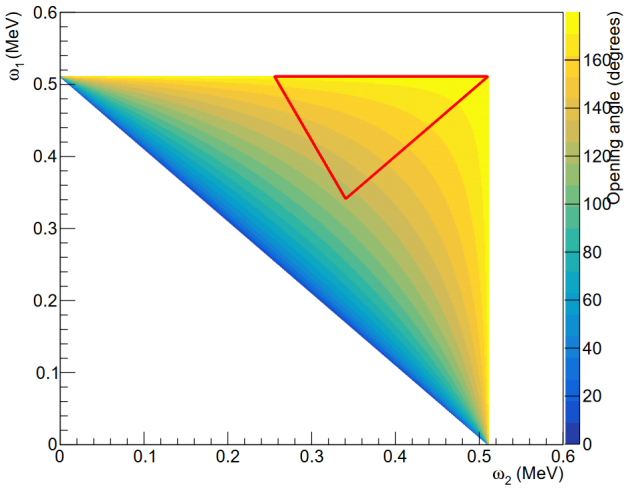

Figure 3.4 Given the energy of two photons ω_1 and ω_2, the opening angle is entirely determined kinematically. In red the phase space restriction of $\omega_1 > \omega_2 > \omega_3$ restricts events to this region.

3.6 Geometric Optimization

To compare different designs we must define a quantitative Figure of Merit that combines the geometric analyzing power with the statistical weight of the number of the events,

$$FoM = G_{an}\sqrt{N} \tag{3.7}$$

It is worth stressing that Φ in Equation 3.4 is the standard cylindrical axial coordinate, not the angle between the two photons, the two are related but that relation depends on the distance between the rings. Now as this is a function of three variables we need to make some simplifications.

Firstly, consider two symmetrically placed rings, $\chi_1 = \chi_2 = \chi$. The Figure of Merit as a function of χ versus Φ is shown in Figure 3.5. This shows that the sensitivity maximizes between $130 - 165°$, with ring placement $0.3 < \chi < 0.8$, this corresponds to an angle between the central ring and the outer ring of $11° < \beta < 39°$.

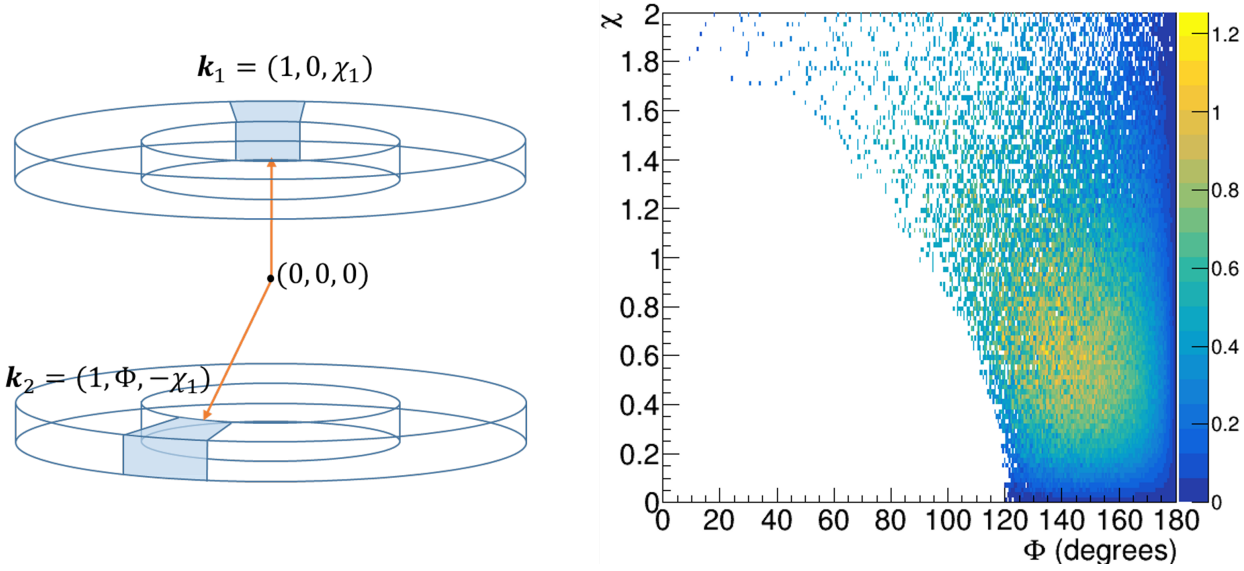

Figure 3.5 Symmetric configuration, two rings symmetrically placed. The corresponding Figure of merit is shown for the ring placement.

Now consider a second configuration, where one ring is centered on the positronium source. Plotting the Figure of Merit for events where the highest energy photon hits the outer ring, and the second highest hits the central ring as a function of the placement of the outer ring gives Figure 3.6. Comparing the two distributions shows the optimal placement of the outer ring lines up for both

configurations. This means we can consider a three ring design, with symmetric configurations and asymmetric configurations.

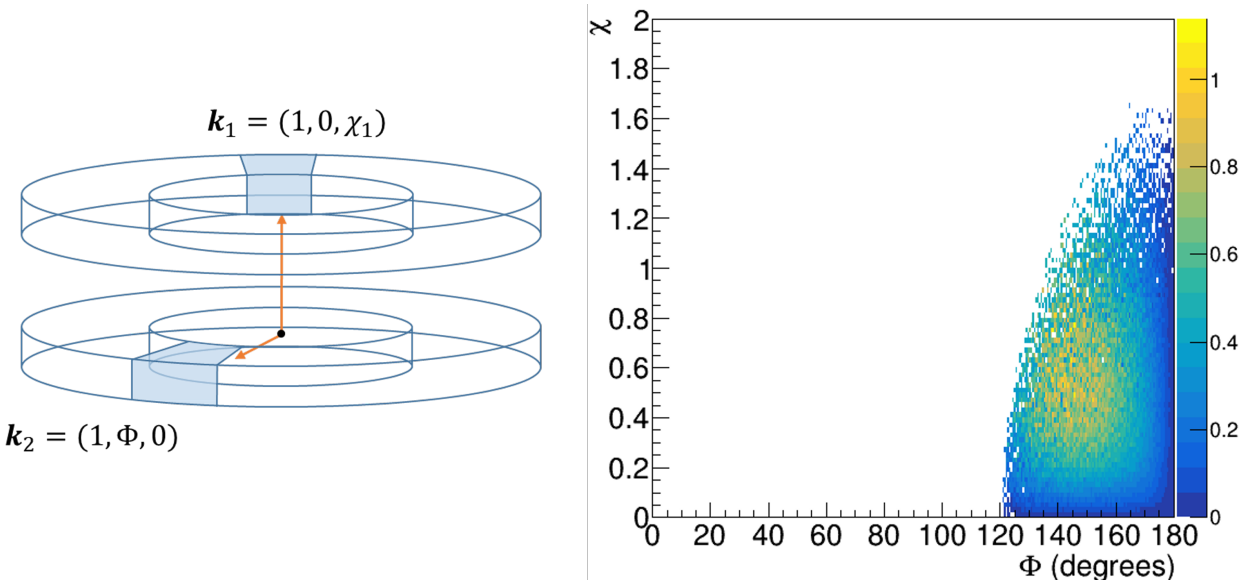

Figure 3.6 Asymmetric configuration, one ring centered around the source with another offset along the B-field axis. The corresponding Figure of Merit is shown for the ring placement.

We will proceed with the design incorporating three rings, two outer rings and one central ring. This design has two categories of events, "Symmetric" events have both photons hit the outer ring, and "Asymmetric" events have one photon hit an outer ring and the other hit the middle ring. The events where $\hat{\mathbf{k}}_1$ hits the central ring has no sensitivity for the analyzing power defined in Equation 3.4. Throughout this chapter "Asymmetric events" exclusively refers to events with $\hat{\mathbf{k}}_1$ in an outer ring.

This is still an idealized distribution. It is easy enough to consider a "solid angle" for the detector by drawing a box over the diagrams, but in truth there is a solid angle to consider for both detectors. This would lead to a smearing out of the distribution shown (smearing out $\hat{\mathbf{k}}_1$ over one detector face), then specifying detector 2 by placing a box on the diagram. Further investigation requires a more complex simulation.

3.6.1 Cylindrical or spherical

There are two simple designs to place the detectors within the warm bore of the magnet, a cylindrical geometry (mirroring the geometry of the warm bore), and a spherical design (where

the outer rings are tilted inwards). These are shown in Figure 3.7. The cylindrical design is much simpler, makes detector mounting substantially easier, and allows the addition of shielding between rings. However, the spherical design features increased solid angle for the outer detectors, and the possibility of a wider opening angle. The tapered crystal design is ideal for the spherical array as the angle is set so the detector takes up optimal space within its solid angle, whereas the cylindrical only leaves room for a taper along the $\hat{\phi}$-direction.

Figure 3.7 Two possible designs, either a set of cylindrical rings with shielding between each ring, or tilted outer rings all aimed at a central source. The tilted design allows for increased solid angle and wider opening angle between the photons but is substantially harder to fabricate.

The distribution of events is shown in terms of the opening angle between the two photons in Figure 3.8. This assumes 16 crystals in a ring, and displays the events in the Symmetric and Asymmetric configurations labeled by the azimuthal angle between the two detectors. The combined distributions is shown in 3.9. The Symmetric events gain from the tilted design, this is due to the increased solid angle for both detectors.

The spherical geometry has an increased geometric acceptance, with an increase of roughly 60%. For this reason we choose to pursue the spherical design despite being more difficult to construct.

3.6.2 Number of crystals

The warm bore has a diameter of 22 cm. The design must include realistic space for the readout and mounting on the back-end of the crystals. We budget 9 cm from the center of the magnet to

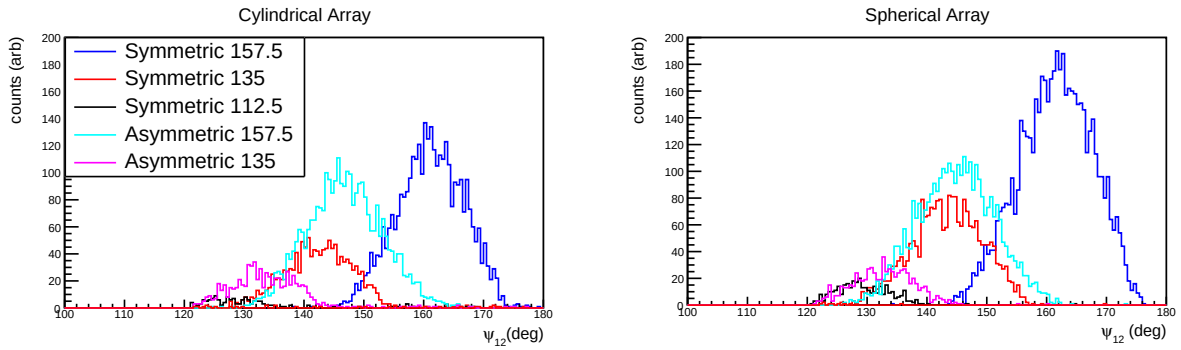

Figure 3.8 Distribution of all events where the highest energy photon hits the outer ring. Shown is the angle between the two photons for each pair of detectors that see the events. The configurations are labeled as 1) symmetric when both photons hit outer rings, or 2) asymmetric when the highest energy photon hits an outer ring, and the second highest hits the inner ring. The number next to Symmetric (Asymmetric) refers to the azimuthal angle between the two detectors).

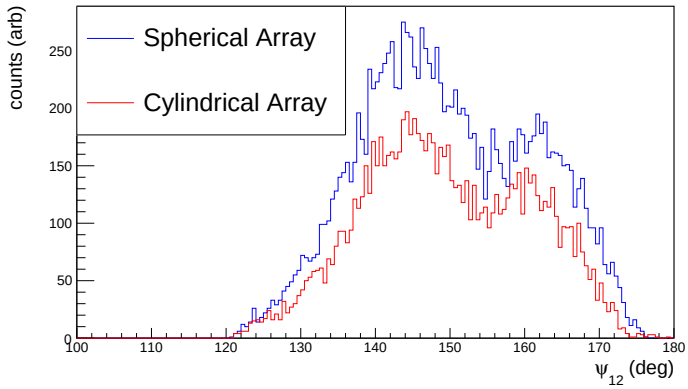

Figure 3.9 Summing all the distributions in Figure 3.8 shows the increase in statistics for the spherical design. Note each configuration has a different sensitivity so directly summing the counts is misleading. Instead consider this as a 1-D projection of the phase space seen by our detector pairs.

the back-end of the crystal (leaving 2 cm behind for mounting and readout).

The design can accommodate 12 or 16 crystals in each ring. Increasing the number of crystals increases the angular granularity of the array, but also decreases the efficiency of the detector themselves (in that they need to be smaller to fit more detectors in the same space). The complicated interplay between the number of detectors in a ring, the size of the detectors, and the angle of the tilt for the outer ring is illustrated in Figures 3.10 and 3.10.

Following the coordinates from Figure 3.10, the geometric constraint goes as,

$$\cot(\alpha/2)\cos(\beta) - \sin(\beta) > \cot(\pi/n) \tag{3.8}$$

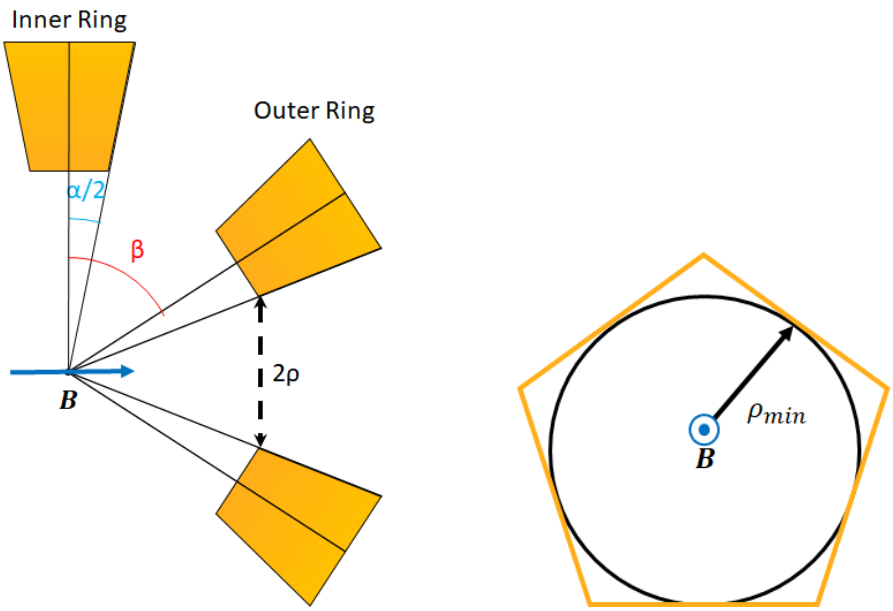

(a) (b)

Figure 3.10 Diagrams illustrating the relationship between the tilt angle of the outer ring, and the geometric constraint on the crystal size. (a) The side view, with detectors of opening angle α, and a ring tilt of β. This gives the cylindrical radius of the outer ring as ρ. (b) Front view for a 5 crystal ring. Once the edges of the crystals are touching we cannot tilt the ring farther. This defines a minimum radius ρ_{min}. This gives the geometric constraint of $\rho > \rho_{min}$, and is given in terms of α and β for an n-detector ring by Equation 3.8.

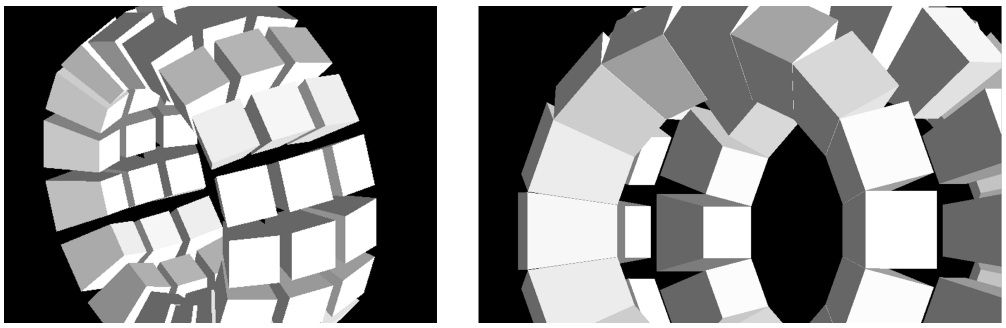

Figure 3.11 Illustration of the geometric concept in Figure 3.10, holding the crystal size constant they get closer and closer as we tilt the outer ring, until they collide.

This is plotted for the twelve crystal array and the sixteen crystal array with a radius of 6 cm in Figure 3.12. In principle any choice beneath the blue (red) curve is valid for the sixteen (twelve) crystal array.

Considering the possible pairings, the 16 detector configuration offers a substantial increase in the number of pairs with kinematic sensitivity. In principle each detector has 2 sets of pairs in the

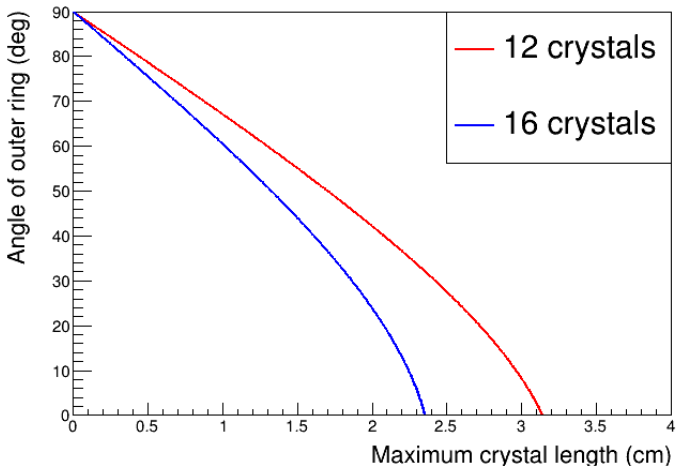

Figure 3.12 The geometric constraint for the crystals based on angle of ring (if the crystal is 6 cm from the source). For a given tilted angle between the central ring and the outer rings, the largest size crystal is shown. In principle any choice below the blue curve is possible for 16 crystal ring, and any below the red is possible for a 12 crystal ring.

other rings for 16 detectors compared to 1 set of pairs for 12 detectors. There is a change in the possible solid angle of the detectors (so the 12 detector array crystals sees more events). However, the increased granularity is worthwhile in and of itself.

3.7 Summary

We will construct an array of detectors to fit inside the FRIB Positron Polarimeter magnets. These will have 3 rings with 16 detectors in each ring. The detectors will be roughly 3 cm deep and have a front face between 1-2 cm in width. The outer two rings will be tilted inwards towards the central source for positronium formation.

CHAPTER 4

γ-DETECTOR PROTOTYPING

4.1 Overview

This experiment will require high statistics to reach the target sensitivity. Since we will be constructing this array from scratch to perform this specific measurement, it is worth spending time optimizing the individual detectors before purchasing and constructing the full array of 48. This chapter is entirely focused on the study of the individual crystals and their response within the energy range of interest (sub MeV photons). We first give a basic overview of scintillation detectors and photomultipliers including the specific devices we choose. This is followed by some simulations of single crystal efficiency as a function of detector geometry. Once we have settled on a design we present the initial testing of single crystal prototypes.

4.2 Scintillation detectors

In general γ-detectors can be simple scintillation detectors. There is a monolithic crystal with a high Z-value, the γ hits the crystal and creates an amount of scintillation light proportional to the energy deposited. The scintillation light is collected by some photomultiplier and is translated into an electrical current that is recorded by a data acquisition system [22]. The principle is illustrated in Figure 4.1. At the energies of interest the γ-ray can either Compton scatter or be fully absorbed. There is the possibility for multiple scatterings as well. The full energy peak is composed of all events that deposit their full energy (either through photoabsorption, or multiple scatterings until full absorption), and the Compton continuum is the plateau of events with a shape determined by kinematics. An ideal detector has all events in the full energy peak, however there is both a material dependence and an energy dependence for the relative cross-sections of these processes. [22]

4.2.1 LYSO crystal

Common inorganic scintillation crystals used for γ-ray spectroscopy are NaI, CsI, $LaBr_3$. These are usually doped with "light emitters", elements that add states in the bandgap and therefore allow scinitllation to occur. A comparative study of these inorganic scintillators for high energy physics

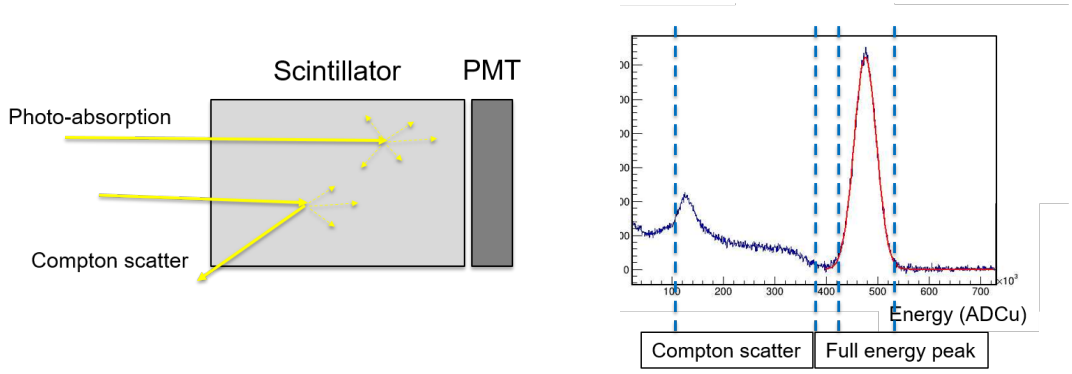

(a) (b)

Figure 4.1 a) Illustration of the interaction of a low energy photon with a scintillation detector. b) A sample spectrum for a ^{137}Cs source with a (background subtracted) LYSO crystal. The x-axis is the digitized current output from the photomultipler. The spectrum shows a clear peak and Compton plateau.

experiments can be found in Ref. [47]. The University of Michigan measurement utilized NaI scintillators [38], and the University of Tokyo measurement utilized LYSO crystals [39], which is the standard in the PET industry [48, 49]. LYSO refers to Cerium doped Lutetium Yttrium Oxyorthosilicate ($Lu_{1.9}Y_{0.1}SiO_5$). These crystals have a density of 7.25 g/cm^3, a decay time of 40 ns, and a light yield of 30 photons/keV. [50]. These crystals are increasingly being used for calorimeters in nuclear and high energy physics experiments [51, 52]. LYSO crystals suffer from internal radioactivity from the ^{176}Lu, creating 3.9 cps/g [53]. This gives a constant background of singles for our detectors. The decay scheme is shown in Figure 4.2.

This is a β-decay followed by a γ-cascade, and completely covers the energy region of interest for ortho-positronium decay (less than 511 keV). Sample spectra are shown in Figure 4.3. To recover the clean spectrum shown in Figure 4.3 we had to run twice, once with a source and once without. Careful matching of the runtime and monitoring for gain shifts allowed us to perform a background subtraction to remove the intrinsic radioactivity backgrounds. This was performed for all single crystal studies presented in this chapter, unless otherwise specified. The internal radioactivity has been extensively studied in Refs. [53, 54].

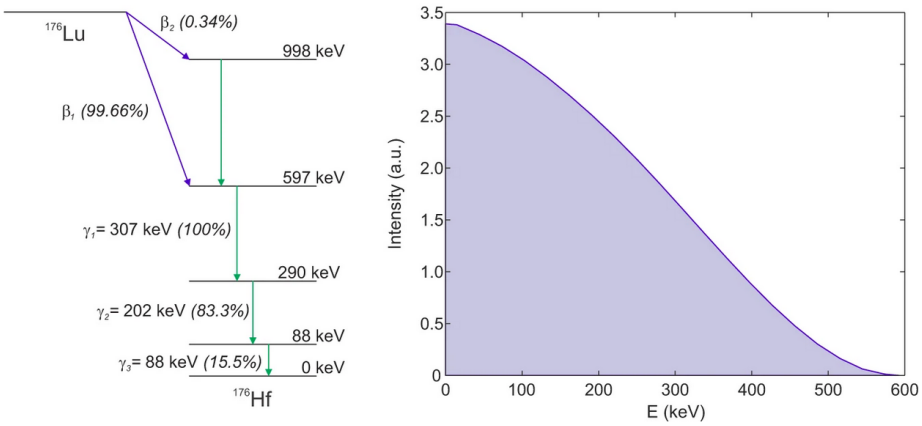

Figure 4.2 Decay scheme for ^{176}Lu, taken from Ref. [53]. The nucleus decays with a half life of 3.76×10^{10} years to ^{176}Hf by β emission with an enpoint energy of 593 keV (right). This is accompanied by 3 characteristic γ-emissions at 307 keV ($6^+ \rightarrow 4^+$), 202 keV ($4^+ \rightarrow 2^+$), and 88 keV ($2^+ \rightarrow 0^+$).

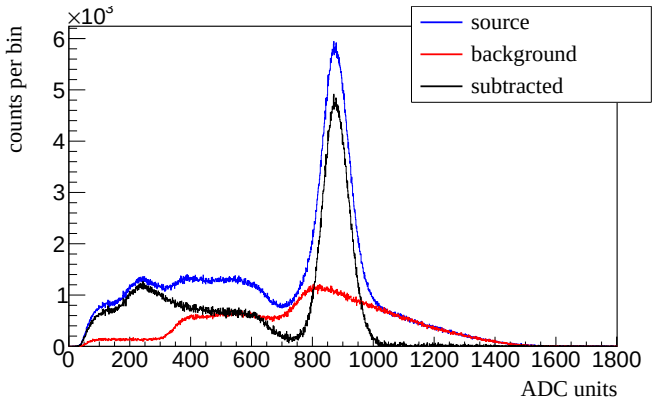

Figure 4.3 Illustration of background subtraction for ^{137}Cs source. We recorded two data sets, one with a source, and one without. We statistically subtracted the background run from the source run and recovered a clean spectrum. Spectra taken at WU

4.2.2 Silicon photomultiplier

A silicon photomultipler is an array of single photon avalanche diodes, held at breakdown voltage. The working principle is that an incoming scintillation photon from the crystal causes the breakdown in the photodiode and allows passage of current. The current from the SiPM is proportional to the number of photodiodes that experienced breakdown, which is ideally proportional to the number of scintillation photons emitted in the crystal, which finally is ideally proportional to the energy deposited by the γ. A thorough overview of silicon photomultipliers can be found in Refs. [55, 56].

For the LYSO array, we plan to use SiPMs in-lieu of PMTs. The SiPMs are much smaller than a PMT, they can run at a much lower voltage (around 25-30 V), and they are not affected by a magnetic field. This will allow us to place our detector modules directly in the warm bore of the magnet itself. The combination of LYSO crystals read out with an SiPM is well characterized and becoming a standard technology in PET systems [48, 49].

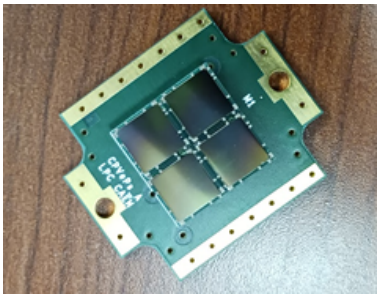

Figure 4.4 Prototype silicon photomultipler for detector readout.

4.3 Initial tests

Initial testing of the LYSO crystals and read out by SiPMs were performed in Spring 2019. We had pairs of LYSO crystals and CsI crystals in small and large sizes, shown in Figure 4.5 and described in Table 4.1. The resolution of the crystal is based on the counting statistics of the scintillation photons. CsI has a higher light output (about 50 photons/keV) than LYSO (about 30 photons/keV), and we therefore expect a worse resolution for LYSO. CsI has a slower primary decay time at 4 μs compared to 40 ns for LYSO [54]. Further benefits of LYSO crystals are that they are non-hygroscopic [50] and therefore do not deteriorate like CsI, and they have a substantially decreased afterglow [57].

These crystals were coupled to a PM3325-WB 2x2 array of 3 mm^2 Ketek SiPMs [58]. The SiPM was coupled with an optical gel of width 1 mm, and read out with the FASTER data acquistion system [59]. The sides of the crystals that were not coupled to the SiPM were coated in three layers of Teflon tape. This acted as a reflective coating to increase the light collection of the scintillation light at the SiPM. The large CsI coupled to the SiPM and connected to a preamplifier is shown in Figure 4.6.

The observed response for all four crystals is shown in Figure 4.7. These show the spectra

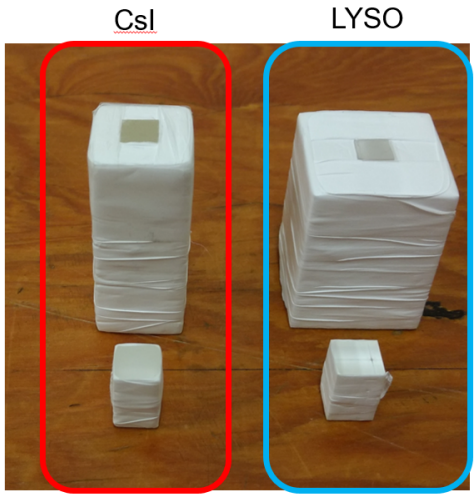

Figure 4.5 Two sets of scintillation crystals, large and small sizes for both CsI and LYSO crystals. The sizes are specified in Table. 4.1.

	CsI	LYSO
Small	10 x 10 x 15 mm^3	10 x 10 x 15 mm^3
Large	20 x 20 x 50 mm^3	30 x 30 x 40 mm^3

Table 4.1 Sizes of the crystals shown in Figure 4.5.

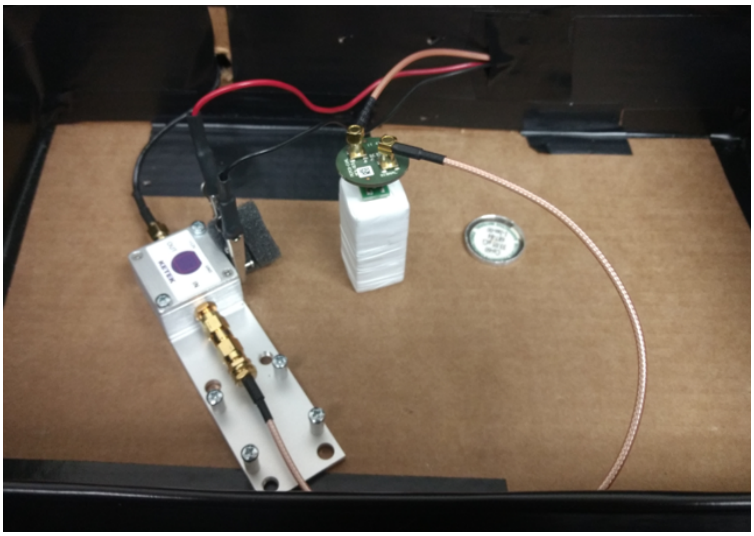

Figure 4.6 Early test setup. The SiPM was attached to the back of a crystal and fed through a pre-amplifier before being read out by the DAQ system. The radioactive source was placed next to the crystal.

for ^{22}Na and ^{60}Co. The LYSO showed degraded resolution relative to the CsI detector. The large LYSO has a resolution of 17.6% at 511 keV. Compare this with 11.7% for the Tokyo experiment [39]. The Tokyo experiment used 30 mm diameter by 30 mm length crystals read out by PMTs.

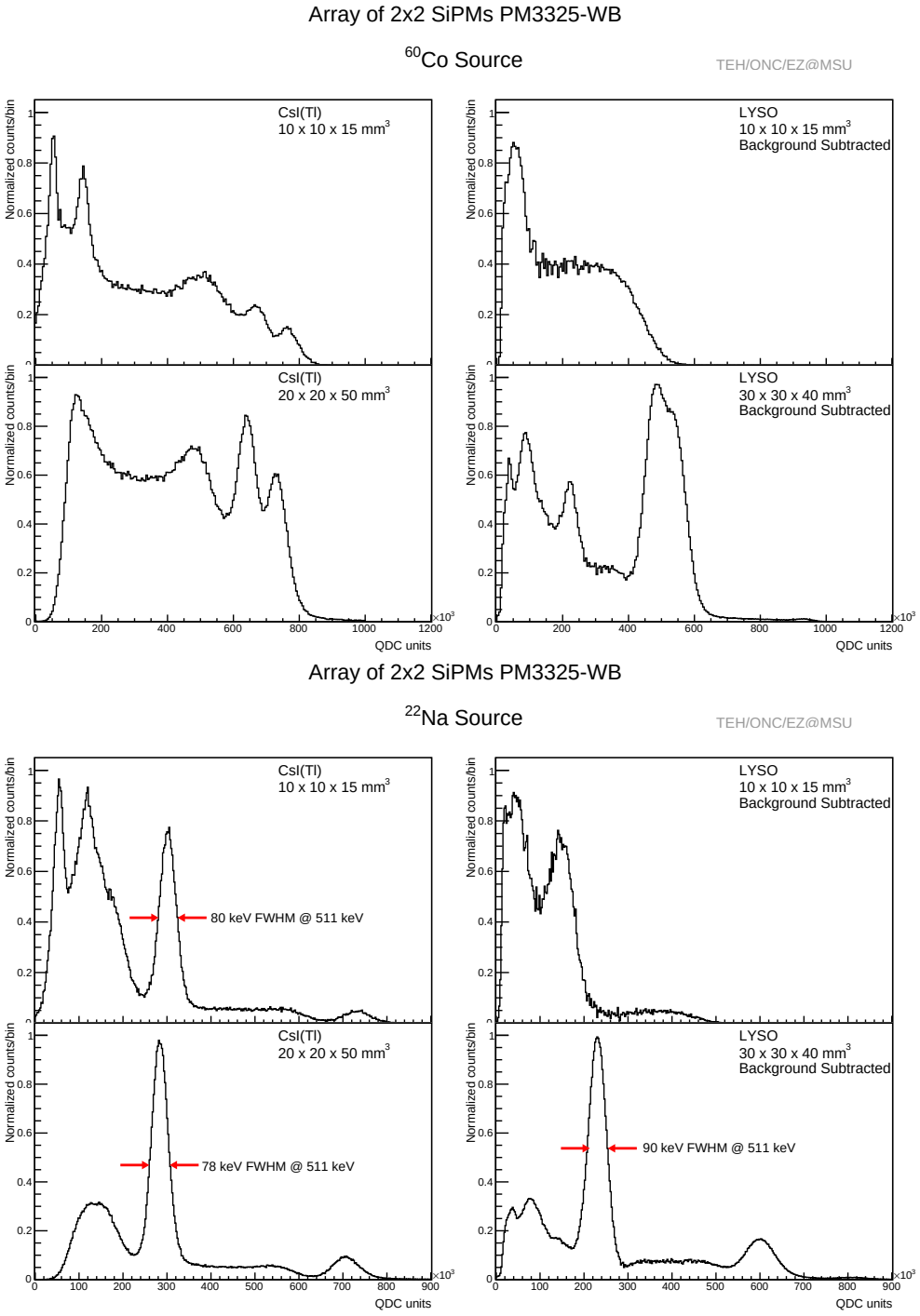

Figure 4.7 γ-spectra for two sources for all four crystals. The CsI showed an improved resolution compared to the LYSO, and the large crystal showed a much cleaner response than the small.

It seems that we are far from a comparable resolution using SiPMs. However, we tested various crystal sizes, but always used the same sized SiPM. A larger SiPM will greatly increase the light collection efficiency and therefore should give a better resolution. Looking at Figures 4.5 and 4.6

the size of the SiPM was small compared to the face of the large crystal. It is reasonable to expect an improved resolution for a larger SiPM designed specifically for our final detectors.

All tests so far indicate that using LYSO crystals read out with SiPMs will be feasible for our final design target. We now proceed to study the geometric dependence of the efficiency to optimize the design for our specific experiment.

4.4 Single crystal design and simulation

The array will feature 3 rings with 16 detectors in each ring, with the detectors aimed at the central source. The sensitivity increases as the tilt of the outer ring approaches 45°, but the detectors will need to be large enough that they will have good photopeak efficiency and solid angle coverage. The warm bore of the magnet is 22 cm diameter which will constrain the widest part of the array. A reasonable range of crystal depths is 2-5 cm, and the width of the front face at most 3.5 - 2.35 cm for those respective depths (this can be ascertained from Figure 3.12).

Further single crystal design work was carried out in concurrent simulations using Geant4 [60, 61] and EGSnrc [62]. Here we present the results from Geant4 tests. These simulations study the response to monochromatic 511 keV γ's, emitted isotropically from a point 6 cm in front of the crystal. We record the energy deposited in the crystal from the initial event (including any secondaries that do not escape the crystal). These simulations do not include any internal optics of the scintillation light, and therefore give no information on finite energy resolution.

These simulations are used to study three aspects of the crystal geometry: length, width, and taper. To compare these aspects we record the total efficiency, and the photopeak efficiency. The total efficiency is merely the "total number of counts" for a fixed number of events regardless of the energy left in the detector (Compton or photopeak). The "photopeak efficiency" is the number of counts in the photopeak divided by the total counts for the detector. This means if both the photopeak and the Compton plateau scale by a factor of two we would quote the same photopeak efficiency. In reality the term "photopeak efficiency" is a bit of a misnomer, the term "total energy peak efficiency" is more accurate. Increasing the size of the crystal increases the number of photons that scatter multiple times and therefore leave all their energy by either subsequent scatterings or

subsequent absorption.

4.4.1 Crystal taper

The gamma detectors will be held in a spherical array and aimed at a central source, this means that, for a cuboid geometry, photons coming from a point source will not see an equal crystal length whether they hit the center of the crystal or the edge. For this reason we could benefit greatly by using a tapered crystal design. This could greatly increase the detection efficiency across the front face of the detector by decreasing the number of photons that "clip" the edge. The basic geometries considered in this study are shown in Figure 4.8. An image from the simulation of a tapered crystal is shown in Figure 4.9.

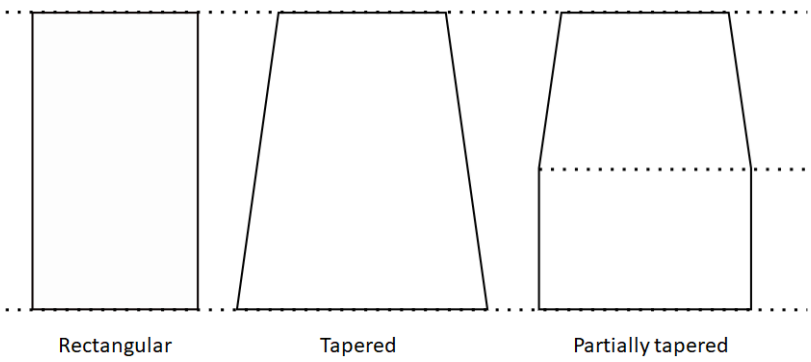

Figure 4.8 The three geometries considered, a rectangular crystal, a tapered crystal, and a partially tapered crystal.

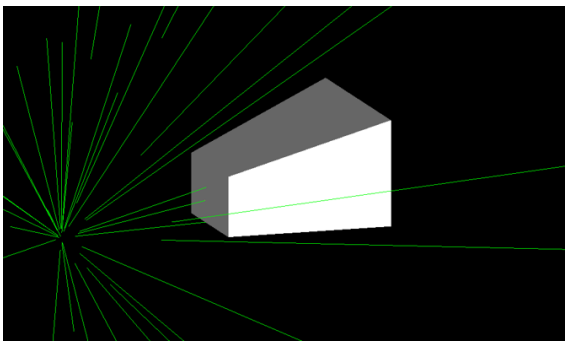

Figure 4.9 Geant4 simulation of a monochromatic point source of 511 keV photons in front of a tapered crystal.

4.4.2 Crystal width

The width of the front face has a large effect on the overall acceptance of the detector. Doubling the width of the front face quadruples the solid angle seen by the detector, and the efficiency should scale roughly as the solid angle. The possible width will largely be determined by the geometric constraint of fitting 16 crystals in a tilted ring inside the cylindrical magnet. In reality all of the detectors will need mounts to hold them in place in the apparatus and this will greatly limit the size of the crystals. The dependence of the efficiency on the varying crystal width is shown in Figure 4.10. This shows that the total efficiency roughly scales as the width squared.

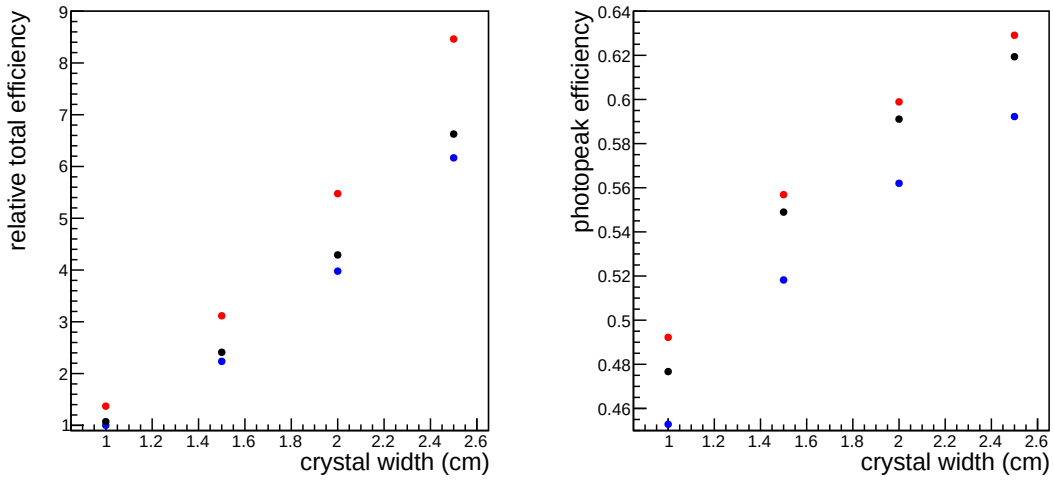

Figure 4.10 Changing width of the crystal holding its front face 6 cm from a point source of 511 keV photons. The length of the crystal is held at 3 cm. Rectangular crystal is shown in blue, tapered (with the angle of taper matching the solid angle of the front face) shown in red, and a partially tapered crystal with the front half tapered shown in black.

4.4.3 Crystal length

The length of the crystal affects the detection efficiency by increasing the amount of material the photon must pass through (increasing the likeliness of interaction). Similarly it also increases the events with multiple scattering, as such it should increase the total efficiency and the photopeak efficiency, although not as dramatically as increasing the width. The effect is shown in Figure 4.11.

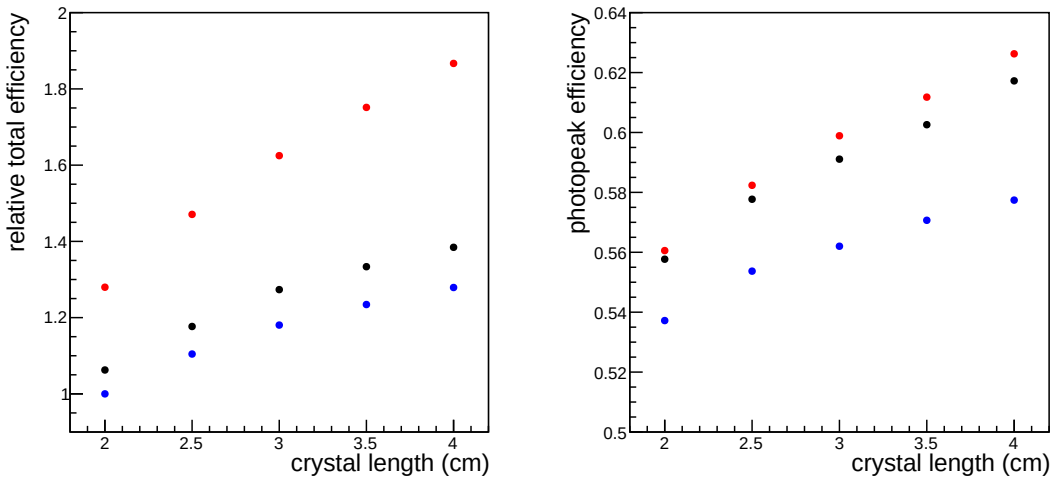

Figure 4.11 Changing the length of the crystal, holding the front face position 6 cm from a point source of 511 keV photons. The front face is fixed at 2x2 cm^2. Rectangular crystal is shown in blue, tapered (with the angle of taper held constant) shown in red, and a partially tapered crystal with the front half tapered shown in black.

4.4.4 Partial taper

The mockup of the detector placement for tapered crystals is shown in Figure 3.10. This has left almost no room for mounting the detectors. We want to make room for mounting, while keeping as much material as possible, as illustrated in Figure 4.12. This can be achieved by using partially tapered crystal. The photons that enter the detector at an angle have a longer path length to the back of the crystal than those that enter head on (for a tapered design). Removing part of the back region of the crystal will not dramatically affect the path length for the majority of the photons that hit the detector.

The benefit of the partial taper is many-fold. Firstly it maintains some of the benefit of the tapered design versus the rectangular. Secondly, it buys substantially more mounting space at the back of the crystal without sacrificing space at the front. The photopeak efficiency and total efficiency for a 1.5x1.5 cm front face by 3 cm deep crystal are shown in Figure 4.13. While the gains in efficiency might not look dramatic, the experiment will record coincident events. This means it is more appropriate (though still rough) to consider the efficiency squared, meaning an 18% increase in single detector efficiency roughly corresponds to a 39% increase in coincidence statistics.

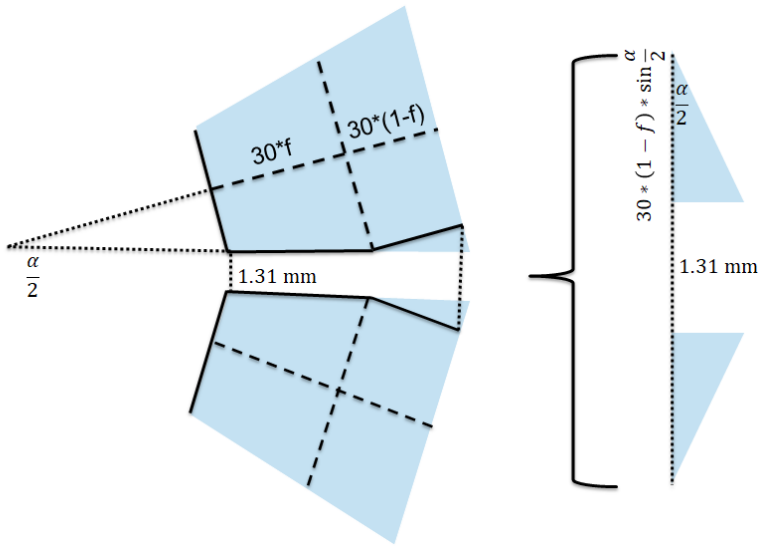

Figure 4.12 Diagram of the space gained between the crystals as we change the fraction that is tapered.

Considering the photopeak efficiency we see a greater increase, roughly as $1.18 * (0.59/0.56) \approx 1.24$ for a single crystal.

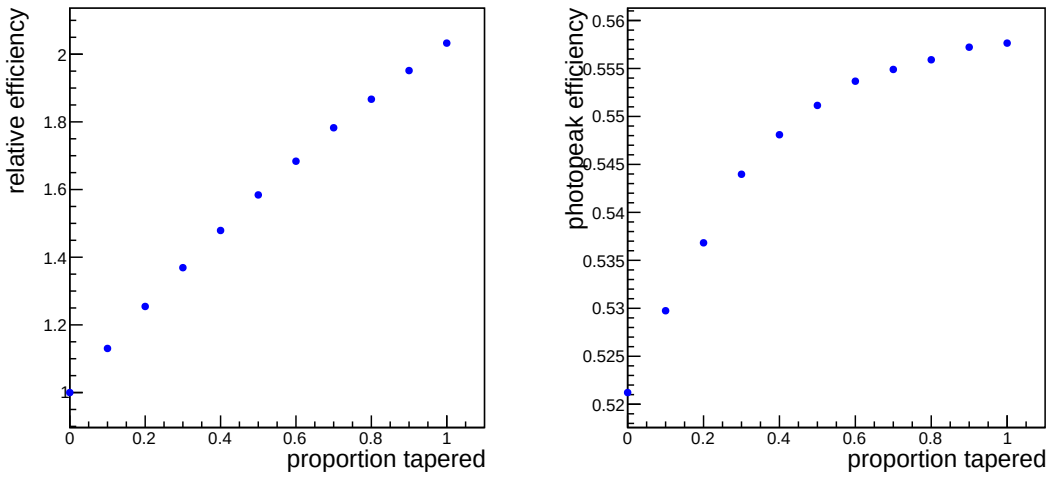

Figure 4.13 Total efficiency and photopeak efficiency as the fraction of the partially tapered crystal is varied. A value of 0.4 corresponds to the front 40% of the crystal being tapered. This is for a crystal of 1.5x1.5 cm front face and 3 cm depth, and the angle of the taper is held constant.

4.5 First prototype and observed distortion

We settled on a design of 1.68 x 1.68 x 3 cm with the front 1.5 cm of the crystal tapered (the back end has dimensions 2.13 x 2.13 cm). The first prototype was studied at WU in January 2021.

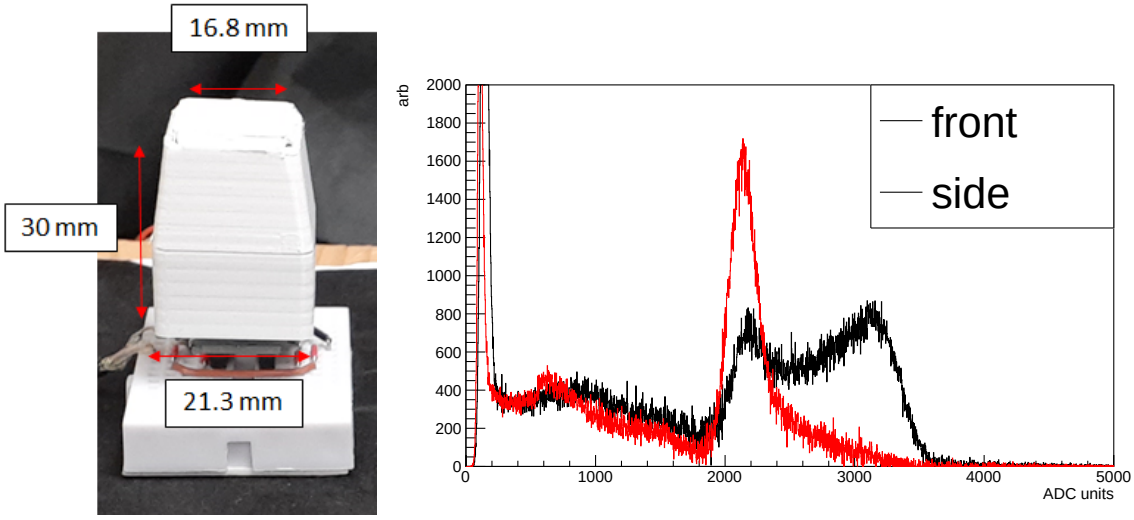

(a) (b)

Figure 4.14 Data taken at WU. (a) The first partially tapered LYSO prototype, in a 3D printed cover. (b) Response of the tapered LYSO prototype to a ^{137}Cs source, taken at UW. Experimental spectra with the source aimed at the front and at the side of the crystal. These results are after background subtraction.

This crystal produced dramatic distortions, shown in Figure 4.14b. The spectra were taken with a ^{137}Cs, and the spectra showed very different responses whether the source was in front of the crystal or to the side. There was a long high energy tail from the front, and a double peak from the side. Scans with a collimated source along the side of the crystal showed a clear position dependence to the gain (and shape of the response). Two possible explanations are, a non-uniformity of the cerium doping, or a position dependent light collection efficiency. With only a single crystal there was no clear non-destructive test to separate these two possible causes.

For this reason we performed a series of destructive tests at LPC-Caen. We started with a rectangular crystal demonstrated that it had a uniform well-behaved response. After the uniformity of the response was verified we had the crystal cut into the partially tapered geometry and measured the response. If this induced a distortion that would be a clear indication that it is a geometric effect.

The setup is shown in Figure 4.15a. We used a ^{22}Na source in a Pb container with a 1 cm diameter opening. This was further collimated with a brass tube of 1 cm outer diameter, 3 mm inner diameter, and 1 cm length. The crystal was read out with a SiPM and was placed on a jack

to move relative to the source. The crystal was moved in increments of 0.5 cm, with position 0 referring to the front face, and positive displacement means towards the readout end.

The rectangular crystal showed no distortions and a very clean spectrum, shown in Figure 4.16a. The peaks were centered and do not move relative to each other as we scanned along the side of the crystal. The changing height of the histogram was an indication of the source not being collimated perfectly, as we scanned the crystal saw more of the cone emitted by the source. This is illustrated in Figure 4.15b. Once the crystal was cut, but the cut sides were still unpolished, we saw a clear shifting of the peak, shown in Figure 4.16b. The peak moved from high energy to low as we scanned from the front face towards the silicon photomultiplier. Finally when the sides of the crystal that were cut were polished (Figure 4.16c), any semblance of a clean response was lost. The peaks were highly asymmetric and non-gaussian when the source was aimed at the tapered region of the crystal.

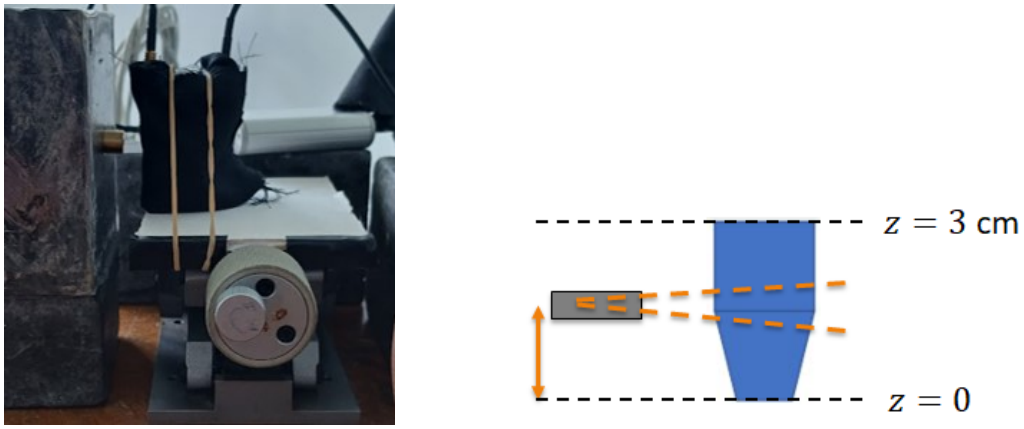

(a) (b)

Figure 4.15 A γ source was collimated and aimed at the side of the crystal. The crystal could be moved using a raising and lowering jack. a) Image of the setup constructed at LPC-Caen. b) Cartoon illustrating the working principle, and how imperfect collimation lead to a change in solid angle.

Results for each configuration with the source aimed at the front face are shown in Figure 4.17. A simple energy calibration was applied to make the peaks lie on top of each other, and the spectra were scaled to have equal geometric area (not integral). Figure 4.17a demonstrates that the rectangular crystal had a clean response that was dramaticaly distorted when the crystal was

cut and polished. However, our collaborators from WU identified a solution to the problem. They painted the crystal with TiO_2 paint and were able to completely remove the effect. As illustrated in Figure 4.17b changing the surface treatment resulted in the distortion going away and a clean response being regained.

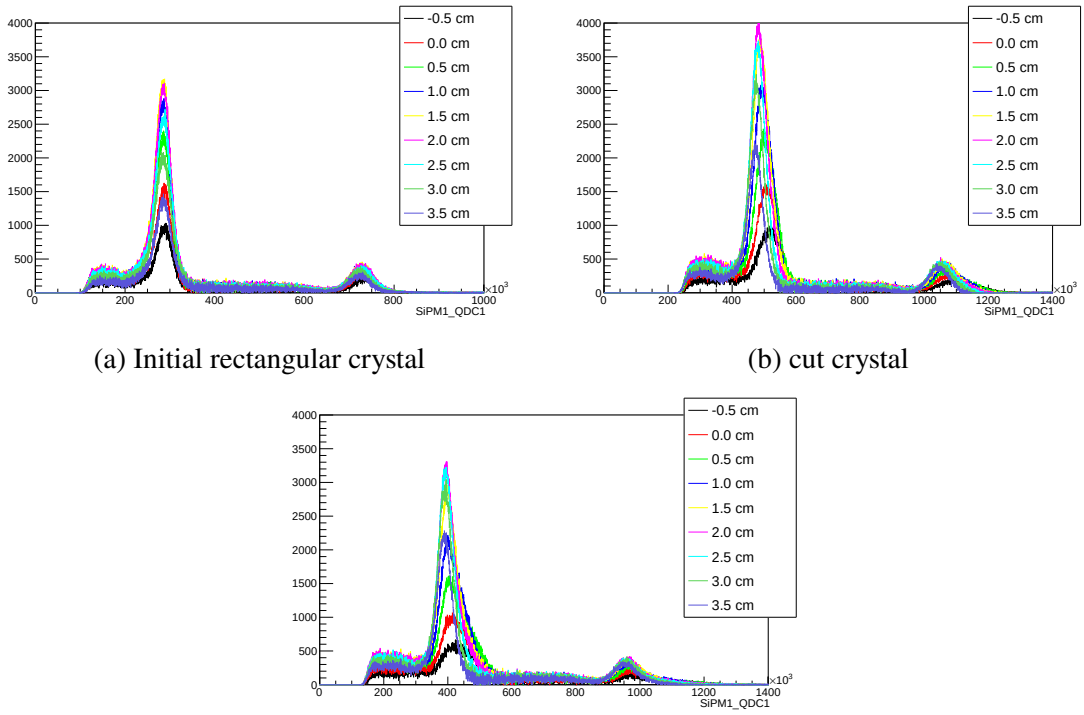

(a) Initial rectangular crystal

(b) cut crystal

(c) cut and polished crystal

Figure 4.16 Measured response of the crystal to a collimated ^{22}Na source aimed at different positions along the side of the crystal. The taper occurs at 1.5 cm. Changes in height are due to imperfect collimation of the source.

This could be caused by a geometric focusing of the scintillation photons. As demonstrated in Ref. [63], in a tapered scintillation crystal when the light bounces off the edges of the crystal it can gain a more favorable angle at the readout face for transmission. This leads to a position dependence to the light collection efficiency along the length of the crystal that is absent for a rectangular crystal. Changing the surface treatment changes the reflective properties which can remove the geometric focusing.

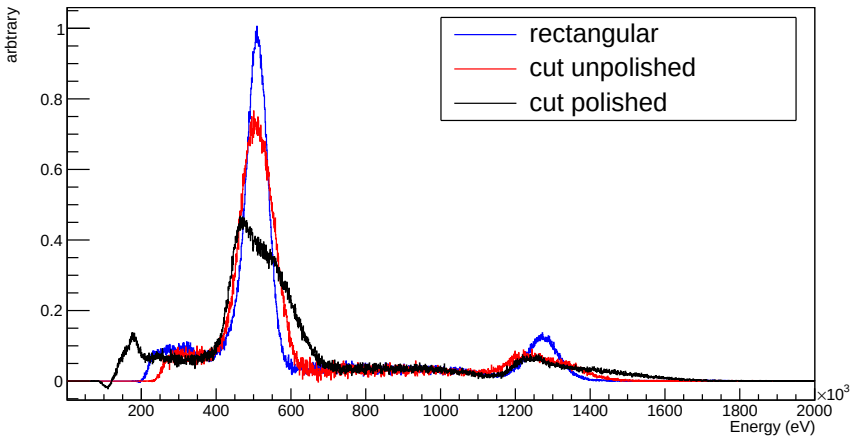

(a) Response after cutting, and after polishing

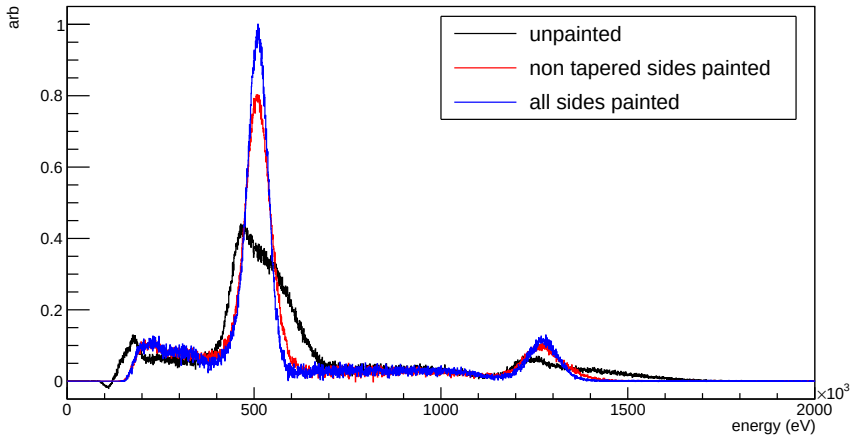

(b) Response after partial painting, and full painting.

Figure 4.17 Response of the crystal to ^{22}Na source aimed at the front face. All histograms were scaled on the x-axis to overlay with a very rough energy calibration. The cut and polished crystal did not provide a good energy calibration, so there is an arbitrariness to the scaling. Similarly all histograms were normalized by geometric area to account for their different bin sizes.

4.6 Final crystal results

With the benefit of painting we will not need to alter the geometry of the crystal. Therefore we use 1.68 x 1.68 x 3 cm^3 crystals where the front 1.5 cm are tapered. Each crystal is read out by a 2x2 array of 6 mm SiPMs. They are coupled with 1 mm thick optical gel to the crystal. Each is painted with at least 3 layers of TiO_2 paint, and then covered with a Tyvek cover. These sit in a custom built crystal clamp. The crystals are shown in Figure 4.18, and their spectra are shown in Figure 4.19. We could achieve roughly 12% FWHM energy resolution for the final crystals Production of

all 48 detectors is ongoing at present.

Figure 4.18 Three finalized γ-detectors in their clamps. Two of these are with prototype SiPM boards, and one had the finalized board (with the proper screw placement to attach the board onto the back of the crystal).

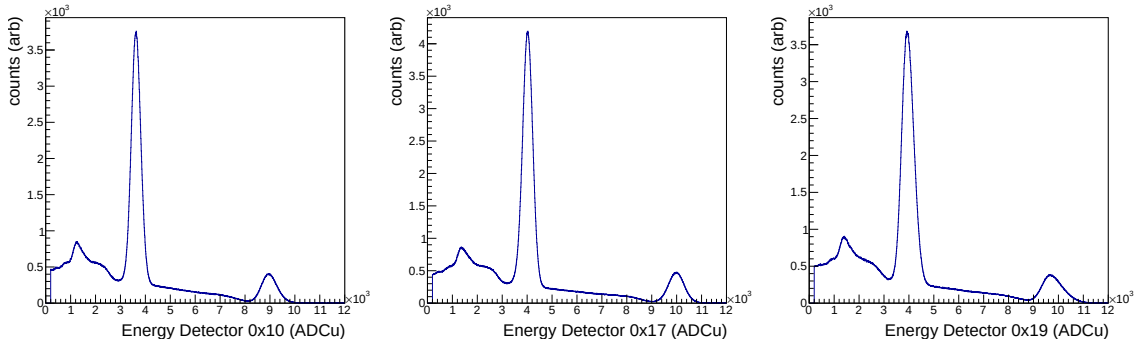

(a) (b) (c)

Figure 4.19 Gamma peaks for all three crystals shown in Figure 4.18, with FWHM resolution at 511 keV of 12.1%, 11.5%, and 14.1% respectively. These spectra were not background subtracted, but instead read out in coincidence with the detection of the β-emission.

CHAPTER 5

POSITRONIUM FORMATION

5.1 Overview

The final rate in our online experiment will be in part determined by how many of the positrons emitted from the β source actually form positronium. This required analysis of different materials for positronium formation. The target is a formation fraction of at least 40%, as achieved in Magnesium Oxide powder in Refs. [64, 65], and a lifetime of at least 125 ns as achieved the previous experiments [38, 39]. For both of these quantities larger values are always better. There has been much activity recently in optimizing positronium formation in large scale antimatter experiments [66, 67].

5.2 Ps formation and Positron Annihiliation Lifetime Spectroscopy

Positron Annihilation Lifetime Spectroscopy (PALS) is a well developed method to study material properties in Condensed Matter and in Material Science [68, 69], as well as exciting new applications in identifying tumor tissues [70]. The time spectrum will reveal material properties about the sample. The positrons either annihilate directly in the bulk, or form positronium. Positronium has a positive work function in materials, so it is repelled to the voids and pores of the material.

Interactions between the positronium and the bulk can cause a spin flip so that ortho-positronium changes to para-positronium and quickly annihilates. As such, the lifetime of the positronium atom depends on the size of the void it exists in. Measuring the distribution of lifetimes for a given sample reveals the relative sizes, and interconnectedness of the pores in the material [68].

The spectrum is built as follows, take a β^+ source that also emits a de-excitation photon. Place two γ-detectors, one for the de-excitation photon (START), and one for measuring annihilation photons (STOP). Record the time of each signal and construct the $\Delta t = t_{STOP} - t_{START}$ spectrum of events. This is shown schematically in Figure 5.1.

Extract the lifetimes and relative amplitudes of the different components. This can reveal

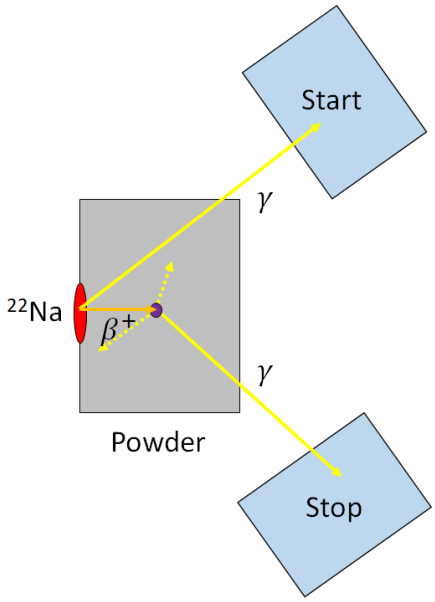

Figure 5.1 Cartoon illustrating the working principle of the powder test stand. First a β decay occurs and the β enters the powder, there is a concurrent 1275 keV de-excitation photon detected with the start detector. The β can form positronium in the powder, eventually annihilating and leaving a signal in the stop detector.

properties of the material, as well as the "formation fraction" of the material. For the studies presented here the goal is purely maximizing the lifetime and the formation fraction.

5.3 Ps test stand construction and testing

We used a ^{22}Na source as our β^+ emitter while testing the powders. The nuclear decay emits a concurrent 1275 keV γ along with the β^+. We used this γ as our START. This source was placed directly against powder held inside an aluminum holder. We placed another powder container on the opposite side. However due to the asymmetry of this source almost no β's escape the back side of the source (layers of plastic and the label).

These containers could be placed inside an aluminum vacuum tube. Spacers inside ensured the powder sits at the same longitudinal position inside the tube from run to run. The vacuum tube was held in a frame that fixed its position on the table. This is illustrated in Figure 5.2.

We utilized two $LaBr_3$ detectors. These were held in frames relative to the vacuum tube for reproducible alignment. The detectors were cylindrical 38.1 mm diameter by 38.1 mm length, and placed 5.5 cm from the powder. Lateral displacements of the powder were constrained by the

frames, longitudinal were controlled by the spacer inside the vacuum tube. The largest variation was the placement of the source within the powder container, which was difficult to constrain. Variations were small compared to the solid angle of the detectors.

Each detector could see the start signal or a stop signal (or both), however they were not back-to-back so they could not see the 511-511 coincidences unless one Compton scattered. We recorded coincident events, the energy (in ADC units), and the timestamp of the event (with CFD timing). The digitization was performed with NSCLDAQ using PIXIE-16 data acquisition modules [71, 72, 73]

Figure 5.2 Positronium test stand. A vacuum tube connected to a roughing pump, with two $LaBr_3$ detectors aimed at a central source in the tube.

We distinguished the start and stop signals by placing energy cuts on the distribution. A data run could take somewhere between one hour to two days depending on the activity of the source used. For this reason we needed to perform energy calibrations to correct for gain shifts.

The ^{22}Na source provides two gamma peaks, we automatically calibrated the spectrum by fitting the two peaks, extracting a gain and offset and then rebuilding the spectrum in units of energy. We applied energy cuts based on the calibrated spectrum which removed the effect of gain drifts between runs. Two uncalibrated energy spectra with fits are shown in Figure 5.3.

We considered a START signal if the hit had between 1200 and 1350 keV (to capture the 1275 keV annihilation photon). We considered two energy windows for the STOP, one called "continuum" between 250 keV to 490 keV, and another called "peak" between 490 keV to 530 keV.

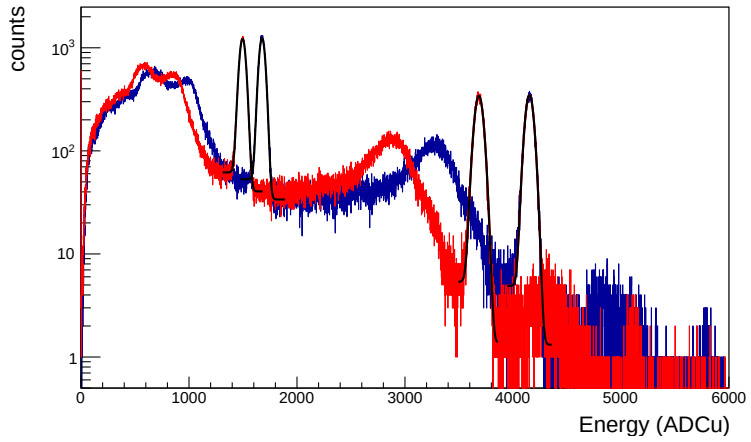

Figure 5.3 The observed energy spectra for both detectors with a ^{22}Na source in ADC units (ADCu). The gain and offset were extracted with the fits of the 511 keV and 1275 keV peaks.

We considered these energy windows for each detector, which gave us four separate time spectra for any given run. In principle these were different methods to construct the same time spectrum, so extracted lifetimes and formation fractions should agree.

5.4 Time spectrum model

The time spectrum was modeled as a delta function plus some finite number of decaying exponentials. We convolved these with a gaussian response function. This gave a gaussian prompt peak, and a complementary error function as the lifetime component. The analytic form of this is,

$$F_i(t) = \left(\frac{A_i}{2\tau_i}\exp\left\{\frac{\sigma^2}{2\tau^2}\right\}\right)\exp\left\{-\frac{t-\mu}{\tau_i}\right\}\left[1+\mathrm{erf}\left(\frac{t-\mu}{\sqrt{2}\sigma}-\frac{\sigma}{\sqrt{2}\tau_i}\right)\right] \tag{5.1}$$

where A_i is the integral of the lifetime component, μ is the start time of the signal, τ_i is the lifetime, and σ is the resolution.

However, actual data showed a different response. In general we saw some small lifetime component that was on par with the time resolution. We show a sample fit function in Figure 5.4, with an asymmetric peak, a 5 ns lifetime component, and a 100 ns lifetime component. So a "fit" corresponds to fitting a function $f(t) = \sum_i F_i(t)$, where all F_i have the same σ and μ, but different A_i and τ_i. A simple log likelihood fits can easily discriminate lifetimes that vary by a factor of 2, however struggles when multiple components have similar lifetimes. This is largely unimportant for our purposes.

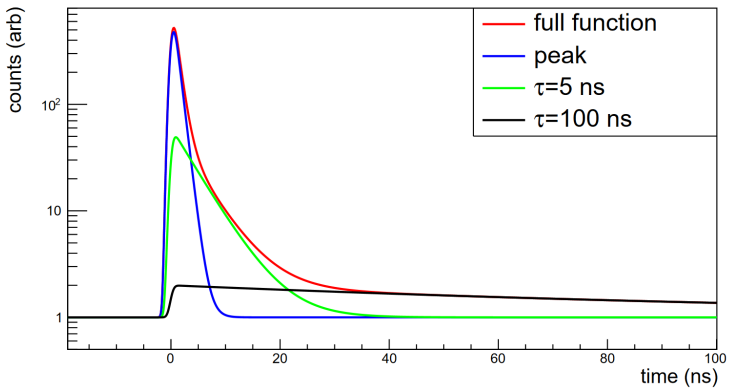

Figure 5.4 Illustration of a lifetime spectrum fit function. This features an asymmetric peak with two lifetime components. All components have the same resolution and are centered on the same time.

5.5 Initial results

5.5.1 Aluminum tests

We carefully prepared aluminum targets to match the density of the MgO powder, both 0.3 and 0.6 g/cm^3. This should have provided the most precise prompt decay measurement. We cut the aluminum foil into small circles, then layered them within our container, shown in Figure 5.5. Spread out over the source they matched the target density. Initial tests seemed accurate, except we saw a high level of accidentals. The accidental rate depends on the rate of the source as $R_{acc} = R^2 \Delta T$ where ΔT is the coincidence time window. The distributions for three different source rates are shown in Figure 5.6.

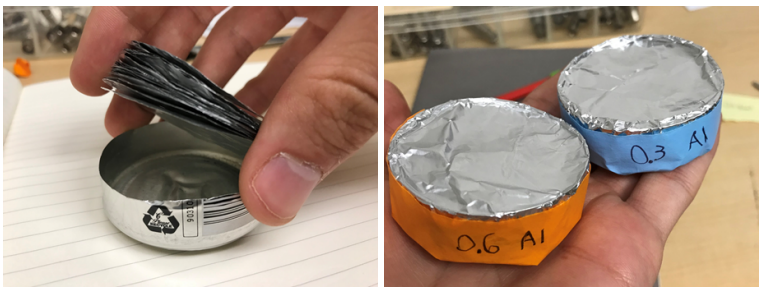

Figure 5.5 Constructed aluminum target designed to match the target densities of the powders to be tested.

At low rate level we saw a long lifetime component in the aluminum container. This lifetime component appeared when we cut on the low energy part of the spectrum not on the 511 keV peak,

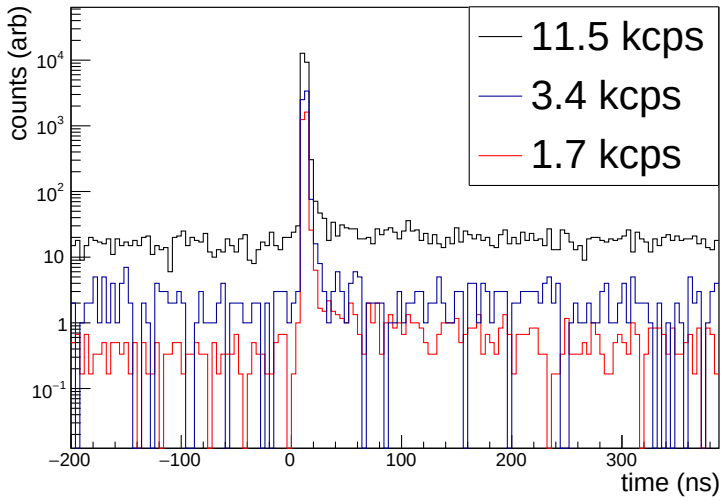

Figure 5.6 Data taken with cuts on continuum energy, showing the peak and the accidentals level. This data was taken with the custom made aluminum target at density 0.3 g/cm^3. At low rate we could resolve a small long lifetime component.

indicating it was positronium forming. For this reason we switched to a solid piece of Aluminum, with results shown in Figure 5.7. The lifetime component had dissappeared, so we could have been seeing positronium forming on the surfaces between the thin foil layers. This shows a clean

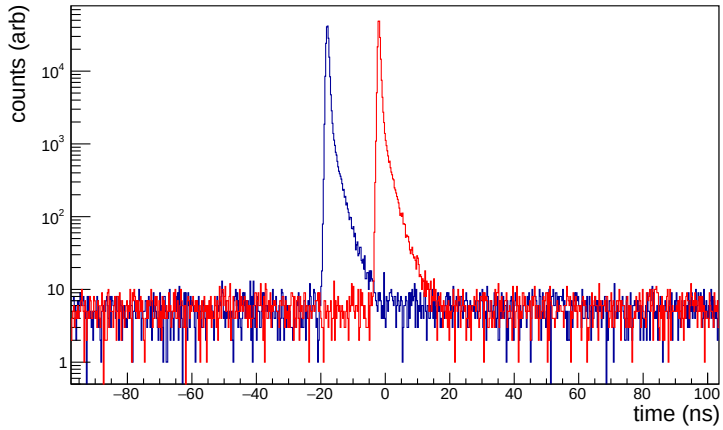

Figure 5.7 Time spectrum for a solid piece of aluminum. Two spectra were constructed depending on which detector is treated as start and which is stop. Note the clear lifetime component with 2 ns lifetime, indicative of positronium formation in plastic.

response for both directions the spectrum was built, and clearly displays a lifetime component of around 2 ns. This is to be expected for positrons forming positronium in plastic. The ^{22}Na source

was deposited on a thin mylar foil, which was further held in a thin plastic layer (with a window so the β's escape). This plastic component is likely from the positronium forming in that plastic of the source itself, and will be present for all tests in this chapter.

5.5.2 MgO powder

We replaced the aluminum with powder and immediately saw a long lifetime component, shown in Figure 5.8. The magnesium oxide powder was 35 nm grain size and compressed to a density of 0.3 g/cm^3. Initial fits returned a long lifetime component of 66±6 ns. The long lifetime component

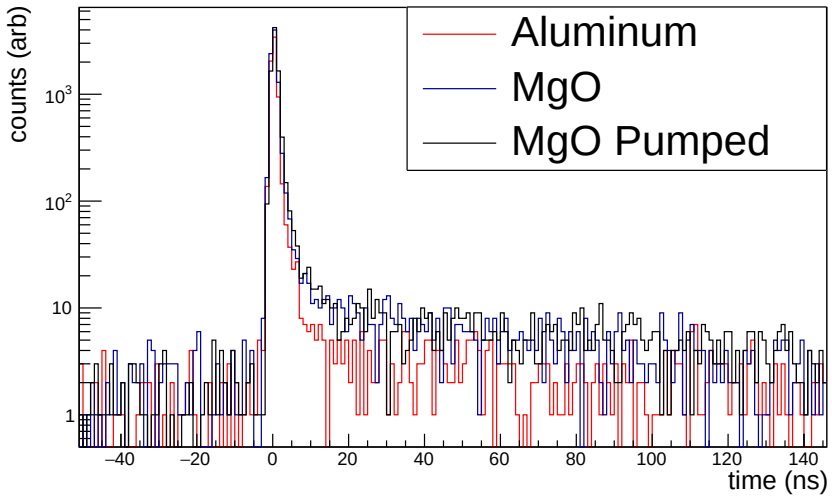

Figure 5.8 Data with unprepared Magnesium Oxide powder. The powder shows a (small) long lifetime component compared to data taken with a solid aluminum block.

was small, so there was not much positronium formation. Also shown is the spectrum when pumped with a roughing pump for 20 hours. Pumping the powder did indeed increase the lifetime with the fit returning a long lifetime of 98±10 ns, but the integral of the long lifetime component was not changed. The result of fitting the MgO powder under vacuum is shown in Figure 5.9. Translating the amplitudes of each lifetime component into a "formation fraction" is non-trivial and requires some modeling to extract the relevant information.

5.6 Extracting lifetime and formation fraction

The positron travels through a series of materials after emission. In each material it can do one of three things, annihilate, possibly form positronium, or pass through the material. Each of these

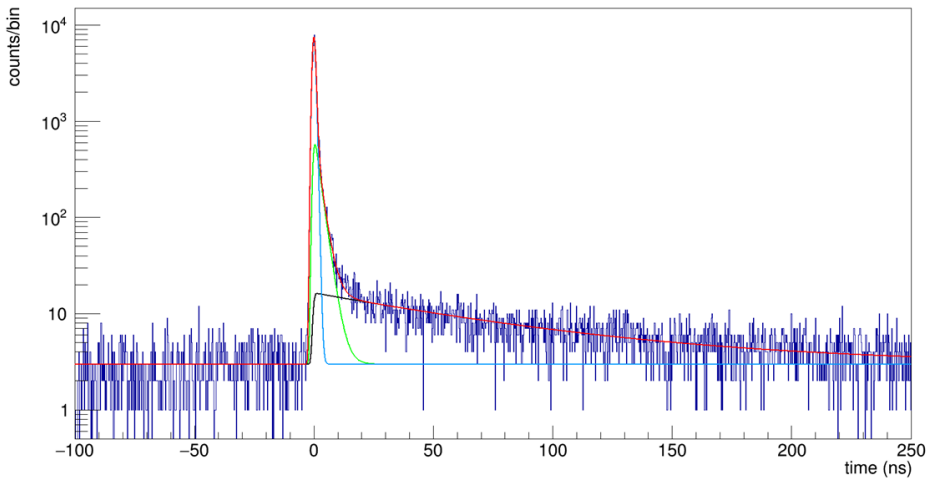

Figure 5.9 Example of a fit of a lifetime spectrum. There is clearly a sharp peak, a lifetime component around 2 ns (plastic), and a long lifetime (o-Ps). The lifetimes and the relative amplitudes are extracted for each component.

options affect both the time and energy distribution of the final gamma distribution.

5.6.1 Positronium state population

In a simplification, consider only 2 materials.

1. "Plastic" - The source itself is in a plastic holder, but we treat all the materials of the source (plastic, mylar foil, paper label) to be the "plastic" material.

2. "Powder" - This is the target we want to study, an aluminum container filled with powder. This model does not include the positrons that annihilate against the aluminum of the container, ideally this number is minimized by choosing a good geometry.

The model is illustrated in Figure 5.10. Starting with with N_β β-decays, some fraction stop in plastic, f^p. The remaining fraction $1 - f^p$ reach the powder target. Finally in each of these materials there is some probability for the positrons to form positronium, we call this the positronium formation fraction f_{Ps}. There is a formation fraction in the plastic f^p_{Ps}, and the powder f_{Ps}. The ultimate goal is to measure f_{Ps} for the given powder, everything that follows is attempting to extract this quantity. One quarter of the positronium forms para-positronium and three quarters form ortho-positronium. Para-positronium has a lifetime of only 124 ps and is indistinguishable from the direct annihilation. This gives the following five distributions,

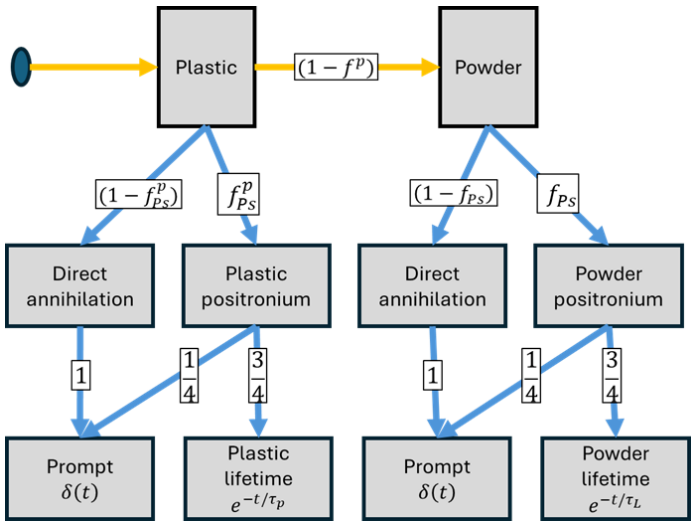

Figure 5.10 Model for positronium lifetime distribution. Positrons are either stopped in plastic of the powder. Both materials have a chance for direct annihilation, or formation of positronium. 1/4 of the formed positronium has a lifetime 124 ps and is indistinguishable from the prompt events, the other 3/4 forms ortho-positronium with a characteristic lifetime.

$$N_{annhilate} = N_\beta(f^p(1-f^p_{Ps}) + (1-f^p)(1-f_{Ps})) \tag{5.2}$$

$$N^{plastic}_{p-Ps} = \frac{1}{4}N_\beta f^p f^p_{Ps} \tag{5.3}$$

$$N^{plastic}_{o-Ps} = \frac{3}{4}N_\beta f^p f^p_{Ps} \tag{5.4}$$

$$N^{powder}_{p-Ps} = \frac{1}{4}N_\beta (1-f^p) f^p_{Ps} \tag{5.5}$$

$$N^{powder}_{o-Ps} = \frac{3}{4}N_\beta (1-f^p) f^p_{Ps} \tag{5.6}$$

Direct annihilation and para-positronium decays have a distinct time signature (a delta function), and the various ortho-positronium decays have distinct lifetimes for each material. This means that these populations can in principle be separated by their various time-dependencies.

$$N^{prompt}(t) = N_\beta\left(f^p(1-f^p_{Ps}) + \frac{1}{4}f^p f^p_{Ps} + (1-f^p)(1-f_{Ps}) + \frac{1}{4}(1-f^p)f_{Ps}\right)\delta(t) \tag{5.7}$$

$$N^{plastic}(t) = \frac{3}{4}N_\beta f^p f^p_{Ps} e^{-t/\tau_{plastic}} \tag{5.8}$$

$$N^{plastic}(t) = \frac{3}{4}N_\beta (1-f^p) f_{Ps} e^{-t/\tau_{powder}} \tag{5.9}$$

Where $N(t)$ is the state population at time t (allowing the liberty of calling "direct annhilation" a "state"). This model assumes that all ortho-positronium forms in the ground state.

5.6.2 Positronium decay

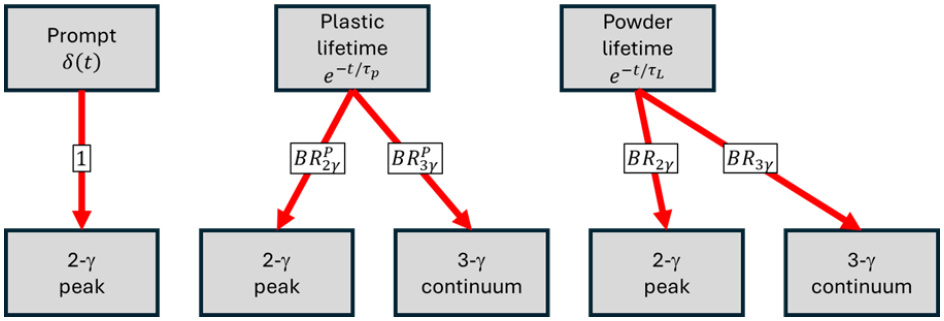

Figure 5.11 Starting with the lifetime distributions (which in-principle we can separate), the Ps decay events are mapped into 2-γ and 3-γ decays dependent on the relative branching ratios (which are material dependent). In principle all 5 of these are distinguishable because they have different time-dependence and different energy distributions. However finite detection efficiency will mix up our ability to completely distinguish 2-γ from 3-γ events.

The angular distribution of the decay products is taken to be isotropic. The 2-γ decay results in two 511 keV photons emitted back-to-back. The 3-γ decay results in three photons in a plane with a continuous energy distribution from 0-511 keV. This means our relative sensitivity to the decay channels depends on the energy cuts. Gating on the 511's biases the results to see less o-Ps decay.

Ortho-positronium in a material has a more complicated time evolution than in vacuum. Assuming a simple uniform material, there are two decay channels for the ortho-positronium. It can either decay to 3-γ, or it can annihilate due to interaction with the surrounding material. The lifetime in the ith material, Γ_i, depends on the decay width due to "pickoff annihilation", $\Gamma_i^{pickoff}$. This gives two competing decay widths:

$$\Gamma_i = \Gamma^{o-Ps} + \Gamma_i^{pickoff} \tag{5.10}$$

$$\tau_i = \frac{1}{\Gamma_i} \tag{5.11}$$

We assume that all pickoff annihilation goes to 2-γ. This gives the branching ratio of o-Ps

$$BR(o-Ps \rightarrow 3\gamma) = \frac{\Gamma^{o-Ps}}{\Gamma_i} = \frac{\tau_i}{\tau_{o-Ps}} \tag{5.12}$$

$$BR(o-Ps \rightarrow 2\gamma) = 1 - \frac{\tau_i}{\tau_{o-Ps}} \tag{5.13}$$

where $\tau_{o-Ps} = 142$ ns, the vacuum lifetime for ortho-Positronium. For plastic with a lifetime of $\tau_P = 2.25$ ns the positronium has $BR(3\gamma) = \frac{2.25}{142} = 1.58\%$. Whereas for the unprepared powder with a lifetime 65 ns, the positronium has $BR(3\gamma) = 45.8\%$.

This means that for each "state" that the β^+ can end in, the model must to account for the final state photons it leads to. The energy distribution for a 2-γ decay is a simple delta function energy at 511 keV. For the 3-γ decays it is a continuous energy distribution with complicated angles between each photon.

The lifetimes are measured when we perform the fits, so the branching ratios are also already being measuring. This must be accounted for to extract the correct state populations. To fully disentangle these effects and extract a formation fraction we need to model the detector response and how the energy cuts bias different final states.

5.6.3 Detector Response

Our final measurement (a set of hits with a timestamp and a reconstructed energy) is complicated by the detector response. Assume that there is a single efficiency for 2-γ decays and for 3-γ decays. They are functions of the energy cuts, but not of time, stopping position, or stopping material, etc. This is certainly an oversimplification, spreading of the source will affect the geometric acceptance, different materials will scatter photons at different rates, etc.

Consider the ratio of the detection efficiencies for a given energy range $\epsilon_{3\gamma}/\epsilon_{2\gamma}$. The detectors are more efficient for lower energies, so this would raise the relative efficiency to a higher number. But Compton scattering also maps some 2-γ events into the energy cuts.

As defined above, the detection efficiency $\epsilon_{2\gamma}^{peak}$ means "for N 2-γ decays, there are $N\epsilon_{2\gamma}^{peak}$ counts in the $peak$ energy window". Similarly for $\epsilon_{2\gamma}^{cont}$, $\epsilon_{3\gamma}^{peak}$, and $\epsilon_{3\gamma}^{cont}$. These values can be estimated in a simple Monte-Carlo. This was performed by David-Michael Peterson (MSU) and shown in Figures 5.12 and 5.13. We place a $LaBr_3$ cylinder 5.5 cm from a point source and fire a definite number of 2-γ and 3-γ events. The number of events within an energy window is an estimate of the detection efficiency. Ultimately the relative efficiencies $\epsilon_{3\gamma}/\epsilon_{2\gamma}$ enter the calculation of the formation fraction, so we are less sensitive to effects like offset of the source. Numbers are

given in Table 5.1.

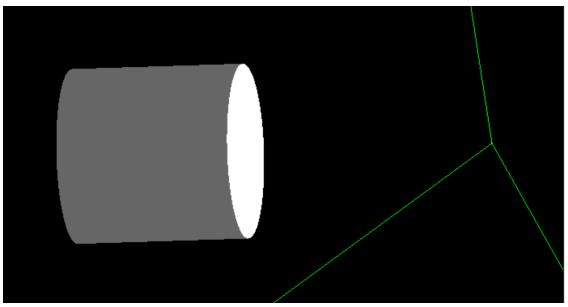

Figure 5.12 Example of a three photon event occuring in front of the $LaBr_3$ detector. Of course, this event leaves no signal in the crystal.

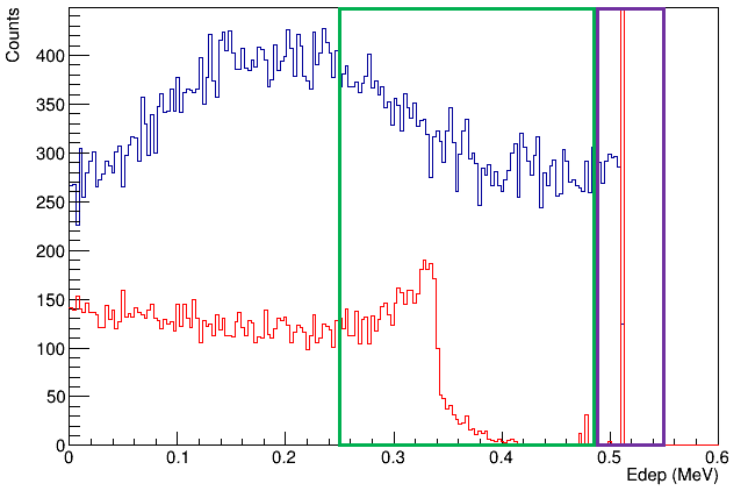

Figure 5.13 Simulated energy deposited in a $LaBr_3$ crystal from a point source of positronium. Blue shows the continuous 3-γ events, and red the back to back 2-γ events. The photopeak at 511 goes well off the plot. The two energy windows are shown in green and purple. This includes no smearing for finite detector resolution.

5.6.4 Final distribution

All of the above effects are combined and give an analytic expression for the amplitude of the lifetime component A_i in terms of the state populations.

$$A_{prompt} = \epsilon_{2\gamma}(N_{annihilate} + N_{p-Ps}^{plastic} + N_{o-Ps}^{powder}) \tag{5.14}$$
$$= N_\beta \epsilon_{2\gamma}(f^p(1 - \frac{3}{4}f_{Ps}^p) + (1 - f^p)(1 - \frac{3}{4}f_{Ps}))$$
$$A_{plastic} = \frac{3}{4}N_\beta \epsilon_{2\gamma} f^p f_{Ps}^p \tag{5.15}$$

	Centered	Offset
$\epsilon_{2\gamma}^{cont}$	0.50%	0.333%
$\epsilon_{3\gamma}^{cont}$	2.56%	1.88%
$\epsilon_{2\gamma}^{cont}/\epsilon_{3\gamma}^{cont}$	0.195	0.185
$\epsilon_{2\gamma}^{peak}$	1.57%	1.18%
$\epsilon_{3\gamma}^{peak}$	0.232%	0.167%
$\epsilon_{2\gamma}^{peak}/\epsilon_{3\gamma}^{peak}$	6.77	7.07

Table 5.1 Detection efficiency for a single $LaBr_3$ detector for a source located 5.5 cm from the front face, and for a source offset to 6.5 cm from the front face.

$$A_{powder} = \frac{3}{4} N_\beta (BR_{2\gamma}\epsilon_{2\gamma} + BR_{3\gamma}\epsilon_{3\gamma})(1 - f^p) f_{Ps} \tag{5.16}$$

which includes the simplifying assumption that all ortho-positronium in plastic decays to two photons. Now, in principle we directly measured A_i from the fits, we measured the lifetimes (and therefore the branching ratios), and we have simulated the detection efficiencies. We cannot extract f_{Ps} directly from these quantities. This is because f^p and f_{Ps}^p are fully correlated (varying the number of positrons that stop in plastic versus the number that form positronium in the plastic affects the counts in the same way). From this data we can extract,

$$f^p f_{Ps}^p = \frac{3}{4} \frac{\bar{A}_{plastic}}{\bar{A}_{prompt} + \bar{A}_{plastic} + \bar{A}_{powder}} \tag{5.17}$$

$$(1 - f^p) f_{Ps} = \frac{3}{4} \frac{\bar{A}_{powder}}{\bar{A}_{prompt} + \bar{A}_{plastic} + \bar{A}_{powder}} \tag{5.18}$$

where $\bar{A}_i$ is the amplitude corrected for the efficiency (or efficiencies weighted by branching ratios). These quantities cannot be disentangled without running some dedicated tests to determine either the stopping fraction in plastic, or the formation fraction in plastic.

5.6.5 Study of plastic

If all of the positrons stop in plastic then Equation 5.17 could be used to directly extract the formation fraction for plastic. Since all decays in this scenario would be 2-γ decays the amplitudes would not need to be corrected for detection efficiency as well. The formation fraction in plastic would be,

$$f_{Ps}^P = \frac{4}{3} \frac{A_{plastic}}{A_{prompt} + A_{plastic}} \tag{5.19}$$

We measured this by taking standard cling wrap and layering it over an aluminum block. The plastic was held flat on a table while the block was flipped over and over to apply multiple layers at once. This plastic was pulled tight to avoid rippling and air pockets within the plastic. This is shown in Figure 5.14. The aluminum block wrapped in plastic was placed on top of the source to not affect the source position and relative efficiencies between runs (although these should cancel run by run).

Figure 5.14 Small aluminum block carefully layered in cling wrap.

The results are shown in Figure 5.15. The spectrum was built using the continuum energy cuts, and the results are shown for both detector combinations (using one as START and the other as STOP or vice-versa). The errors were taken from the fit results, but were overestimated as the amplitude for the two fit components were negatively correlated.

Assuming that the formation fraction in the plastic did not change, and only the number of positrons in plastic changed, then adding more layers should approach the limit $f^p \rightarrow 1$. This means the data in Figure 5.15 should asymptote to the value of f^P_{Ps}.

These tests gave a formation fraction for plastic between 25-33%. The values found in literature give 58% [74], however this appears to be a typo, referring to their source for this claim we find a value of 28 ± 3% [75] in agreement with the measurement presented here. The formation fraction for plastic as defined in this dataset was not purely plastic, but included the effect of the mylar foil, paper label, etc. This also assumed a single formation fraction for the different kinds of plastic.

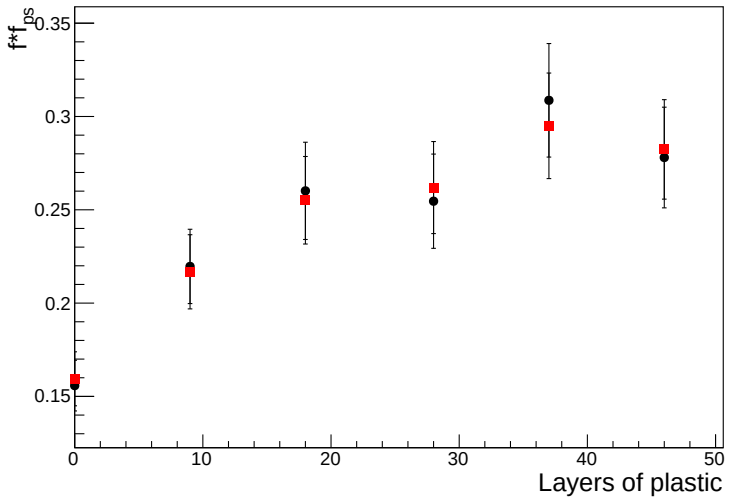

Figure 5.15 Extrapolating $f_p f_{Ps}$ from the plastic data as adding more and more layers of plastic. Red and black are are the results depending on which detector we call "START" and "STOP". Note that errors are from the fit results and do not include correlated errors.

Taking the formation fraction in plastic as 28% and using the results from the previous MgO powder tests shown in Figure 5.8, we extract a "stopping fraction" $f^p = 0.6$. This is reasonable as half of the positrons are entirely stopped in the back half of the source.

5.7 Powder tests

Initial tests of 35 nm MgO powder at 0.3 g/cm^3 density were shown in Figure 5.8. These featured a very small long lifetime component, and a lifetime around 70 ns. The chamber was connected to a roughing pump and the pump ran overnight. In principle the vacuum pump removes moisture from the powder, and oxygen in the voids, and should therefore increase the lifetime. Indeed for the MgO powder we saw the lifetime increase to 90 ns under vacuum.

Previous experiments that used MgO powder prepared the powder in a vacuum oven to fully desiccate it. The powder was then kept under vacuum or flushed with dry air. Recent experiments have increasingly been using chunks of silica aerogel (SiO_2) for positronium formation. We studied both "unprepared" 35 nm MgO powder at 0.3 g/cm^3 density and "unprepared" SiO_2 powder at 1200 μm grain sizes powders at 0.1 g/cm^3 density. The time spectra are shown in Figure 5.16.

We saw a substantial improvement in the SiO_2 powder without having to place it in an oven. We produced the spectra using two sets of energy cuts for the stop signal. We considered the

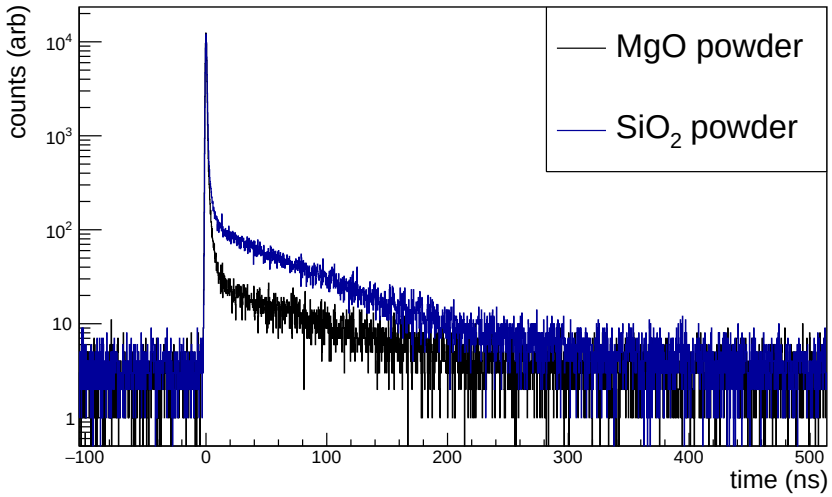

Figure 5.16 Lifetime spectrum for MgO powder and SiO_2 powder, showing a substantial increase in the long lifetime component.

"peak cut" between 490-520 keV, and the continuum cut between 250-490 keV. These should have different efficiencies for 2-γ and 3-γ events. The results for the same powder in air and under vacuum are shown in Figures 5.17a and 5.17b respectively, with the observed time spectra for the peak energy cut (red) and continuum energy cut (blue). The two datasets did not have the same total normalization. Before pumping we saw a lifetime of 72 ± 0.8 ns, after pumping we saw a long lifetime of 132 ± 2.8 ns (compared with 142 ns theoretical lifetime for o-Ps). The disappearance of the long lifetime counts for the peak cut energy region was the direct effect of the relative branching ratios dependence on the lifetime. With 72 ns lifetime 50% of the ortho-positronium decayed to 2 photons, but at 132 ns only 7% of the ortho-positronium decayed to 2 photons, resulting in almost no 511 keV events in the long lifetime component.

The relative detection efficiencies can also be estimated from the data in Figure 5.17. For a lifetime of 72 ns the branching ratios are nearly 0.5 for both channels. This means that the relative amplitudes of the peak counts versus the continuum cuts should give an estimate of the relative detection efficiency of 2-γ/3-γ events that can be compared to the Monte-Carlo results. The ratio of the amplitudes of the long lifetime components should give,

$$\frac{A_{long}^{peak}}{A_{long}^{cont}} = \frac{0.5\epsilon_{2\gamma}^{peak} + 0.5\epsilon_{3\gamma}^{peak}}{0.5\epsilon_{2\gamma}^{cont} + 0.5\epsilon_{3\gamma}^{cont}} \tag{5.20}$$

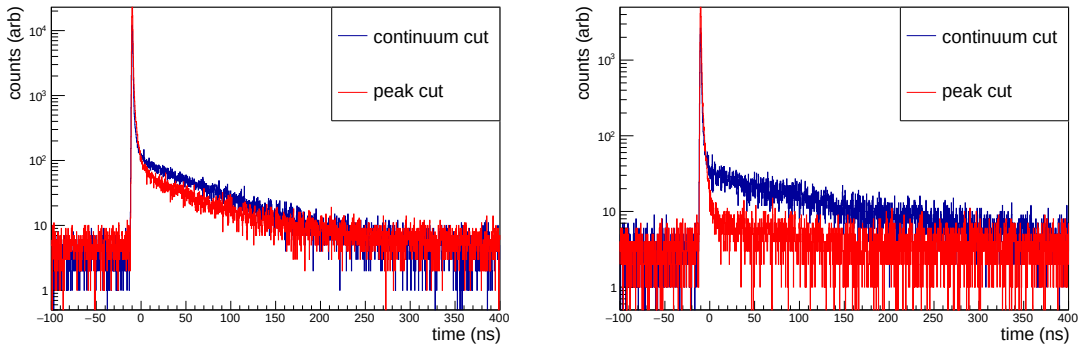

(a) SiO_2 in air (b) SiO_2 in vacuum

Figure 5.17 This data shows a large increase in lifetime when the powder was pumped under vacuum. This shows the change to the branching ratios for 2-γ to 3-γ decays. The "peak" cut primarily saw 511 keV back to back photons, and the "continuum" cut primarily saw the continuous 3-γ distribution. Clearly the number of events in the peak for the long lifetime component was dramatically reduced when the powder was under vacuum.

The Monte-Carlo simulation give relative efficiencies of 0.59 for the centered source, and 0.61 for the offset source. Compare this with the relative amplitudes in Figure 5.17, which gave 0.6. This somewhat obscures the effect of offsetting the source, as that varies the relative efficiencies in opposite directions which cancels when the efficiencies are summed in this way.

The extracted formation fractions for the MgO powder, SiO_2 in air, and SiO_2 in vacuum are presented in Table 5.2. The results are quoted for both sets of efficiencies that were simulated. The different estimated efficiencies shift the extracted formation fractions by a 10% relative shift. There is a large formation fraction for SiO_2 powder under vacuum, at around 50%, exceeding our target formation fraction.

	f_{Ps} (%)	f_{Ps} varied ϵ (%)
MgO	11.4	10.4
SiO_2	41.3	38.1
SiO_2 vacuum	52.5	48.0

Table 5.2 Measured formation fraction using results from fits and correcting for relative efficiencies. All cuts are on the continuum energy. The two columns correspond to using the efficiencies in each column of Table 5.1.

With these results we should be able to achieve the source rate needed to reach the target final statistics. We achieved a lifetime of 132 ns, compared to 124 ns for the Michigan measurement

[38], and 126 ns for the Tokyo experiment [39]. The use of SiO_2 powder has removed the necessity of disassembling the apparatus to re-prepare the powder (by baking it in a vacuum desiccator), this will be a large benefit over the course of the experiment.

CHAPTER 6

DESIGN AND SIMULATION OF INNER MODULE

6.1 Overview

The inner module consists of the β^+ source, the start detectors, and the powder for positronium formation. The size and geometry of the start detector itself affects how many β's reach the powder, and where they stop in the powder. This directly affects the spatial distribution of the positronium atoms. A broader spatial distribution will change the acceptances for both 2-γ and 3-γ events in the experiment, and means the positronium will have a broader distribution of lifetimes due to inhomogeneities in the magnetic field. These effects were studied for different combinations of start detectors and powders in dedicated Monte-Carlo simulations. In this chapter we present the results from the Geant4 simulations that were primarily performed by David-Michael Peterson (MSU). These effets were also studied by Paul A. Voytas and Elizabeth A. George (WU).

6.2 Start detector and powder formation

There are two common methods to build the lifetime spectrum of positronium, γ-γ coincidence, and β-γ coincidence. Throughout Chapter 5 we investigated the lifetime spectrum built between two γ events. The actual experiment will directly measure the β from the β-decay. This will give a much higher trigger rate for the start signals, and it will allow the use of a source that does not emit γ's (which can induce accidentals in the measurement).

"Organic" scintillators are commonly used for charged particles, herein referred to as plastic scintillators. The basic principle is the same as an inorganic scintillator, but the mechanism of scintillation and sensitivity to different particles is different [22]. An optimal start detector will detect the β's, but not stop them from reaching the powder. Ideally it will have as large of a solid angle coverage as possible, and will cover the powder so that no β can reach the powder without passing through the scintillator.

We utilize a thin plastic scintillator for the detector. We need it to be thick enough to generate enough scintillation light to trigger on, but also thin enough that it does not stop the β's. This is

non-trivial as the β's below 1 MeV do not penetrate very far through plastic (to be shown below). Even a very thin layer of plastic can stop a substantial fraction of the β's, and dramatically reduce the number that reach the powder to form positronium. Further, different sources have different endpoint energies, and the higher the β energy, the more likely it is to punch through the detector, as illustrated in Figure 6.1a.

Beyond that, we need some way to read out the thin scintillator, some lightguide that can be coupled to some form of photomultipler. This will all sit in the middle of our detector array, so it must be low mass, and function in a magnetic field. The plan for the online experiment is to couple the light guide to a PMT outside the magnet warm bore using optical fibers. For the tests performed throughout this work we simply read the lightguide with SiPMs.

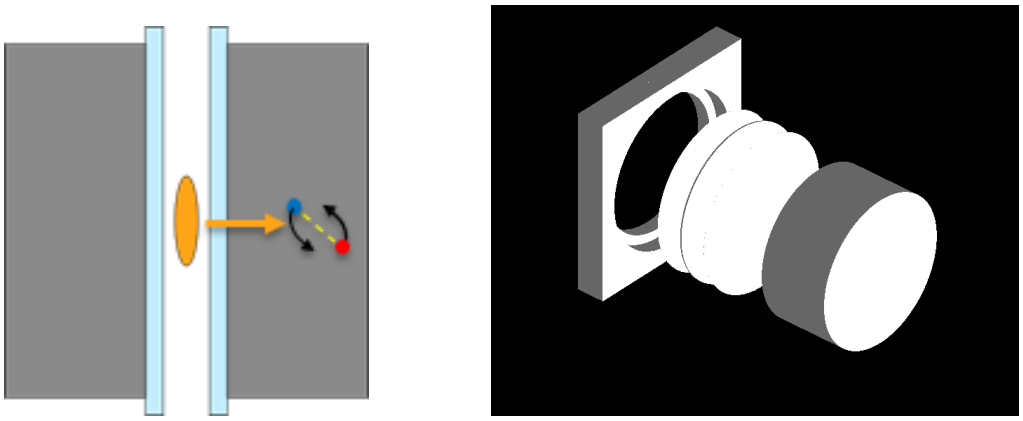

(a) (b)

Figure 6.1 (a) Cartoon of the design, a β source emits positrons that travel through a plastic scintillator and stop in powder to form positronium. (b) A realization of this idea expanded to show each individual piece, a lightguide (square with cylinder cut out) to couple the scintillator to a readout, the scintillator with a layer of Al foil on each side, and finally the powder. This would be one side of the combined start detector and powder module, with a symmetrically placed setup on the opposite side of the source.

For these studies we use a square plexiglass lightguide with a circular cut through the center. The scintillator itself is Eljen-212 [76]. There are two thicknesses, 0.5 mm and 0.15 mm. These have dramatically different amounts of scintillation light and stopping fractions. Note that unlike with the γ detectors, the coating of the scintillator can't be neglected when considering particle propagation. Two layers of aluminum foil on the scintillator dramatically increases the width of the

scintillator and stop a large fraction of the positrons that would otherwise make it through. At the same time, with no coating we do not get enough scintillation light to our photomultipliers.

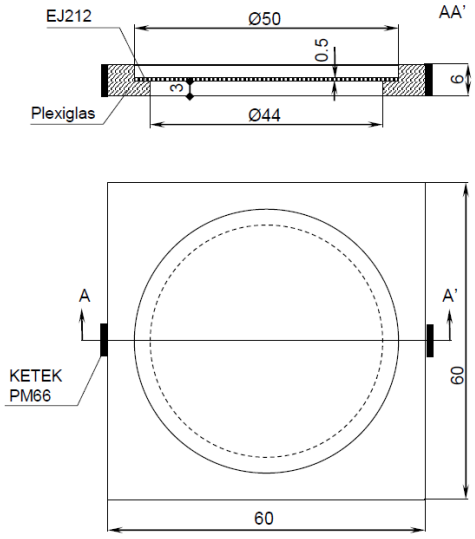

Figure 6.2 One design for the light guide (with the scintillator in the center). This features the 6 mm thick light guide and the 0.5 mm scintillator.

As the plastic scintillator will need to be read out in the magnetic field we currently utilize SiPMs. These will not be used in the final experiment for three reasons, 1) they break the symmetry of the setup, 2) they add too much matter between the powder and the γ-detectors, and 3) they cannot handle the high rate expected for our source.

6.3 Simulation and tracking

This simulation records the initial energy and direction of the β^+, its stopping position, as well as the ID of the object it stopped in. In principle we can therefore study, for a given number of β emissions what percentage stop in the powder (and what stop in other materials as well). We can then see where the β stopped within that specific material. In practice we only look at this for the powder.

6.4 β-primary generator

We study two β^+ sources, ^{22}Na, and ^{68}Ga. The resulting spectra for these sources are generated using the betaShape program [77, 78]. These are high precision spectra calculations that account

for competing electron capture processes. As shown in Figure 6.3, the gallium source has a much

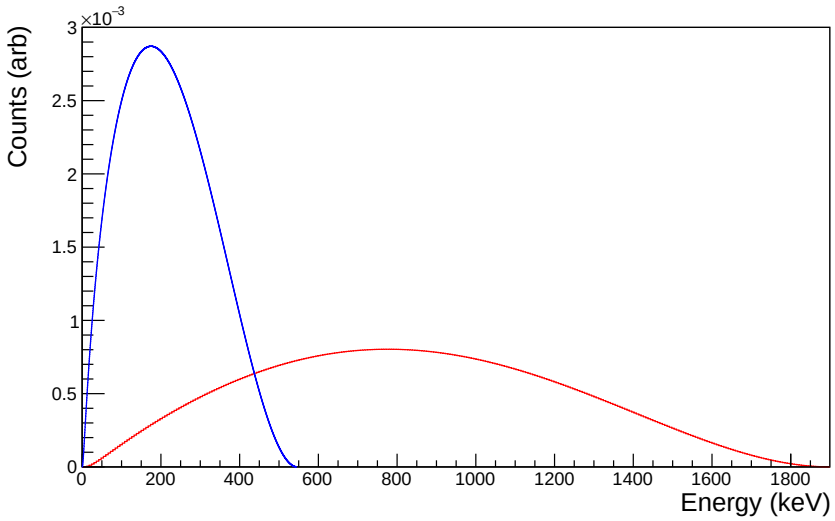

Figure 6.3 Energy distribution for β^+ coming from ^{22}Na (blue) and ^{68}Ga (red), generated using the betaShape program [77, 78].

higher end-point energy. This will translate to more positrons punching through the start detector, but also to a much larger spreading of the source throughout the powder.

Unless specified, all results shown until the very end of this chapter are for a point source of radioactivity. All positrons are emitted isotropically in the forward half-sphere ($+\hat{z}$).

6.5 Specification of geometry

The simulations estimate the stopping positions of the initial β's. Secondaries and any material that the β's cannot reach are unimportant. The inner module must include 4 pieces,

1. the lightguide,
2. the scintillator,
3. the wrapping for the scintillator,
4. the powder.

This does not include the β-source itself, or the aluminum container that holds the powder. These will both have an effect on stopping position. The source itself is more important as it can

stop positrons that backscatter off the scintillator and reach the powder in the opposite direction. The aluminum container is beyond the powder, and its main contribution would be the β's that backscatter off of it and stay in the powder. Most combinations of start detector and powder stop the positrons before they reach the exterior edge of the powder, with one notable except. We have also neglected the TiO_2 paint that covers the lightguide. As our final interest is in the powder (and materials between the source and the powder) this should have minimal impact.

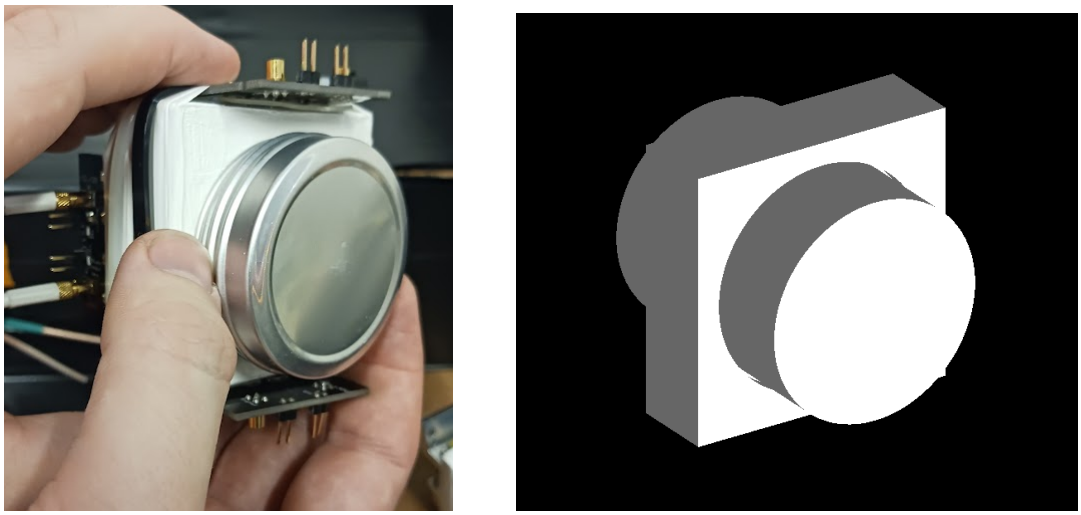

(a) (b)

Figure 6.4 (a) Prototype of start detector and powder container. (b) Reproduction in Geant4. Note that the SiPMs along with the aluminum can are not included in the Geant4 construction.

Here we present the study of 3-different start-detectors, and three different kinds of powder. The powder is always a cylinder of 2.5 cm radius and 2.3 cm length. This is always making direct contact with the scintillator (or more accurately with the foil on the scintillator).

6.5.1 Start detector

We present 3 designs for the start detector that vary in the geometry of the lightguide, the thickness of the scintillator, and the wrapping on the scintillator.

The first design, called the "5 mm inset square" is a thicker version of the geometry specified in Figure 6.2, with a 0.5 mm thick scintillator, and two layers of Al foil estimated at 0.016 mm thick each. This is an implementation of the actual physical modules we will test in Chapter 8. Notably, this design has a 5 mm inset where the radius of the cutout changes. This means that the powder

will always be offset from the source by at least 5 mm.

The second design, called the "3 mm inset square" is identical to the first design, but now matches the geometry in Figure 6.2. The thickness of the lightguide is 6 mm, meaning there is a 3 mm inset and the powder is therefore closer to the source.

The third design has not been constructed or tested, but it serves as an estimate for what an "optimized design" might look like. It is called the "0.5 mm inset cylinder". It is a cylindrical lightguide shown in Figure 6.5. The main benefit is that the cylindrical inset is reversed, the wider part (2.7 cm) faces the source and the narrower part (2.5 cm) holds the powder. This allows for optically coupling the scintillator to the resulting 2 mm inset, but also allows the scintillator to be much closer to the source. The scintillator itself is 0.15 mm thick, and is wrapped with 2 μm aluminized Mylar (2% aluminum).

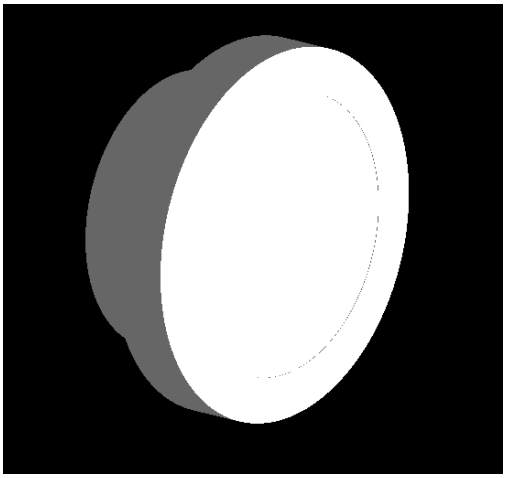

Figure 6.5 The implementation of the 0.5 mm inset cylindrical start detector. This moves the scintillator and the powder as close to the source as possible. The direction of the inset is reversed, so that the powder sits in the narrower regions.

6.5.2 Powder

We study three kinds of powders, all three of which have been prepared, though further work will be required for quantifying positronium formation in the different powders. The powder container is specified as a 2.5 cm radius cylinder of length 2.3 cm. The powder is assumed to have uniform density throughout.

We model the powder from Chapter 5 as 0.1 g/cm^3 SiO_2 powder uniform in density. We also have MgO powder at two densities, 0.3 g/cm^3 and 0.6 g/cm^3. The expected benefit of increased powder density is making the formation region smaller, at the cost of potentially reduced lifetime or positronium formation.

6.6 Stopping fraction and stopping position

Here we explore the parameter space by varying the powders while keeping the start detector the same, then varying the start detector while keeping the powder the same. All results in this section are for a point source of β^+.

Here we quote 4 quantities for the different combinations. Firstly the stopping fraction is the number of β's that stopped in the powder divided by the total number of β emissions. The larger this number the better, as it directly relates to the final event rate. We quote the mean offset in the z-direction relative to the $z = 0$ position at the source, the standard deviation in z and in ρ. This quantifies the offset of the formation region, and the general size of the spreading throughout the powder.

Table 6.1 shows the results for varying the powder. These are all run with the 5 mm inset square start detector, and as such the powder starts at 5 mm from the source.

Powder	Density (g/cm^3)	Source	Stops in Powder (%)	$\langle z \rangle$ (mm)	Δz (mm)	$\Delta\rho$ (mm)
SiO_2	0.1	^{22}Na	10.6	7.17	1.85	1.84
SiO_2	0.1	^{68}Ga	40.3	14.28	6.17	6.14
MgO	0.3	^{22}Na	10.6	5.75	0.62	0.62
MgO	0.3	^{68}Ga	74.0	10.77	4.43	3.79
MgO	0.6	^{22}Na	10.6	5.39	0.31	0.32
MgO	0.6	^{68}Ga	73.3	7.83	2.22	1.89

Table 6.1 The percentage of β^+ that stop in the powder, their mean depth, and the standard deviation of the depth and radial coordinate. All results run with the 0.5 mm thick scintillator in the 5 mm inset square start detector.

Clearly the gallium source has almost 7 times as many β^+ survive the start detector and reach the powder compared to the sodium source. For the low density SiO_2 powder with a gallium source we see that almost 41% of the β^+ that reach the powder do not get stopped in the powder

and escape. The offset along the z-axis is dominated by the size of the inset in the start detector (5 mm) for all combinations except low density SiO_2 with gallium source. Increasing the density dramatically reduces the size of the stopping distribution, more than 3 times smaller in z and six times smaller in ρ. Figure 6.6 shows the distribution of stopping positions for the SiO_2 powder and the 0.6 g/cm^3 MgO. The ρ-axis is scaled by $1/\rho$ to account for the cylindrical geometry, meaning this corresponds to the distribution seen in a "slice" through the powder.

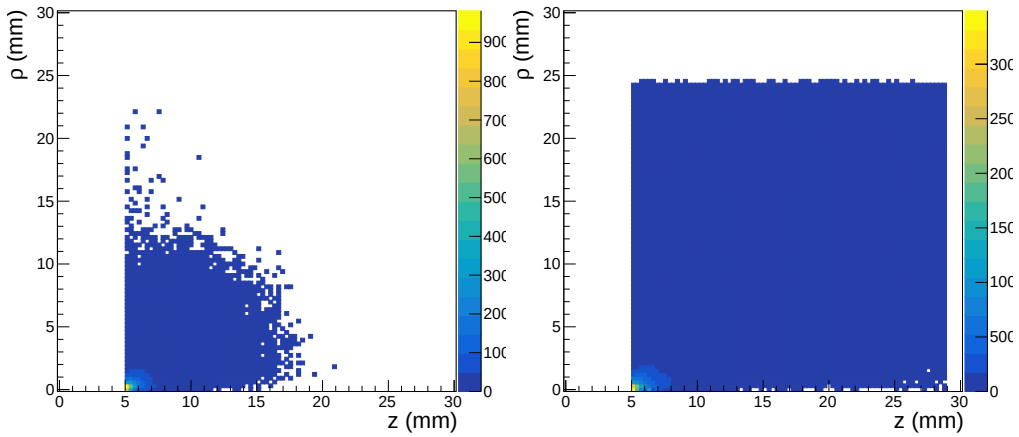

(a) ^{22}Na in SiO_2 at 0.1 g/cm^3 (b) ^{68}Ga in SiO_2 at 0.1 g/cm^3

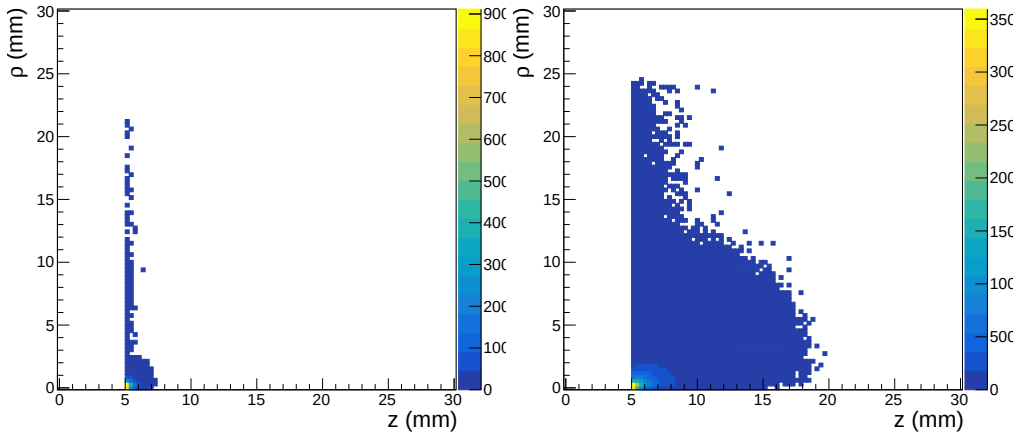

(c) ^{22}Na in MgO at 0.6 g/cm^3 (d) ^{68}Ga in MgO at 0.6 g/cm^3

Figure 6.6 Stopping positions for two β sources in two different powders, using the same start detector design. The ^{22}Na source in 0.6 g/cm^3 MgO is substantially more localized than all other combinations, and is entirely dominated by the geometry of the start detector (the 5 mm inset).

Next we consider changing the geometry of the start detector while using the 0.6 g/cm^3 MgO powder. These results are shown in Table 6.2. Changing the size of the inset dramatically changes

$\langle z \rangle$, as expected from moving the powder closer to the source. However, it does not decrease the spread in ρ, as the powder moves closer to the source more and more β's emitted at an angle will reach the source. In the final design, switching to the 0.15 mm scintillator means dramatically more angled β's survive the start detector and reach the powder.

Design	Source	Stops in Powder (%)	$\langle z \rangle$ (mm)	Δz (mm)	$\Delta\rho$ (mm)
5 mm inset	^{22}Na	10.6	5.39	0.31	0.32
5 mm inset	^{68}Ga	74.4	7.83	2.22	1.89
3 mm inset	^{22}Na	10.6	3.63	0.31	0.44
3 mm inset	^{68}Ga	74.4	6.07	2.22	2.03
0.5 mm inset	^{22}Na	52.5	0.96	0.42	0.89
0.5 mm inset	^{68}Ga	87.3	3.56	2.35	1.96

Table 6.2 The percentage of β^+ that stop in the powder, their mean depth, and the standard deviation of the depth and radial coordinate. All results run with 0.6 g/cm^3 MgO powder.

Now comparing the currently implemented design (5 mm inset square with 0.5 mm thick scintillator and 0.1 g/cm^3 powder), with a more optimized design (0.5 mm inset cylinder with 0.15 mm thick scintillator and 0.6 g/cm^3 powder) we see a dramatic improvement to almost all recorded quantities. These correspond to the first two lines in Table 6.1, and the last two lines in Table 6.2. Considering the ^{22}Na source specifically, the more optimal design has about 5 times as many positrons survive the start detector and reach the powder. This directly translates to a 5 times higher event rate in the final experiment. The mean z-position is about 1 mm, decreased by a factor of 7. We will have two start detectors and two powder containers, one in $+\hat{z}$ and on in $-\hat{z}$. This means the two powder containers with the two positronium distributions will be about 2 mm apart compared to 14 mm apart. Finally the spreading in z is reduced by a factor of 4, and in ρ by a factor of 2.

The spreading of the positronium position has two separate effects, 1) sampling a wider range of field values and therefore broadening the distribution of pseudo-triplet lifetimes and directions of tensor polarization, and 2) changing the geometry of the 2-γ and 3-γ events the detector pairs see.

6.7 Estimation of pseudo-triplet lifetime

The magnetic field map was provided in 0.25 inch steps. These are linearly interpolated to provide a more fine grained map of the field. The field values used are shown in Figure 6.7. We track the $\hat{z}$-component of the B-field, and the $\hat{\rho}$-component. The lifetime is determined by the absolute value of the field, the direction of the alignment is determined by the field direction.

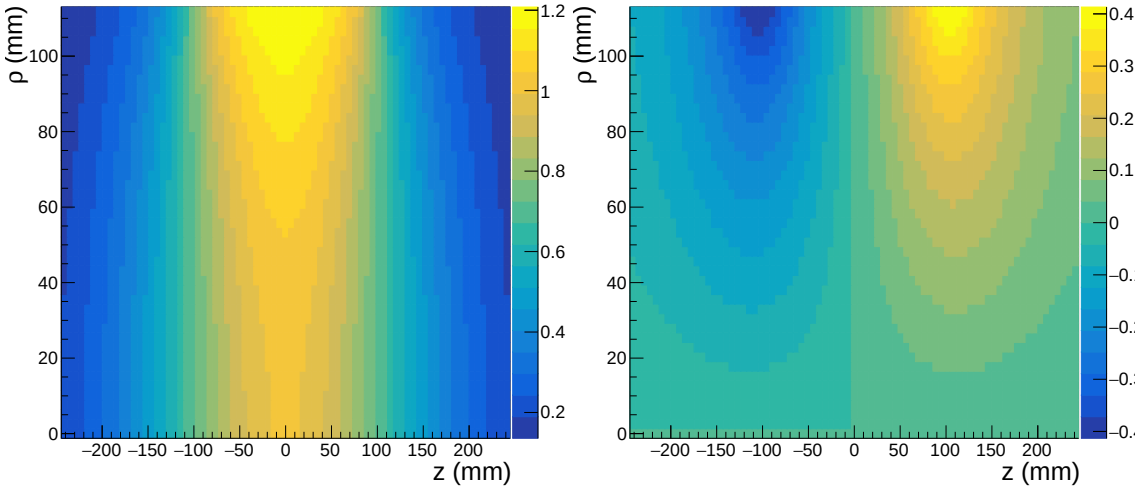

(a) $\mathbf{B}_z$ (b) $\mathbf{B}_\rho$

Figure 6.7 Field maps for the $\hat{z}$-component and $\hat{\rho}$-component of the magnetic field. Values are normalized to the "nominal" value at the center of the field.

We take the stopping positions from the earlier section and for each β that stops in the powder we record the two field components at its position. The distributions for the 5 mm inset square light guide with 0.1 g/cm^3 SiO_2 powder are shown in Figure 6.8. This configuration is sampling the broadest range of field values.

We need to consider how the field value affects the lifetime (as discussed in Chapter 3), and how the direction of the field affects the value of P_2. The B-field induces an alignment along its axis. The detector geometry is sensitive to distortions induced by alignment along the $\hat{z}$ axis. Relating the direction of induced alignment P_2', to the direction along the $\hat{z}$-axis goes as $P_2 = P_2'\cos(2\theta)$, where θ is the angle between the axes. This follows from P_2 being a component of a (traceless) symmetric second rank tensor. In reality for both sources the range of values of $\cos(2\theta)$ is miniscule, with

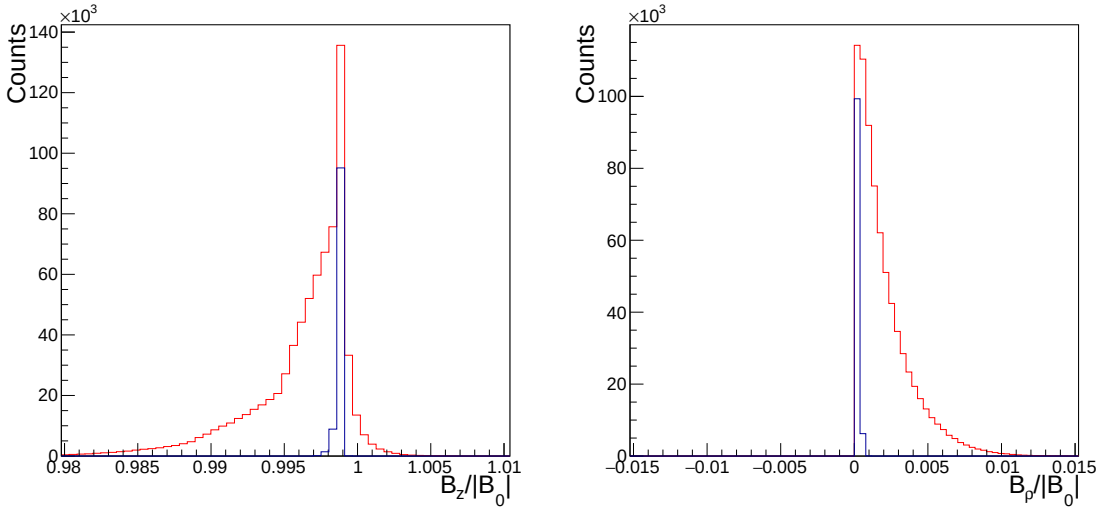

(a) $\mathbf{B}_z$ for forward β^+ (b) $\mathbf{B}_\rho$ for forwards β^+

Figure 6.8 Firing β^+ in a forwards aimed half-sphere for ^{22}Na (blue) and ^{68}Ga (red). The distribution of field values are plotted separated between the β^+ that scatter forwards and those that backscatter into the second powder container. Field values are normalized to the "nominal" value at the center of the magnet.

over 90% of events having less than a 0.00001% reduction.

The magnitude of the field affects the lifetime. We take the "nominal field value" (the value a the center of the magnet) as 0.4 T. We show the normalized distributions of lifetimes for two configurations, the currently implemented design, and the more optimized design with higher density MgO powder in Figure 6.9. For ^{22}Na we get a sharply peaked distribution of lifetimes that all fall within a few hundred ps range. The ^{68}Ga shows more spreading than the ^{22}Na, but almost the full distribution still falls within 1 ns, with the majority of events within a 500 ps time window. Returning to Chapter 5, with $LaBr_3$ we do not get sub-ns resolution on the lifetime fits.

As such, for all combinations of powders and start detectors studied here we expect that the spreading of source will have a minimal effect on the tensor polarization. Our magnet is homogeneous enough that the variation of field directions has little affect on the alignment. The variation in the lifetimes is also small enough to fall below the expected resolution of the electronics. The connection between the lifetime and the size of the signal will be the main topic of Chapter 10.

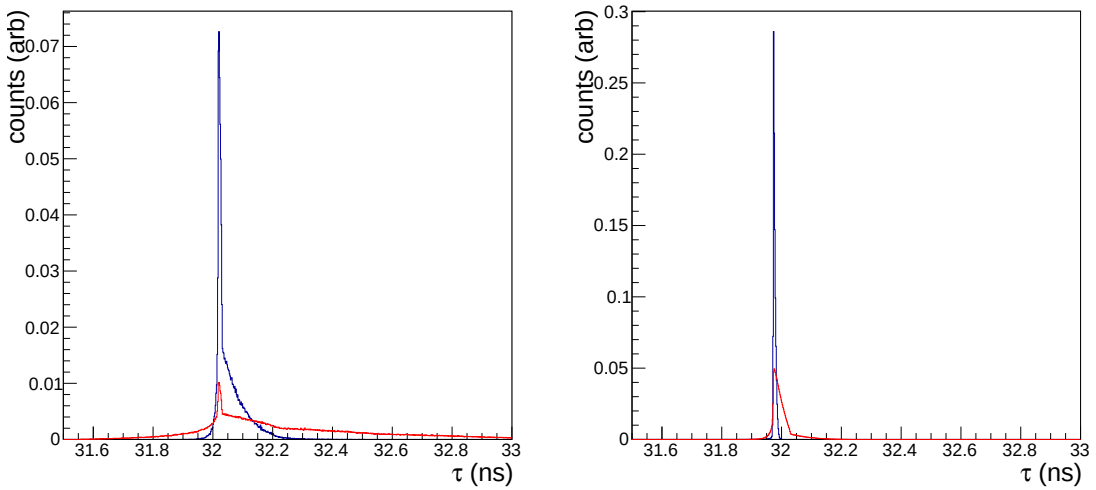

(a) Current start detector, SiO_2 at 0.1 g/cm^3 (b) Optimized start detector, MgO at 0.6 g/cm^3

Figure 6.9 Distribution of lifetimes for ^{22}Na (blue) and ^{68}Ga (red) for the two start detector designs studied. Clearly the galium source is sampling a wider range of field values, but the majority of all the distributions fall within a 1 ns range.

6.8 Results for three designs

Before concluding this discussion we present full results for three finalized designs. One of which is already constructed, one which could be reasonably constructed and tested with current prototypes, and one which is far more optimized. We label these as Design (A), Design (B), and Design (C). The results for these designs will be used in later chapters.

All results presented so far are missing one large effect, the spreading of the radioactivity for our source is not point-like, but is instead on the millimeter scale, and therefore will have a large effect when compared with $\langle\rho\rangle$ values estimated above. For this reason we include an estimate of the spread position of the radioactivity as an input for the following results. We model the radioactivity as having a gaussian profile in the x-y plane, a reasonable estimate would be a σ = 1.5 mm, although depending on the manufacturing method for the source it could be larger than this, and likely will not have a gaussian profile.

6.8.1 Design (A)

This is an implementation of the actual start detector prototype we have tested. This is the 5 mm inset start detector with 0.5 mm width scintillator with foil on both sides, shown in Figure 6.2.

Design	thickness of PVT	thickness of coating	distance to powder	powder density
(A)	0.5 mm	16 μm	5 mm	0.1 g/cm^3
(B)	0.5 mm	16 μm	3 mm	0.3 g/cm^3
(C)	0.15 mm	2 μm	0.5 mm	0.6 g/cm^3

Table 6.3 Summary of the main properties of the 3 Designs we will study going forwards.

The powder container is 0.1 g/cm^3 SiO_2 powder. We do not have plans to use this setup in the final experiment (or in the magnet at all), so we do not enter into estimating the lifetime distribution. The stopping position distribution is given in Figure 6.10, and the number of positrons stopping in the powder, and their spreading is given in Table 6.4.

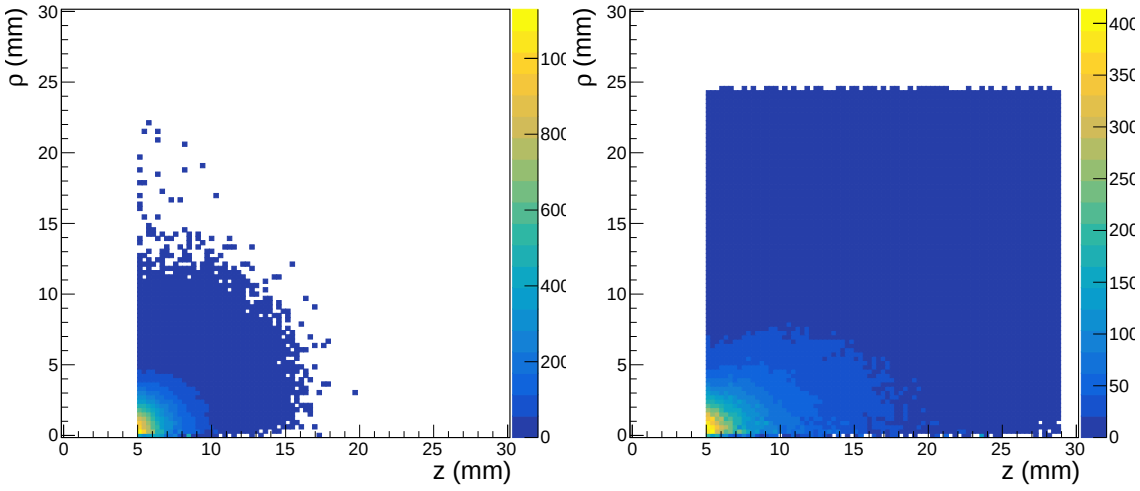

(a) ^{22}Na (b) ^{68}Ga

Figure 6.10 Stopping position for Design (A), representing the currently implemented start detector and powder combination.

Source	Stopping fraction (%)	Δz (mm)	$\Delta\rho$ (mm)
^{22}Na	10.6	1.85	1.95
^{68}Ga	43.9	6.17	6.06

Table 6.4 Source spreading for Design (A)

6.8.2 Design (B)

This is an improved implementation that could reasonably and quickly be used in further tests. This is the 3 mm inset start detector with 0.5 mm width scintillator with foil on both sides. The

powder container is 0.3 g/cm^3 MgO powder. The stopping position distribution is given in Figure 6.11, and the number of positrons stopping in powder, and their spreading is given in Table 6.5.

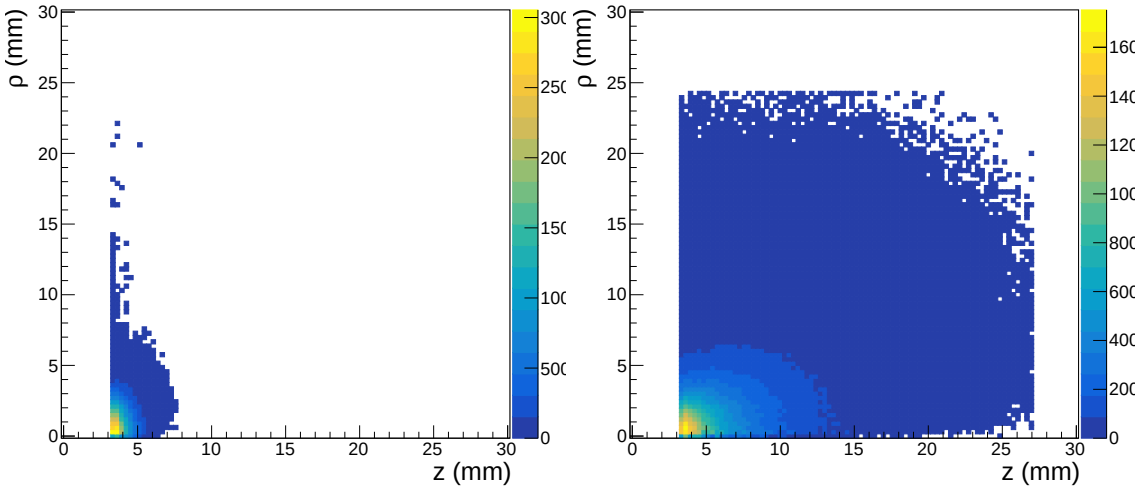

(a) ^{22}Na (b) ^{68}Ga

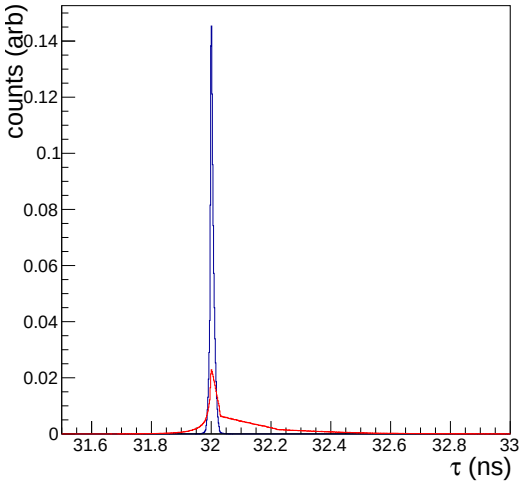

(c) pseudo-triplet lifetime

Figure 6.11 (a), (b) Stopping position for Design (B), representing a more optimized combination of start detector and powder using existing prototypes. (c) The pseudo-triplet lifetime distribution in 0.4 T field for ^{22}Na (blue) and ^{68}Ga (red).

6.8.3 Design (C)

This is the optimized design for the start detector presented above. This also uses MgO powder at a higher density of 0.6 g/cm^3. This is an achievable design, but would require further prototyping

Source	Stopping fraction (‰)	Δz (mm)	$\Delta\rho$ (mm)
^{22}Na	10.6	0.62	1.14
^{68}Ga	74.9	4.44	3.82

Table 6.5 Source spreading for Design (B)

and testing work to be performed. The stopping position distribution is given in Figure 6.12, and the number of positrons stopping in powder, and their spreading is given in Table 6.6.

Source	Stopping fraction (‰)	Δz (mm)	$\Delta\rho$ (mm)
^{22}Na	54.5	0.42	1.25
^{68}Ga	87.6	2.35	2.05

Table 6.6 Source spreading for Design (C)

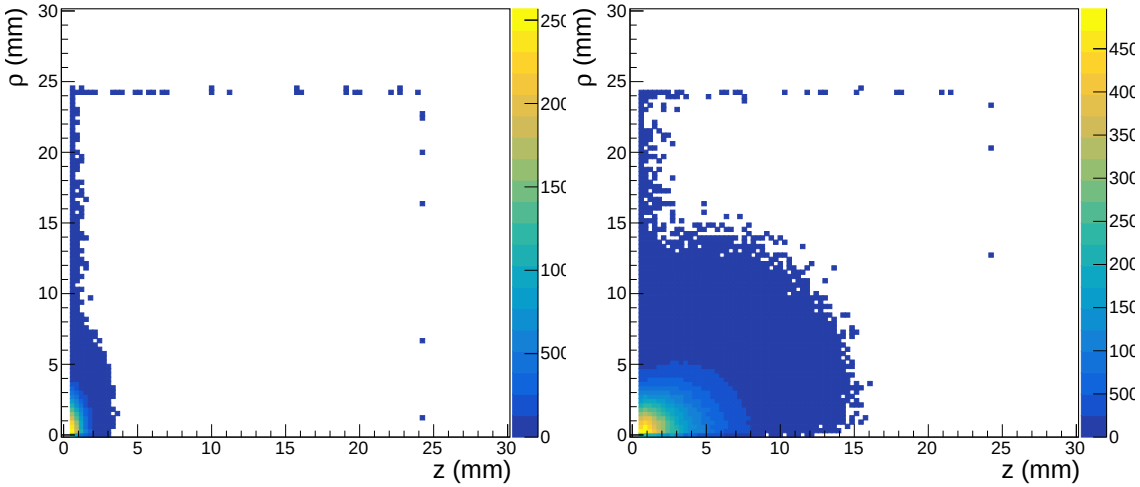

(a) ^{22}Na (b) ^{68}Ga

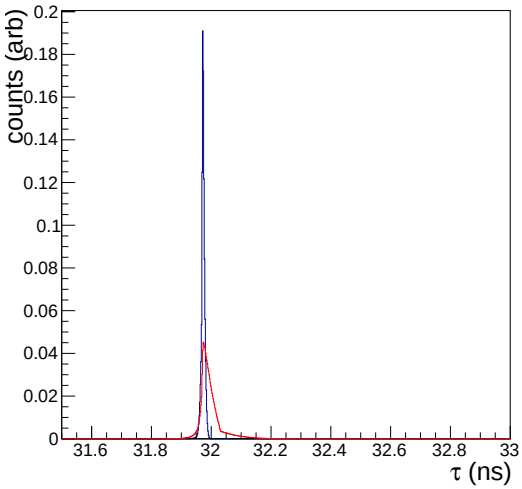

(c) pseudo-triplet lifetime

Figure 6.12 (a), (b) Stopping position for Design (C), representing an optimized design to maximize the amount of positrons reaching the powder, and minize their spreading through the powder. (c) The pseudo-triplet lifetime distribution in 0.4 T field for ^{22}Na (blue) and ^{68}Ga (red).

CHAPTER 7

SIMULATION OF γ-DETECTOR ARRAY

We have established the conceptual outline of the experiment, and identified a general structure for the array of γ-detectors. We plan for three rings with 16 detectors in each ring, and the outer two rings are angled inwards, as illustrated in Figure 3.7.

In this chapter we cover the more detailed design and optimization of the array. This extends the analytic work done in Chapter 3, to a full Monte-Carlo simulation in Geant4. These studies include optimizing the angle of the outer rings, determining the geometric analyzing power of each configuration, estimating the effect of finite energy resolution and spreading of the source. These simulations study both 3-γ events and 2-γ backgrounds. Finally we consider adding shielding between the rings in the array.

The simulations in this chapter were performed using Geant4. Much of this work was studied in parallel by Paul A. Voytas and Elizabeth A. George (WU) using EGSnrc [62].

7.1 Primary event generator

This chapter is concerned with the 2-γ and 3-γ events and their interplay with the array geometry. The first half of this section is concerned with positronium decay at a point exactly in the center of the detector array. The latter half of this chapter discusses the effect of spreading of the source. The event generator is described below.

7.1.1 2-γ events

These are very simple, a random vector $\hat{\mathbf{k}}$ is thrown, then the event consists of two photons with 511 keV. One in the $+\hat{\mathbf{k}}$-direction, and the other in the $-\hat{\mathbf{k}}$-direction.

7.1.2 3-γ events

At the beginning of the run a vector polarization and a tensor polarization are specified for the positronium atom. The matrix element is created including the Ore-Powell distribution, $a(\omega_1, \omega_2)$, and the tensor term $\sum_{ij} s_{ij} C_{ij}(\mathbf{k}_1, \mathbf{k}_2, \mathbf{k}_3)$. We do not consider the vector term in this work, $\mathbf{s} \cdot \mathbf{B}(\mathbf{k}_1, \mathbf{k}_2, \mathbf{k}_3)$. The matrix element is normalized to have a maximum value of 1 (in reality this

is slightly more complicated due to the divergence mentioned in Appendix B). This chapter only presents simulations using the isotropic distribution.

A complete description of the 3-γ phase space was given in Chapter 2. The phase space is flat in the energies, two of the angles, then has the standard $\sin(\theta)$ distribution for the polar spherical coordinate. For generation of events the matrix element (squared) is treated as a probability distribution on the phase space. A random ω_a and ω_b are sampled from the kinematically allowed region, and a third energy is determined by $\omega_c = 2m_e - \omega_a - \omega_b$. These are then ordered by their energies $\omega_1 > \omega_2 > \omega_3$. This is tantamount to restricting the generation to the red triangle in Figure 7.1. A random isotropic unit vector is sampled and assigned to $\hat{\mathbf{n}}$. The three photons are initialized with $\hat{\mathbf{k}}_1$ along $\hat{x}$, and $\hat{\mathbf{n}}$ along $\hat{z}$. The three momenta are then collectively rotated by randomly sampled Euler angles.

Finally the matrix element for this primary event is evaluated, and a random number between 0 and 1 is thrown. If that number is larger than the matrix element then the event is discarded and a new event is generated. If the number is less than the matrix element then the event is used in the simulation.

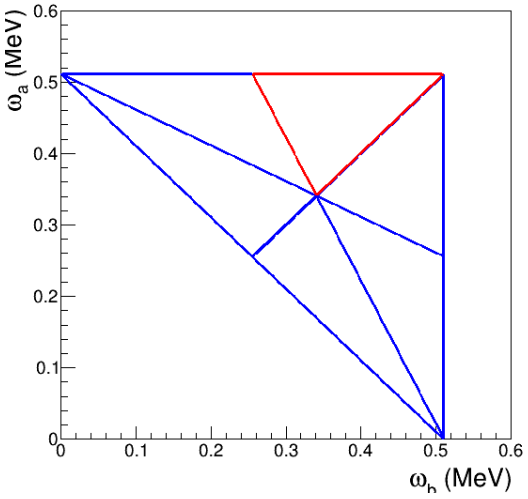

Figure 7.1 The kinematically allowed regions for two of the three energies from 3-γ decay. Each triangle corresponds to a different ordering of photons. Due to photon indistinguishability all considerations can be restricted to a single triangle. The red triangle is where $\omega_a > \omega_b > 2m_e - \omega_a - \omega_b$.

7.2 Detector array and configurations

The experiment will measure coincidences in pairs of detectors. Each pair will have a partner pair that is its image under parity (combined with rotation). Call this set of three detectors a "configuration". Each configuration has one dedicated "highest energy detector", and two "second highest energy" detectors. Two configurations are illustrated in Figure 7.2. Take the highest energy detector marked in green. This forms a configuration with two detectors marked in red, and a second configuration with two detectors marked in blue. As these two configurations have different opening angles, and therefore different energy ranges (see Figure 3.4) they select different parts of the phase space. This induces geometric structure onto the distributions measured in (ω_1,ω_2). For this chapter we refer to the 2-D energy plane restricted to the range $\omega_1 > \omega_2 > \omega_3$ as the "phase space" (in fact it is a 2-D projection of the full 5-D phase space).

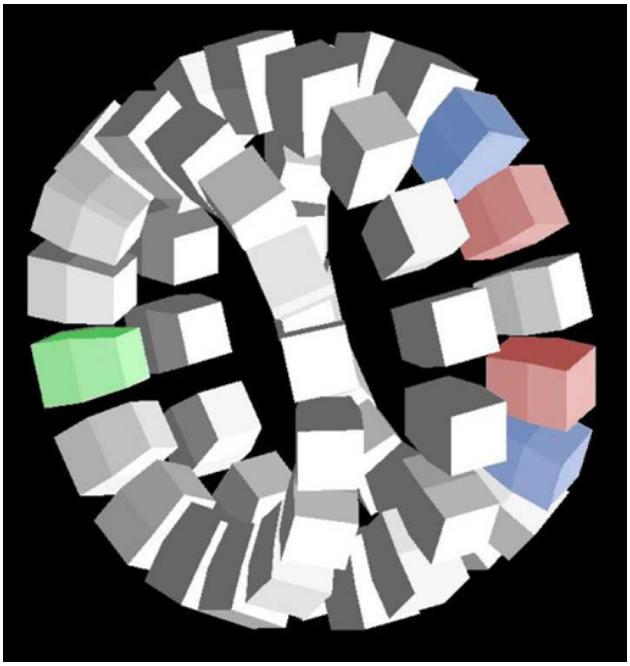

Figure 7.2 Array of detectors with no mounting. Two configurations are highlighted, the Symmetric 157.5° between the green and red detectors, and the Symmetric 135° between the green and blue detectors.

The following configurations have sensitivity for the tensor term $\kappa_{1z}(\hat{\mathbf{k}}_1 \times \hat{\mathbf{k}}_2)_z$,

1. Symmetric

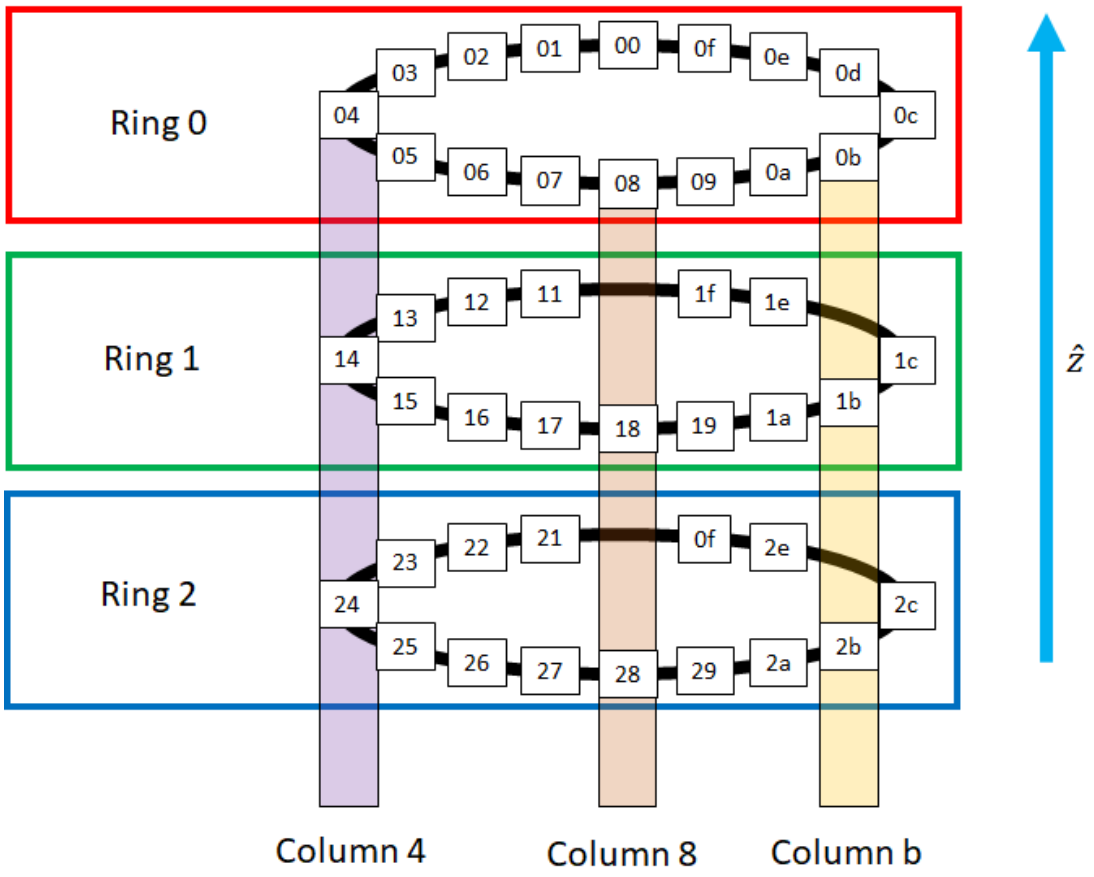

Figure 7.3 Coordinates of the full array. Detector ID is specified by two digits in hexadecimal. The first digit is the ring number, increasing for $-\hat{z}$. The second digit is the ID of the detector within the ring. Detectors in different rings, but with the same index within a ring are referred to as a column, for example column 1 is the set of detectors {0x01,0x11,0x21}.

a) 157.5°

b) 135°

c) 112.5°

2. Asymmetric

a) 157.5°

b) 135°

c) 112.5°

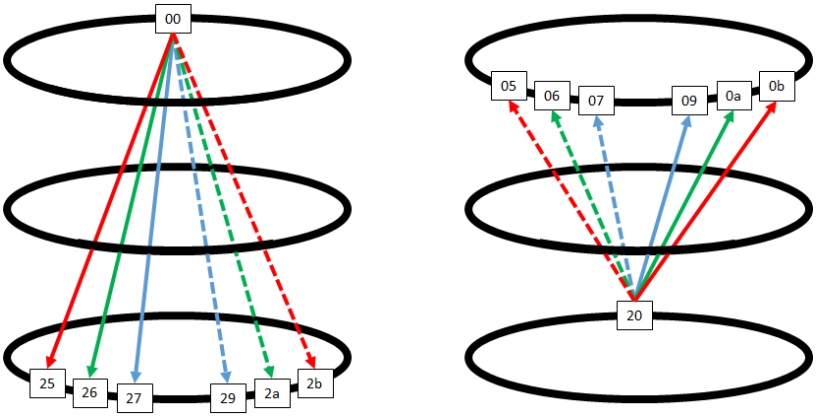

(a) Detectors involved in "Symmetric events"

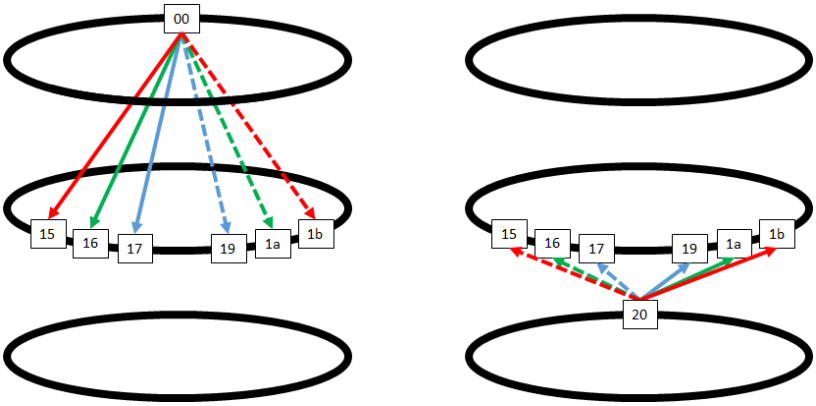

(b) Detectors involved in "Asymmetric events"

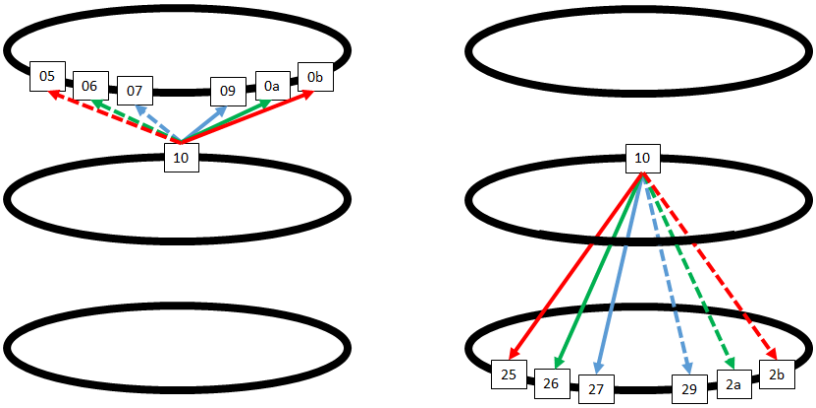

(c) Detectors involved in "Asymmetric with $\hat{\mathbf{k}}_1$ in center ring"

Figure 7.4 The various classes of events. The arrow starts at the detector that $\hat{\mathbf{k}}_1$ hit and points towards the detector that $\hat{\mathbf{k}}_2$ hit. Within a subfigure (Symmetric, Asymmetric, etc.) arrows with the same color have the same analyzing power, dashed (full) line corresponds to negative (positive) value for analyzing power.

where the angle refers to the cylindrical azimuthal angle between detectors, which is not equal to the opening angle between the photons in the decay plane. "Symmetric" refers to both hits in the outer rings, "Asymmetric" refers to events where the highest energy photon is in an outer ring, and the second highest is in the middle ring. Any detector in the outer rings can serve as the "highest energy detector". So there are two sets of independent Symmetric configurations with the highest energy in the upper ring (ring 0), and in the lower ring (ring 2).

The flipped Asymmetric events, where the highest energy photon is in the middle ring, have no sensitivity for the tensor term. This is because these events have $\hat{\mathbf{k}}_1$ is perpendicular to the $\hat{z}$-axis.

7.2.1 Detector numbering

We introduce labels for all 48 detectors by simply numbering them in hexadecimal. The first digit corresponds to ring number, and the second to detector number. This is illustrated in Figure 7.3.

A hit refers to an ordered pair of detectors IDs ($\hat{\mathbf{k}}_1$,$\hat{\mathbf{k}}_2$). Detector 0x00 forms configurations with the following sets of detectors,

1. Symmetric
    a) 157.5° – {(0x00,0x27),(0x00,0x29)}
    b) 135° – {(0x00,0x26),(0x00,0x2a)}
    c) 112.5° – {(0x00,0x25),(0x00,0x2b)}
2. Asymmetric
    a) 157.5° – {(0x00,0x17),(0x00,0x19)}
    b) 135° – {(0x00,0x16),(0x00,0x1a)}
    c) 112.5° – {(0x00,0x15),(0x00,0x1b)}

This is illustrated in Figure 7.4. Due to azimuthal symmetry we only consider events where the highest energy photon was in "column 0", for this chapter we only consider events where one of

the photons hit detector 0x00. All of these events have a pair with the same sensitivity where the highest energy photon hit the lower ring. This is illustrated in Figure 7.4.

7.3 Outline of analysis

A specified detector configuration has a set of coincident hits, with the recorded energy of each hit. An example is shown in Figure 7.5. This shows the energy deposited in detector 0x00 on the y-axis, and energy deposited in detector 0x27 (0x29) on the x-axis for the left (right) plot. An asymmetry is formed between coincidences in detectors (0x00,0x27) versus (0x00,0x29). Some energy cuts are specified on this distribution which correspond to integrating all the counts within the 2-D cuts. For this chapter we merely draw a red triangle for the phase space of the 3-γ event, where $\omega_1 > \omega_2 > \omega_3$.

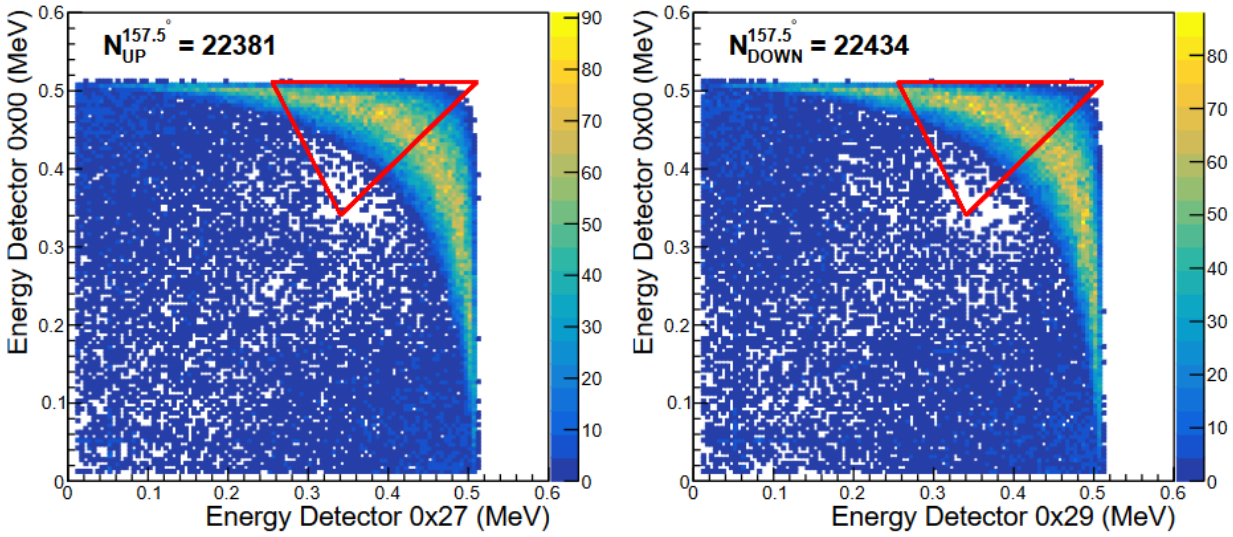

Figure 7.5 2-D energy distribution for coincident hits in the "Symmetric 157.5°" configuration. An count asymmetry is measured between the counts in the red trangle on the left versus the right.

Now following Refs. [38, 39], the analyzing power for the signal is $\kappa_{1z}(\hat{\mathbf{k}}_1 \times \hat{\mathbf{k}}_2)_z$. For the Monte-Carlo simulations this can be directly calculated from the generated kinematic vectors. The averaged geometric analyzing power for the distribution in Figure 7.5 is shown in Figure 7.6, but where each entry is weighted by the geometric analyzing power, then normalized by the number of events in that bin. This illustrates which events have a positive and negative value of $\kappa_{1z}(\hat{\mathbf{k}}_1 \times \hat{\mathbf{k}}_2)_z$.

Directly connecting this to a sensitivity to $\mathcal{CP}$-violation is not straight forward, and is the content of Chapter 9.

A configuration a has three quantities of interest,

1. Counts – N^a
2. Average Geometric Analyzing power – $G^a_{an} = (1/N^a)\sum_i G^a_{an,i}$
3. Figure of Merit – $\sqrt{\sum_i^N (G^a_{an,i})^2}$

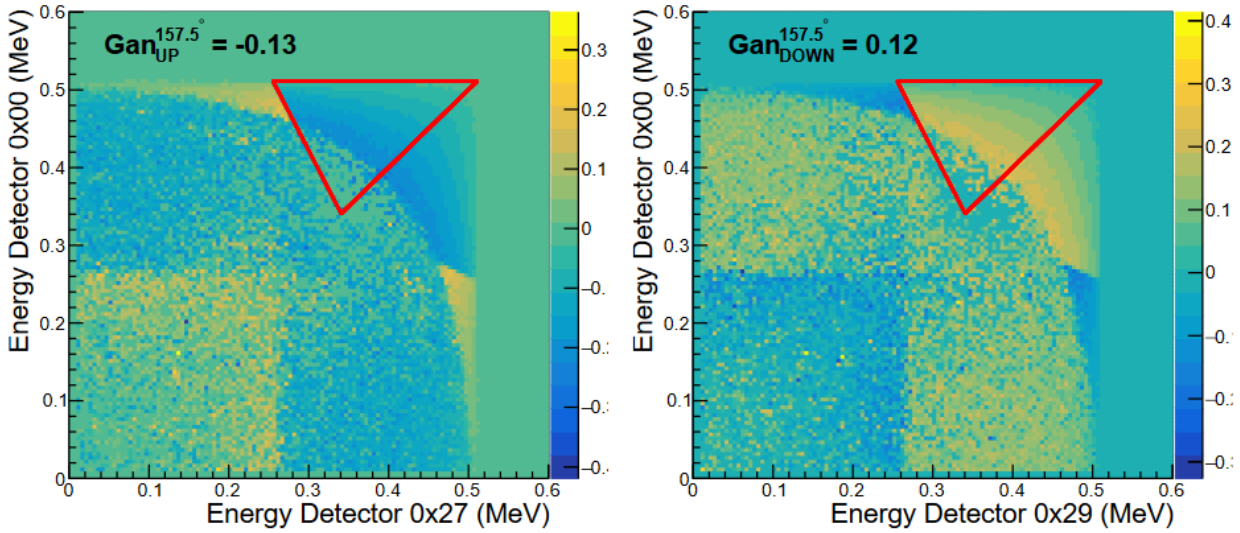

Figure 7.6 The same events as in Figure 7.5, but where each bin has been weighted by the averaged geometric analyzing power. Note many bins outside the main kinematic region are affected by the low number of counts in that region.

The average geometric analyzing power can be discerned from Figure 7.6 by integrating within the energy cuts, then dividing by the counts within those cuts (calculated from integrating Figure 7.5). The Figure of Merit, as described in Chapter 3, corresponds to the statistical sensitivity for those kinematic events. This is shown in Figure 7.7.

7.4 Coincidence cuts

Investigation of the observed distributions shows some oddities. In particular, in Figure 7.8, there appears to be spurious structures in the energy distribution. There is an apparent dip along

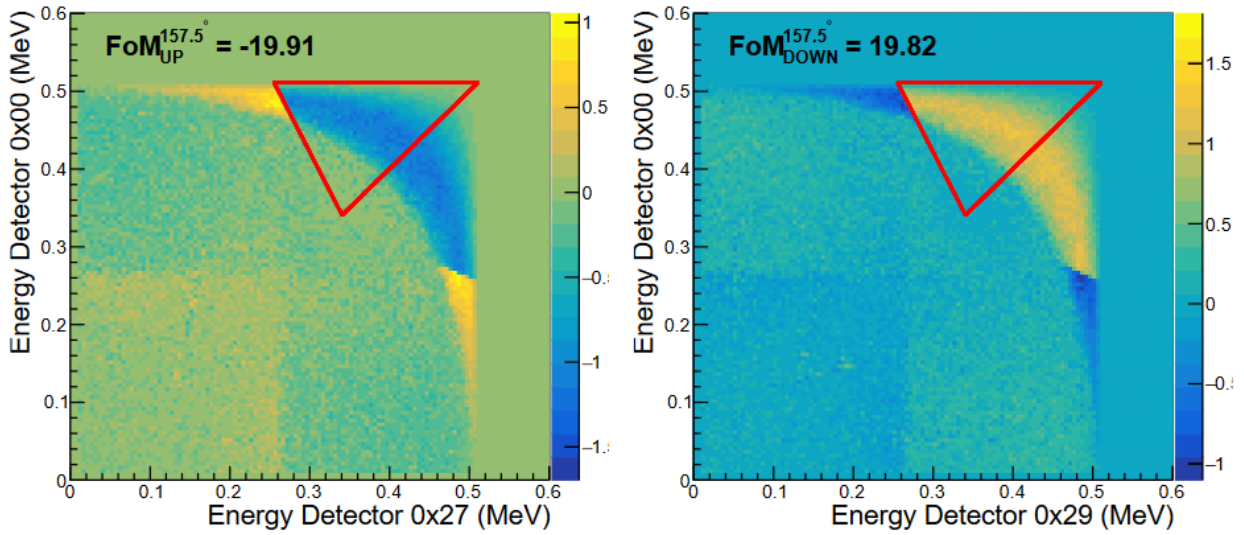

Figure 7.7 "Figure of Merit" for the same data shown in Figure 7.5. This corresponds to the sum of the analyzing power weighted by the square root of the number of events, and is indicative of our statistical sensitivity.

the $E_1 = E_2$ line, but only for some configurations and not others.

Consider the geometry of the event as the energy of the photons changes. The three photons lie in a plane and their momentum sums to zero. Geometrically, $\hat{\mathbf{k}}_3$ is confined to lie between $-\hat{\mathbf{k}}_1$ and $-\hat{\mathbf{k}}_1 - \hat{\mathbf{k}}_2$, as illustrated in Figure 7.9. $\hat{\mathbf{k}}_3 = -\frac{1}{\sqrt{2}}(\hat{\mathbf{k}}_1 + \hat{\mathbf{k}}_2)$ as $\omega_2 \to \omega_1$ (stated otherwise, momentum conservation means $\mathbf{k}_3 = -\mathbf{k}_1 - \mathbf{k}_2$, when $|\mathbf{k}_1| = |\mathbf{k}_2|$ this can be translated to their unit vectors). Reconsider Figure 7.8, the vectors $\hat{\mathbf{k}}_1$ and $\hat{\mathbf{k}}_2$ are fixed to hit the two detectors, as the energies change $\hat{\mathbf{k}}_3$ moves through the plane.

The plane is defined the highest energy detector, second highest energy detector, and the origin (where the decay occured). This is shown graphically for Symmetric 157.5° events and 135° events in Figure 7.10. The lowest energy photon lies in the plane and falls somewhere between the reflection of $\mathbf{k}_1$ and the intersection of the decay plane and the x-y plane (z=0). When $\omega_2 \to \omega_1$, then the lowest energy photon is constrained to the lie in the x-y plane (which coincides with the central ring of detectors). For the 135° events it is aimed directly at detector 0x16 and therefore all 3 photons are detected. For the 157.5° pair it lies between detectors 0x15 and 0x16, but as $\hat{\mathbf{k}}_3$ sweeps out an arc in this plane as $\omega_2 \to \omega_1$ it can cross through detector 0x16 when $\omega_2 \lesssim \omega_1$.

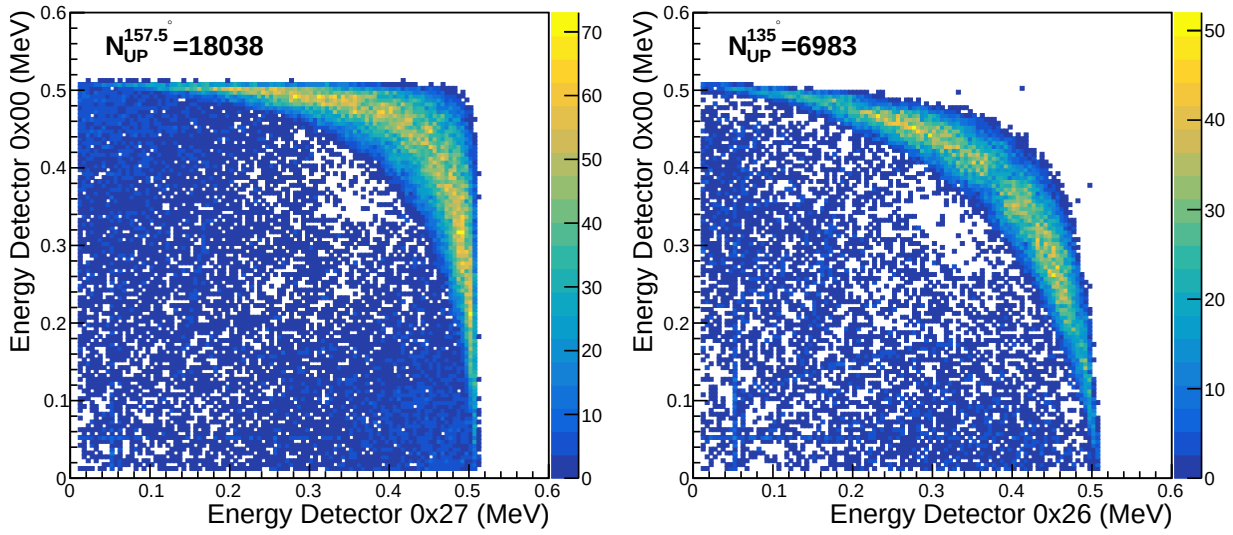

Figure 7.8 Symmetric events at 157.5° (left) and Symmetric events at 135° (right) with an exclusive 2 hit coincidence condition. Note the visible structure within the band, most clearly visible in the 135° pair as a dip on the E1=E2 diagonal. There are possibly six similar dips in the 157° pair. The quoted number of counts corresponds to the number within the phase space triangle, not drawn here so as to not cover any structure.

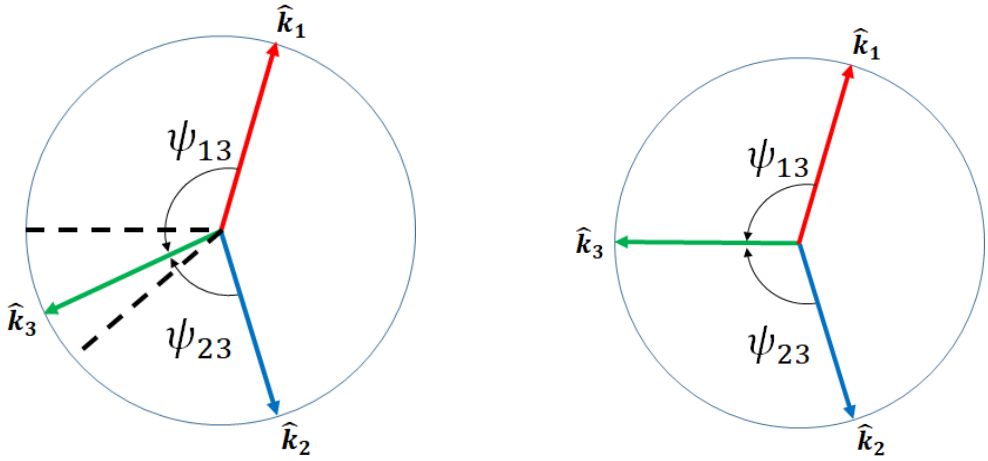

(a) $\omega_1 \neq \omega_2 \neq \omega_3$ (b) $\omega_1 \approx \omega_2$

Figure 7.9 Distribution of photons within the decay plane, with $\hat{\mathbf{k}}_1$ in red, $\hat{\mathbf{k}}_2$ in blue, and $\hat{\mathbf{k}}_3$ in green. (a) The general range that $\hat{\mathbf{k}}_3$ can lie in, constrained between the two dashed lines. (b) When $\omega_2 \rightarrow \omega_1$ then $\psi_{23} \rightarrow \psi_{13}$ by momentum conservation. The bounds of the region for $\hat{\mathbf{k}}_3$ are perpendicular to $\hat{\mathbf{k}}_1 + \hat{\mathbf{k}}_2$ for $\omega_1 = \omega_2$, and the reflection of $\hat{\mathbf{k}}_2$ over $\hat{\mathbf{k}}_1$ for $\omega_2 = (1/2)\omega_1$

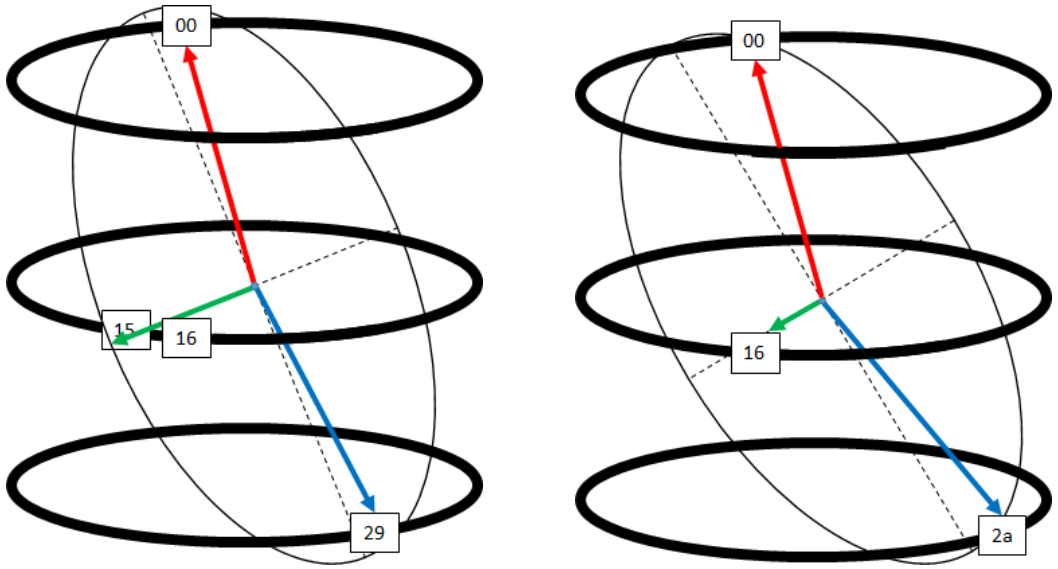

(a) Symmetric 157.5° (b) Symmetric 135°

Figure 7.10 Taking the event in the decay plane from Figure 7.9 and embedding it into the detector array shows how certain configurations restrict $\hat{\mathbf{k}}_3$ to hit specific detectors in an energy dependent way.

The analysis above applies cuts based on the number of hits, specifically a strict two hit coincidence is imposed. This restriction is removing perfectly good events where all 3 photons are detected. This is inherently related to the geometry of the event, and through the argument above, directly related to the 2-D energy distribution of the observed photons. So restricting to strictly 2 hits results in dips in the 2-D energy distribution. Updating the coincidence condition to allow for events with 3-hits (in specific conditions) removed much of this structure. This is shown in Figure 7.11. This is most notable for the 135° pair and increases the counts by 42%, the two dips closest to the diagonal for the 157.5° are also reduced but only result in an 11% increase in counts.

The specific 3-hit coincidence condition is, 3 hits, each in a separate ring, their summed energy is near 1022 keV, and that no back-to-back detectors were hit. Looking at the 157.5° configuration in Figure 7.11, there are still some dips. Reflecting on the geometry, there are still configurations where the third photon crosses through the lower ring. These are rejected by the current coincidence conditions. This coincidence condition is used for the rest of this work.

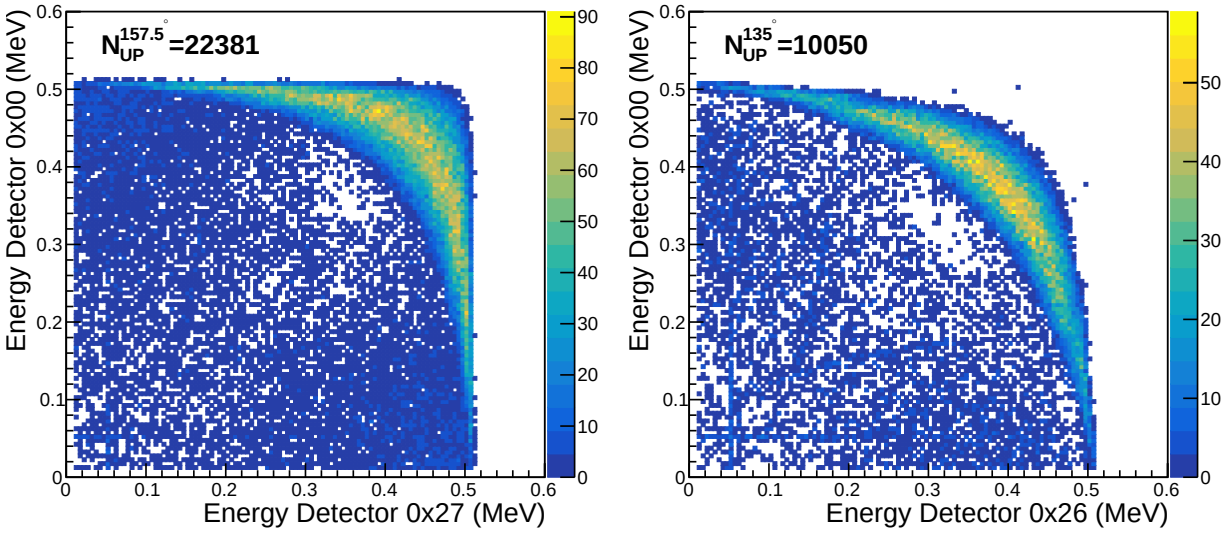

Figure 7.11 Loosening the restriction of only 2-hits by allowing a third hit in the middle ring removes the structures visible in Figure 7.8. The counts increase by about 11% for the 157.5° pair, and 42% for the 135° pair respectively.

7.5 Optimization of geometric sensitivity

At this point the geometry is largely determined based on the discussions in Chapter 3. The main undetermined quantity is the angle of the tilt of the outer ring. Before discussing this it is worth surveying the sensitivities of the various configurations first, and how they can be combined into a net Figure of Merit.

7.5.1 Sensitivity of each configuration

Hold the outer rings tilted at 30°. The counts for all six configurations are shown in Figure 7.12. The geometric analyzing powers are shown in Figure 7.13. Finally the Figures of Merit are shown in Figure 7.14. These are summarized in Table 7.1 where these quantities are integrated over the energy cuts, taken to be the phase space triangle.

Each of these configurations select different parts of the phase space. The Figures of Merit are combined into a aggregate Figure of Merit by the square root of the sum of squares of the individual detector configurations.

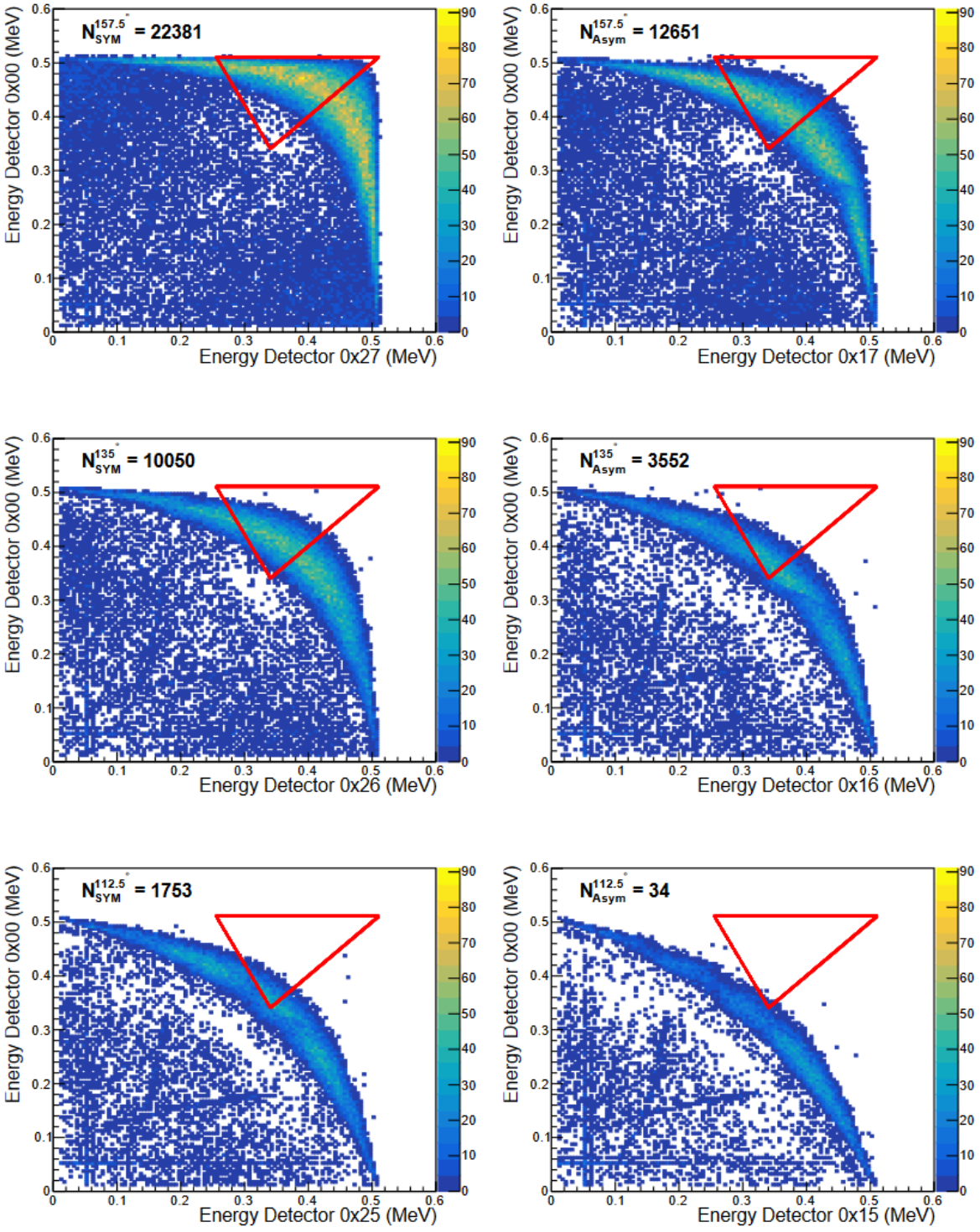

Figure 7.12 Coincidence counts for all 6 configurations considered here, all with $\hat{\mathbf{k}}_1$ hitting detector 0x00. These correspond to the plots shown in Figure 7.5.

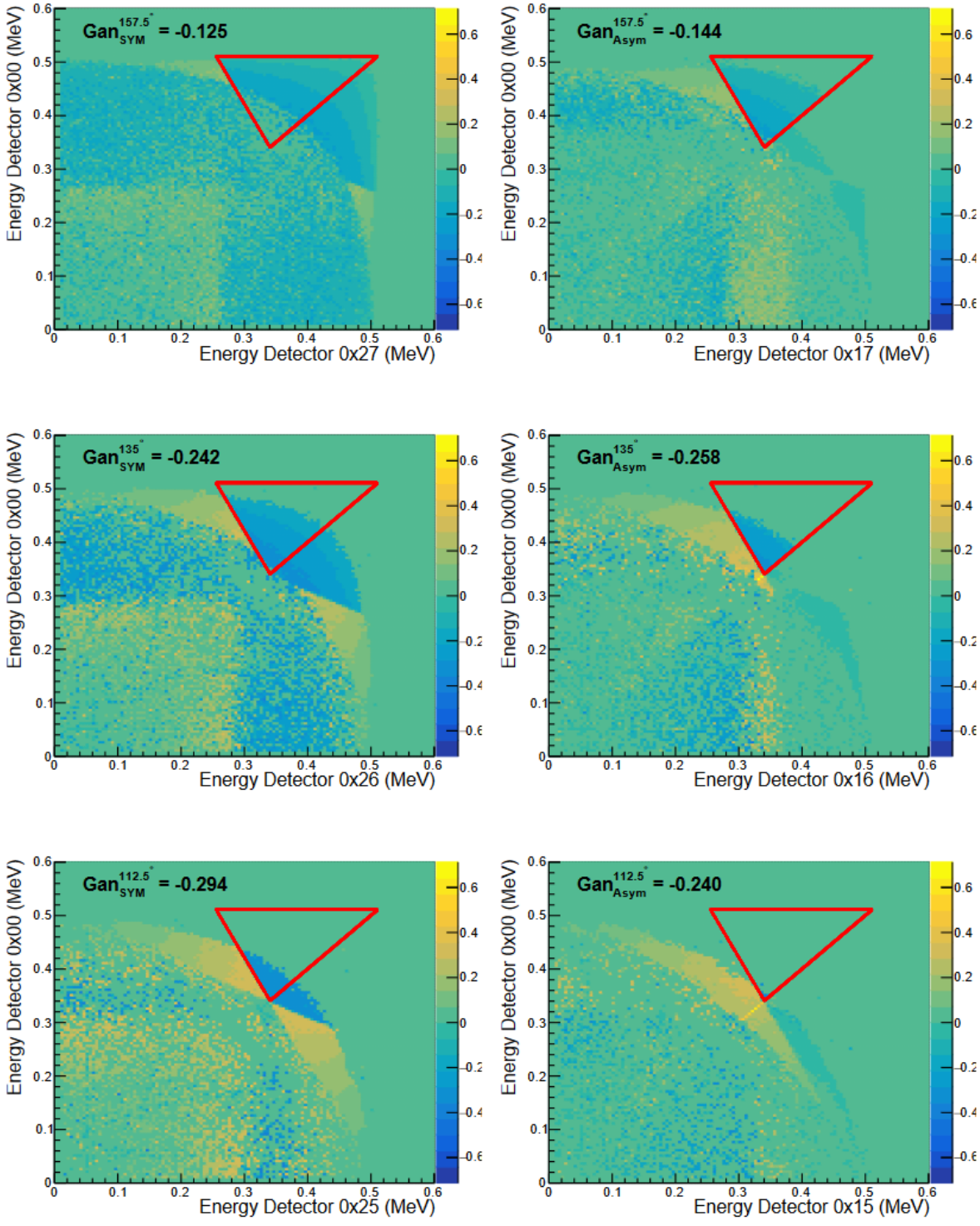

Figure 7.13 Geometric analyzing power for all 6 configurations, corresponding to the information shown in Figure 7.6.

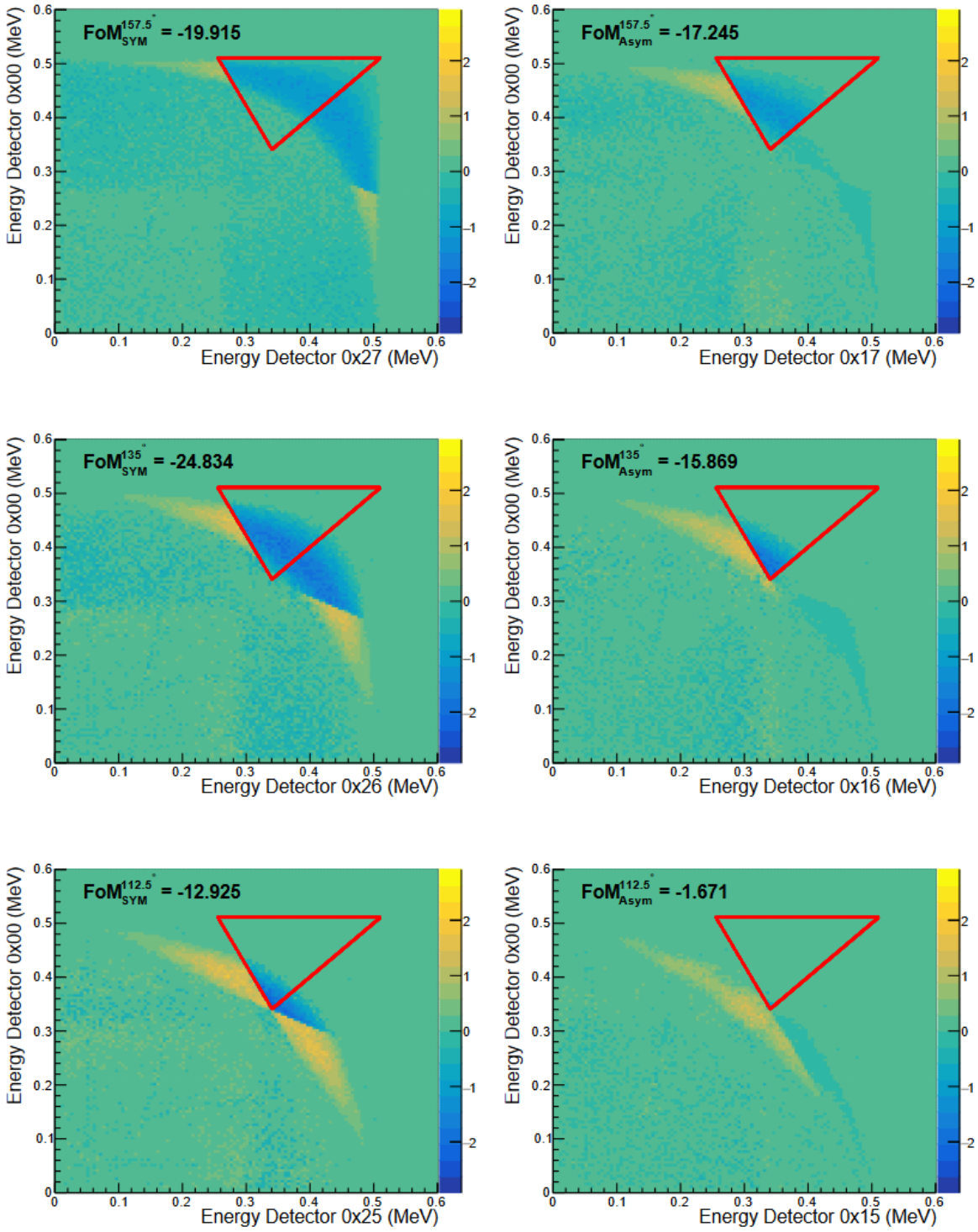

Figure 7.14 Figure of Merit (FoM) for all six configurations, corresponding to the information shown in Figure 7.7.

Configuration	Counts	G_{an}	FoM
S157.5	22381	0.125	19.92
S135	10050	0.242	24.83
S112.5	1753	0.294	12.93
A157.5	12651	0.144	17.25
A135	3552	0.258	15.87
A125.5	34	0.240	1.67

Table 7.1 Relative counts, geometric analyzing powder, and Figure of Merit for each configuration considered in this chapter. This is with the tilt of the rings fixed at 30°.

7.5.2 Outer ring tilt

As defined the geometric analyzing power is largely dependent upon the opening angle between the photons. Increasing the angle of the outer ring up to 45° has 3 features: 1) it increases the opening angle between the photons, 2) it makes κ_{1z} larger, and 3) it makes n_z larger. The results of changing the tilt of the outer ring are given for an angle of tilt between 20° to 32.5° in Table 7.2. The results are presented for the Symmetric configurations and the Asymmetric separately.

Outer ring tilt (°)	N^{SYM}	G_{an}^{SYM}	FoM^{SYM}	N^{ASYM}	G_{an}^{ASYM}	FoM^{ASYM}
20	26338	0.126	22.76	23791	0.127	21.72
22.5	28495	0.139	25.97	21693	0.141	22.72
25	30245	0.150	28.79	20335	0.153	23.72
27.5	32082	0.160	31.62	18290	0.163	23.96
30	34184	0.168	34.36	16238	0.169	23.50
32.5	36336	0.175	36.86	14499	0.176	23.14

Table 7.2 Effect of increasing the outer ring tilt. The summed counts, averaged geometric analyzing powder, and aggregate Figure of Merit are quoted for the Symmetric and Asymmetric events separately.

The Figure of Merit merely increases as the angle increases. Having a larger tilt makes the support structure much more complicated, but it appears vital to reaching the sensitivity needed. We opt for a tilt at 30°.

7.6 Estimation of final statistical sensitivity

Now we can estimate a statistical sensitivity for our planned experiment to compare with the previous searches. For the purposes of this chapter we are considering only using the unperturbed triplet lifetime state reducing the statistics by only considering two of the three states. The statistical

sensitivity from an asymmetry measurement should go as $\Delta C_{CP} = 1/(G_{an}\sqrt{2N}) = 1/(\sqrt{2}FoM)$ using the aggregate Figure of Merit defined above. These simulations correspond to 100 million ortho-positronium decays and have a total $FoM = 41.66$. If we plan to run for 35 continuous days with a 1.85 MBq source with 50% of the positrons surviving the start scintillator, then 50% forming positronium in the powder, 1/2 in $m = \pm 1$ ortho-positronium, then this simulations corresponds to 1/7000 of our full planned statistics. This translates to $\Delta C_{CP} = 2 \times 10^{-4}$ a factor of 10 times higher statistical sensitivity than the previous search. This is if we assume the same tensor polarization as they claim. This level of increased sensitivity will also require a reduction in systematic uncertainties by a factor of 3. The primary systematics for the Tokyo experiment were from the stepper motor that rotated their setup. This is completely removed for our array, and replacing the permanent magnets with an electromagnet will allow careful characterization of many systematic effects.

7.7 Spreading of the source, finite energy resolution, and 2-γ backgrounds

7.7.1 2-γ events

Some portion of the positronium decays through 2-γ annihilation, resulting in two back-to-back 511 keV photons. One photon could Compton scatter off of inactive material and hit a detector in a configuration we record. Currently this simulation has no inactive material, and the final experiment will have all material between the source and the detector made from low Z material, which will minimally scatter the photons.

Including finite spreading of the source makes the detector configurations geometrically sensitive to back-to-back photons. This is illustrated in Figure 7.15 for the central ring detectors, drawn roughly to scale. Spreading of the source means the decay is no longer at the origin, and if it spreads far enough then a straight line can connect two detectors and the positronium decay position. For the 157.5° pairs, highlighted in darker blue, The configuration is sensitive to 2-γ decays once the decay occurs within the region banded by the two red or purple lines. Also drawn are circles of radii 1 cm and 2 cm. Further complicating issues, the combinations shown in this figure do not represent any of the configurations in Figure 7.4. The combinations sensitive to the signal are those

between detector rings, which have an even sharper opening angle than that shown.

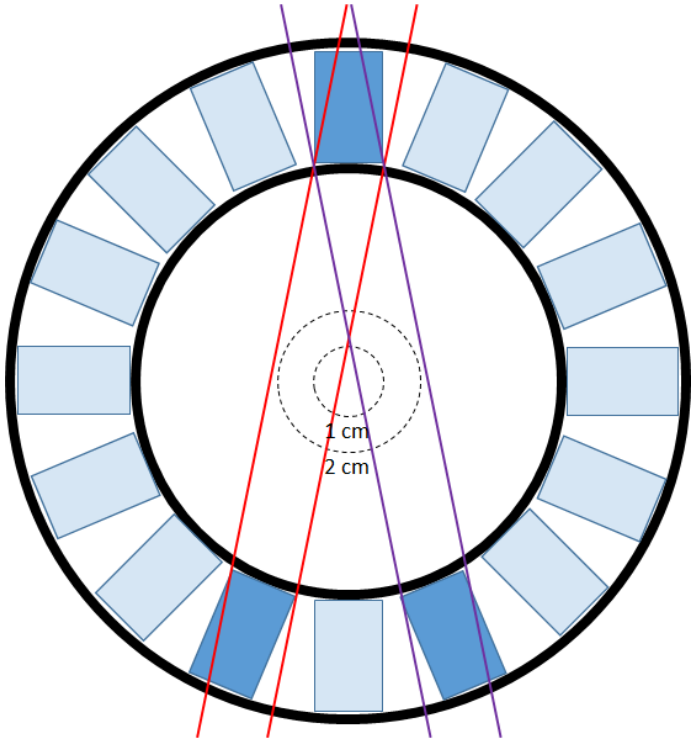

Figure 7.15 Pairs of detectors in the central ring, highlighting the regions where $2-\gamma$ decays are visible (between the red lines or the purple lines). Some scale is given for the central circles, to be compared with the stopping position simulations in Chapter 6. Note this is the geometry for coincidences within the central ring, which we do not consider here. For coincidences between the outer ring the angle between detectors is closer to 180°, and the two bands are even closer.

Even with source spreading, the event leaves a clear energy signature in the detectors. The 3-γ events form a continuous distribution, but the 2-γ events should be a peak at 511-511 keV (and Compton continua parallel to the x- and y-axes at 511 keV). These are strictly speaking the boundaries of the phase space for 3-γ decay. In reality the detectors have something like 12% FWHM resolution at 511 keV. This spreads out the peak and leaks some of these 2-γ events into the energy cuts.

Ultimately all of these effects need to be considered together. Here we present how these effects are implemented in the Monte-Carlo, and the effect of adding one at a time, finally including all at once.

7.7.2 Finite source spread

The positronium source is not point-like. The spreading of the source is dependent on the β source used. The ^{68}Ga source produces substantially broader spreading of the positronium compared to ^{22}Na.

To estimate the effect of spreading we directly take the stopping distributions from Chapter 6. The 2-D histograms of stopping positions is used as an input to be sampled as a cumulative distribution function. One limitation is that the 2-D histogram is taken as a distribution for z and ρ, and a random ϕ is generated, as well as randomly choosing whether $z > 0$ or $z < 0$. All inputs generate an azimuthally symmetric source with mirror symmetry between positive and negative z. The caveat to this exception is that the entire source distribution can be shifted to an arbitrary position, so the origin for the distribution can be shifted away from the origin of the detector array.

The 2-D energy distributions for the 3-γ and 2-γ events for the Symmetric 157.5° configuration for a point source, a ^{22}Na source, and a ^{68}Ga source are shown in Figure 7.16 for Design (B), and in Figure 7.17 for Design (C). The dilution due to 2-γ is substantially worse for the Symmetric 157.5° configuration than for any other configuration (this is the closest to back-to-back). There are far more back to back photons when spreading of the source is included, however these events leave a very distinct energy pattern in the detectors. The spreading of the source increases the amount of phase space selected, but it does not lead to misidentification of events, the energy recorded is still the energy of the photon (up to the effect of Compton scattering and X-ray escapes). It is an interesting coincidence that the corner of phase space where all 3 photons have the same energy ($\omega_1 = \omega_2 = (2/3)m_e$) is exactly equal to the "double Compton shoulder".

The 2-γ distribution is still separable with energy cuts. The coincidence counts for each configuration for both sources in Design (B) and (C) is given in Table 7.3. The spreading generally reduces the number of events in the configurations that select large regions of phase space (157.5°), but increase the number of events for the configurations that are only sensitive to a small corner of phase space (112.5°).

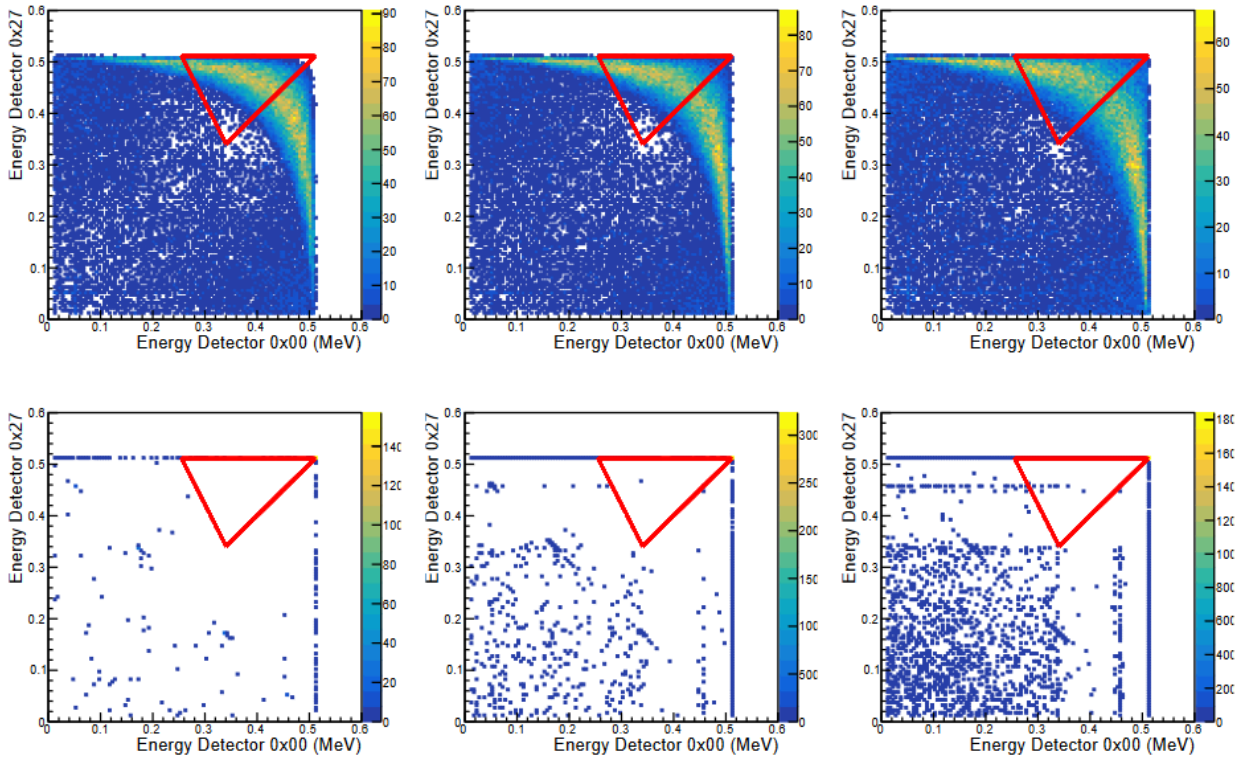

Figure 7.16 Point source (left), ^{22}Na (middle), and ^{68}Ga (right) coincidence events for 3-γ decays (top) and 2-γ decays (bottom) using the Design (B) for the start detector and powder. Note the spreading of the source merely makes more of the phase space visible, but does not map events into or out of the phase space (with the exception of the included effect of Compton scattering).

	$N_{3\gamma}^{ptsrc}$	(B) $N_{3\gamma}^{Na}$	(B) $N_{3\gamma}^{Ga}$	(C) $N_{3\gamma}^{Na}$	(C) $N_{3\gamma}^{Ga}$
S157.5	22412	22056	20252	22526	22274
S135	10122	9254	7989	9982	9327
S112.5	1711	1769	1571	1804	1827
A157.5	12651	13072	1300	12679	13051
A135	3552	3860	4305	3663	3921
A112.5	34	91	346	66	132

Table 7.3 3-γ coincidences for each configuration including the spreading of the source. Design (C) shows the least amount of spreading of the positronium.

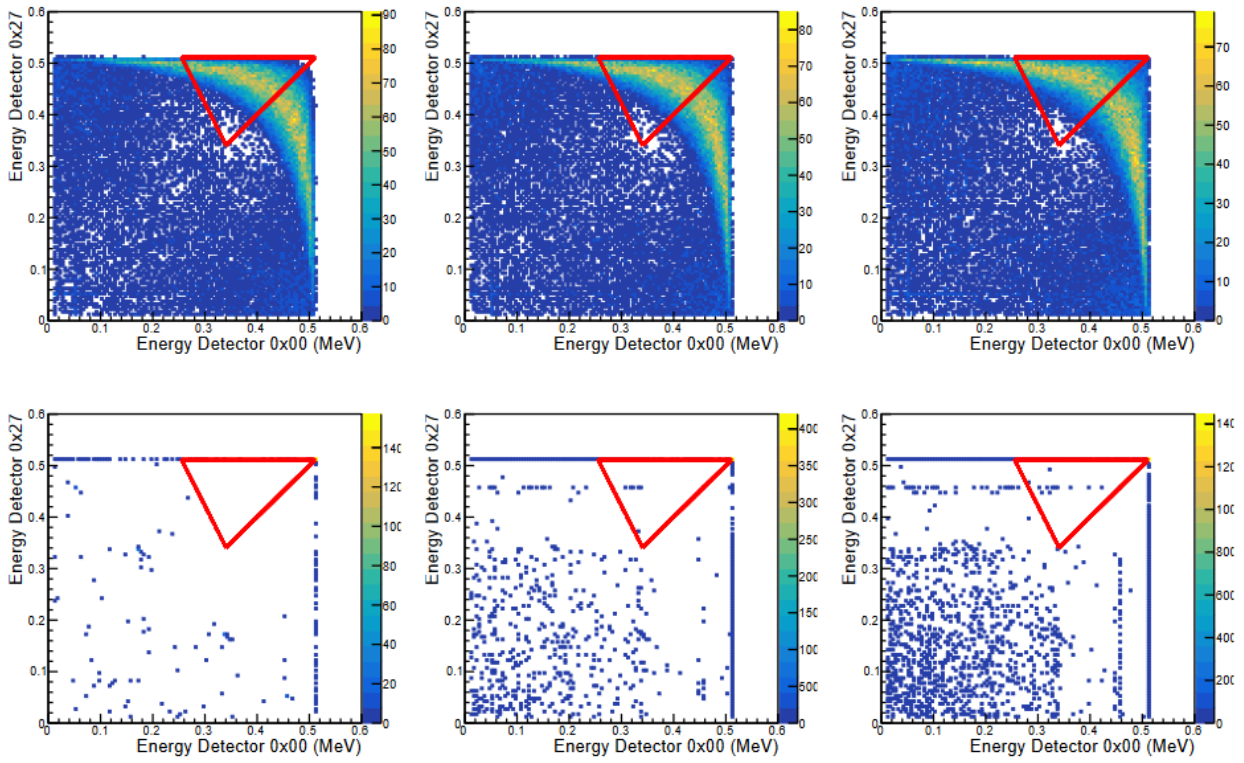

Figure 7.17 Point source (left), ^{22}Na (middle), and ^{68}Ga (right) coincidence events for 3-γ decays (top) and 2-γ decays (bottom) using the Design (C) for the start detector and powder. Note the spreading of the source merely makes more of the phase space visible, but does not map events into or out of the phase space (with the exception of the included effect of Compton scattering).

7.7.3 Finite energy resolution

The detectors will have roughly 12% FWHM resoltuion at 511 keV and a $1/\sqrt{E}$ scaling. More specifically we take the function,

$$\sigma(E)/E = \left(0.0433\right)/\sqrt{E\ (\text{MeV})} \tag{7.1}$$

as extracted from data that will be presented in Chapter 8. For any event with a given deposited energy, a random number gaussian distributed around E with width σ_E is sampled. This is illustrated in Figure 7.18. The Symmetric 157.5° configuration's 3-γ distribution for a point source is shown in Figure 7.19.

Returning to estimating the effect on the measured distributions, for Design (B) in Figure 7.20, and Design (C) in Figure 7.21.

The smearing of the 3-γ events is not particularly nefarious, it simply moves events around

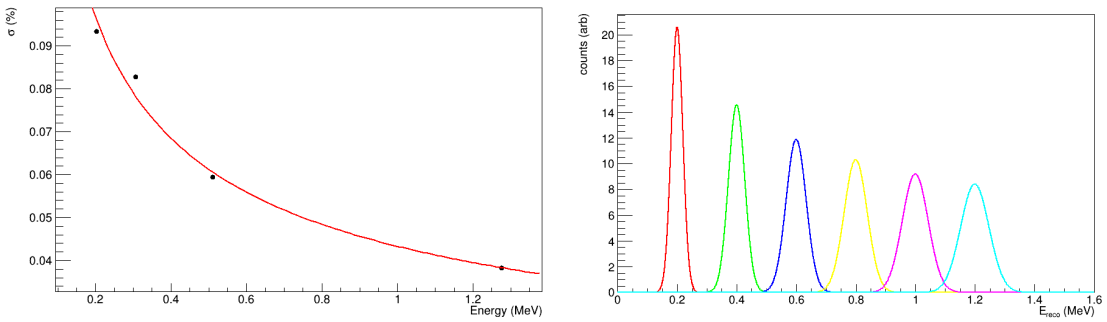

Figure 7.18 Estimation of the response function for our final crystals. These values are taken from data in Chapter 8. The width of the peak is taken for the 202, 307, 511, and 1275 keV peaks and fit with $1/\sqrt{E}$. The right plot demonstrates the Gaussian response with the corresponding width at each energy.

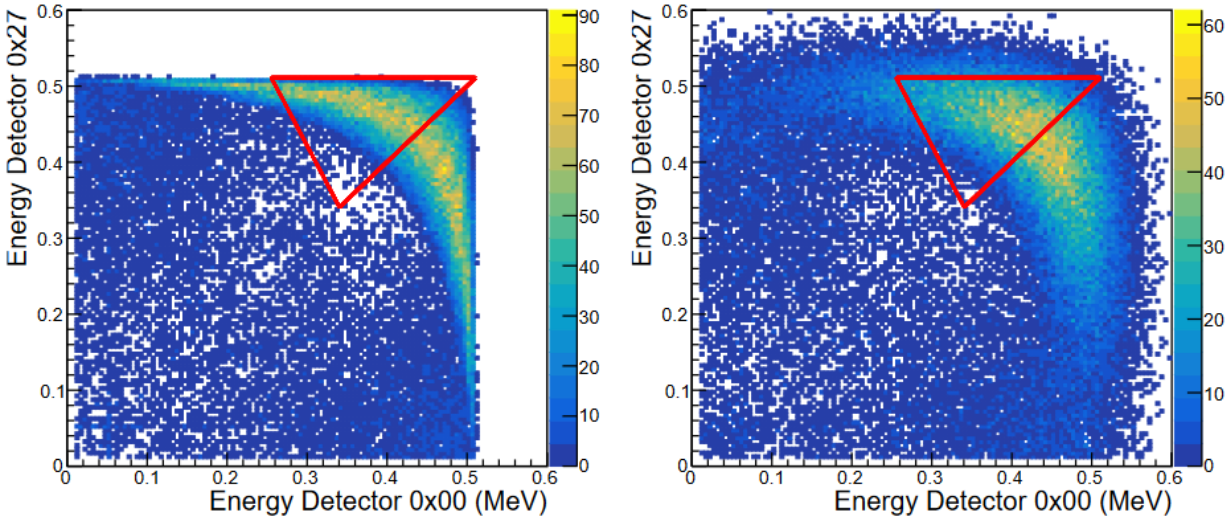

Figure 7.19 Coincidence distribution for Symmetric 157.5° pair of detectors (and a point source). This shows the same event distribution with (right) and without (left) applying the response function from Figure 7.18.

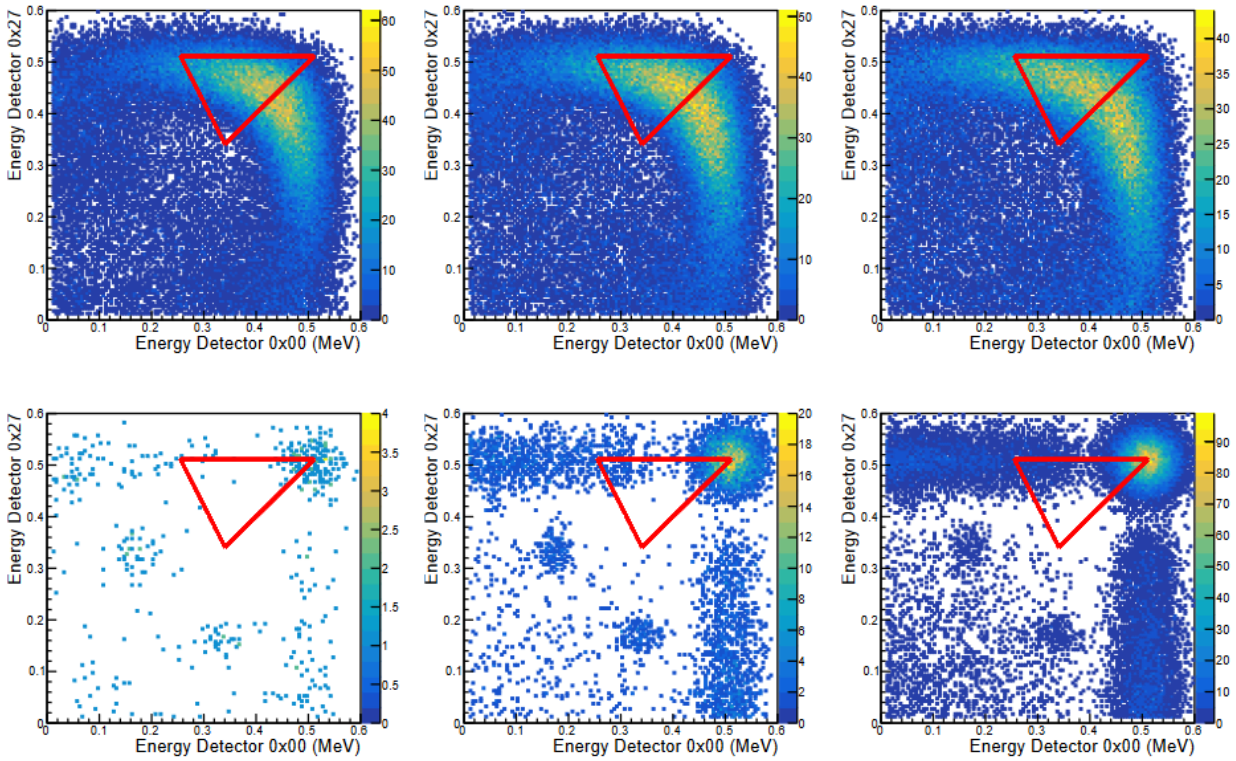

Figure 7.20 Same events as shown in Figure 7.16 for Design (B), now with the response function from Figure 7.18 applied event by event.

inside of the wide energy cuts. The primary concern is when it leads to a misidentification of which photon had highest energy and which had second highest. By intuition this might seem like a disastrous thing to happen, however inspection of the tensor term shows that flipping $\hat{\mathbf{k}}_1 \leftrightarrow \hat{\mathbf{k}}_2$ does not change the sign of the signal for Symmetric events. This is because flipping the two photon labels flips the normal of the decay plane, but it also flips κ_{1z}. It is clear that there is no energy cut that removes all 2-γ events without also removing good 3-γ events.

7.7.4 Dilution for various start detector designs

Now the effects of the combined radioactive source, start detector geometry, powder density, and energy resolution can be combined. The reduction in counts for all configurations for these combinations is given in Table 7.4. There is a reduction in overall counts on the scale of 10-20%. This reduces the statistical sensitivity of the experiment and will require slightly longer runtime. For the Symmetric 157.5° configuration the 3-γ and 2-γ counts are given in Table 7.5. These are

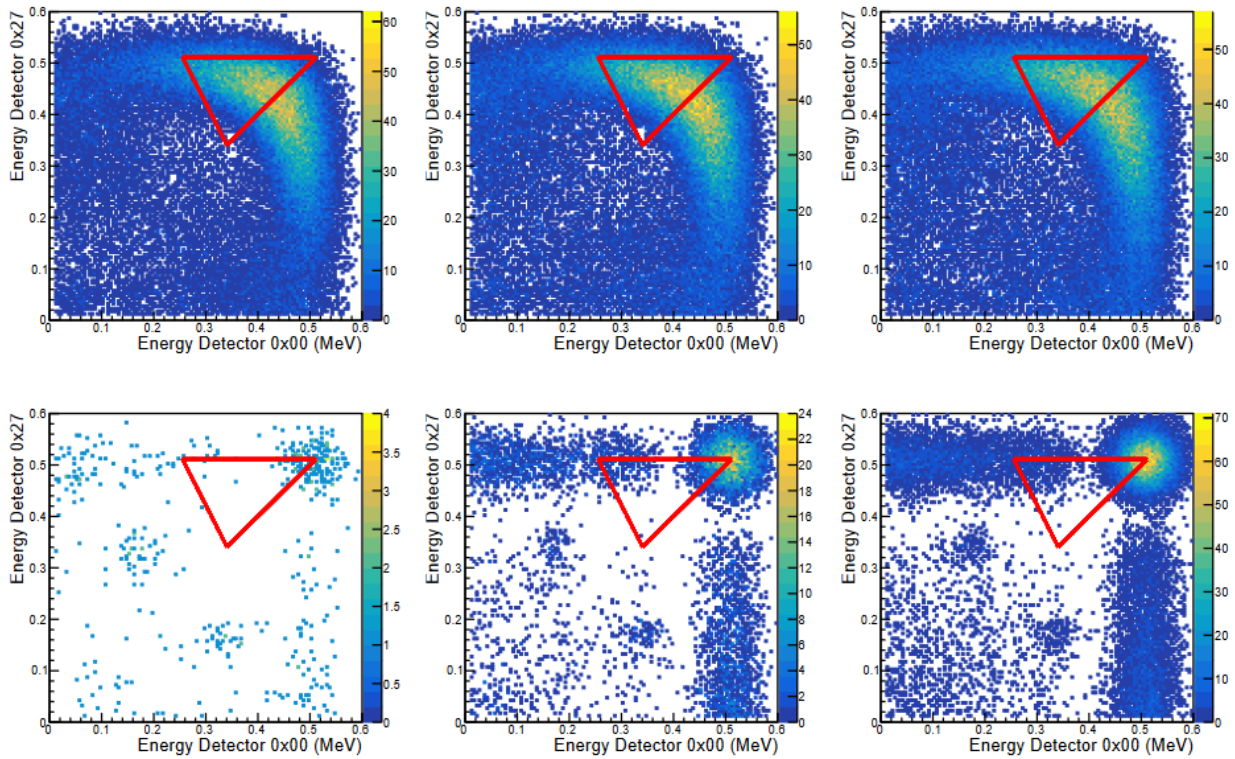

Figure 7.21 Same events as shown in Figure 7.17 for Design (C), now with the response function from Figure 7.18 applied event by event.

the number of coincidences in the energy cuts of the "phase space triangle", for 100 million 3-γ decays and 100 million 2-γ decays.

	$N_{3\gamma}^{ptsrc,\sigma_\infty}$	$N_{3\gamma}^{ptsrc}$	(B) $N_{3\gamma}^{Na}$	(B) $N_{3\gamma}^{Ga}$	(C) $N_{3\gamma}^{Na}$	(C) $N_{3\gamma}^{Ga}$
S157.5	22412	18549	17923	16821	18531	18223
S135	10122	9239	8386	7292	9123	8512
S112.5	1711	1948	1965	1849	2000	2027
A157.5	12651	11783	12035	11937	11724	12046
A135	3552	3368	3742	4205	3437	3724
A112.5	34	224	342	608	285	348

Table 7.4 Combined effect of source spreading and finite resolution on the number of 3-γ coincidences observed for each coincidence configuration. This is presented for both radioactive sources and both inner module designs.

7.8 Inter-ring Shielding

The array will feature a lot of detectors, and each detector sees a lot of detectors. Nearly 90% of the pseudo-triplet decays to two photons, and a large fraction of those Compton scatter and only

Design	source	$N_{3\gamma}$	$N_{2\gamma}$
point source, infinite resolution	ptsrc	22412	–
point source, finite resolution	ptsrc	18549	26
Design (B) finite resolution	^{22}Na	17923	485
Design (B) finite resolution	^{68}Ga	16821	2733
Design (C) finite resolution	^{22}Na	18531	641
Design (C) finite resolution	^{68}Ga	18223	2031

Table 7.5 Detection efficiency for 2-γ and 3-γ events for the 157.5 ° pair of detectors in all three configurations.

deposit part of their energy. This leads to lots of events where a photon scatters to its neighbor and yields hits with lower energy. There is no room to add shields between detectors in a ring, however it might be feasible to add shielding between the rings, and this could substantially reduce the amount of Compton coincidences. Consider a "wedge" shield specified as in Figure 7.22. This forms a circular wedge between the rings.

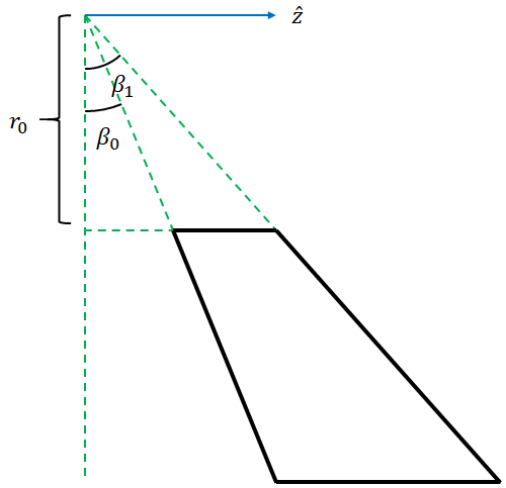

Figure 7.22 Geometry of the shield, showing a radial slide through the shield. (currently a placeholder).

Two shields are shown in Figure 7.23, with $\beta_0 = 9°$, $\beta_1 = 23°$, and two different inner radii (r_0). These shields need to extend inwards beyond the detector face to truly block the detectors from each other, the inner 3 cm radially are budjected to the inner module for positronium formation. This does not leave much room for shields to block detectors on opposite sides of the rings.

Firstly, consider the dependence on the material for the shielding. The shielding should block photons scattered off the detectors. At the same time adding shielding adds events that scatter off

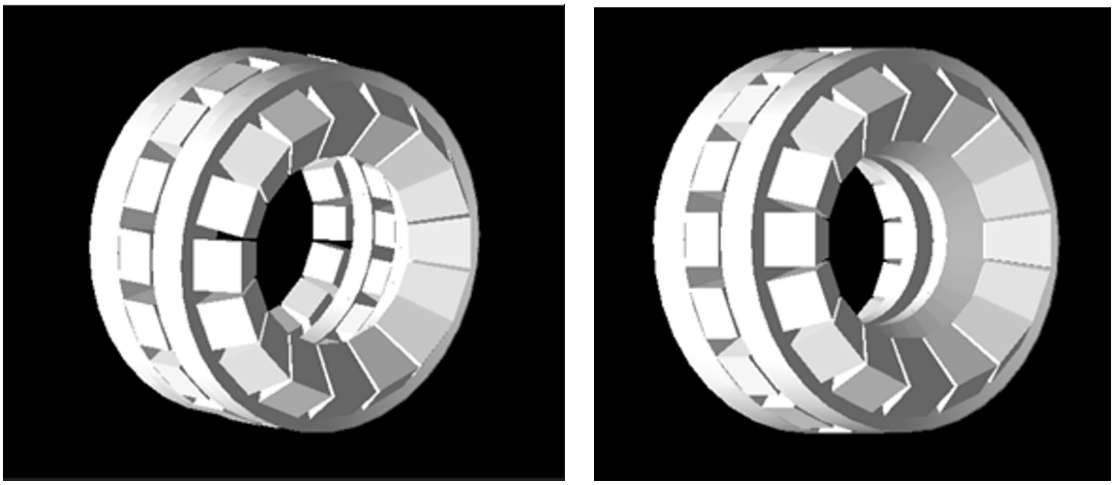

(a) (b)

Figure 7.23 Array with shielding between the rings. The left shows shielding with an inner radius of 4 cm, and the right shows inner radius of 6 cm.

the shield and hit the detectors. Shown in Figure 7.24 is the energy deposited in the shield for 511 keV photons fired isotropically in the array. This features the two likely shielding options, lead and brass, and also includes silver simply because it lies between the two options in terms of atomic number and density. The amount of Compton scatter versus photopeak events is highly dependent on the material, quickly reducing as the atomic number is decreased.

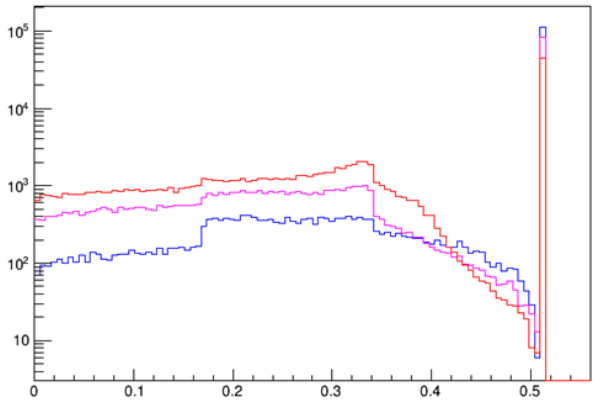

Figure 7.24 Energy deposited in the shield by isotropic 511 keV photons. Brass is shown in red, Silver in pink, and lead in blue. Note the relative heights of the Compton continuum versus the photopeak. Lead will provide the best shielding as it is produces almost an order of magnitude less scattering.

There are a few ways to slice up the data to glean insights into this design. Record events with 2 hits, and create a matrix where the x-index corresponds to the first object hit, and the y-index to the

second object hit. All hits within a ring are summed, and the two shields are treated as one object. This is shown for the detector array with no shielding in Figure 7.25. The diagonal elements mean a photon scattered from one detector to another within the same ring. An off-diagonal means it scattered from one ring to another.

	Ring 0	Ring 1	Ring 2	Shield
Ring 0	4274	1769	552	0
Ring 1	1721	3004	1677	0
Ring 2	543	1754	4294	0
Shield	0	0	0	0

Figure 7.25 Quantifying the scattering between detector rings for isotropic 511 keV photons. The x-axis is the first object hit and the y-axis is the second object hit.

Figure 7.26 corresponds to the array with shielding. This shows a decrease to events scattering between rings. For a shield of inner radius 6 cm (in line with the front face of the detectors) scattering from outer rings to inner rings is reduced from 1700 events to 300 events with a shield. Extending the shield inwards to 4 cm radial distance this number dramatically drops again down to about 45 events.

The amount of photons that scatter off the shielding and hit a detector far outweigh any reduction of scatters between crystals. For the inner ring has an additional 8700 events where the photon scattered off the shield, and for the smaller radius shield this number goes up to 10200. In effect this adds a huge amount of background, but only minimally reduces the coincidence hits between detectors. This is worse than it seems, for two neighboring crystals in the real experiment both hits are recorded and this does not look like a signal. The shielding is not an active detector element, so for hits scattering off the shielding the events cannot be simply vetoed. This amounts to a large distortion to the spectrum to fix a problem that could largely be removed by coincidence logic.

Now consider some more finely grained information. Take a slice in ϕ centered on three detectors, column 0 (0x00, 0x10, and 0x20). The observed spectra for these detectors and the neighboring crystals in column 1 and 2, with and without the shielding is shown for a lead shield

	Ring 0	Ring 1	Ring 2	Shield
Ring 0	4241	353	377	4967
Ring 1	387	2994	391	8717
Ring 2	339	353	4294	4970
Shield	1824	2709	1797	468

(a) 6 cm inner radius

	Ring 0	Ring 1	Ring 2	Shield
Ring 0	4187	45	72	5852
Ring 1	54	2916	43	10229
Ring 2	94	35	4221	5812
Shield	1642	2035	1579	2814

(b) 4 cm inner radius

Figure 7.26 Scattering between detector rings and shielding for lead shielding.

matching the design described above in Figure 7.27, extending to 6 cm inner radius. The spectra in blue are with no shielding, and in red is with shielding. This has no trigger on number of hits so it includes multiple scatterings.

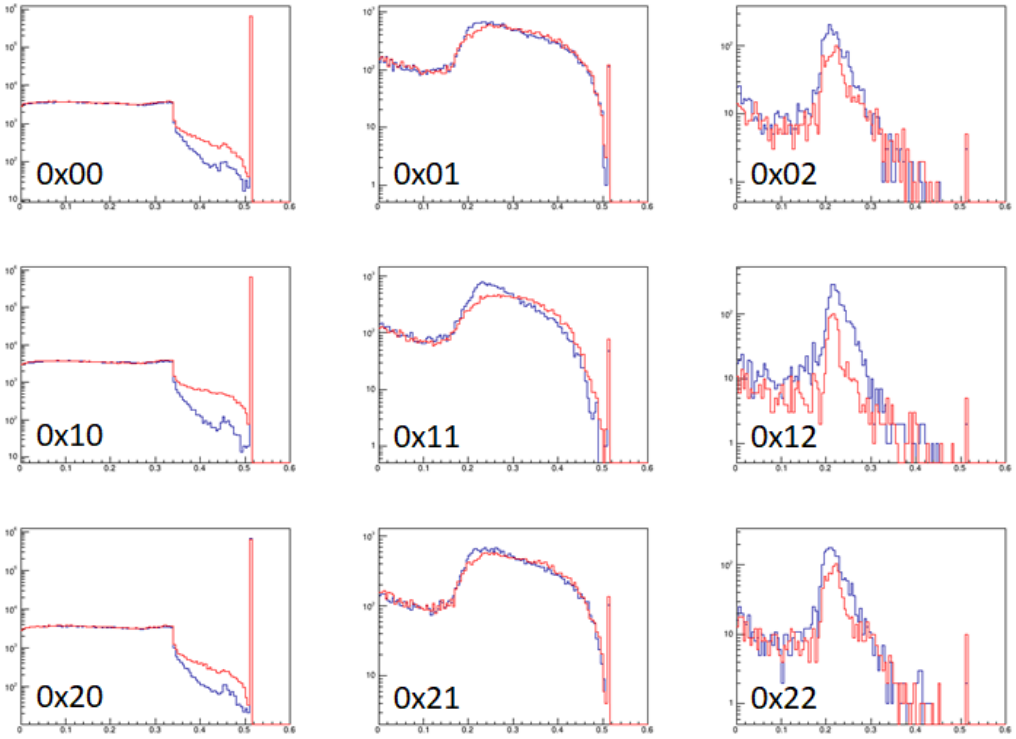

Figure 7.27 Energy spectra of column 0, 1, and 2 detectors for 511 keV singles when aimed at column 0. Shown for no shielding (blue) and Pb shielding extending to 4 cm radius (red). There is in general a large increase in events due to photons scattering off the shield and hitting the detectors.

There is little to no benefit looking at the nearest neighbor, it seems to reduce the low energy hits, but increase the high energy. There is a clear reduction in hits to the crystals two away.

However, compare the y-axis scales shows that any effects on neighboring crystals is very small compared to the increase in counts in the central crystals.

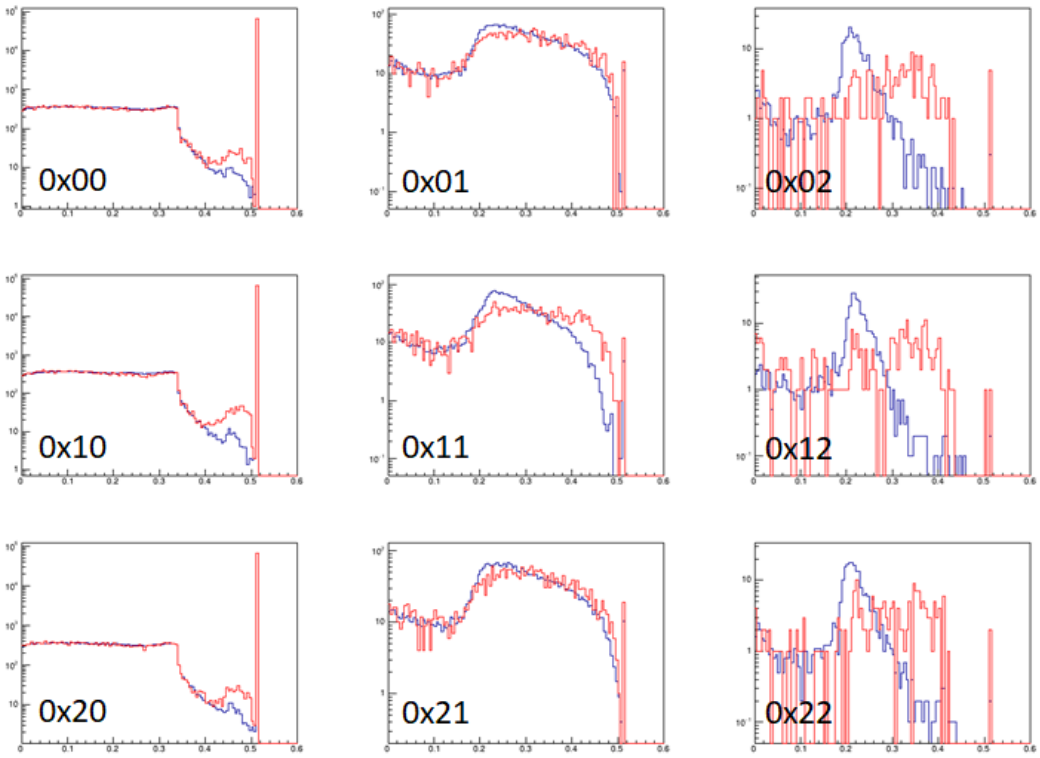

Figure 7.28 Energy spectra of column 0, 1, and 2 detectors for 511 keV singles when aimed at column 0. The best results found for shielding between detectors. A very thin Pb shield extending down to 1.5 cm from the origin. Still the spectra with shielding (red) does not appear to have a net improvement to the spectra with no shielding (blue).

This was the pattern throughout the full parameter space. In general, making the shield thinner and going to a smaller radius reduces the spurious scatterings. The closest design to something that would be considered beneficial (reduction in scattering events relative to no shielding) was when the shielding was made of lead, angled at $\beta_0 = 15°$ and $\beta_1 = 17°$, and extended all the way to 1.5 cm radius. The results are shown in Figure 7.28. This unrealistic design has a front edge that is less than a mm wide.

Brass shielding, which is far easier to produce, was purely detrimental in all configurations tested. We chose to not pursue shielding between rings. It seems to almost exclusively be detrimental, adding spurious counts while reducing very little of the backgrounds that matter.

CHAPTER 8

FIRST PROTOTYPE TESTING

8.1 Overview

Now we have a satisfactory design for the array of γ-detectors, and have tested individual detector prototypes. In this chapter we present the design of the support structure that will hold the array of detectors in the magnet. This is followed by the design and printing of a support for the start detector and powder that will hold the prototype inner module in the center of the detector array.

This is followed by tests with three finalized crystals mounted on the central support ring and read out with the start detector in the center of the ring. We studied the timing properties of the system, the various coincidences observed, and the positronium physics observed.

8.2 Gamma array support structure

The γ-detectors will all be placed in custom designed frames that both mount the crystal onto the frame, and hold the SiPM on the back of the crystal. This piece must handle the tilt of the outer rings, as such there are two designs of frames. The frames with an angle of 60° are labeled the "outer frames", and those with a 90° angle are the "central frames". An outer frame is shown in Figure 8.1 The frame features a base that directly attaches to the support structure, and a "clamp"

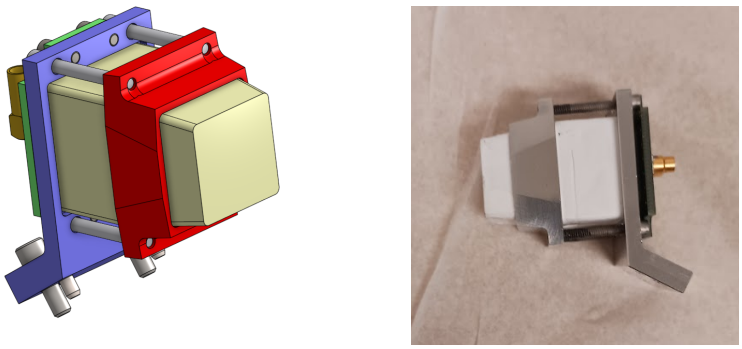

(a) (b)

Figure 8.1 Frame for mounting the detector onto the support structure. It features a "clamp" that screws onto a back frame that holds the crystal onto the frame. (a) The combined frame and crystal in the CAD file. (b) A finalized crystal in the constructed frame.

that screws onto the base. The clamp holds the crystal onto the base from about halfway along the length of the crystal. This ensures that there will be little material between the front face of the detector and the central source. The back of the frame has a set of holes for the SiPM to screw directly into.

The frames attach onto an aluminum ring, with sixteen detectors attached on one side. Figure 8.2 shows two outer ring crystals attached onto the support. The tilted outer ring crystals sit very close to each other.

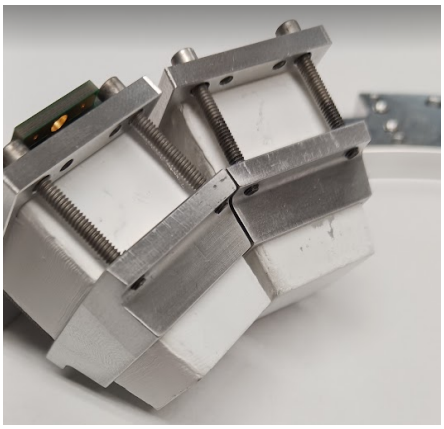

Figure 8.2 Two final LYSO crystals in the tilted frames attached to the support ring. The inner clamp of the frames are nearly touching. The final LYSO crystals will be covered by a Tyvek foil over the TiO_2 paint not included in this image.

The main support structure consists of two aluminum rings, each with 16 tilted detectors attached on the outer edges. The central detectors can be attached to the inner side of either ring. This design is shown in Figure 8.3.

Finally, this three ring structure is connected by four support legs onto outer rings that attach to the outer sides of the magnet. The full model for the support structure with all crystals is shown in Figure 8.4. The manufactured structure without crystals (or crystal frames) is shown installed in the warm bore of one of the FRIB Positron Polarimeter magnets in Figure 8.5.

The diameter of the warm bore of the magnet is about 22 cm, accounting for the mounting and the crystals that are 3 mm in length leaves about a 12 cm cylinder for the entire inner detector support structure.

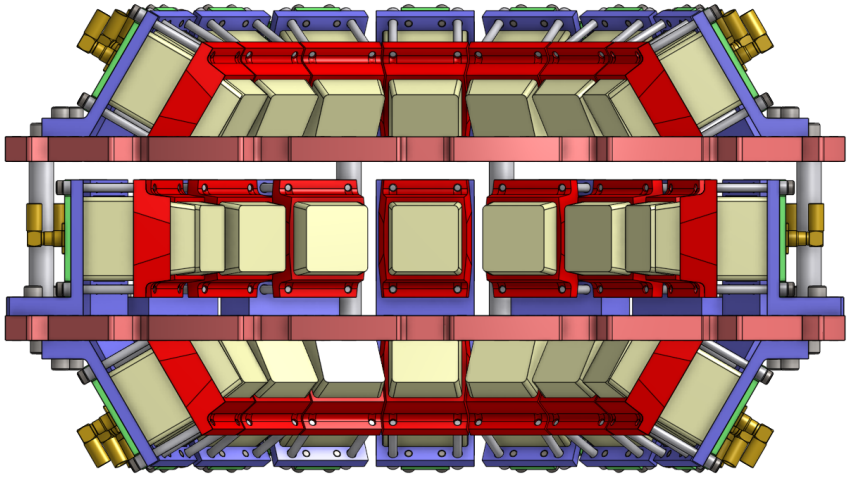

Figure 8.3 Cross section of detector array, showing all three rings of detectors mounted on the central aluminum support. Each central detector can attach to either the upper or lower ring, but here are attached to the lower ring.

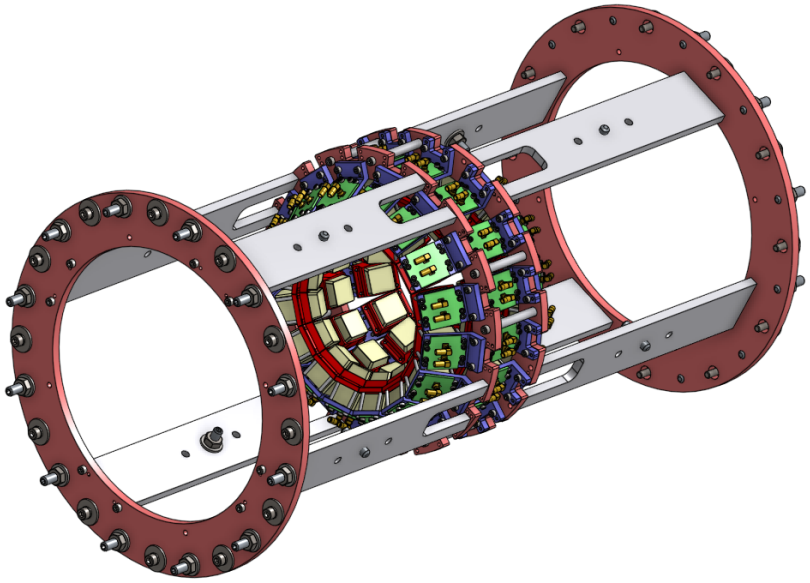

Figure 8.4 Full array support structure. The central aluminum frame is attached to two large rings that will attach to the outer frame of the magnet. This is shown in Figure 8.5.

8.3 Start detector support structure

The start detector and the powder need to be held in the center of the array. The position the inner module should be adjustable to moderately high precision to avoid any offsets of the source. The powder and start detector are on the scale of 2-3 cm radially, with 6 cm radius to the crystals.

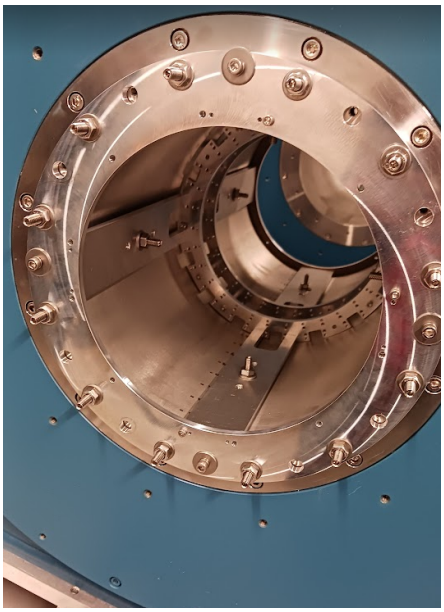

Figure 8.5 Aluminum support structure installed in one of the Positron Polarimeter magnets.

There is still the possibility of manufacturing a smaller start detector and powder container (at the cost of losing some β's that could have formed positronium), but for now we proceed with the current prototypes that we have on hand.

Two students, Vimbainashe Chado (MSU) and David-Michael Peterson (MSU), worked on designing a support structure to hold the inner module. This be non-magnetic, and induce as little scattering as possible. The natural solution is to 3D print a support structure that can attach to the main support frame. 3D printers mainly print in polylactide (PLA) plastic which is low Z and will induce minimal scattering in the final experiment.

The support accommodates the current start detector read out with SiPMs. This breaks the azimuthal symmetry of the structure and will not be the design for the final experiment. The structure is shown in Figure 8.6, and in the full array support in Figure 8.7. The piece highlighted in dark blue holds the start detector, and places enough pressure onto the SiPMs to couple them to the sides of the start detector. This piece will be used for future tests to be performed in the magnet.

8.4 Demonstrator

We constructed a demonstrator using the 3 finalized γ-detectors and the start detector and powder specified in Design (A). In principle this is all that is needed for the experiment, as the

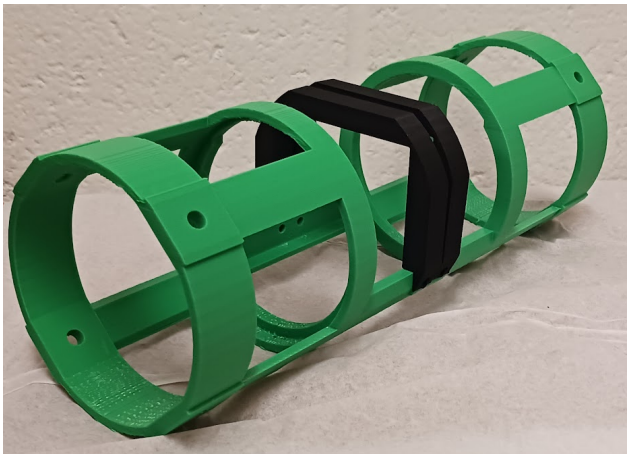

Figure 8.6 Prototype design for the inner module support structure for initial tests in the magnet.

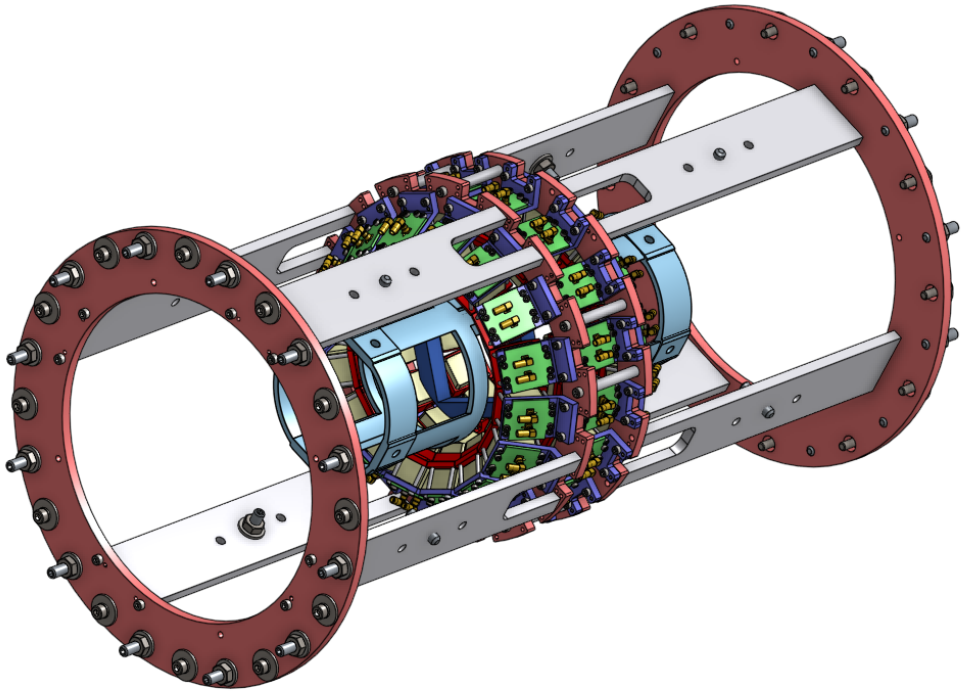

Figure 8.7 Model of the inner module support placed in the full detector array. Not featured are the screws that will attach the outer ring of the inner support structure to the legs of the γ-detector support structure.

count asymmetries will always use independent sets of 3 detectors.

The prototype is shown in Figure 8.8. The three crystals correspond to a configuration with 157.5° opening angle. This is not a final configuration that will be included in the asymmetry, as all the detectors were in the middle ring. Following Figure 7.3 the detectors are labeled starting at

the top of the ring and proceeding counterclockwise as 0x10, 0x17, and 0x19. The start detector and powder were placed in the center of the ring. There was no mechanism to carefully fine tune the position of the source and powder. This is visibly evident in Figure 8.8. The entire setup was raised 18 inches off the table by foam supports which dramatically reduced backscatter of photons from the wooden table.

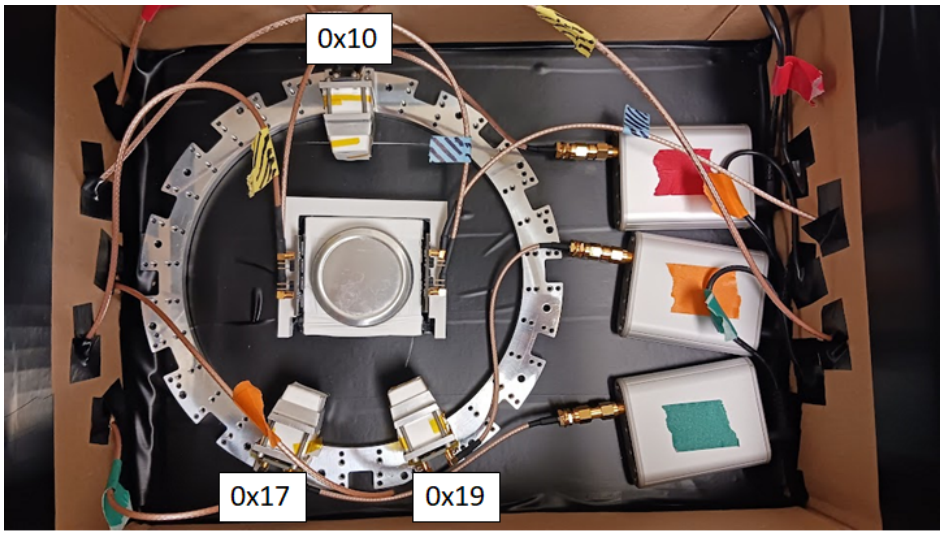

Figure 8.8 Demonstrator with three finalized crystals and a start detector read out by SiPMs. The detectors are ordered following Chapter 7, starting with 0x10 at the top, 0x17, and 0x19 in counterclockwise order. Note the asymmetric placement of the start detector and powder. Similarly the source itself was not perfectly centered beneath the start detector.

The two sides of the start detector were summed and amplified before going to the DAQ. This amplified the range of the ADC bits used and gave increased timing resolution [73]. No preamplification was used on the LYSO crystals, which were digitized directly.

The signals were digitized using 250 MHz PIXIE-16 modules with NSCLDAQ [72, 73]. The digitization used CFD timing on the signals to get improved timing from just recording timestamps. The timing parameters for the fast filter and the CFD were tuned for the plastic and the LYSO individually.

Most of the results in this chapter used a ^{22}Na source beneath the start detector. At the very end of the chapter we will present the results for a ^{68}Ga source. As such, almost all plots have coincidences between the β^+ annihilation and the 1275 keV photon. This added structure helped to

characterize the system, but is inherent to the sodium source and should be absent when we using a gallium source.

8.5 Timing properties

The system has two timing properties that are important. These are the time resolution between a hit in the start detector and a hit in a LYSO crystal, and also the timing between the LYSO's. Compare with the work done in Chapter 5, with two $LaBr_3$ detectors. The timing between these two detectors in that setup is analogous to the timing between the plastic and LYSO in this setup. The start signal is in the plastic and the stop in a LYSO. The timing between the two LYSO crystals is useful for rejection of backgrounds. The final experiment will record triple coincidences between two LYSO crystals and the start detector. Sharper timing resolution between LYSO crystals will give a stronger ability to separate true coincidences from accidentals.

All timing properties presented in this section were built with an exclusive 2 hit coincidence condition. When using a ^{22}Na source there were 3 classes of coincidences between the γ-detectors, 1) 1275 keV de-excitation photon with an annihilation photon, 2) two of the annihilation photons, 3) inherent radioactivity coincidence.

All 6 coincidence time spectra are shown in Figures 8.9 and 8.10. The timing between two LYSO crystals was more or less straightforward. The timing between the plastic and the LYSO was more difficult. The plastic signals were very noisy, and because the SiPM was slow the start detector experience pileup. This ultimately required a moderately high energy cut to remove improperly digitized events. Some structure persisted in the time spectrum shown in Figure 8.10. The combined results for the time resolution are quoted in Table 8.1. We achieved a timing resolution of roughly 3.2 ns FWHM between the plastic and LYSO, and 4.3 ns between two LYSO crystals. There is much room for optimization when comparing these with the previous experiment [39] which achieved near 1 ns FWHM resolution between LYSO crystals. This data was taken with the 0.1 g/cm^3 SiO_2 powder, and a long lifetime component was visible.

A more thorough analysis must be performed that more carefully studies the timing properties versus the reconstructed energies. Ultimately the final experiment will use a much faster start

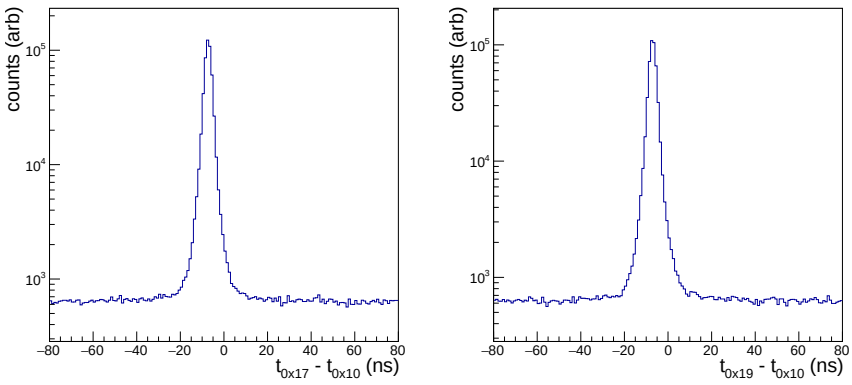

(a)

(b)

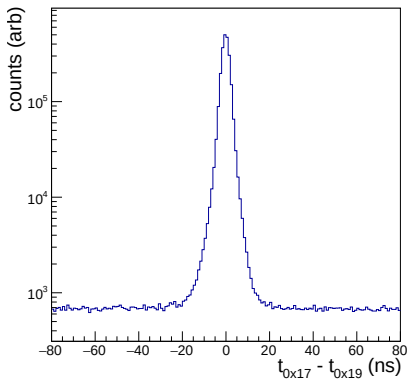

(c)

Figure 8.9 Timing between each pair of LYSO detectors giving between 4.1 and 4.5 ns FWHM for each pair. These events had an exclusive 2 hit coincidence condition, and the y-axis is log-scale

	start	0x10	0x17	0x19
start	–	3.13	3.20	3.39
0x10		–	4.14	4.47
0x17			–	4.38
0x19				–

Table 8.1 FWHM time resolution between each pair of detectors in ns. Further optimization is needed to balance faster timing versus proper digitization of energy.

detector by replacing the SiPMs by PMTs, so a careful optimization of the timing was not pursued at this time.

8.6 Crystal coincidences

The studied of single LYSO detectors in Chapter 4 required a "background subtraction", that is running without a source to remove the counts from internal radioactivity of the ^{176}Lu (Figure 4.2).

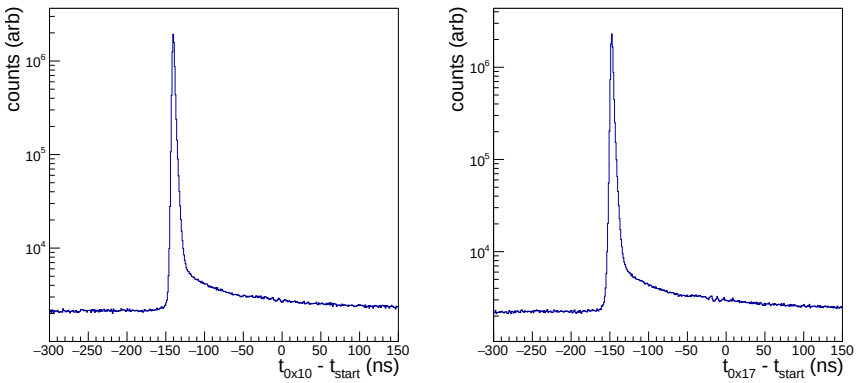

(a)

(b)

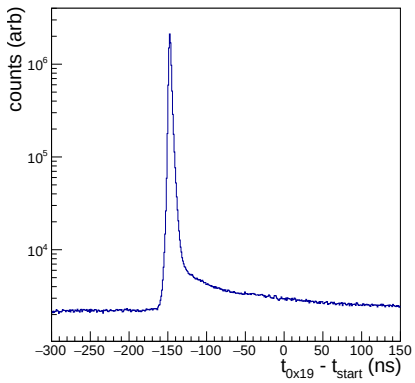

(c)

Figure 8.10 Time spectrum when an event had only two hits, one in the start detector, and one in a LYSO crystal. The y-axis is log-scale. There was some structure before the peak and some structure around 130 ns after the peak.

These counts are expected to be removed in the online experiment by a coincidence condition with the start detector.

The 2-D energy distributions for coincidences between LYSO crystals is shown in Figure 8.11. All these were coincidences between the LYSO crystals that were not in time with the plastic start detector. Some of these were from the ^{22}Na source which emits a 1275 keV photon. However the structure was dominated by the 3 peaks of ^{176}Lu below 511 keV, at 307, 202, and 88 keV γ-rays. This structure in the coincidence spectrum occurs when one or more of the γ's from the ^{176}Lu decay escape the crystal and hit another LYSO crystal. For this reason we saw substantially more of these events for the two crystals that were closer to each other (0x17 and 0x19).

Looking at the 1-D spectra for these detectors (by projecting the plots above down onto the

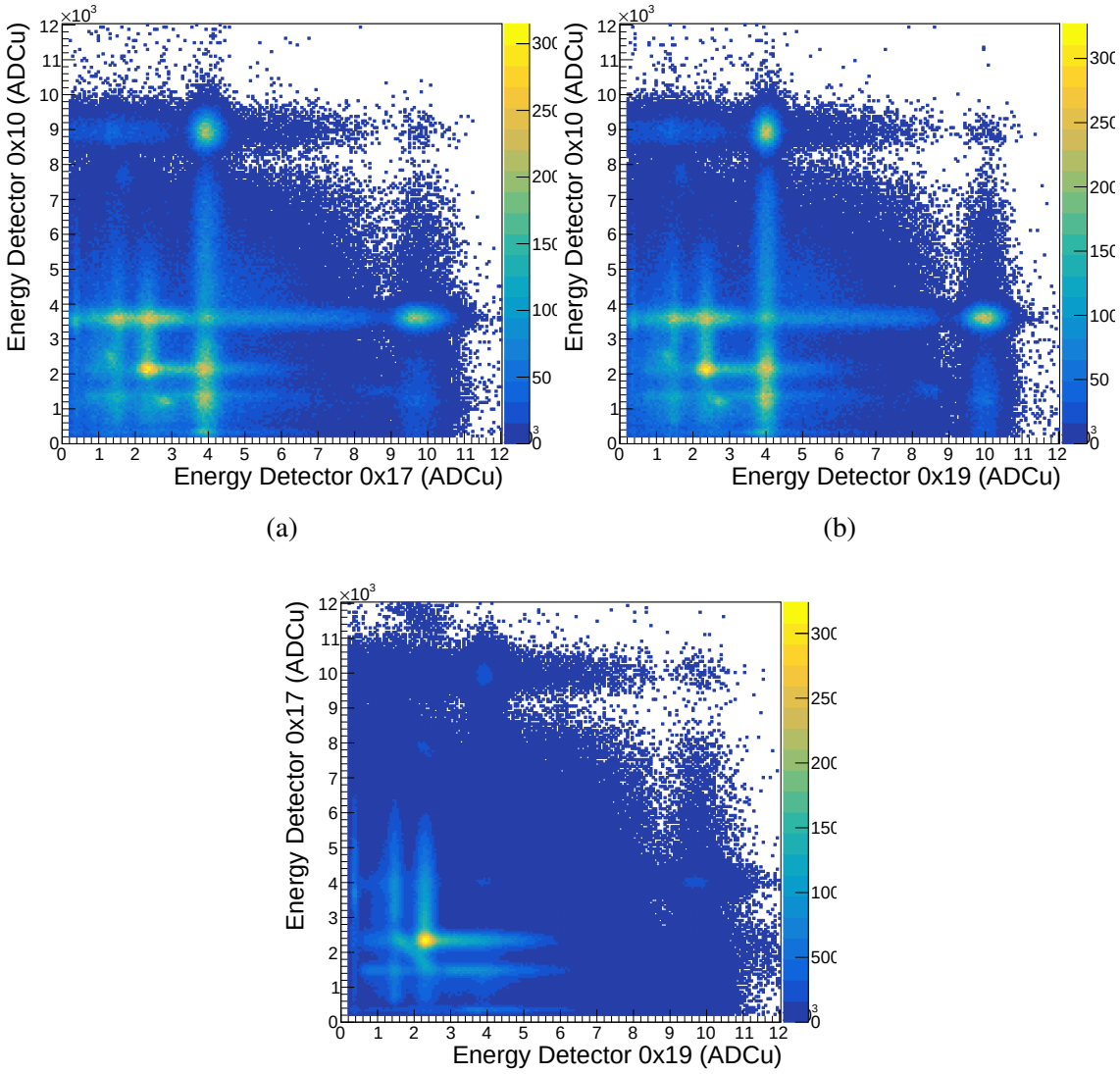

(a) (b)

(c)

Figure 8.11 2-D energy distribution from LYSO coincidences with an exclusive 2-hit coincidence trigger. (a) and (b) correspond to crystals on opposite sides of the ring and show clear ^{22}Na coincidence spectra, and three γ lines below 511 keV, along with continuous spectra from the internal radioactivity. (c) The two crystals were much closer, and the three γ lines are more pronounced than the 511 keV and 1275 keV from the ^{22}Na source.

x-axis or y-axis) would show the structure dominated by the continuous β distribution. However, this projection throws away a lot of info. We can make better informed cuts on the 2-D distributions. The maximum γ is at 307 keV, there was a hit with energy above that in one crystal means the β from the intrinsic radioactivity had to be in that crystal, and the γ in the other. Some flaws in this argument are that both the 202 and 307 keV could be in the same crystal, but this would require

both to escape the original crystal and then hit the same crystal. This occurs, but is not as likely as the high energy signal being from the β. We divide into 3 regions illustrated in Figure 8.12. These separate the structure from the 511-1275 keV coincidences from the sodium source.

Plotting the distribution in each of these regions we gave spectra shown in Figure 8.13. These cuts on the coincidence 2-D energy distribution demonstrated an immensely cleaner internal radioactivity spectra. This set of cuts almost entirely removed the continuous β distribution above 307 keV. The 202 and 307 keV peaks from this data were two of the peaks used to extract the resolution used in Figure 7.18.

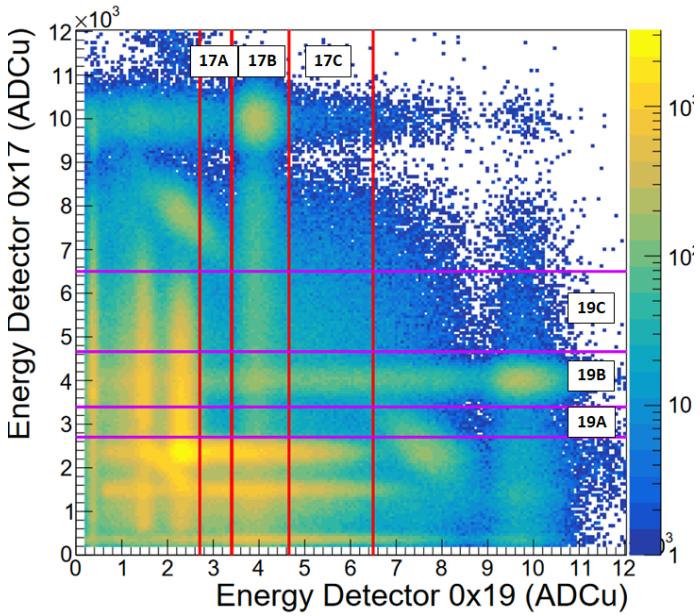

Figure 8.12 Same data shown in Figure 8.11c, now plotted log scale clearly showing more structures. Three energy windows are displayed on the x-axis and y-axis corresponding to cutting between the 307 keV peak and the 511 keV peak, isolating the 511 keV peak, and cutting above the 511 keV peak.

Imposing a timing coincidence with the start detector should remove the internal radioactivity events. The measured spectra in each LYSO crystal in coincidence with the start detector is shown in Figure 8.14. This recovered a clean ^{22}Na spectrum from the crystals without performing a background subtraction. These two peaks served as the other two data points used in Figure 7.18 for the energy resolution. These are also the "final γ-detector spectra" shown at the end of Chapter

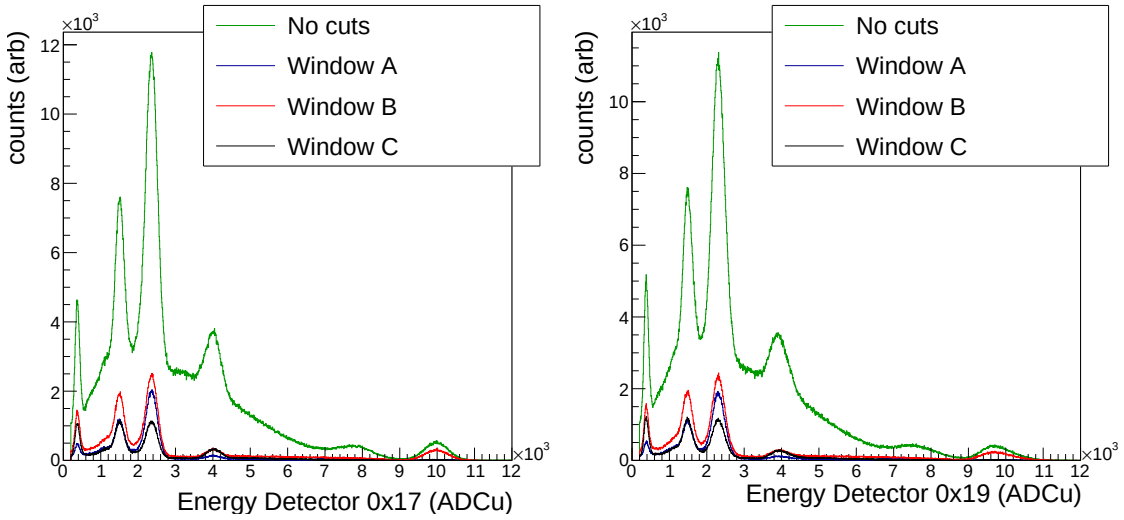

(a) (b)

Figure 8.13 The measured spectra for the internal radioactivity coincidences. Including no cuts on the 2-D distribution, and each of the three windows shown in Figure 8.12.

4. The two coincidence spectra for detectors 0x17 and 0x19 are shown in Figure 8.15. This shows the internal radioactivity events summed from windows A and C in black, and the coincidence spectra with the start detector (scaled down by a factor of 16) in blue. This data was from the same run, simply using different coincidence conditions. Note the unfortunate overlap between the Compton shoulder for the 511 keV peak (340 keV) and the backscatter peak (170 keV) with two of the γ peaks from ^{176}Lu at 307 keV and 202 keV.

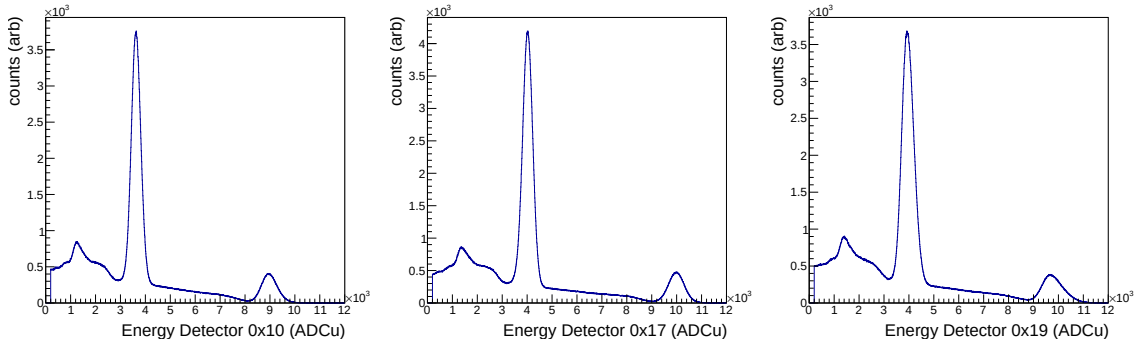

(a) (b) (c)

Figure 8.14 The observed ^{22}Na spectrum in each individual LYSO crystal when a coincidence condition was applied with the plastic detector.

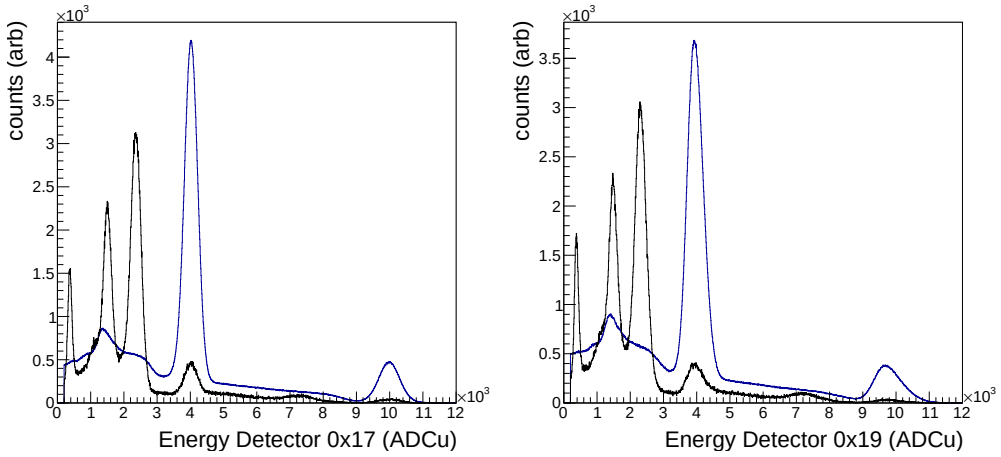

(a) (b)

Figure 8.15 Two spectra from the same run, blue is the LYSO crystal in coincidence with the start detector (scaled down by a factor of 16), black is the sum of the first and third window cuts from Figure 8.13. These are shown for detector 0x17 and 0x19 but not 0x10 as that detector was much farther away and did not get much statistics for the internal coincidences.

8.7 Triple coincidences

Next we studied the timing properties with a triple coincidence. We required one hit in the plastic, and two LYSO hits. The time spectra for the (0x10,0x17) and (0x10,0x19) pairs in Figure 8.16. In comparison with the exclusive 2 hit data shown in Figure 8.10 the triple coincidence data had a lower level of accidentals, a more prominent long lifetime component, and clear structure before the peak. The detector placement was positioned to favor seeing 3-γ decay and therefore made the long lifetime component look more prominent than the simple double coincidence condition.

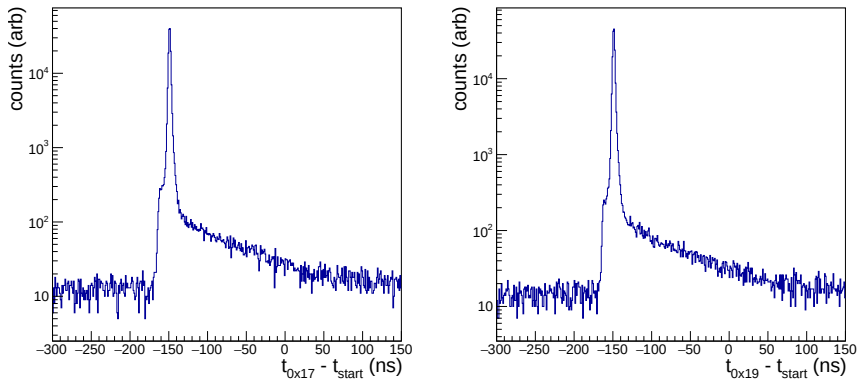

(a) (b)

Figure 8.16 Time spectra with a 3-hit coincidence, the start detector and two LYSO crystals.

The data was cut into two time windows, one on the peak, and one on the long lifetime. This gave two very distinct energy distributions. Define the "peak" window between -156 ns $< \Delta T < -140$ ns, and the "long lifetime" window between -130 ns $< \Delta T < 60$ ns. The resulting distributions for both time windows is shown in Figure 8.17. This data clearly showed the continuous energy distribution in the data that resembles the simulations from Chapter 7. There was also a dramatic decrease in the 511-1275 keV coincidences. This demonstrates that our planned detector configurations will be able to separate the continuous energy distribution from 3-γ decay of ortho-positronium from the spurious coincidences from the source, and from the internal radioactivity (which is entirely absent in these plots). Even with the DAQ un-optimized, and the start detector in particularly performing below our planned specifications, we were still able to resolve this distribution.

The spectra shown in Figure 8.17 look much cleaner than the energy spectra shown in the Tokyo experiment (Ref. [39]). This is a misleading comparison as the setup presented here had the source about 26.7 mm below the center of the detector ring. This geometry favors seeing 3-γ events and largely removes 2-γ events, and does not represent the planned placement of the β source and powder.

8.8 ^{22}Na vs. ^{68}Ga

We performed these studies with a ^{68}Ga source for comparison with the ^{22}Na data. This source has a halflife of 270 days compared to ^{22}Na with 2.6 years. It also had a much higher activity at nearly 50 μCi compared to the sodium source at 7.5 μCi. This created substantially more pileup in the start detector. The time spectrum is shown in Figure 8.18, and it was indeed less clean than those for the sodium source. The structures correspond to improperly digitized start signals that lead to a misconstructed time spectrum, in particular due to retriggering.

The start detector and powder corresponds to Design (A) from Chapter 6, and as shown there is immense spreading of the positronium throughout the powder for this source. The spreading of the positronium leads to the possibility of seeing back-to-back photons. The illustration shown in Figure 7.15 actually corresponds to the exact geometry of this current setup. The expected spreading of the positronium in this powder is given in Figure 6.12, and it clearly extends all the

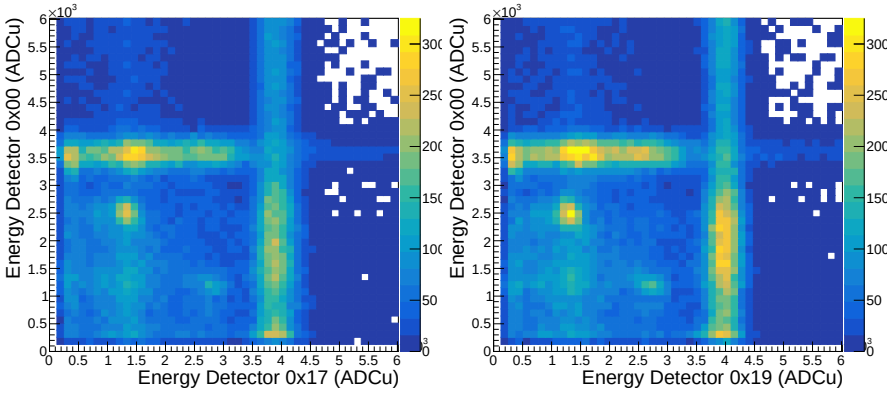

(a) -156 ns $<$ dT <-140 ns (b) -156 ns $<$ dT <-140 ns

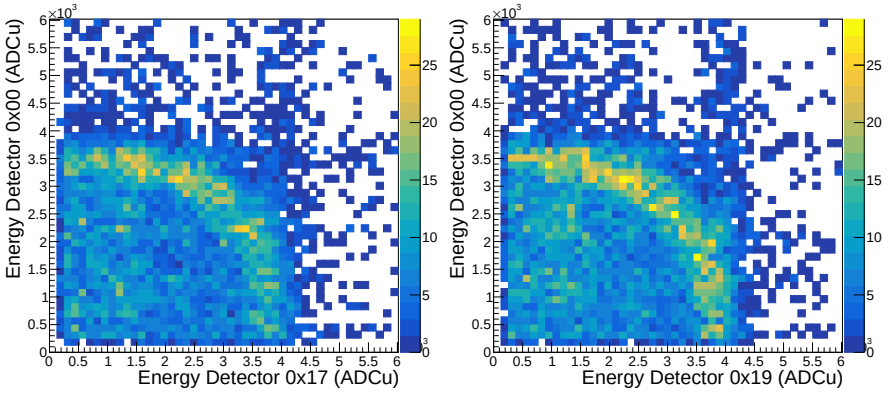

(c) -130 ns $<$ dT $<$ 60 ns (d) -130 ns $<$ dT $<$ 60 ns

Figure 8.17 The 2-D Energy distribution between two LYSO crystals with a 3 hit coincidence condition where the third hit is in the start detector. We apply cuts on the time spectra in Figure 8.16. (a) and (b) cut on the prompt peak. (c) and (d) cut on the long lifetime component of ortho-positronium.

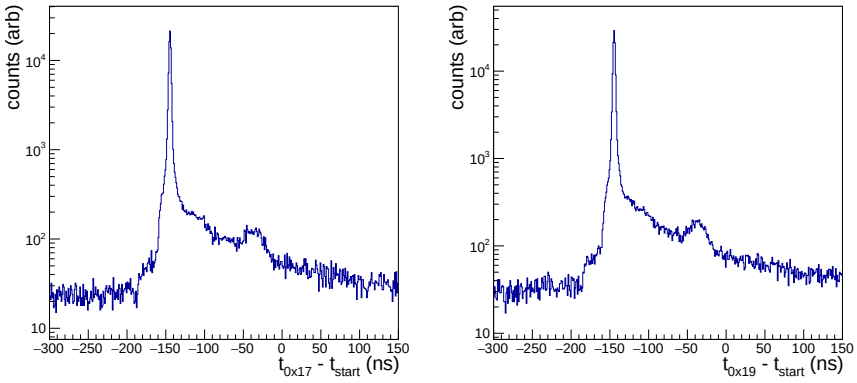

(a) (b)

Figure 8.18 Time distributions comparable to Figure 8.16 for the ^{68}Ga source.

way out to beyond the 2 cm radius. As mentioned, this source and powder are below the plane of the detector ring. The observed energy distribution for both time cuts is shown in Figure 8.19, and can be compared with those in Figure 8.17. This data displayed many more back-to-back events with the gallium source than the data for the sodium source.

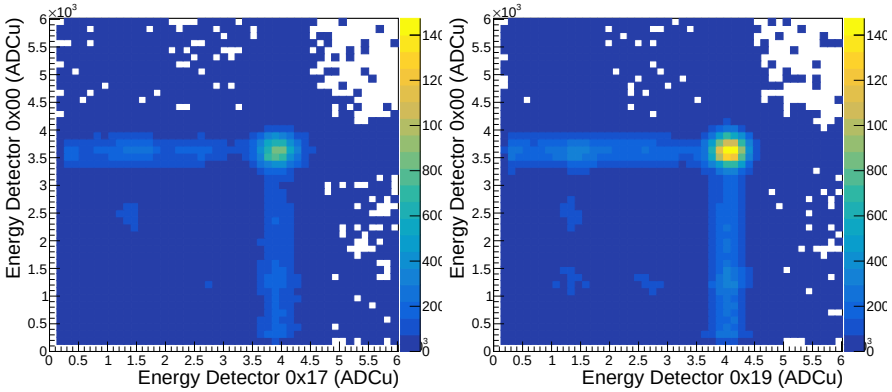

(a) −156 ns < dT < −140 ns (b) −156 ns < dT < −140 ns

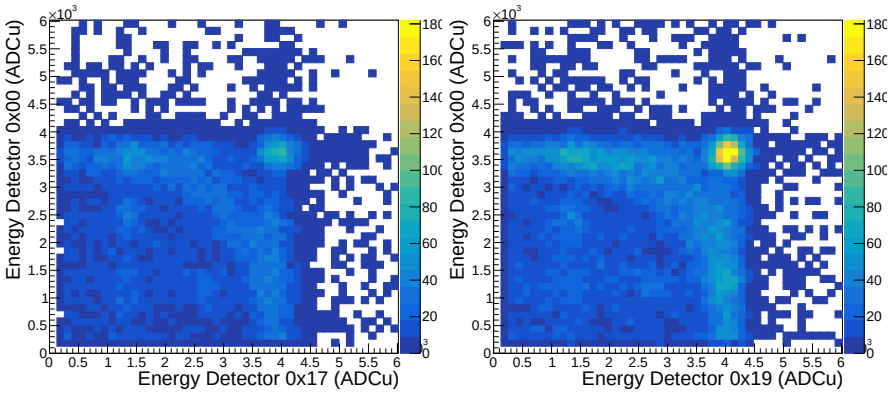

(c) −130 ns < dT < 60 ns (d) −130 ns < dT < 60 ns

Figure 8.19 2-D energy distribution obtained with a ^{68}Ga source.

Changing of the source required removing the start detector and the powder, and the demonstrator had no mechanism to ensure a careful alignment of the source and powder in the center of the ring. This was evident in the gallium results where the (0x00,0x19) pair saw a much larger contribution from back-to-back photons. This is in agreement with the picture of the setup in Figure 8.8, where the start detector and powder (and most likely the source as well) are offset from the center of the ring towards the right of the box. This means it was closer to the 0x19 detector than the 0x17 detector.

8.9 Simulation

We are able to specify this setup in the Geant4 simulation, and run the expected 3-γ and 2-γ events the β source using Design (A), offset below the ring to appropriately match the setup. Since this powder had a lifetime of 70 ns there is a 50/50 weighting of the two spectra. The 2-γ and 3-γ distributions for both sources are shown in Figure 8.20.

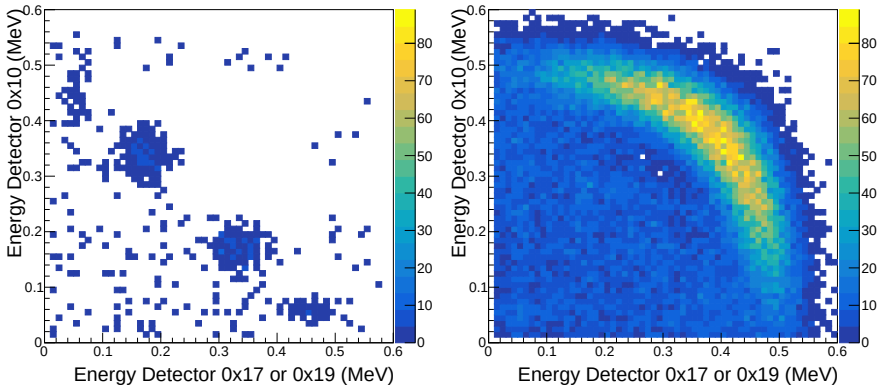

(a) ^{22}Na 2-γ (b) ^{22}Na 3-γ

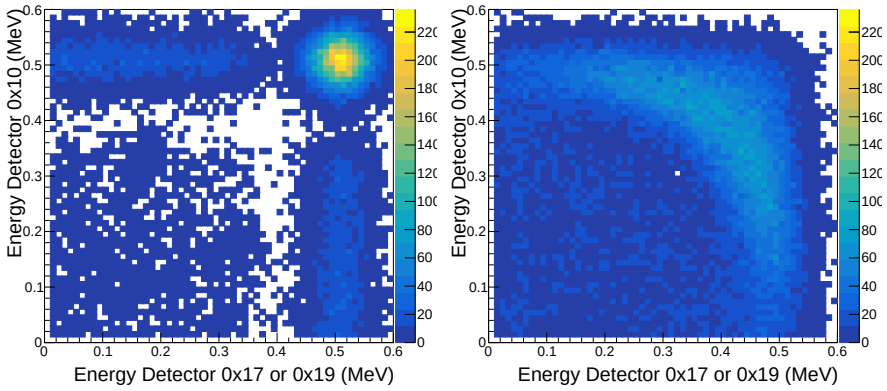

(c) ^{68}Ga 2-γ (d) ^{68}Ga 3-γ

Figure 8.20 Monte-Carlo simulation of the 2-D histograms obtained with a ^{22}Na and a ^{68}Ga source under the condition of the test, for 2-γ and 3-γ events. The combinations are shown in Figures 8.21 and 8.22.

This simulation takes the stopping positions throughout the powder and generates either a 2-γ event at that position or a 3-γ event. The powder and start detector are not currently implemented in the γ-simulation, they are included in the β-stopping simulation, but then when importing that into the second simulation we currently treat the positronium as if it is decaying in air. Indeed there

are no inactive elements in the current simulation, and therefore the coincidences where one photon scattered off of material in the demonstrator will not be present. The combined spectra along with both measured distribution are shown for ^{22}Na and ^{68}Ga in Figures 8.21 and 8.22 respectively.

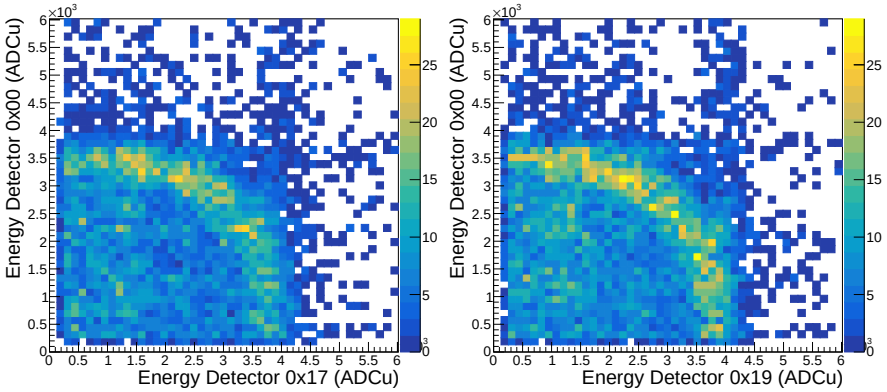

(a) Data for (0x10,0x17) (b) Data for (0x10,0x19)

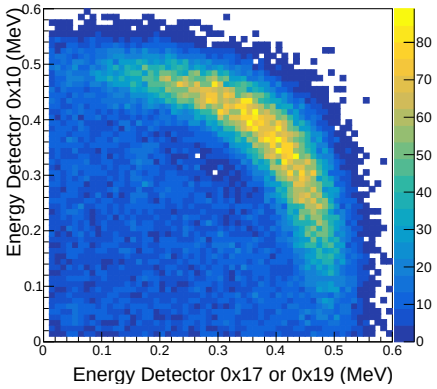

(c) Simulation

Figure 8.21 (a), (b) Measured energy distribution for events in the long lifetime component. (c) Simulation of the combined results for 2-γ events and 3-γ events for ^{22}Na from Figure 8.20.

We are able to reproduce the combined peak and continuum structure. The source was not carefully centered which created an asymmetry in the coincidences between the two detector pairs. The gallium data showed extra structure that matches up with backscatter peaks, where one 511 keV photon hit our detector, and the other scattered off of material in the setup and then hit one of our detectors.

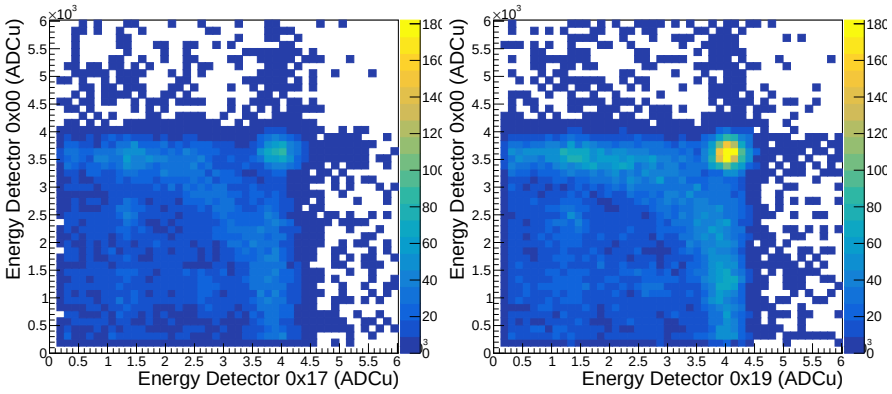

(a) Data for (0x10,0x17) (b) Data for (0x10,0x19)

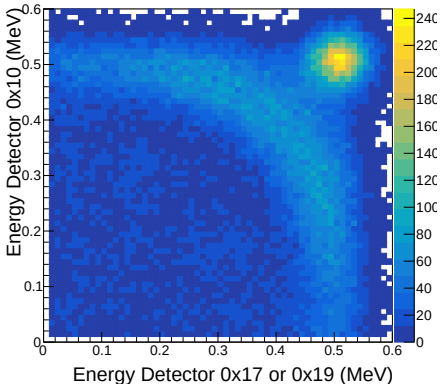

(c) Simulation

Figure 8.22 (a), (b) Measured energy distribution for events in the long lifetime component. (c) Simulation of the combined results for 2-γ events and 3-γ events for ^{68}Ga from Figure 8.20.

CHAPTER 9

ANGULAR CORRELATIONS IN 3-γ DECAY OF POSITRONIUM

We have now demonstrated that we can observe the continuous 2-D energy distribution from 3-γ decay. It is necessary to investigate how symmetry violations would affect this distribution. The full theoretical description of symmetry violations in angular correlations of 3-γ decay of ortho-positronium (when photon polarizations are not measured) was worked out by Bernreuther, Löw, Ma, and Natchmann in Ref. [19]. This work was reviewed in Chapter 2. In this chapter we connect the measurement of an asymmetry with extracting the $\mathcal{CP}$-violating form factors proposed in Ref. [19]. This requires re-thinking some aspects of the analysis. Much of this chapter is also directly applicable to searches for the form factor b_3 (referred to as "the correlation $\hat{\mathbf{s}} \cdot \hat{\mathbf{n}}$" that has been searched for in Refs. [37, 41, 42, 43, 44] and the planned upcoming searches in Refs. [79, 80]. However to date no model has been proposed for this form factor. For the purposes of this work we will focus on the $\mathcal{CP}$-violating signature our array will search for.

We first provide a brief review of the form factors describing 3-γ spin-1 positronium decay, and which form factors correspond to our signal. The rest of this chapter relates the measurement to extracting these form factors. This requires including detector acceptances into the calculation of asymmetries. This is pursued as far as possible without assuming a model. Finally we end the chapter by interpreting the experiment in the context of $\mathcal{CP}$-violating state mixing in positronium.

9.1 Form factors in ortho-positronium decay

All measurements of angular distributions of the photon momenta in the decay of spin-1 positronium to 3 photons can be fully described by 9 irreducible tensors each multiplied by a model dependent form factor (that is itself a function of the energies of the photons). Below the form factors are tabulated, including the positronium trait that drives the distortion and the angular correlatoins that are induced by these terms. Following Chapter 2, denote the components of the unit vectors,

$$\hat{\mathbf{k}}_a = \kappa_{ax}\hat{\mathbf{x}} + \kappa_{ay}\hat{\mathbf{y}} + \kappa_{az}\hat{\mathbf{z}} \tag{9.1}$$

Form factor	Tensor structure	Ps dependence	Expectation values
$a(\omega_1,\omega_2)$	1_{3x3}	$\mathrm{Tr}(\rho)$	$N_{3\gamma}$
$b_1(\omega_1,\omega_2)$	κ_{1i}	$\mathbf{s}_i$	$\langle\kappa_{ai}\rangle$
$b_2(\omega_1,\omega_2)$	κ_{2i}	$\mathbf{s}_i$	$\langle\kappa_{ai}\rangle$
$b_3(\omega_1,\omega_2)$	n_i	$\mathbf{s}_i$	$\langle n_i\rangle$
$c_1(\omega_1,\omega_2)$	$\kappa_{1i}\kappa_{1j}$	s_{ij}	$\langle\kappa_{ai}\kappa_{bj}\rangle, \langle n_i n_j\rangle$
$c_2(\omega_1,\omega_2)$	$\kappa_{2i}\kappa_{2j}$	s_{ij}	$\langle\kappa_{ai}\kappa_{bj}\rangle, \langle n_i n_j\rangle$
$c_3(\omega_1,\omega_2)$	$\kappa_{1i}\kappa_{2j}$	s_{ij}	$\langle\kappa_{ai}\kappa_{bj}\rangle, \langle n_i n_j\rangle$
$c_4(\omega_1,\omega_2)$	$\kappa_{1i}n_j$	s_{ij}	$\langle\kappa_{ai}n_j\rangle$
$c_5(\omega_1,\omega_2)$	$\kappa_{2i}n_j$	s_{ij}	$\langle\kappa_{ai}n_j\rangle$

Table 9.1 The nine form factors fully describing angular distributions of spin-1 positronium decay to 3-γ. a and b can stand for any of the 3 photons. Any object with two indices should be interpreted as a traceless symmetric tensor.

$$\mathbf{n} = \hat{\mathbf{n}} = n_x\hat{\mathbf{x}} + n_y\hat{\mathbf{y}} + n_z\hat{\mathbf{z}} \tag{9.2}$$

the normal to the decay plane $\mathbf{n}$ is always taken to be normalized. For brevity the notation for traceless symmetric tensors is shortened, for instance we write $\langle\kappa_{ai}\kappa_{bj} + \kappa_{aj}\kappa_{bi} - \frac{2}{3}\hat{\mathbf{k}}_a\cdot\hat{\mathbf{k}}_b\delta_{ij}\rangle \rightarrow \langle\kappa_{ai}\kappa_{bj}\rangle$. These terms are given in Table 9.1

The term $a(\omega_1,\omega_2)$ is the Ore-Powell distribution for isotropic ortho-positronium decay. b_1 and b_2 are $C\mathcal{P}$-violating vector terms. b_3 is indicative of new physics as it is very small in the Standard Model, being induced by final state photon-photon scattering. It is not however indicative of $C\mathcal{P}\mathcal{T}$-violation as argued in Refs. [37, 42, 41, 44, 81]. c_i for $1 \leq i \leq 3$ are distortions to the angular distribution induced by QED, similar to a quadrupole deformation. Finally c_4 and c_5 correspond to the $C\mathcal{P}$-violating form factors we intend to search for. Note that the definition of the tensor polarization in Ref. [19] and used here differs from the alignment P_2 as defined in Refs. [38, 39] by $P_2 = 3s_{zz}$. The form factors c_4 and c_5 are "clean signatures" of $C\mathcal{P}$-violation, in that they are not $\mathcal{T}$-odd signatures that then invoke $C\mathcal{P}\mathcal{T}$-symmetry to equate with a violation with $C\mathcal{P}$-violation. As such they cannot be mimicked by radiative corrections and final state interactions, unless those interactions violate $C\mathcal{P}$ themselves [18, 19]. It is incorrect to state that this signal is induced at $O(10^{-10})$ by final state interactions as stated in Refs. [39, 81].

The sum of these form factors (weighted by the Ps dependence) gives the expected change in

counts for an event with photons $(\mathbf{k}_1, \mathbf{k}_2, \mathbf{k}_3)$,

$$N(\mathbf{k}_1, \mathbf{k}_2, \mathbf{k}_3) = a(\omega_1, \omega_2) + \mathbf{s} \cdot \mathbf{B}(\mathbf{k}_1, \mathbf{k}_2, \mathbf{k}_3) + s_{ij} C_{ij}(\mathbf{k}_1, \mathbf{k}_2, \mathbf{k}_3) \tag{9.3}$$

In order to turn this into an asymmetry in counts we need to incorporate a description of the detector placement and energy cuts into the theoretical description.

9.2 Detector acceptance and phase space cuts

All realistic experiments have finite detector acceptances and efficiencies. These manifest as restrictions to the phase space integration. This is included in the description by following Appendix D in Ref. [19]. Define the "characteristic function", for a pair of detectors with a highest energy detector with placement Ω_1 and a second highest energy detector with placement Ω_2,

$$\chi_a(\mathbf{k}_1, \mathbf{k}_2, \mathbf{k}_3) = \begin{cases} 1, & \hat{\mathbf{k}}_1 \in \Omega_1, \hat{\mathbf{k}}_2 \in \Omega_2 \\ 0, & \text{o/w} \end{cases} \tag{9.4}$$

this is an estimation of the apparatus if the detectors have detection efficiency, and are only affected by solid angle and geometry. Specifically it returns 1 when both $\hat{\mathbf{k}}_1$ hits the highest energy detector and $\hat{\mathbf{k}}_2$ hits the second highest energy detector, or it returns 0 otherwise. In effect this means that by specifying the detector placement and energy cuts we are selecting a region of phase space. For this reason the authors of Refs. [18, 19, 20] refer to these as "phase space cuts". Now the number of coincidence counts for a given pair a is,

$$N_a = \int \mathrm{d}f^{3\gamma} \chi_a(\mathbf{k}_1, \mathbf{k}_2, \mathbf{k}_3) R_{ij}(\mathbf{k}_1, \mathbf{k}_2, \mathbf{k}_3) \rho_{ji} \tag{9.5}$$

$$= \int \mathrm{d}f^{3\gamma}_{\Omega_1\Omega_2} R_{ij}(\mathbf{k}_1, \mathbf{k}_2, \mathbf{k}_3) \rho_{ji} \tag{9.6}$$

$$= \int \mathrm{d}f^{3\gamma}_{\Omega_1\Omega_2} \big(a(\omega_1, \omega_2) + \mathbf{s} \cdot \mathbf{B}(\mathbf{k}_1, \mathbf{k}_2, \mathbf{k}_3) + s_{ij} C_{ij}(\mathbf{k}_1, \mathbf{k}_2, \mathbf{k}_3)\big) \tag{9.7}$$

where $\int \mathrm{d}f^{3\gamma}_{\Omega_1\Omega_2}$ is the phase space restricted to only the regions where the two photons hit the detectors (and pass the energy cuts). This is the coincidence counts for a pair of detectors after integrating over the energy cuts. Consider a second pair of detectors that is the $\mathcal{CP}$-image of pair a. This is referred to in ref. [18, 82] as "$\mathcal{CP}$-invariant phase space cuts". Hold the highest energy

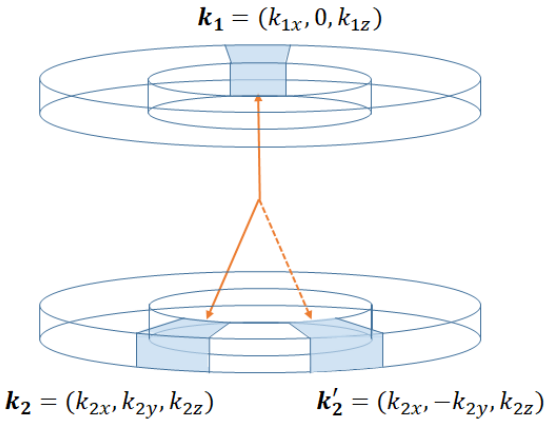

Figure 9.1 Sketch of the detector rings showing the highest energy detector to lie in the x-z plane and the two pairs are related by flipping the y-component of $\hat{\mathbf{k}}_2$. This is true for Symmetric and Asymmetric configurations, and all 16 sets can be related by an azimuthal rotation.

detector the same at Ω_1, and choose a second detector to form a pair, Ω_2' (Figure 9.1),

$$N_b = \int \mathrm{d}f^{3\gamma}_{\Omega_1\Omega_2'} R_{ij}(\mathbf{k}_1, \mathbf{k}_2, \mathbf{k}_3)\rho_{ji} \tag{9.8}$$

$$= \int \mathrm{d}f^{3\gamma}_{\Omega_1\Omega_2'} \left(a(\omega_1, \omega_2') + \mathbf{s}\cdot\mathbf{B}(\mathbf{k}_1, \mathbf{k}_2, \mathbf{k}_3) + s_{ij}C_{ij}(\mathbf{k}_1, \mathbf{k}_2, \mathbf{k}_3)\right) \tag{9.9}$$

The detector placement is chosen such that between two pairs the terms we are not interested in are equal, and the terms we are interested in are equal but opposite in sign. This will be expanded upon in the context of our experiment below. To lighten the notation we shorten $\Omega_1\Omega_2$ to simply Ω.

9.3 Extraction of count asymmetry terms

Consider a positronium state with no vector polarization, and no off-diagonal terms in the tensor polarization. This gives, $s_i = 0$, $s_{xy} = s_{yz} = s_{zx} = 0$. There is a net tensor polarization, s_{zz}, and compensating diagonal terms to ensure traceless-ness $s_{xx} = s_{yy} = -\frac{1}{2}s_{zz}$. We follow the convention for tensor polarization used in Ref. [19], $-2/3 < s_{zz} < 1/3$. This is addressed in appendix A.

Working out the term that depends on tensor polarization,

$$s_{ij}C_{ij}(\mathbf{k}_1, \mathbf{k}_2, \mathbf{k}_3) = s_{xx}C_{xx} + s_{yy}C_{yy} + s_{zz}C_{zz} \tag{9.10}$$

$$= s_{zz}\left(C_{zz} - \frac{1}{2}(C_{xx} + C_{yy})\right) \tag{9.11}$$

the same simplification applies for $C_{xx} + C_{yy} = -C_{zz}$ (due to the tracelessness of the tensor). This

gives the tensor distortion,

$$s_{ij}C_{ij} = \frac{3}{2}s_{zz}\Bigg\{\Bigg((\hat{\mathbf{k}}_{1z}^2 - \frac{1}{3})c_1(\omega_1,\omega_2) + (\hat{\mathbf{k}}_{2z}^2 - \frac{1}{3})c_2(\omega_1,\omega_2) + (2\kappa_{1z}\kappa_{2z} - \frac{2}{3}\hat{\mathbf{k}}_1\cdot\hat{\mathbf{k}}_2)c_3(\omega_1,\omega_2)\Bigg) + \Bigg(2\kappa_{1z}n_z c_4(\omega_1,\omega_2) + 2\kappa_{2z}n_z c_5(\omega_1,\omega_2)\Bigg)\Bigg\} \tag{9.12}$$

In the context of our experiment it is now beneficial to break this object up into two separate terms. Consider the first three terms as the QED induced anisotropy, and the second two terms as the $C\mathcal{P}$-violating signal,

$$s_{ij}C_{ij} = s_{zz}D(\mathbf{k}_1,\mathbf{k}_2,\mathbf{k}_3) + s_{zz}C(\mathbf{k}_1,\mathbf{k}_2,\mathbf{k}_3) \tag{9.13}$$

where D corresponds to the terms that are $C\mathcal{P}$-even (and non-zero in QED), and C is the terms that are $C\mathcal{P}$-odd (and zero in QED). Taking the detector response to be the same as above gives an updated 3-γ distribution,

$$\begin{aligned} N_\Omega &= \int \mathrm{d}f_\Omega^{3\gamma} a(\omega_1,\omega_2) + s_{zz}\int \mathrm{d}f_\Omega^{3\gamma} D(\mathbf{k}_1,\mathbf{k}_2,\mathbf{k}_3) + s_{zz}\int \mathrm{d}f_\Omega^{3\gamma} C(\mathbf{k}_1,\mathbf{k}_2,\mathbf{k}_3) \\ &= \mathcal{A}^\Omega + s_{zz}\mathcal{D}^\Omega + s_{zz}C^\Omega \end{aligned} \tag{9.14}$$

where the last term is a definition, writing a shorthand for the function of energies integrated over the detector placement and energy cuts. This gives $\mathcal{A}^\Omega$ as the isotropic Ore-Powell contribution, the term $\mathcal{D}^\Omega$ is akin to a quadrupole deformation of the distribution of $\hat{\mathbf{k}}_i$ over our detector solid angles, finally C^Ω is the part of the distribution sensitive to $C\mathcal{P}$-violation. C^Ω is the combination of the two form factors that produce the asymmetry. This is the quantity that most closely corresponds to the "coefficient multiplying the angular correlation", written as $C_{CP}\kappa_{1z}(\hat{\mathbf{k}}_1\times\hat{\mathbf{k}}_2)_z$ in Refs. [38, 39], but has a much more complicated form,

$$C^\Omega = 3\int \mathrm{d}f_\Omega^{3\gamma}\Bigg(\kappa_{1z}n_z c_4(\omega_1,\omega_2) + \kappa_{2z}n_z c_5(\omega_1,\omega_2)\Bigg) \tag{9.15}$$

This cannot be separated into a purely geometric factor and a purely energy dependent factor, because the tensor factors are different. Further we cannot make the simplifying assumption that only one term exists and then recover a form more closely related to the coefficient searched for in

the past. This is because c_4 and c_5 are related by photon indistinguishability, as demonstrated in Appendix B. We conclude that all experiments to date were sensitive to a combination of "$\kappa_{1z} n_z$" and "$\kappa_{2z} n_z$".

Consider any of the configurations shown in Figure 7.2, take $\hat{\mathbf{k}}_1$ to lie in the $x-z$ plane, then the difference between any two pairs of detectors in a configuration is flipping the sign of κ_{2y} (which therefore flips the sign n_z). This is illustrated in Figure 9.1. Measuring with these two pairs of detectors only changes the sign of the $C\mathcal{P}$-violating term that arises from a tensor polarized source,

$$N_\Omega = \mathcal{A}^\Omega + s_{zz}\mathcal{D}^\Omega + s_{zz}C^\Omega \tag{9.16}$$

$$N_{\Omega'} = \mathcal{A}^\Omega + s_{zz}\mathcal{D}^\Omega - s_{zz}C^\Omega \tag{9.17}$$

Measuring a count asymmetry between these detector pairs gets a signal that goes as,

$$A = \frac{N_\Omega - N_{\Omega'}}{N_\Omega + N_{\Omega'}} = s_{zz}\frac{C^\Omega}{\mathcal{A}^\Omega + s_{zz}\mathcal{D}^\Omega} \tag{9.18}$$

This isolates the $C\mathcal{P}$-violating part of the decay matrix. The term in the numerator is the term of interest. The term in the denominator is the non-cancelling backgrounds.

Now we are in a position to study, for a given detector placement and energy cuts, what size of signal we expect and finally arrive at a method to derive a sensitivity to $C\mathcal{P}$-violating physics. This must be done in the context of a specific model. Before proceeding to do this we first comment on a different method that could be used to perform this measurement, as the two methods are distinct but have gotten mixed up in the literature.

9.4 Count asymmetry versus expectation value

Another way to do this experiment would be to measure the expectation value of an observable that is sensitive to the symmetry violation. For example the expectation value $\langle \kappa_{1z} n_z \rangle$ could be measured. This would require that recording $\kappa_{1z} n_z$ for each event and calculating the average of the recorded values. If good phase space cuts are chosen such that there is equal acceptances for events with negative value and positive value then a non-zero expectation value would be indicative of $C\mathcal{P}$-violation. But the expectation value cannot be directly compared to a count asymmetry for the same phase space cuts.

Consider a simpler analogy, searching for a $\mathcal{P}$-violating interaction in 1-D quantum mechanics. Take a state, $\psi(x)$, that starts with a well defined parity and evolves into a new state that may or may not have definite parity. We could measure an operator that is odd under parity, like x, meaning measure many equivalent systems and record the value of x for each measurement and calculate $\langle x \rangle = (1/N) \sum_i^N x_i$. Another method would be to simply count how many times the particle has a positive value for x, N_+, or a negative value for x, N_-. The difference in counts, $A = (N_+ - N_-)/(N_+ + N_-)$ would also indicate parity violation. Importantly though these two quantities are not equal, $A \neq \langle x \rangle$. The two are roughly related as $\langle x \rangle \approx \langle |x| \rangle A$ if the parity violation is small.

Now consider measuring a count asymmetry between how many ortho-positronium decays have the decay plane along $+\hat{\mathbf{z}}$ versus $-\hat{\mathbf{z}}$. Compare that to measuring $\langle \hat{\mathbf{z}} \cdot \hat{\mathbf{n}} \rangle$, the latter quantity will always be smaller because each event is weighted by a number less than one. This makes comparison of the searches for b_3 complicated. Three groups to date measured a simple count asymmetry [37, 41, 43]. One group weighted each event by three different functions of energies [42], but were careful to explain what their analysis involved and which weightings can be compared to previous measurements. This weighting is distinct from the functions b_i, c_i that appear in the decay matrix. The most recent search measured an expectation value and equate it with previous count asymmetry measurements [44]. A direct comparison of the expectation value versus the count asymmetry artificially inflates the sensitivity of the search measuring an expectation value, since $\langle |\hat{\mathbf{s}} \cdot \hat{\mathbf{n}}| \rangle = \langle |\cos(\theta)| \rangle \leq 1$.

In short, it is important to distinguish between "measuring a term in the decay distribution that goes as $\mathbf{s} \cdot \hat{\mathbf{n}}$" and "measuring the expectation value of the observable $\langle \mathbf{s} \cdot \hat{\mathbf{n}} \rangle$". This is another reason we find that describing these quantities as "form factors" is more clear than calling them "coefficients of angular correlations" as has been the norm in these measurements. The latter is the standard nomenclature in nuclear β-decay, but in such cases the form factors are simply coefficients, not energy dependent functions, at least at tree level [83].

9.5 Application to our analysis

Now we adapt the theory description to our planned detector array. Hold κ_1 to always be in the same detector and lie in the $x-z$ plane. There are two detectors for $\hat{\mathbf{k}}_2$ that only change the sign of κ_{2y} but not the other components. This is illustrated in Figure 9.1. This also changes $n_x \rightarrow -n_x$ and $n_z \rightarrow -n_z$. The angular distribution we aim to measure does change sign, $\kappa_{az} n_z \rightarrow -\kappa_{az} n_z$ where $a = 1, 2$.

9.5.1 Phase space volume

Here we demonstrate the structure of these energy dependent functions (a, b_i, c_i...). This is shown for the Symmetric 157.5° pairs of detectors (0x00,0x27) and (0x00,0x29) and the Asymmetric 157.5° pairs of detectors (0x00,0x17) and (0x00,0x19). All of these functions are defined on the phase space, described by the true kinematic variables. However cuts are applied on detector level variables. The two are not in direct correspondence but are instead related by some form of a convolution matrix $\chi(E_a, E_b, \omega_1, \omega_2)$. This maps the kinematic phase space into the detector level variables. In Figure 9.2a the phase space defined on the kinematic variables is plotted, and in Figure 9.2b the "volume of phase space" that the 157.5° Symmetric detector pair selects is plotted (for each two energies).

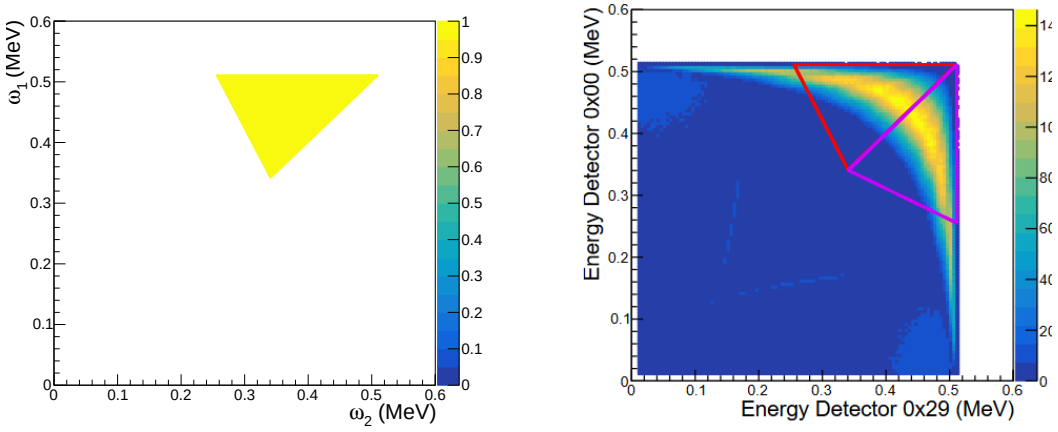

(a) (b)

Figure 9.2 (a) The phase space defined in terms of the photons energies ω_1 and ω_2. (b) That phase space mapped into detector level variables, namely the energy deposited in both detectors.

This is purely kinematics, any positronium physics would manifest in structure on top of this distribution. Any "phase space cuts" are applied to detector level variables, such as coincidence conditions and energy cuts. Figure 9.3 shows the phase space volume selected by the Symmetric and Asymmetric 157.5° pairs. They indicate that going from the Symmetric to the Asymmetric confugration decreases the opening angle, and the energy distribution selected moves closer to the diagonal $E_1 + E_2 = m_e$. These are demonstrating that this Monte-Carlo can reproduce Figure 3.4. Any positronium physics would manifest as distortions on top of this distribution by the matrix element for positronium decay. Now using the distribution of events shown above the form factors are evaluated event by event.

9.5.2 QED terms

The Ore-Powell distribution for isotropic decay is shown in Figure 9.4a on the phase space, and in Figure 9.4b shows this mapped into structure on the coincidence distribution for the detector pairs. Note that the distortion from phase space (Figure 9.3) is not very large for the Ore-Powell distribution. This is shown for the Symmetric and Asymmetric 157.5° configurations in Figure 9.5. This gives the expected distribution for isotropic ortho-positronium decay and corresponds to the plots shown in Chapter 7. The induced structure over the phase space is small.

A net tensor polarization induces a $\mathcal{CP}$-symmetric distortions to the counts. This is the $\mathcal{D}^{\Omega}$ term as defined above. These are shown in Figure 9.6 for a tensor polarization of $s_{zz} = +1/3$ (maximal positive alignment). This is a combination of the form factors c_1, c_2, and c_3 each multiplied by their relevant kinematic tensor. It induces a quadrupole-like distortion to the individual photons distributions, and the decay plane distribution. This is exactly the angular anisotropy measured in Refs. [35, 36]. This distortion is symmetric between our detector pairs within a configuration, and therefore should cancel in the numerator of an asymmetry. The size of the distortion has a nontrivial energy dependence that differs from the isotropic energy dependence.

At this point we can extract a form of sensitivity for the experiment. If we measure an asymmetry,

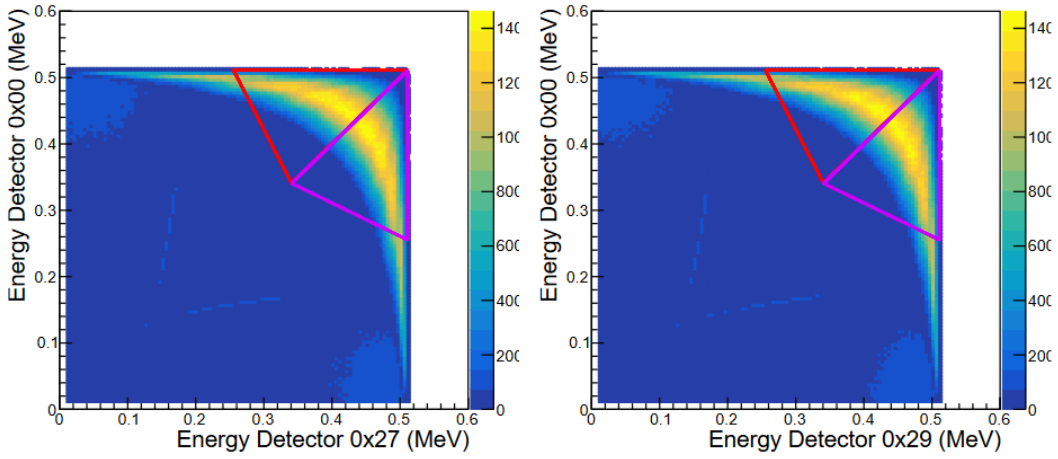

(a) Symmetric 157.5° configuration

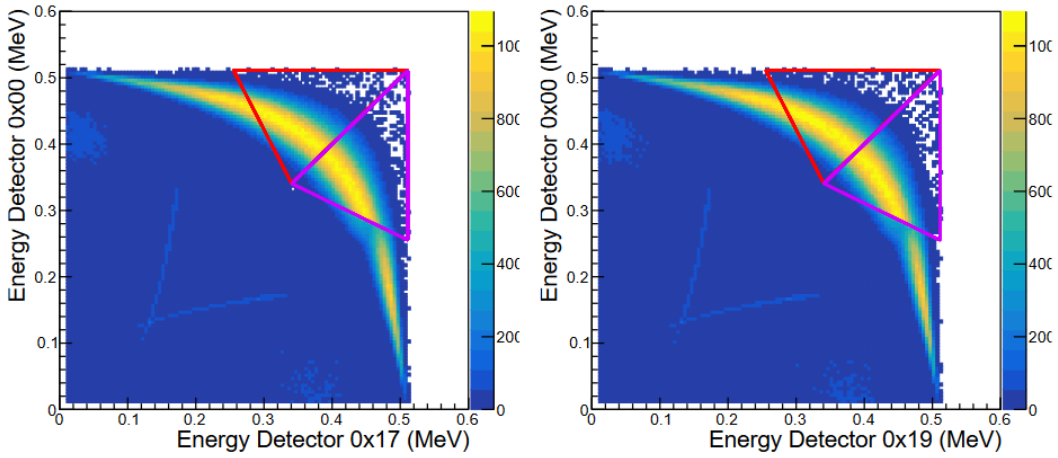

(b) Asymmetric 157.5° configuration

Figure 9.3 Phase space selected by the detector pairs for both the Symmetric and Asymmetric 157.5° configurations.

A_a, for configuration a, the asymmetry is given as,

$$A_\Omega = s_{zz} \frac{C^\Omega}{\mathcal{A}^\Omega + s_{zz}\mathcal{D}^\Omega} \tag{9.19}$$

$$C^\Omega = \frac{1}{s_{zz}} (\mathcal{A}^\Omega + s_{zz}\mathcal{D}^\Omega) A_\Omega \tag{9.20}$$

The tensor polarization s_{zz} is known (taken as a given for now, discussed in Chapter 10), and we can estimate $\mathcal{A}^\Omega + s_{zz}\mathcal{D}^\Omega$ from these simulations. This enables the extraction the purely $\mathcal{CP}$-violating contribution to the asymmetry C^Ω. For the experiment as outlined, and a source with tensor polarization perfectly aligned along the $\hat{z}$-axis, this term can only be induced by $\mathcal{CP}$-

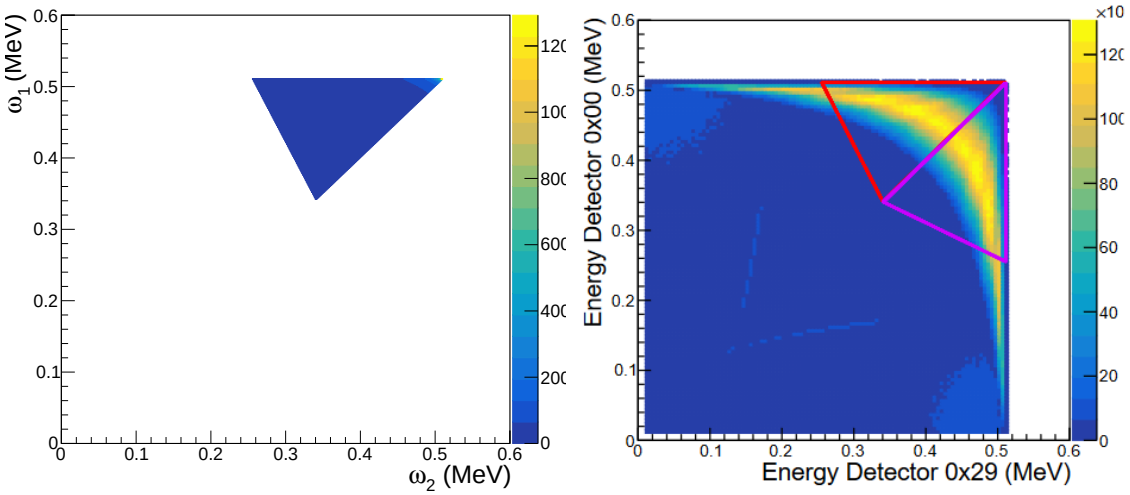

(a) (b)

Figure 9.4 (a) The QED distribution for isotropic ortho-positronium decay plotted on the phase space. This distribution is sharply peaked at high energies. (b) The same distribution mapped into detector level variables.

violating physics. Formally this term is given in Equation 9.15, however without a specific model we do not have the form of $c_4(\omega_1, \omega_2)$ and $c_5(\omega_1, \omega_2)$ and this cannot be simplified further. This means that sensitivities cannot be directly compared between experiments with different detector placement and energy cuts in a model independent way. Further we cannot even compare different configurations within our experiment in a model independent way (except those related by an azimuthal rotation).

We now proceed to consider a specific model, given in Ref. [19] for mixing of positronium states. We identify the phase space dependence, and what signal it would induce in the planned experiment.

9.5.3 $\mathcal{CP}$-violating mixing of 1^3S_1 and 2^1P_1 positronium states

In Ref. [19] the authors propose searching for indirect $\mathcal{CP}$-violation in ortho-positronium decay. Direct violation in 3-γ decay would be dominated by a permanent electric dipole moment (eEDM) which has been excluded to a high precision [16]. Instead there could be possible combinations of terms such that the production of an eEDM is suppressed, but $\mathcal{CP}$-violating state mixing is not suppressed. They considered the $\mathcal{CP}$-violating mixing of the 1^3S_1 and 2^1P_1 states. Note that the

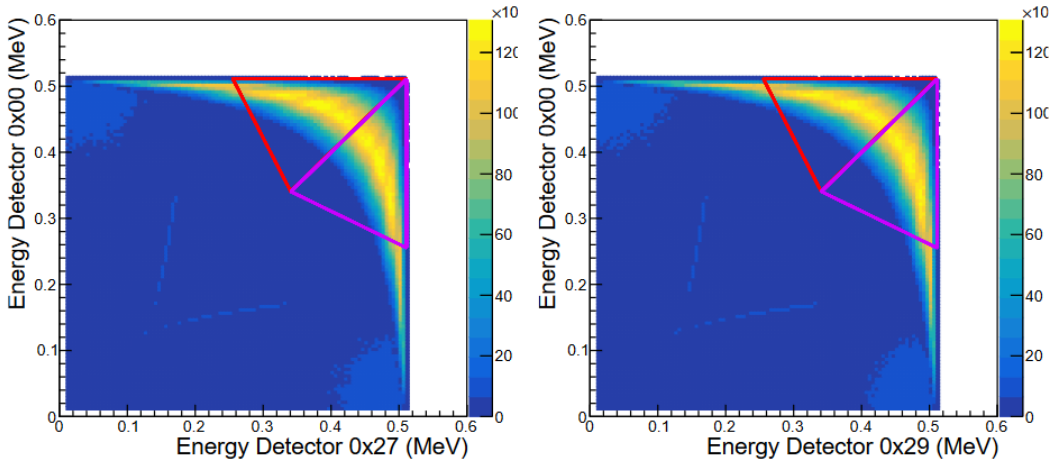

(a) Symmetric 157.5° configuration

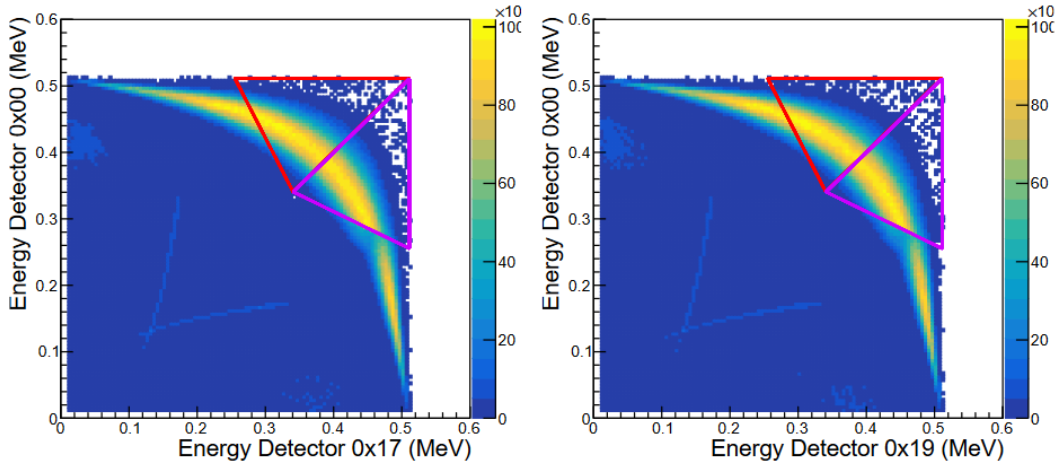

(b) Asymmetric 157.5° configuration

Figure 9.5 For each event in Figure 9.3 (meaning a 3 photon event that survives our phase space selection) the function $a(\omega_1, \omega_2)$ is evaluated and the value recorded to the bin for the corresponding detector variables (E_a, E_b). This gives the QED distribution of events for unpolarized positronium.

decay of 2^1P_1 positronium is suppressed due to the atomic structure of positronium, this supresses the effects of state mixing by a factor of $\alpha/(2\sqrt{8}) \approx 1/775$. The phenomenology of direct versus indirect $\mathcal{CP}$-violation is explored in Appendix B, and the source of this suppression is illustrated. This large factor dominates any estimated sensitivity, effectively reducing it by a factor of 10^3.

With a specific model the count asymmetry can be translated into a sensitivity to a new physics parameter. Here the parameter is the real part of the mixing term between the two Ps states, $\mathrm{Re}(\delta_1)$

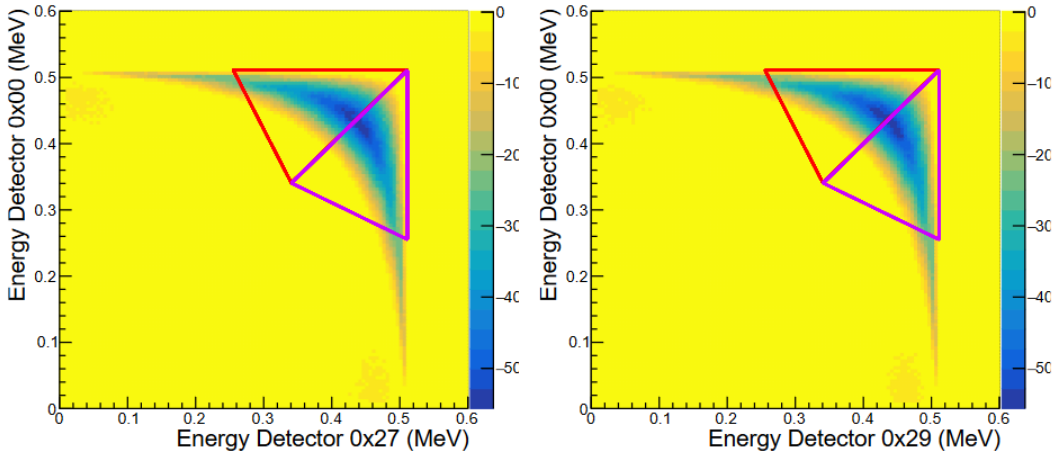

(a) Symmetric 157.5° configuration

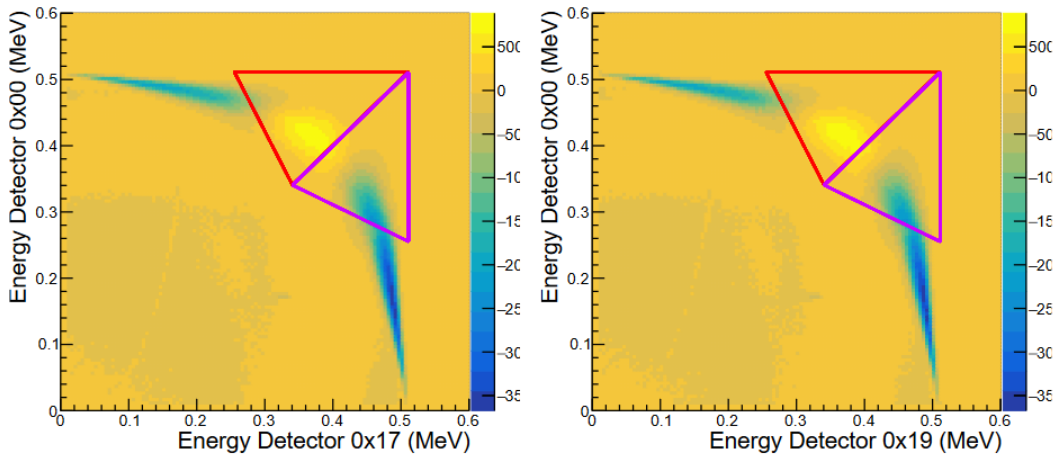

(b) Asymmetric 157.5° configuration

Figure 9.6 For each event in Figure 9.3 (meaning a 3 photon event that survives our phase space selection) the appropriately summed form factors $c_i(\omega_1, \omega_2)$ for $0 \leq i \leq 3$, weighted by their respective kinematic tensors, is evaluated and the value recorded to the bin for the corresponding detector variables (E_a, E_b). This gives the QED distortion for maximally aligned positronium.

[19]. We can pull this term out of the model dependent function of energies,

$$C^{\Omega}_{mix} = \mathrm{Re}(\delta_1)\bar{C}^{\Omega}_{mix} \tag{9.21}$$

Now we evaluate $\bar{C}^{\Omega}_{mix}$ over the detector placement and energy cuts, which produces a signal with size $s_{zz}\mathrm{Re}(\delta_1)\bar{C}^{\Omega}_{mix}$. This is plotted in Figure 9.7. It is immediately evident that, in contrast to Figures 9.5 and 9.6, the $C\mathcal{P}$-violating distribution does indeed change sign between the two detector pairs within a configuration and will therefore create an asymmetry in coincidence counts.

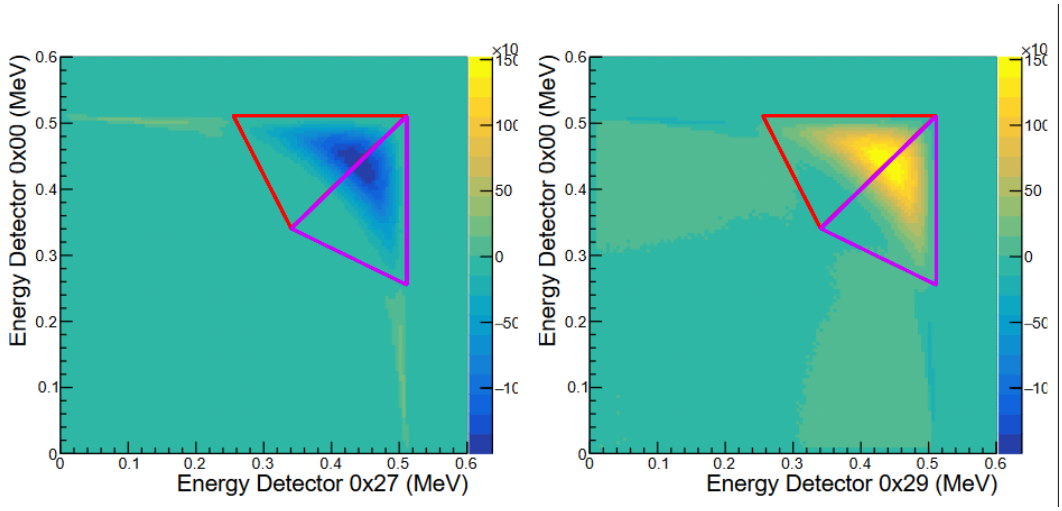

(a) Symmetric 157.5° configuration

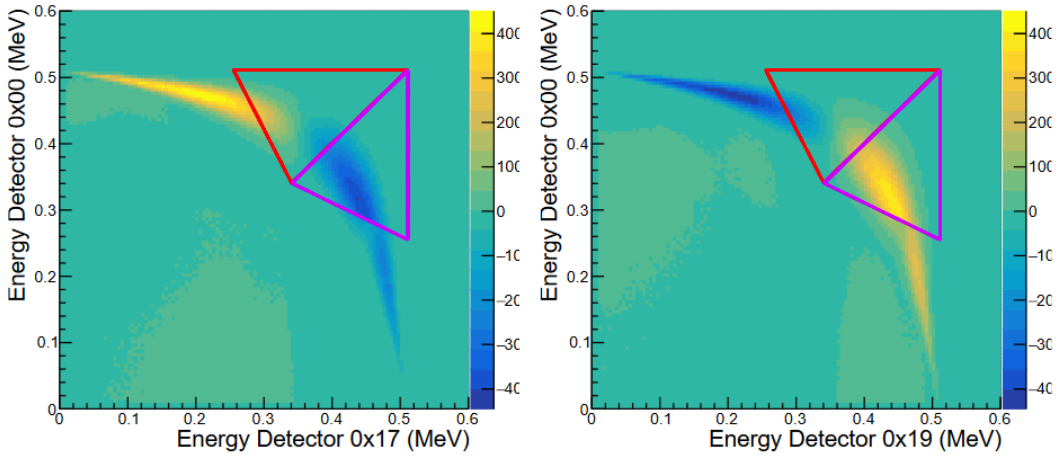

(b) Asymmetric 157.5° configuration

Figure 9.7 Taking the events from Figure 9.3 and evaluating the $\mathcal{CP}$-violating functions that arise in state mixing for ortho-positronium given in [19]. Unlike the QED contributions in Figures 9.5 and 9.6, this does create an asymmetry between our detector pairs.

Now an "analyzing power" can be defined for this specific model. A measured asymmetry A_a can be related to the new physics parameter as,

$$A_a = s_{zz}\mathrm{Re}(\delta_1)\left(\frac{\bar{C}^{\Omega}_{mix}}{\mathcal{A}^{\Omega} + s_{zz}\mathcal{D}^{\Omega}}\right) \tag{9.22}$$

where the term in parenthesis is (the inverse of) the analyzing power. This means we want to maximize $\bar{C}^{\Omega}_{mix}$ and minimize $\mathcal{A}^{\Omega} + s_{zz}\mathcal{D}^{\Omega}$. This cannot be called a geometric analyzing power as there is no clean way to separate the energy dependence and the geometric tensor objects (since $\hat{\mathbf{k}}_1 \cdot \hat{\mathbf{k}}_2 \neq 0$). If $\bar{C}^{\Omega}_{mix}$ only got contributions from one term this would be possible (for example this

separation can be made in the searches for the form factor $\hat{\mathbf{s}} \cdot \hat{\mathbf{n}} b_3(\omega_1, \omega_2)$).

Looking at Figure 9.7 the major change compared to the discussion in Chapters 3 and 7 is that the previously ignored events, where $\hat{\mathbf{k}}_1$ hit the middle ring and $\hat{\mathbf{k}}_2$ hit an outer ring, are now just as important as the standard Asymmetric events. This is because the signal gets contributions not just from the c_4 form factor that multiplies $\kappa_{1z} n_z$, but also the previously neglected c_5 form factor that multiplies $\kappa_{2z} n_z$. This means the argument in Chapter 7, that the events where $\hat{\mathbf{k}}_1$ hit the middle ring have no sensitivity because $\kappa_{1z} = 0$ no longer hold. These events still have $\kappa_{1z} = 0$, but can instead get a contribution from the c_5 term because $\kappa_{2z} \neq 0$. Events where both photons hit the middle ring still have no sensitivity. Each of these terms is tabulated for each configuration in Table 9.2. For the Asymmetric events where the highest energy photon is in the central ring we integrate in the purple triangle drawn on those figures. The amount of phase space selected by the Asymmetric 112.5° pair is so small we no longer track it.

configuration	hit order	$\int_\Omega \mathrm{d}f_{3\gamma}$ (%)	$\mathcal{A}^\Omega$	$\mathcal{D}^\Omega$	$\bar{C}^\Omega_{mix}$
Sym 157.5°	(0,2)	2.91×10^{-2}	2.70×10^{-3}	-9.31×10^{-4}	-8.19×10^{-7}
Sym 135°	(0,2)	1.35×10^{-2}	1.24×10^{-3}	-4.94×10^{-4}	-2.50×10^{-7}
Sym 112.5°	(0,2)	2.35×10^{-2}	2.11×10^{-4}	-7.8×10^{-5}	-1.81×10^{-8}
Asym 157.5°	(0,1)	1.67×10^{-2}	1.53×10^{-3}	6.75×10^{-5}	2.54×10^{-8}
Asym 135°	(0,1)	4.90×10^{-3}	4.45×10^{-4}	-1.23×10^{-4}	7.88×10^{-9}
Asym 112.5°	(0,1)	5.3×10^{-7}	–	–	–
Asym 157.5°	(1,0)	1.67×10^{-2}	1.48×10^{-3}	-1.34×10^{-4}	-2.22×10^{-7}
Asym 135°	(1,0)	4.40×10^{-4}	4.40×10^{-3}	-1.38×10^{-4}	-5.37×10^{-8}
Asym 112.5°	(1,0)	5.1×10^{-7}	–	–	–

Table 9.2 Each function from Figures 9.3 through 9.7 integrated over the "phase space" triangle that imposes the ordering of the hits by energy.

It is clear looking at Figure 9.7 that strictly cutting along the "phase space" triangle as in Chapter 7 does not necessarily line up with the contributions of the $C\mathcal{P}$-violation. Look at the Asymmetric pair and there is almost a full cancellation within one of the considered regions. It is also worth considering extending to the regions where we detect $(\hat{\mathbf{k}}_2, \hat{\mathbf{k}}_3)$ and $(\hat{\mathbf{k}}_3, \hat{\mathbf{k}}_1)$, for the Asymmetric events these get a large contribution. Those regions get contributions from 2-γ decays where one Compton scatters off of inactive material which could obfuscate the signal contribution.

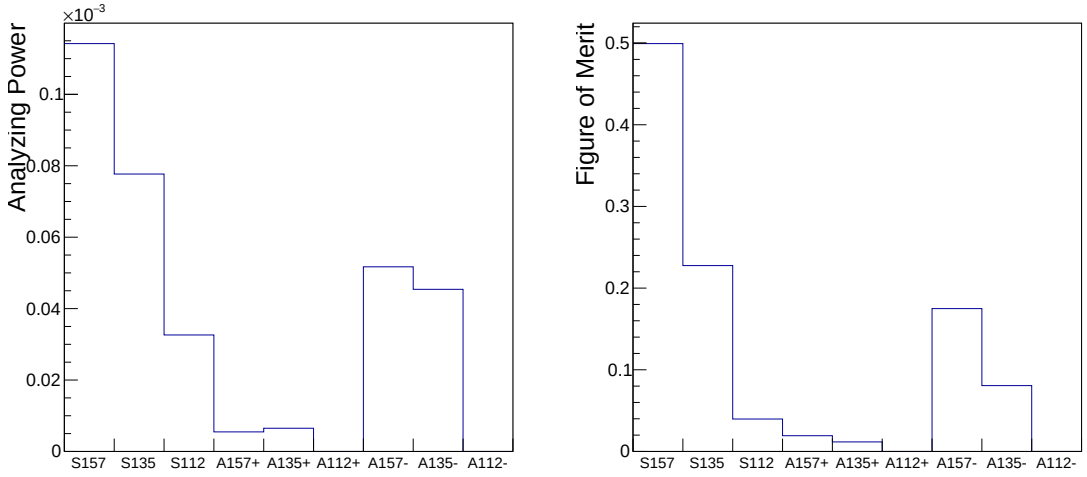

(a) Sensitivities

(b) Figure of Merit

Figure 9.8 (a) Absolute value of the analyzing power for each configuration showing which configurations will have the greatest effect from new physics. (b) Absolute value of the Figure of Merit for each configuration showing which configurations have the greatest statistical sensitivity to new physics. Figure of Merit is calculated as $S_{an}\sqrt{N}$ where N is the counts in one pair if there were no new physics. S157 refers to "Symmetric 157.5°", A157+ refers to "Asymmetric 157.5° when $\hat{\mathbf{k}}_1$ is in the outer ring", and A157- refers to $\hat{\mathbf{k}}_1$ in the middle ring. All plotted configurations have a partner configuration with the same analyzing power using the lower ring instead of the upper ring, doubling the statistics.

The absolute values of the analyzing power and Figure of Merit for all configurations is given Figure 9.8. The analyzing power is calculated using the last factor in Equation 9.22. This is using the "phase space triangle" cuts, which as discussed are not optimal. The contributions for the Asymmetric 112.5° are artificially set to zero for this plot because the value is so low that this simulation did not have high enough statistics to get an accurate estimate. This Figure of Merit is calculated as if we perform a simple asymmetry measurement. It scales the analyzing power by $\sqrt{2N}$ where N is the counts in one pair if there were no new physics. These numbers are for all 16 azimuthally related configurations summed for 1 billion ortho-positronium decays. Equivalently this corresponds to the counts for one configuration for 16 billion ortho-positronium decays.

9.5.4 Statistical sensitivity estimate

We intend to use a source with an activity of 1.85 MBq, estimating that at least 50% of these β's will reach the powder, we can expect around 40% of those will form positronium. As proposed

in this chapter we allow the pseudo-triplet to decay so we are only recording 1/2 of the positronium populations. For a lifetime of 135 ns 95% of the ortho-positronium decay to 3-γ, and if the initial time cut will be at 20 ns (to allow all pseudo-triplet to decay with a high B-field value), then 86% of the $m = \pm 1$ positronium will decay in the time window. This gets a rate of good $m = \pm 1$ positronium decays of 150 thousand per second.

The expected counts in each configuration is $N_a = RT(\mathcal{A}^{\Omega} + s_{zz}\mathcal{D}^{\Omega})$, where $R = 150 \times 10^3 (1/s)$ and T is the time (35 days). We can then estimate our uncertainty on the asymmetry as $\delta A_a = 1/\sqrt{2N_a}$. The expected sensitivities for each configuration is quoted in Table 9.3, with the sensitivity including the 32 sets of configurations with identical sensitivities.

configuration	hit order	$\mathcal{A}^{\Omega} + s_{zz}\mathcal{D}^{\Omega}$	S_{an}	N_a	$\sigma_{\mathrm{Re}(\delta_1)}$
Sym 157.5°	(0,2)	2.39×10^{-3}	-1.14×10^{-4}	1.08×10^{9}	0.19
Sym 135°	(0,2)	1.08×10^{-3}	-7.72×10^{-5}	4.89×10^{8}	0.41
Sym 112.5°	(0,2)	1.85×10^{-4}	-3.26×10^{-5}	8.39×10^{7}	2.37
Asym 157.5°	(0,1)	1.51×10^{-3}	5.61×10^{-6}	6.85×10^{8}	4.82
Asym 135°	(0,1)	4.04×10^{-4}	6.50×10^{-6}	1.83×10^{8}	8.03
Asym 157.5°	(1,0)	1.44×10^{-3}	-5.14×10^{-5}	6.51×10^{8}	0.54
Asym 135°	(1,0)	3.94×10^{-4}	-4.54×10^{-5}	1.79×10^{6}	1.34
Combined	–	–	–	–	0.10

Table 9.3 Estimated analyzing power and number of events for each detector configuration. Finally translated into an expected optimal statistical sensitivity for the model of $C\mathcal{P}$-violating state mixing.

All combined configurations can reach a sensitivity of 0.1 for the $C\mathcal{P}$-violating mixing between the positronium states. In the end the sensitivity for this model is dominated by the factor of $1/775$ that arises from the atomic physics of positronium. This is discussed in Appendix B.

At this point it is worth emphasizing that all of the values in Table 9.2 are purely determined by the geometry, energy cuts, stopping positions, and the model used for the new physics. The effect of positronium state populations (and therefore alignment) and the branching ratios of 2-γ and 3-γ decays enter in as weightings when these quantities are summed together to get the final coincidence counts for a given configuration. The relative weights due to state populations and 2-γ branching ratios are intrinsically related, and determined by the B-field and our time cuts. All time dependence is carried by the positronium state populations and therefore only the relative

weighting of these terms will change in time, but not the intrinsic geometry or time dependence of each term.

CHAPTER 10

TIME DEPENDENCE IN A MAGNETIC FIELD

The time dynamics of the symmetry violating signal was treated inconsistently between the previous two experiments [38, 39]. This signal requires tensor polarization for the positronium being studied. However, the signal is not proportional to the instantaneous tensor polarization. In Ref. [19], the authors showed that the tensor anisotropies in 3-γ decay of ortho-positronium have the same dependence on the state population, for both the QED anisotropies, and possible $\mathcal{CP}$-violating anisotropies. The early precision tests of QED in Refs. [35, 36] measured the QED induced anisotropy and observed a net anisotropy in the distribution of final state photons. The searches for the QED anisotropy and the $\mathcal{CP}$-violating distribution started with unpolarized positronium in a magnetic field. If the angular anisotropy is proportional to the instantaneous tensor polarization then both experiments would see a net isotropic distribution, since the positronium starts evenly populated and eventually all the states decay. This conflict arises from invoking rotational invariance to calculate the time dependence of the angular anisotropies. The addition of an external magnetic field has broken rotational invariance in these experiments.

In this chapter we extend the theoretical analysis to include the non-trivial time dynamics induced by the magnetic field. This gives the time dependence of the signal and background contributions for an initially unpolarized positronium atom in a static magnetic field along the z-axis in terms of the magnitude of the field, and the initial and final time of the integration window.

This introduces changing contributions from the signal and increasing 2-γ dilution. As the analysis of Chapter 9 is directly applicable to a system with the triplet decays isolated from the pseudo-triplet, it is first worth identifying shortcomings in performing the measurement this way, and how including the pseudo-triplet events gives us further handles on systematics. This chapter concludes with a discussion of a few systematics related to the magnetic field, namely the 2-γ dilution, and the effect of a field misalignment.

10.1 Detector efficiencies inducing false asymmetries

The planned analysis will require measuring coincident events with two pairs of detectors. Calculating the sensitivity to a specific model required including the acceptances and efficiencies of the detectors. This was done by introducting the "characteristic function" for the setup as $\chi(\mathbf{k}_1, \mathbf{k}_2, \mathbf{k}_3)$. This function carries the geometric acceptances and detection efficiencies. We assumed perfect detectors, but in reality each detector α will have some energy dependent intrinsic efficiency $\epsilon_\alpha(\omega)$. Worse yet there can be correlated efficiencies for the pair of detectors $\epsilon_{\alpha\beta}(\omega_\alpha, \omega_\beta)$. Update the definition of the characteristic function to,

$$\chi_a(\mathbf{k}_1, \mathbf{k}_2, \mathbf{k}_3) = \begin{cases} \epsilon_{\alpha\beta}(\omega_1, \omega_2), & \hat{\mathbf{k}}_1 \in \Omega_1, \hat{\mathbf{k}}_2 \in \Omega_2 \\ 0, & \text{o/w} \end{cases} \tag{10.1}$$

This gives an updated estimate of coincidences,

$$\begin{aligned} N_\Omega = \int \mathrm{d}f_\Omega^{3\gamma} \epsilon_{\alpha\beta}(\omega_1, \omega_2) a(\omega_1, \omega_2) + s_{zz} \int \mathrm{d}f_\Omega^{3\gamma} \epsilon_{\alpha\beta}(\omega_1, \omega_2) D(\mathbf{k}_1, \mathbf{k}_2, \mathbf{k}_3) \\ + s_{zz} \int \mathrm{d}f_\Omega^{3\gamma} \epsilon_{\alpha\beta}(\omega_1, \omega_2) C(\mathbf{k}_1, \mathbf{k}_2, \mathbf{k}_3) \end{aligned} \tag{10.2}$$

we now make some simplifying assumptions about the detector efficiencies. Assume they are smooth functions of energy multiplied by some intrinsic efficiency, further take the energy dependence to be flat $\epsilon_{\alpha\beta} \approx \bar{\epsilon}_{\alpha\beta}$. For two configurations (with the same high energy detector) this gives the following coincidence counts,

$$N_{\alpha\beta} = \bar{\epsilon}_{\alpha\beta}(\mathcal{A}^\Omega + s_{zz}\mathcal{D}^\Omega + s_{zz}C^\Omega) \tag{10.3}$$

$$N_{\alpha\beta'} = \bar{\epsilon}_{\alpha\beta'}(\mathcal{A}^\Omega + s_{zz}\mathcal{D}^\Omega - s_{zz}C^\Omega) \tag{10.4}$$

The isotropic counts no longer cancel in an asymmetry and therefore the $\mathcal{CP}$-violating signal is not cleanly isolated. Changing the sign of s_{zz} would allow the measurement of two asymmetries, one between detector pairs, and one between the differing values of s_{zz}. This would facilitate canceling the leading effect of the multiplicative efficiencies.

We will demonstrate in this chapter that the contribution from the $\mathcal{CP}$-violating form factor does not change sign between two time windows. It does have a time dependence that is induced by

the B-field. This will give a handle on the signal to change its magnitude (by varying the magnetic field or changing time windows) to separate it from the isotropic distribution while still using the same detectors with the same intrinsic efficiencies.

We treat this problem in an overly formal manner for the purposes of this chapter. In Appendix A we extend the calculation to derive the full time dependence of all angular distributions (including possible new physics form factors) for a positronium atom formed with a polarized β^+ hitting unpolarized electrons. Such dynamics have been studied in Refs. [84, 85, 86, 87], but to our knowledge this is the first calculation to include possible symmetry violating beyond Standard Model factors.

10.2 Decaying systems

Introducing a few formal terms and ideas that will make the discussion easier. For this entire chapter there is no implied summation on repeated indices. The dynamics of a decaying system can be approximating using a non-hermitian Hamiltonian,

$$H = M + \frac{i}{2}\Gamma \tag{10.5}$$

where M is the "mass matrix", and Γ as the absorptive part of the Hamiltonian (reserving the term "decay matrix" to refer to the quantity $R_{ij}(\mathbf{k}_1, \mathbf{k}_2, \mathbf{k}_3)$ defined in Ref. [19]). The eigenvectors have definite energies and lifetimes,

$$|\psi_\alpha, t\rangle = e^{-it\omega_\alpha - \frac{1}{2}t\Gamma_\alpha} |\psi_\alpha, t = 0\rangle \tag{10.6}$$

where $\omega_\alpha + \frac{i}{2}\Gamma_\alpha$ is the αth eigenvalue of H.

The elements of the absorptive part of the Hamiltonian are $\Gamma_{ij} = \sum_f \langle f|\mathscr{T}|i\rangle^* \langle f|\mathscr{T}|j\rangle = \sum_f \Gamma^f_{ij}$, where Γ^f_{ij} corresponds to the partial decay to the final state f. This gives a density matrix with time evolution,

$$\rho(t) = \sum_{\alpha\beta} e^{-it(\omega_\alpha - \omega_\beta) - \frac{1}{2}t(\Gamma_\alpha + \Gamma_\beta)} \rho_{\alpha\beta}(t = 0) |\psi_\alpha\rangle \langle\psi_\beta| \tag{10.7}$$

for the states ψ_α that are eigenvectors of the Hamiltonian. This gives the instantaneous rate of population of a given final state,

$$\dot{N}^f(t) = -\mathrm{Tr}(\Gamma^f \rho(t)) \tag{10.8}$$

10.3 Combined spin-0 and spin-1 Hilbert Space

The magnetic field induces a mixing between spin-0 and spin-1 positronium, and therefore the time dynamics should be treated in the combined Hilbert space. Indeed this is the usual starting point when considering the individual spins $\{|\uparrow\uparrow\rangle, |\downarrow\uparrow\rangle, |\uparrow\downarrow\rangle |\downarrow\downarrow\rangle\}$, then the combinations with definite J^2 are identified and considerations are restricted to those subspaces. In the absence of a magnetic field the Hamiltonian takes the simple form,

$$H_{B=0} = \left(\omega_{p-Ps} + \frac{i}{2}\Gamma_{p-Ps}\right) 1_{4x4} + \left(\delta E + \frac{i}{2}\delta\Gamma\right) J^2 \tag{10.9}$$

This differs from the standard case of a magnetic dipole interaction with an external field. Two components of angular momentum (those that are not parallel to the field) no longer commute with the Hamiltonian and are therefore no longer conserved. The standard magnetic dipole interaction goes as $\hat{\mathbf{J}} \cdot \mathbf{B}$, and still conserves the magnitude of angular momentum J^2, since $[J^2, \hat{J}_i] = 0$. This is not true for the positronium interaction with an external field. This interaction takes the form of $\mu(\hat{\mathbf{J}}_e - \hat{\mathbf{J}}_{\bar{e}}) \cdot \mathbf{B}$. It is not dependent on a component of angular momentum $\hat{\mathbf{J}}_e + \hat{\mathbf{J}}_{\bar{e}}$, but instead on the difference of the two particles angular momenta. This difference does not commute with J^2, and as such the dynamics of the system is not confined to a subspace of the Hilbert space with definite J^2. This is equivalent to saying that the para-positronium and ortho-positronium states mix despite having different angular momenta, and that the mixed states can decay to 2-γ or 3-γ despite those having $J = 0$ and $J = 1$ respectively.

The addition of an external magnetic field induces off-diagonal terms in M. Representing the states in the pseudo-singlet and pseudo-triplet basis diagonalizes the mass matrix specifically. Writing this out explicitly gives,

$$M = \begin{pmatrix} \omega_{p-Ps} & 0 & 0 & -\mu_z B_z \\ 0 & \omega_{o-Ps} & 0 & 0 \\ 0 & 0 & \omega_{o-Ps} & 0 \\ -\mu_z B_z & 0 & 0 & \omega_{o-Ps} \end{pmatrix} \tag{10.10}$$

$$\Gamma = \begin{pmatrix} \Gamma_{p-Ps} & 0 & 0 & 0 \\ 0 & \Gamma_{o-Ps} & 0 & 0 \\ 0 & 0 & \Gamma_{o-Ps} & 0 \\ 0 & 0 & 0 & \Gamma_{o-Ps} \end{pmatrix} \tag{10.11}$$

For S-wave positronium take $\mu_z \approx \mu_e s_z^e - \mu_{\bar{e}} s_z^e = \mu_e (s_z^e - s_z^{\bar{e}})$, where μ_e is the magnetic moment of the electron. This ignores any structure effects that renormalize the electron magnetic moment in positronium. These two matrices do not commute. This means representing the time evolution in the pseudo-singlet and pseudo-triplet basis gives off-diagonal elements to the absorptive part of the Hamiltonian.

Following the discussion in Chapter 2, the absorptive part of the Hamiltonian Γ_{ij} is the sum of the partial decay rates. The partial decay rate for ortho-positronium to a given 3-γ state (summing over photon polarizations) is given as,

$$\Gamma_{ij}(\mathbf{k}_1, \mathbf{k}_2, \mathbf{k}_3) = \Gamma_{o-Ps} R_{ij}(\mathbf{k}_1, \mathbf{k}_2, \mathbf{k}_3) \tag{10.12}$$

where R_{ij} is the decay matrix as defined in Ref. [19]. This matrix carries the form factors a, c_1, c_2, etc. Representing this matrix acting on the combined spin-0/spin-1 Hilbert space in the pseudo-singlet/pseudo-triplet basis makes the decay matrix have many complicated entries. It is easier for this purpose to stay in the spin-0 and spin-1 basis in which $\Gamma_{ij}(\mathbf{k}_1, \mathbf{k}_2, \mathbf{k}_3)$ is simple, and calculate the time dependence of $\rho(t)$ in this basis.

The non-hermitian hamiltonian method (the Wigner-Weisskopf method) is an approximation but it is well founded in this case as the binding energy released in the decay is small compared to the mass [88]. The use of pseudo-singlet and pseudo-triplet states is also an approximation as they do not diagonalize $H = M + (i/2)\Gamma$, but only M. This means all effects of level broadening are ignored [89, 88]. This effect is unimportant for the current calculation as it mostly results in energy level shifts. There is a very small correction to the mixing coefficients that turns them slightly imaginary and would result in a small correction to the density matrix terms. One further approximation is that the magnetic field only affects the states but does not affect the matrix elements for the decay.

This is a safe estimation for this current calculation purposes, but may not be a small effect for para-positronium to 3-γ. This is unimportant for our discussion but is discussed in Ref. [88].

Generically the density matrix will have time dependent entries,

$$\rho(t) = \begin{pmatrix} \rho_{00}(t) & \rho_{0x}(t) & \rho_{0y}(t) & \rho_{0z}(t) \\ \rho^*_{0x}(t) & \rho_{xx}(t) & \rho_{xy}(t) & \rho_{xz}(t) \\ \rho^*_{0y}(t) & \rho^*_{xy}(t) & \rho_{yy}(t) & \rho_{yz}(t) \\ \rho^*_{0z}(t) & \rho^*_{xz}(t) & \rho^*_{yz}(t) & \rho_{zz}(t) \end{pmatrix} \tag{10.13}$$

however, the partial decay matrices to 2-γ and 3-γ final states remain simple,

$$\Gamma_{2\gamma} = \Gamma_{p-Ps} \begin{pmatrix} 1 & 0 & 0 & 0 \\ 0 & 0 & 0 & 0 \\ 0 & 0 & 0 & 0 \\ 0 & 0 & 0 & 0 \end{pmatrix} \tag{10.14}$$

$$\Gamma_{3\gamma}(\mathbf{k}_1, \mathbf{k}_2, \mathbf{k}_3; t) = \Gamma_{o-Ps} \begin{pmatrix} 0 & 0 & 0 & 0 \\ 0 & R_{xx} & R_{xy} & R_{xz} \\ 0 & R^*_{xy} & R_{yy} & R_{yz} \\ 0 & R^*_{xz} & R^*_{yz} & R_{zz} \end{pmatrix} \tag{10.15}$$

giving the time dependence of the 2-γ events, and the 3-γ events including the full angular distribution as,

$$\dot{N}_{2\gamma}(t) = \Gamma_{p-Ps}\rho_{00}(t) \tag{10.16}$$

$$\begin{aligned} \dot{N}_{3\gamma}(\mathbf{k}_1, \mathbf{k}_2, \mathbf{k}_3; t) = \Gamma_{o-Ps}\Big\{ & R_{xx}\rho_{xx}(t) + 2\mathrm{Re}(R_{xy}\rho^*_{xy}(t)) + 2\mathrm{Re}(R_{xz}\rho^*_{xz}(t)) \\ & + R_{yy}\rho_{yy}(t) + 2\mathrm{Re}(R_{yz}\rho^*_{yz}(t)) + R_{zz}\rho_{zz}(t) \Big\} \end{aligned} \tag{10.17}$$

This has simplified the problem down to calculating $\rho_{00}(t)$ and $\rho_{ij}(t)$ in terms of the states with simple time evolution (pseudo-singlet and pseudo-triplet). These two bases are related by the

matrix,

$$\begin{pmatrix} \psi_{pS,m=0} \\ \psi_{S=1,x} \\ \psi_{S=1,y} \\ \psi_{pT,m=0} \end{pmatrix} = \begin{pmatrix} c & 0 & 0 & -s \\ 0 & 1 & 0 & 0 \\ 0 & 0 & 1 & 0 \\ s & 0 & 0 & c \end{pmatrix} \begin{pmatrix} \psi_{S=0,m=0} \\ \psi_{S=1,x} \\ \psi_{S=1,y} \\ \psi_{S=1,z} \end{pmatrix} \tag{10.18}$$

where $c = \cos(\zeta) = \frac{1}{\sqrt{2}}\sqrt{1 + \frac{1}{\sqrt{1+x^2}}}$ and $s = \sin(\zeta) = \sqrt{1-c^2}$ and $x = |B|/(3.63\text{ Tesla})$ [45]. This calculation is extended in Appendix A to include an arbitrary net positron polarization and identify the full time dependence for comparison to related experiments on the "pulsing" angular distribution in positronium decay measured in Refs. [85, 86, 87]. The final experiment will have two powder containers, each of which will have a net vector polarization due to parity violation in nuclear β-decay. For this work the polarizations are treated to be exactly opposite in sign and therefore cancel.

10.4 Time evolution for unpolarized positronium

Starting with an even state population the density matrix in the pseudo-singlet/pseudo-triplet at time t is very simple,

$$\rho_{pS,pT}(t) = \begin{pmatrix} \frac{1}{4}e^{-t\Gamma_{pS}} & 0 & 0 & 0 \\ 0 & \frac{1}{4}e^{-t\Gamma_{o-Ps}} & 0 & 0 \\ 0 & 0 & \frac{1}{4}e^{-t\Gamma_{o-Ps}} & 0 \\ 0 & 0 & 0 & \frac{1}{4}e^{-t\Gamma_{pT}} \end{pmatrix} \tag{10.19}$$

where Γ_{pS} is the pseudo-singlet lifetime, Γ_{pT} is the pseudo-triplet lifetime, and Γ_{o-Ps} is the triplet lifetime, here taken to be in vacuum. The state represented in the definite angular momentum basis has a more complicated structure. The full time dependence is quoted below,

$$\rho_{S=0,S=1}(t) = \begin{pmatrix} \rho_{00}(t) & 0 & 0 & \rho_{0z}(t) \\ 0 & \rho_{xx}(t) & 0 & 0 \\ 0 & 0 & \rho_{yy}(t) & 0 \\ \rho^*_{0z}(t) & 0 & 0 & \rho_{zz}(t) \end{pmatrix} \tag{10.20}$$

$$\rho_{00}(t) = \frac{1}{4}\left(c^2 e^{-t\Gamma_{pS}} + s^2 e^{-t\Gamma_{pT}}\right) \tag{10.21}$$

$$\rho_{0z}(t) = \frac{1}{4}cs\left(e^{-t\Gamma_{pS}} + e^{-t\Gamma_{pT}}\right) \tag{10.22}$$

$$\rho_{xx}(t) = \rho_{yy}(t) = \frac{1}{4}e^{-t\Gamma_{pT}} \tag{10.23}$$

$$\rho_{zz}(t) = \frac{1}{4}\left(s^2 e^{-t\Gamma_{pS}} + c^2 e^{-t\Gamma_{pT}}\right) \tag{10.24}$$

Restricting to times greater than 1 ns means all pseudo-singlet contributions can be neglected. This gives an instantaneous rate of 2-γ events, and also 3-γ events with angular distribution $(\mathbf{k}_1, \mathbf{k}_2, \mathbf{k}_3)$,

$$\dot{N}_{2\gamma}(t) = \frac{1}{4}\Gamma_{p-Ps}\left(s^2 N_{pT} e^{-t\Gamma_{pT}}\right) \tag{10.25}$$

$$\begin{aligned}\dot{N}_{3\gamma}(\mathbf{k}_1, \mathbf{k}_2, \mathbf{k}_3; t) = &\frac{1}{4}\Gamma_{p-Ps}\left(R_{xx}(\mathbf{k}_1, \mathbf{k}_2, \mathbf{k}_3) + R_{yy}(\mathbf{k}_1, \mathbf{k}_2, \mathbf{k}_3)\right)e^{-t\Gamma_{o-Ps}} \\ &+ \frac{1}{4}\Gamma_{o-Ps}R_{zz}(\mathbf{k}_1, \mathbf{k}_2, \mathbf{k}_3)(c^2 e^{-t\Gamma_{pT}})\end{aligned} \tag{10.26}$$

The branching ratio and quenched lifetimes are directly related by $c^2\Gamma_{o-Ps} = BR_{3\gamma}^{pT}\Gamma_{pT}$, and following Chapter 9, $R_{ii} = a(\omega_1, \omega_2) + C_{ii}$ and $C_{xx} + C_{yy} + C_{zz} = 0$. This simplifies Equation 10.26 to,

$$\begin{aligned}\dot{N}_{3\gamma}(\mathbf{k}_1, \mathbf{k}_2, \mathbf{k}_3; t) = \Big\{&a(\omega_1, \omega_2)\left(2\Gamma_{o-Ps}e^{-t\Gamma_{o-Ps}} + BR_{3\gamma}^{pT}\Gamma_{pT}e^{-t\Gamma_{pT}}\right) \\ &+C_{zz}(\mathbf{k}_1, \mathbf{k}_2, \mathbf{k}_3)\left(2\Gamma_{o-Ps}e^{-t\Gamma_{o-Ps}} - 2BR_{3\gamma}^{pT}\Gamma_{pT}e^{-t\Gamma_{pT}}\right)\Big\}\end{aligned} \tag{10.27}$$

Integrating this in a finite time window reproduces the quantity in Equation2.39, but now correctly including the effects of mixing/different branching ratios. This means that the contribution from the pseudo-triplet to the angular distortion is reduced by the relevant branching ratio. Both the QED anisotropy and the $C\mathcal{P}$-violating tensor form factors are contained in $C_{zz}(\mathbf{k}_1, \mathbf{k}_2, \mathbf{k}_3)$. The negative contribution from the pseudo-triplet is smaller than the positive contribution from the triplet decays at all times. There is not just a net anisotropy (as measured in Ref. [36]), but the distortion term never changes sign between time windows.

10.5 Including pseudo-triplet events

Returning to the analysis from Chapter 9, consider the detector configuration with solid angles $(\Omega_1, \Omega_2) = \Omega$. The coincidence events are recorded within a time window $\Delta T = [t_i, t_f]$. This gives the coincident counts for this detector pair in this time window,

$$N_{\Omega}^{\Delta T} = \int_{t_i}^{t_f} \mathrm{d}t \int \mathrm{d}f_{\Omega}^{3\gamma} \dot{N}_{3\gamma}(\mathbf{k}_1, \mathbf{k}_2, \mathbf{k}_3; t) \tag{10.28}$$

Following the analysis in Chapter 9, consider a second detector configuration Ω' such that the symmetry violating term changes sign. The symmetry violating term can be extracted by forming an asymmetry in counts,

$$A_{\Omega}^{\Delta T} = \frac{N_{\Omega}^{\Delta T} - N_{\Omega'}^{\Delta T}}{N_{\Omega}^{\Delta T} + N_{\Omega'}^{\Delta T}} \tag{10.29}$$

$$A_{\Omega}^{\Delta T} = \frac{\eta C^{\Omega}}{\mathcal{A}^{\Omega} + \eta \mathcal{D}^{\Omega}} \tag{10.30}$$

this matches Equation 9.19 with the replacement of s_{zz} with the term η which depends on the field strength and the time window. This term goes as,

$$\eta_{B,t_i,t_f} = \frac{2e^{-t\Gamma_{o-Ps}}\big|_{t_f}^{t_i} - 2BR_{3\gamma}^{pT} e^{-t\Gamma_{pT}}\big|_{t_f}^{t_i}}{2e^{-t\Gamma_{o-Ps}}\big|_{t_f}^{t_i} + BR_{3\gamma}^{pT} e^{-t\Gamma_{pT}}\big|_{t_f}^{t_i}} \tag{10.31}$$

This factor is reminiscent of the calculation of the "averaged tensor polarization" in Equation 2.39, but now it includes the effect of the 2-γ branching ratio. The time dependence of the asymmetry is shown in Figure 10.1, for fields ranging from 0 T to 0.5 T. This is plotted for the Symmetric 157.5° configuration assuming that C^{Ω} is proportional to the phase space selected. Any model would result in a rescaling of this plot vertically.

This is in disagreement with the claim from the Michigan experiment that the signal is proportional to the alignment and changes sign between time windows [38]. The quantity η that linearly scales the signal matches the method that the Tokyo group used to calculate the tensor polarization when extracting their sensitivity in Ref. [39]. We do not agree with calling this quantity a "tensor polarization" or an "alignment", as those are intrinsic quantities to the positronium state that quantify its state populations, and are defined irrespective of any decay channel.

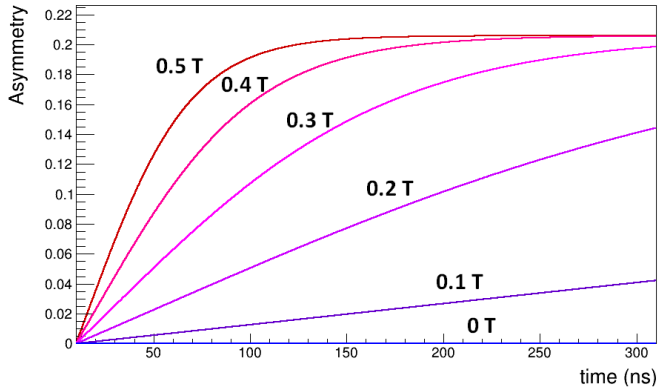

Figure 10.1 The time dependence of an asymmetry in counts in the presence of new physics. This plots Equation 10.30 for the Symmetric 157.5° configuration assuming the new physics is proportional to the volume of phase space selected. The magnetic field strength varies from 0 T (red) to 0.5 T (green) and the width of the integration window is taken as 1 ns.

10.6 Energy cuts and 2-γ dilution

The 2-γ decays that survive the energy cuts have no signal sensitivity and therefore reduce the final sensitivity. The 3-γ decays and 2-γ decays have distinct energy distributions, but due to finite energy resolution some of the 2-γ events will leak the energy cuts. Estimating the reduction to sensitivity requires estimating the spreading of the positronium, the acceptance of 2-γ events, the finite energy resolution, and the relative weighting of 2-γ to 3-γ events. The 2-γ decays occur because quenching of the lifetime from the magnet. This induces a time dependence for the weighting of 2-γ to 3-γ events. Equation 10.30 can be extended to include the 2-γ dilution,

$$A_a = \frac{\eta C^{\Omega}}{\mathcal{A}^{\Omega} + \eta \mathcal{D}^{\Omega} + \xi \mathcal{F}^{\Omega}} \tag{10.32}$$

where $\mathcal{F}^{\Omega}$ is the proportion of 2-γ events that survive the phase space cuts, and ξ is the relative weighting of 2-γ decays to 3-γ decays. This gives,

$$\xi_{B,t_i,t_f} = \frac{BR_{2\gamma}^{pT} e^{-\Gamma_{pT} t}\big|_{t_f}^{t_i}}{2e^{-\Gamma_{o-Ps} t}\big|_{t_f}^{t_i} + BR_{3\gamma}^{pT} e^{-\Gamma_{pT} t}\big|_{t_f}^{t_i}} \tag{10.33}$$

This quantity never becomes large due to a magnetic field. At most if all pseudo-triplet decays to 2-γ then $\eta \to \frac{1}{2}$. This definition does not include the 2-γ decays induced by interaction with the powder.

The 2-γ dilution will be largest for the Symmetric 157.5° configuration. In principle the other configurations will have a small amount as well, but the 3-γ distribution for those detector pairs

does not extend up towards the 511-511 keV region and can be more cleanly separated from the 2-γ events. Given that this model of $\mathcal{CP}$-violation is peaked going to high energies, the Symmetric 157.5° configuration warrants special attention. A cut on the summed energies can be added to separate the region that is primarily 2-γ events from the region that is primarily 3-γ events. The values of $\mathcal{A}^{\Omega}$, $\mathcal{D}^{\Omega}$, $\mathcal{C}^{\Omega}$, and $\mathcal{F}^{\Omega}$ will all shift as the energy cut is varied. Figure 10.2 shows the isotropic distribution, the QED anisotropy, the $\mathcal{CP}$-violating signal, and the 2-γ events for the Symmetric 157.5° configuration using events sampled from the stopping distribution for Design (C) with a ^{22}Na source. The value of these functions for each summed energy cut is given in Table 10.1 for a ^{22}Na source, and Table 10.2 for a ^{68}Ga source.

E_{sum} cut (MeV)	$\mathcal{A}^{\Omega}$	$\mathcal{D}^{\Omega}$	$\bar{\mathcal{C}}^{\Omega}_{mix}$	$\mathcal{F}^{\Omega}$
1.022	$2.14 * 10^{-3}$	$-7.27 * 10^{-4}$	$-6.77 * 10^{-7}$	$3.74 * 10^{-7}$
1.000	$2.14 * 10^{-3}$	$-7.26 * 10^{-4}$	$-6.76 * 10^{-7}$	$3.34 * 10^{-7}$
0.975	$2.12 * 10^{-3}$	$-7.22 * 10^{-4}$	$-6.69 * 10^{-7}$	$2.33 * 10^{-7}$
0.950	$2.07 * 10^{-3}$	$-7.05 * 10^{-4}$	$-6.44 * 10^{-7}$	$1.33 * 10^{-7}$
0.925	$1.97 * 10^{-3}$	$-6.71 * 10^{-4}$	$-5.96 * 10^{-7}$	$8.75 * 10^{-8}$
0.900	$1.78 * 10^{-3}$	$-6.08 * 10^{-4}$	$-5.17 * 10^{-7}$	$7.13 * 10^{-8}$

Table 10.1 The variation of each function as the summed energy cut is changed for the symmetric 157.5° configuration. Increasing the cut dramatically increases the amount of 2-γ events. These are for the ^{22}Na source using the Design (C) start detector and powder.

E_{sum} cut (MeV)	$\mathcal{A}^{\Omega}$	$\mathcal{D}^{\Omega}$	$\bar{\mathcal{C}}^{\Omega}_{mix}$	$\mathcal{F}^{\Omega}_{^{68}Ga}$
1.022	$2.09 * 10^{-3}$	$-5.82 * 10^{-4}$	$-5.96 * 10^{-7}$	$1.31 * 10^{-6}$
1.000	$2.09 * 10^{-3}$	$-5.82 * 10^{-4}$	$-5.95 * 10^{-7}$	$1.16 * 10^{-6}$
0.975	$2.07 * 10^{-3}$	$-5.79 * 10^{-4}$	$-5.89 * 10^{-7}$	$7.61 * 10^{-7}$
0.950	$2.03 * 10^{-3}$	$-5.67 * 10^{-4}$	$-5.68 * 10^{-7}$	$4.39 * 10^{-7}$
0.925	$1.93 * 10^{-3}$	$-5.43 * 10^{-4}$	$-5.27 * 10^{-7}$	$2.95 * 10^{-7}$
0.900	$1.76 * 10^{-3}$	$-5.00 * 10^{-4}$	$-4.61 * 10^{-7}$	$2.40 * 10^{-7}$

Table 10.2 The variation of each function as the summed energy cut is changed for the symmetric 157.5° configuration. Increasing the cut dramatically increases the amount of 2-γ events. These are for the ^{68}Ga source using the Design (C) start detector and powder.

These energy cuts are not tuned, for instance there is large overlap with the Compton continuum along the 511-keV line. This simulation does not include any inactive material, but the final experiment will have a supporting structure and an inner module that 511 keV photons will scatter

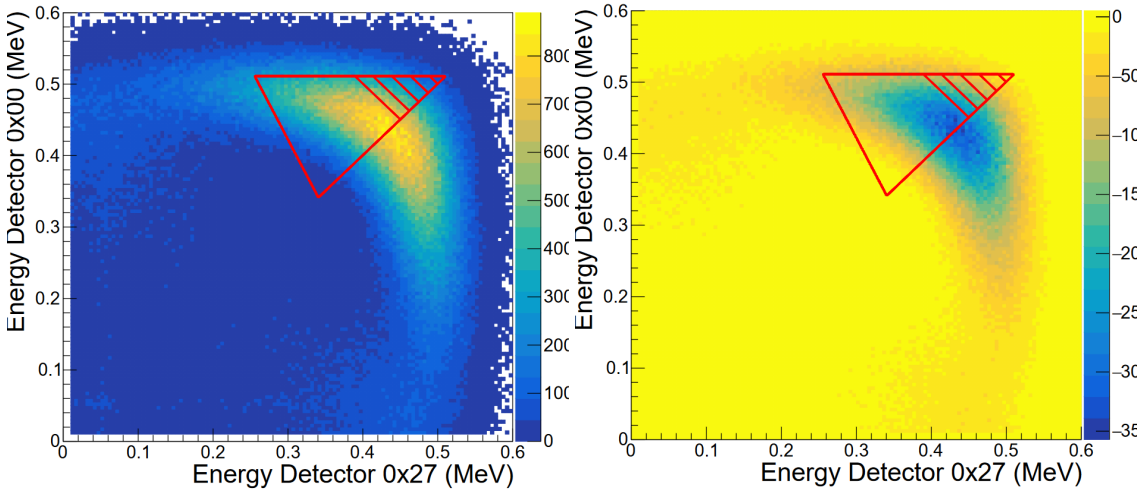

(a) Isotropic distribution

(b) QED anisotropy

(c) $\mathcal{CP}$-violating signal

(d) 2-γ events

Figure 10.2 The effect of varying the summed energy cut for the symmetric 157.5° configuration. All four functions have different energy dependence's, and must be considered when we decide on the optimal energy cuts.

off of. This will generally make $\mathcal{F}^{\Omega}$ larger, and impede efforts to lower the energy cuts to the regions that select $(\hat{\mathbf{k}}_2, \hat{\mathbf{k}}_3)$. Tables 10.1 and 10.2 show that $\mathcal{F}^{\Omega}$ is very small compared to $\mathcal{A}^{\Omega}$. Since ξ never becomes large the 2-γ distortion is a small shift to the backgrounds, substantially smaller than the QED anisotropy distortion to counts. Proceeding from here we ignore the 2-γ dilution as it is a small effect for all time cuts (so long as they are sufficiently far from the peak).

10.7 Intrinsic detection efficiency

Returning to the discussion of finite detection efficiency, the asymmetry takes the following form (to first order in C^{Ω}),

$$A_a = \frac{\eta C^{\Omega}}{\mathcal{A}^{\Omega} + \eta \mathcal{D}^{\Omega}} + \frac{\epsilon_{\alpha\beta} - \epsilon_{\alpha\beta'}}{\epsilon_{\alpha\beta} + \epsilon_{\alpha\beta'}} \tag{10.34}$$

the quantity η is dependent on the value of the B-field and our time cuts. This means it is a tuneable parameter that can separate out the signal from systematics. In this case the efficiencies giving an asymmetry value when the field is not applied (and therefore when there is no $\mathcal{CP}$-violating signal). This is a large benefit of using an electromagnet. Compare with the previous experiments in Refs. [38, 39], we will be able to vary the magnetic field value without physically moving any components of the experiment, which could change the scattering characteristics for the setup.

Figure 10.3 shows the asymmetry as a function of time, assuming a signal on the scale estimate in Chapter 7, and including a 1% difference in efficiency between the two detectors. The new physics manifests as a time dependent shift to the asymmetry that is distinct from the constant offset of mismatched detector efficiencies.

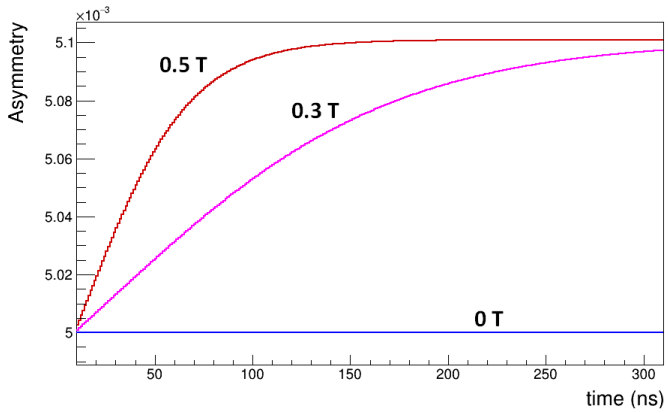

Figure 10.3 Estimation of the time dependent asymmetry induced in the 157.5° configuration assuming a 1% difference in detection efficiency and new physics at the scale of sensitivity estimated in Chapter 9. This uses 1 ns time windows.

10.7.1 All form factors that contribute to an asymmetry

The final systematic we will address in this work is the count asymmetry induced by a misaligned detector array. For the purposes of this discussion it is easier to fix the coordinates to the detector

array, and consider a misalignment of the field axis. Take the detector pairs shown in Figure 9.1. The highest energy photon is fixed to lie in the x-z plane, and there are two detectors for the second highest energy photon that differ by changing the sign of κ_y. This also changes the sign of n_x and n_z. The following expectation values change sign between our detector pairs (terms with two indices should be interpreted as components of symmetric traceless tensors),

1. Vector terms – $\langle \kappa_{2y} \rangle$, $\langle n_x \rangle$, $\langle n_z \rangle$
2. $\mathcal{CP}$ conserving tensor terms – $\langle \kappa_{1x}\kappa_{2y} \rangle$, $\langle \kappa_{1z}\kappa_{2y} \rangle$, $\langle \kappa_{2x}\kappa_{2y} \rangle$, $\langle \kappa_{2z}\kappa_{2y} \rangle$, $\langle n_x n_y \rangle$, $\langle n_y n_z \rangle$
3. $\mathcal{CP}$ violating tensor terms – $\langle \kappa_{1z} n_z \rangle$, $\langle \kappa_{2z} n_z \rangle$, $\langle \kappa_{1x} n_x \rangle$, $\langle \kappa_{1x} n_z \rangle$, $\langle \kappa_{1z} n_x \rangle$, $\langle \kappa_{2x} n_x \rangle$, $\langle \kappa_{2x} n_z \rangle$, $\langle \kappa_{2z} n_x \rangle$, $\langle \kappa_{2y} n_y \rangle$

Any term with one index could be induced by a vector polarization in that direction, and any term with two indices could be induced by a field misalignment along those axes. This relationship is summarized in Table 9.1. Of the 18 correlations that could contribute to an asymmetry in counts between the detector pairs, 10 of them correspond to new physics. The first vector term corresponds to $\mathcal{CP}$-violation, the second two to new physics (though not necessarily new physics that violates any discrete symmetries). The last 9 tensor correlations that involve combinations of one photon momentum and the normal to the decay plane are the signal we will search for. We have optimized the geometry to be most sensitive to the zz terms.

The primary concern is the 6 tensor terms in the second line. These are all induced in QED, and appear if the positronium has an off-diagonal term in the tensor polarization. Off-diagonal terms can be induced by the B-field not being aligned perfectly along the $\hat{z}$-axis. Take the magnetic field axis in the direction $\hat{\mathbf{B}} = (\sin(\theta)\cos(\phi), \sin(\theta)\sin(\phi), \cos(\theta))^T$ this would induce the off-diagonal components with the following magnitude,

$$s'_{xy}/s_{zz} = \frac{3}{4}\sin^2(\theta)\sin(2\phi) \tag{10.35}$$

$$s'_{yz}/s_{zz} = \frac{3}{4}\sin(2\theta)\sin(\phi) \tag{10.36}$$

$$s'_{zx}/s_{zz} = \frac{3}{4}\sin(2\theta)\cos(\phi) \tag{10.37}$$

where s_{zz} is the alignment if the field is perfectly aligned, and s'_{ij} is the ij-component if there is a misalignment. We expect the field will be very well aligned so it is safe to assume θ is small, however the value of ϕ can fall anywhere between 0 and 2π. This makes the xy term is very small. The yz and zx terms, while not large, are not suppressed either. This analysis is considering a single set of detectors. Each detector configuration has 16 equivalent configurations related by an azimuthal rotation. This means that a misalignment of the field relative to the array induces an asymmetry, but that asymmetry would have a sinusoidal modulation for two detector configurations related by an axial rotation around the ring. The $\mathcal{CP}$-violating signal (along the zz-direction) is unchanged by an axial rotation. This means that the small count asymmetries that a misalignment of the field could induce will be distinguishable from the signal due to the axial symmetry of our detector array.

CHAPTER 11

SUMMARY AND FUTURE WORK

We have presented the initial design, prototyping, and tests of a dedicated apparatus to search for $C\mathcal{P}$-violation in the 3-γ decay of ortho-Positronium. We reviewed some of the history of angular correlations in o-Ps decay, and some inconsistencies in the literature. This motivated an in-depth reanalysis of the planned experiment.

The array will consist of 48 γ-detectors arranged in three rings, the two outer rings will be tilted inwards to a central source. The entire array will fit in the FRIB Positron Polarimeter magnet. The central source will contain a β^+ emitting source, plastic scintillators for triggering, and containers of powder for positronium formation. We achieved a 50% formation fraction for low density SiO_2 powder, and under a roughing pump we achieved a lifetime at 95% the vacuum lifetime. Further work will be required, as this was achieved low density powder. Similar formation fractions have been achieved at much higher density of MgO powder, if that powder is baked in a vacuum oven.

The γ-detectors will be LYSO crystals in a partially tapered design to maximize detection efficiency while still leaving room for mounting. These crystals will read out by Silicon photo-multipliers that will allow the full array to be placed directly in the warm bore of the magnet The final detector modules tested achieved a 12% FWHM energy resolution at 511 keV. The full set of detectors is currently in production at Wittenberg University and will soon be ready to install in the magnet. These detectors can be reliably digitized and read out in coincidence with the plastic start detector using NSCLDAQ and 250 MSPS PIXIE-16 boards. Reading the γ-detectors in coincidence with the plastic detector entirely removed the backgrounds from the intrinsic radioactivity of the crystals. The continuous 2-D energy distribution were separated from the 511 keV annihilation events by cutting on the long lifetime component in the lifetime spectrum.

The design of the inner module and the γ-detector array was studied in Monte-Carlo simulations using Geant4. This facilated study of both the spreading out of the position of decay, and the geometric acceptance and detection efficiency for 2-γ and 3-γ decays. This included finite energy resolution, and the various coincidence conditions.

The model dependence of this search was highlighted, in particular differentiation this search for a "form factor" from similar searches for "coefficients" in nuclear β-decay. This was followed by a discussion of some systematic effects for the measurement, including misalignment of the field, differing detector resolutions, and dilution from 2-γ events. These will leave distinctive signatures in the count asymmetries, and incorporating the time dependence induced by the magnetic field facilitates separating the signal from some systematic offsets.

This work has outlined how to account for various systematics, and how to perform the analysis accounting for model dependence. The Monte Carlo framework as constructed is flexible enough to run an arbitrarily polarized source sampling an arbitrary position for the decay. This will allow quantitative studies of systematic effects such as offsets of the source and misalignment of the detector array. The primary bulk of the work to be performed before data collection are completion of construction for the γ-detectors and testing and construction of a higher rate start detector read out by photomultiplier tubes.

With our design we will be able to achieve an over 10-fold improvement on current limits for this signal, and due to the highly symmetric design of the detector array we will have a strong ability to separate signal from systematics.

BIBLIOGRAPHY

[1] M. E. Peskin and D. V. Schroeder. *An Introduction to quantum field theory*. Addison-Wesley, Reading, USA, 1995.

[2] B. G. Chen, D. Derbes, D. Griffiths, B. Hill, R. Sohn, and Y.S. Ting. *Lectures of Sidney Coleman on Quantum Field Theory*. WORLD SCIENTIFIC, 2018.

[3] Stib. World line, 2007. https://commons.wikimedia.org/wiki/File:World_line.svg.

[4] S. Weinberg. *The Quantum Theory of Fields*. Cambridge University Press, 1995.

[5] R. P. Feynman and S. Weinberg. *Elementary Particles and the Laws of Physics: The 1986 Dirac Memorial Lectures*. Cambridge University Press, 1987.

[6] T. D. Lee and C. N. Yang. Question of parity conservation in weak interactions. *Phys. Rev.*, 104:254–258, Oct 1956.

[7] C. S. Wu, E. Ambler, R. W. Hayward, D. D. Hoppes, and R. P. Hudson. Experimental test of parity conservation in beta decay. *Phys. Rev.*, 105:1413–1415, Feb 1957.

[8] E. D. Commins and P. H. Bucksbaum. *Weak Interactions of Leptons and Quarks*. Cambridge University Press, 1983.

[9] J. H. Christenson, J. W. Cronin, V. L. Fitch, and R. Turlay. Evidence for the 2π decay of the K_2^0 meson. *Phys. Rev. Lett.*, 13:138–140, Jul 1964.

[10] R. L. Workman et al. Review of Particle Physics. *PTEP*, 2022:083C01, 2022.

[11] K. Abe, R. Akutsu, A. Ali, C. Alt, C. Andreopoulos, L. Anthony, M. Antonova, S. Aoki, A. Ariga, T. Arihara, Y. Asada, Y. Ashida, E. T. Atkin, Y. Awataguchi, S. Ban, M. Barbi, G. J. Barker, G. Barr, D. Barrow, C. Barry, M. Batkiewicz-Kwasniak, A. Beloshapkin, F. Bench, V. Berardi, S. Berkman, L. Berns, S. Bhadra, S. Bienstock, A. Blondel, S. Bolognesi, B. Bourguille, S. B. Boyd, D. Brailsford, A. Bravar, D. Bravo Berguño, C. Bronner, A. Bubak, M. Buizza Avanzini, J. Calcutt, T. Campbell, S. Cao, S. L. Cartwright, M. G. Catanesi, A. Cervera, A. Chappell, C. Checchia, D. Cherdack, N. Chikuma, M. Cicerchia, G. Christodoulou, J. Coleman, G. Collazuol, L. Cook, D. Coplowe, A. Cudd, A. Dabrowska, G. De Rosa, T. Dealtry, P. F. Denner, S. R. Dennis, C. Densham, F. Di Lodovico, N. Dokania, S. Dolan, T. A. Doyle, O. Drapier, J. Dumarchez, P. Dunne, A. Eguchi, L. Eklund, S. Emery-Schrenk, A. Ereditato, P. Fernandez, T. Feusels, A. J. Finch, G. A. Fiorentini, G. Fiorillo, C. Francois, M. Friend, Y. Fujii, R. Fujita, D. Fukuda, R. Fukuda, Y. Fukuda, K. Fusshoeller, K. Gameil, C. Giganti, T. Golan, M. Gonin, A. Gorin, M. Guigue, D. R. Hadley, J. T. Haigh, P. Hamacher-Baumann, M. Hartz, T. Hasegawa, S. Hassani, N. C. Hastings, T. Hayashino, Y. Hayato, A. Hiramoto, M. Hogan, J. Holeczek, N. T. Hong Van, F. Iacob, A. K. Ichikawa, M. Ikeda, T. Ishida, T. Ishii, M. Ishitsuka, K. Iwamoto, A. Izmaylov, M. Jakkapu, B. Jamieson,

S. J. Jenkins, C. Jesús-Valls, M. Jiang, S. Johnson, P. Jonsson, C. K. Jung, X. Junjie, P. B. Jurj, M. Kabirnezhad, A. C. Kaboth, T. Kajita, H. Kakuno, J. Kameda, D. Karlen, S. P. Kasetti, Y. Kataoka, T. Katori, Y. Kato, E. Kearns, M. Khabibullin, A. Khotjantsev, T. Kikawa, H. Kikutani, H. Kim, J. Kim, S. King, J. Kisiel, A. Knight, A. Knox, T. Kobayashi, L. Koch, T. Koga, A. Konaka, L. L. Kormos, Y. Koshio, A. Kostin, K. Kowalik, H. Kubo, Y. Kudenko, N. Kukita, S. Kuribayashi, R. Kurjata, T. Kutter, M. Kuze, L. Labarga, J. Lagoda, M. Lamoureux, M. Laveder, M. Lawe, M. Licciardi, T. Lindner, R. P. Litchfield, S. L. Liu, X. Li, A. Longhin, L. Ludovici, X. Lu, T. Lux, L. N. Machado, L. Magaletti, K. Mahn, M. Malek, S. Manly, L. Maret, A. D. Marino, L. Marti-Magro, J. F. Martin, T. Maruyama, T. Matsubara, K. Matsushita, V. Matveev, K. Mavrokoridis, E. Mazzucato, M. McCarthy, N. McCauley, J. McElwee, K. S. McFarland, C. McGrew, A. Mefodiev, C. Metelko, M. Mezzetto, A. Minamino, O. Mineev, S. Mine, M. Miura, L. Molina Bueno, S. Moriyama, J. Morrison, Th. A. Mueller, L. Munteanu, S. Murphy, Y. Nagai, T. Nakadaira, M. Nakahata, Y. Nakajima, A. Nakamura, K. G. Nakamura, K. Nakamura, S. Nakayama, T. Nakaya, K. Nakayoshi, C. Nantais, C. E. R. Naseby, T. V. Ngoc, K. Niewczas, K. Nishikawa, Y. Nishimura, E. Noah, T. S. Nonnenmacher, F. Nova, P. Novella, J. Nowak, J. C. Nugent, H. M. O'Keeffe, L. O'Sullivan, T. Odagawa, K. Okumura, T. Okusawa, S. M. Oser, R. A. Owen, Y. Oyama, V. Palladino, J. L. Palomino, V. Paolone, M. Pari, W. C. Parker, S. Parsa, J. Pasternak, P. Paudyal, M. Pavin, D. Payne, G. C. Penn, L. Pickering, C. Pidcott, G. Pintaudi, E. S. Pinzon Guerra, C. Pistillo, B. Popov, K. Porwit, M. Posiadala-Zezula, A. Pritchard, B. Quilain, T. Radermacher, E. Radicioni, B. Radics, P. N. Ratoff, E. Reinherz-Aronis, C. Riccio, E. Rondio, S. Roth, A. Rubbia, A. C. Ruggeri, C. A. Ruggles, A. Rychter, K. Sakashita, F. Sánchez, G. Santucci, C. M. Schloesser, K. Scholberg, J. Schwehr, M. Scott, Y. Seiya, T. Sekiguchi, H. Sekiya, D. Sgalaberna, R. Shah, A. Shaikhiev, F. Shaker, A. Shaykina, M. Shiozawa, W. Shorrock, A. Shvartsman, A. Smirnov, M. Smy, J. T. Sobczyk, H. Sobel, F. J. P. Soler, Y. Sonoda, J. Steinmann, S. Suvorov, A. Suzuki, S. Y. Suzuki, Y. Suzuki, A. A. Sztuc, M. Tada, and The T2K Collaboration. Constraint on the matter–antimatter symmetry-violating phase in neutrino oscillations. *Nature*, 580(7803):339–344, Apr 2020.

[12] W. Bernreuther. CP violation and baryogenesis, 2002. arXiv, hep-ph/0205279.

[13] A. D. Sakharov. Violation of CP Invariance, C asymmetry, and baryon asymmetry of the universe. *Pisma Zh. Eksp. Teor. Fiz.*, 5:32–35, 1967.

[14] R. Gannouji. Introduction to Electroweak Baryogenesis. *Galaxies*, 10(6), 2022.

[15] M. Kobayashi and T. Maskawa. CP-Violation in the Renormalizable Theory of Weak Interaction. *Prog. Theor. Phys.*, 49(2):652–657, 02 1973.

[16] T. S. Roussy, L. Caldwell, T. Wright, W. B. Cairncross, Y. Shagam, K. Boon Ng, N. Schlossberger, S.n Yool Park, Anzhou Wang, Jun Ye, and Eric A. Cornell. An improved bound on the electron's electric dipole moment. *Science*, 381(6653):46–50, 2023.

[17] A. De Rújula, J.M. Kaplan, and E. de Rafael. Elastic scattering of electrons from polarized protons and inelastic electron scattering experiments. *Nucl. Phys. B*, 35(2):365–389, 1971.

[18] W. Bernreuther and O. Nachtmann. A note on CP-odd and T-odd observables at e^+e^- colliders. *Phys. Lett. B*, 268(3):424–428, 1991.

[19] W. Bernreuther, U. Löw, J. P. Ma, and O. Nachtmann. How to test CP, T, and CPT invariance in the three photon decay of polarized $^3S_1$ positronium. *Z. Phys.C*, 41(1):143–158, Mar 1988.

[20] W. Bernreuther, U. Löw, J. P. Ma, and O. Nachtmann. CP violation and Z boson decays. *Z. Phys.C*, 43(1):117–132, Mar 1989.

[21] S. S. Schweber. *QED and the Men Who Made It: Dyson, Feynman, Schwinger, and Tomonaga*, volume 104. Princeton University Press, 1994.

[22] G. F. Knoll. *Radiation Detection and Measurement*. Wiley, 4th edition, 2010.

[23] C. D. Anderson. The positive electron. *Phys. Rev.*, 43:491–494, Mar 1933.

[24] J. A. Wheeler. Polyelectrons. *Ann. N. Y. Acad. Sci.*, 48(3):219–238, 1946.

[25] A. E. Ruark. Positronium. *Phys. Rev.*, 68:278–278, Dec 1945.

[26] A. Ore and J. L. Powell. Three-photon annihilation of an electron-positron pair. *Phys. Rev.*, 75:1696–1699, Jun 1949.

[27] D. J Griffiths. *Introduction to elementary particles; 2nd rev. version*. Physics textbook. Wiley, New York, NY, 2008.

[28] L. D. Landau. On the angular momentum of a system of two photons. *Dokl. Akad. Nauk SSSR*, 60(2):207–209, 1948.

[29] C. N. Yang. Selection rules for the dematerialization of a particle into two photons. *Phys. Rev.*, 77:242–245, Jan 1950.

[30] M. Deutsch. Evidence for the formation of positronium in gases. *Phys. Rev.*, 82:455–456, May 1951.

[31] M. Deutsch. Three-quantum decay of positronium. *Phys. Rev.*, 83:866–867, Aug 1951.

[32] A. Zichichi. *The Superworld II*. Springer New York, NY, Jan 1990.

[33] M. Deutsch and E. Dulit. Short range interaction of electrons and fine structure of positronium. *Phys. Rev.*, 84:601–602, Nov 1951.

[34] R. M. Drisko. Spin and polarization effects in the annihilation of triplet positronium. *Phys. Rev.*, 102:1542–1544, Jun 1956.

[35] J. Wheatley and D. Halliday. The quenching of ortho-positronium decay by a magnetic field. *Phys. Rev.*, 88:424–424, Oct 1952.

[36] V. W. Hughes, S. Marder, and C. S. Wu. Hyperfine structure of positronium in its ground state. *Phys. Rev.*, 106:934–947, Jun 1957.

[37] B. K. Arbic, S. Hatamian, M. Skalsey, J. Van House, and W. Zheng. Angular-correlation test of CPT in polarized positronium. *Phys. Rev. A*, 37:3189–3194, May 1988.

[38] M. Skalsey and J. Van House. First test of CP invariance in the decay of positronium. *Phys. Rev. Lett.*, 67:1993–1996, Oct 1991.

[39] T. Yamazaki, T. Namba, S. Asai, and T. Kobayashi. Search for CP violation in positronium decay. *Phys. Rev. Lett.*, 104:083401, Feb 2010.

[40] H. Schieck and Paetz gen. Schieck H. *Nuclear Physics with Polarized Particles, Lecture Notes in Physics v. 842*, volume 842. Springer, 01 2012.

[41] S.K. Andrukhovich, N. Antovich, and A.V. Berestov. A spectrometer for the study of angular correlations in polarized-orthopositronium decay. *Instrum. Exp. Tech.*, page 453–459, 2000.

[42] P. A. Vetter and S. J. Freedman. Search for CPT-odd decays of positronium. *Phys. Rev. Lett.*, 91:263401, Dec 2003.

[43] N. M. Antović and S. K. Andrukhovich. Asymmetry in experiments testing CPT in ortho-Ps decay. *Rad. & App.*, 1:177–182, Feb 2016.

[44] P. Moskal, A. Gajos, M. Mohammed, J. Chhokar, N. Chug, C. Curceanu, E. Czerwiński, M. Dadgar, K. Dulski, M. Gorgol, J. Goworek, B. C. Hiesmayr, B. Jasińska, K. Kacprzak, Ł Kapłon, H. Karimi, D. Kisielewska, K. Klimaszewski, G. Korcyl, P. Kowalski, N. Krawczyk, W. Krzemień, T. Kozik, E. Kubicz, S. Niedźwiecki, S. Parzych, M. Pawlik-Niedźwiecka, L. Raczyński, J. Raj, S. Sharma, S. Choudhary, R. Y. Shopa, A. Sienkiewicz, M. Silarski, M. Skurzok, E. Ł Stępień, F. Tayefi, and W. Wiślicki. Testing CPT symmetry in ortho-positronium decays with positronium annihilation tomography. *Nat. Commun.*, 12(1):5658, Sep 2021.

[45] J. Govaerts. Positronium spectroscopy in a magnetic field. 1993. arXiv, hep-ph/9308247.

[46] T.E. Haugen, E. A. George, O. Naviliat-Cuncic, and P. A. Voytas. Search for CP-Violation in ortho-Positronium Decay. *EPJ Web Conf.*, 282:01003, 2023.

[47] R. Mao, L. Zhang, and R.Y. Zhu. Optical and scintillation properties of inorganic scintillators in High Energy Physics. *IEEE Trans. Nucl. Sci.*, 55(4):2425–2431, 2008.

[48] A. Zatcepin and S. I. Ziegler. Detectors in positron emission tomography. *Z Med Phys*,

33(1):4–12, October 2022.

[49] J. Du, Y. Wang, L. Zhang, Z. Zhou, Z. Xu, and X. Wang. Physical properties of LYSO scintillator for NN-PET detectors. *2009 2nd Int. Conf. on Bio. Eng. and Info.*, pages 1–5, 2009.

[50] LYSO:ce Crystal - LYSO(ce) scintillator - Epic Crystal. https://www.epic-crystal.com/oxide-scintillators/lyso-ce-scintillator.html.

[51] R. Mao, L. Zhang, and R.Y. Zhu. LSO/LYSO crystals for future HEP experiments. *JPCS*, 293(1):012004, Apr 2011.

[52] J. Chen, L. Zhang, and R.Y. Zhu. Large size LSO and LYSO crystal scintillators for future high-energy physics and nuclear physics experiments. *Nucl. Instrum. Meth. A*, 572(1):218–224, 2007. Frontier Detectors for Frontier Physics.

[53] H. Alva-Sánchez, A. Zepeda-Barrios, V.D. Díaz-Martínez, and et al. Understanding the intrinsic radioactivity energy spectrum from ^{176}Lu in LYSO/LSO scintillation crystals. *Sci. rep.*, 8, 2018.

[54] I. Mouhti, A. Elanique, M.Y. Messous, A. Benahmed, J.E. McFee, Y. Elgoub, and P. Griffith. Characterization of CsI(Tl) and LYSO(Ce) scintillator detectors by measurements and monte carlo simulations. *Appl. Radiat. Isot.*, 154:108878, 2019.

[55] F. Acerbi and S. Gundacker. Understanding and simulating SiPMs. *Nucl. Instrum. Meth. A*, 926:16–35, 2019. Silicon Photomultipliers: Technology, Characterisation and Applications.

[56] S. Gundacker and A. Heering. The silicon photomultiplier: fundamentals and applications of a modern solid-state photon detector. *Phys. Med. Biol.*, 65(17):17TR01, 2020.

[57] A. Douraghy, D. L. Prout, R. W. Silverman, and A. F. Chatziioannou. Evaluation of scintillator afterglow for use in a combined optical and PET imaging tomograph. *Nucl. Instrum. Meth. A*, 569(2):557–562, 2006. Proc. of the 3rd Int. Conf. on Imag. Tech. in Bio. Sci.

[58] https://www.ketek.net/wp-content/uploads/2018/12/KETEK-PM3325-WB-D0-Datasheet.pdf.

[59] Fast Acquisition System for nuclEar Research. http://faster.in2p3.fr/.

[60] S. Agostinelli, J. Allison, K. Amako, J. Apostolakis, H. Araujo, P. Arce, M. Asai, D. Axen, S. Banerjee, G. Barrand, F. Behner, L. Bellagamba, J. Boudreau, L. Broglia, A. Brunengo, H. Burkhardt, S. Chauvie, J. Chuma, R. Chytracek, G. Cooperman, G. Cosmo, P. Degtyarenko, A. Dell'Acqua, G. Depaola, D. Dietrich, R. Enami, A. Feliciello, C. Ferguson, H. Fesefeldt, G. Folger, F. Foppiano, A. Forti, S. Garelli, S. Giani, R. Giannitrapani, D. Gibin, J.J. Gómez Cadenas, I. González, G. Gracia Abril, G. Greeniaus, W. Greiner, V. Grichine, A. Grossheim,

S. Guatelli, P. Gumplinger, R. Hamatsu, K. Hashimoto, H. Hasui, A. Heikkinen, A. Howard, V. Ivanchenko, A. Johnson, F.W. Jones, J. Kallenbach, N. Kanaya, M. Kawabata, Y. Kawabata, M. Kawaguti, S. Kelner, P. Kent, A. Kimura, T. Kodama, R. Kokoulin, M. Kossov, H. Kurashige, E. Lamanna, T. Lampén, V. Lara, V. Lefebure, F. Lei, M. Liendl, W. Lockman, F. Longo, S. Magni, M. Maire, E. Medernach, K. Minamimoto, P. Mora de Freitas, Y. Morita, K. Murakami, M. Nagamatu, R. Nartallo, P. Nieminen, T. Nishimura, K. Ohtsubo, M. Okamura, S. O'Neale, Y. Oohata, K. Paech, J. Perl, A. Pfeiffer, M.G. Pia, F. Ranjard, A. Rybin, S. Sadilov, E. Di Salvo, G. Santin, T. Sasaki, N. Savvas, Y. Sawada, S. Scherer, S. Sei, V. Sirotenko, D. Smith, N. Starkov, H. Stoecker, J. Sulkimo, M. Takahata, S. Tanaka, E. Tcherniaev, E. Safai Tehrani, M. Tropeano, P. Truscott, H. Uno, L. Urban, P. Urban, M. Verderi, A. Walkden, W. Wander, H. Weber, J.P. Wellisch, T. Wenaus, D.C. Williams, D. Wright, T. Yamada, H. Yoshida, and D. Zschiesche. Geant4–a simulation toolkit. *Nucl. Instrum. Meth. A*, 506(3):250–303, 2003.

[61] J. Allison, K. Amako, J. Apostolakis, P. Arce, M. Asai, T. Aso, E. Bagli, A. Bagulya, S. Banerjee, G. Barrand, B.R. Beck, A.G. Bogdanov, D. Brandt, J.M.C. Brown, H. Burkhardt, Ph. Canal, D. Cano-Ott, S. Chauvie, K. Cho, G.A.P. Cirrone, G. Cooperman, M.A. Cortés-Giraldo, G. Cosmo, G. Cuttone, G. Depaola, L. Desorgher, X. Dong, A. Dotti, V.D. Elvira, G. Folger, Z. Francis, A. Galoyan, L. Garnier, M. Gayer, K.L. Genser, V.M. Grichine, S. Guatelli, P. Guèye, P. Gumplinger, A.S. Howard, I. Hrivnácová, S. Hwang, S. Incerti, A. Ivanchenko, V.N. Ivanchenko, F.W. Jones, S.Y. Jun, P. Kaitaniemi, N. Karakatsanis, M. Karamitros, M. Kelsey, A. Kimura, T. Koi, H. Kurashige, A. Lechner, S.B. Lee, F. Longo, M. Maire, D. Mancusi, A. Mantero, E. Mendoza, B. Morgan, K. Murakami, T. Nikitina, L. Pandola, P. Paprocki, J. Perl, I. Petrović, M.G. Pia, W. Pokorski, J.M. Quesada, M. Raine, M.A. Reis, A. Ribon, A. Ristić Fira, F. Romano, G. Russo, G. Santin, T. Sasaki, D. Sawkey, J.I. Shin, I.I. Strakovsky, A. Taborda, S. Tanaka, B. TomÃ©, T. Toshito, H.N. Tran, P.R. Truscott, L. Urban, V. Uzhinsky, J.M. Verbeke, M. Verderi, B.L. Wendt, H. Wenzel, D.H. Wright, D.M. Wright, T. Yamashita, J. Yarba, and H. Yoshida. Recent developments in geant4. *Nucl. Instrum. Meth. A*, 835:186–225, 2016.

[62] I. Kawrakow, D.W.O. Rogers, E. Mainegra-Hing, F. Tessier, R.W. Townson, and B.R.B. Walters. EGSnrc toolkit for Monte Carlo simulation of ionizing radiation transport, 2000.

[63] E. Auffray, F. Cavallari, M. Lebeau, P. Lecoq, M. Schneegans, and P. Sempere-Roldan. Crystal conditioning for high-energy physics detectors. *Nucl. Instrum. Meth. A*, 486:22–34, 2002.

[64] A. S. Carnoy, J. Deutsch, T. A. Girard, and R. Prieels. Limits on nonstandard weak currents from the positron decays of ^{14}O and ^{10}C. *Phys. Rev. Lett.*, 65:3249–3252, Dec 1990.

[65] N. Severijns, J. Deutsch, F. Gimeno-Nogues, B. H. King, I. Pepe, R. Prieels, P. A. Quin, J. Camps, P. De Moor, P. Schuurmans, W. Vanderpoorten, L. Vanneste, J. Wouters, M. Allet, O. Navilliat-Cuncic, and B. R. Holstein. Limits on right-handed charged weak currents from a polarization-asymmetry correlation experiment with ^{107}In. *Phys. Rev. Lett.*, 70:4047–4050, Jun 1993.

[66] G. Consolati, R. Ferragut, A. Galarneau, F. Di Renzo, and F. Quasso. Mesoporous materials for antihydrogen production. *Chem Soc Rev*, 42(9):3821–3832, December 2012.

[67] D. Trezzi. *Study of Positronium Converters in the Aegis Antimatter Experiment*. PhD thesis, Milan U., 2010.

[68] Y C Jean, P E Mallon, and D M Schrader. *Principles and Applications of Positron and Positronium Chemistry*. WORLD SCIENTIFIC, 2003.

[69] D. W. Gidley, H.G. Peng, and R. S. Vallery. Positron annihilation as a method to characterize porous materials. *Annu. Rev. Mater. Res.*, 36(Volume 36, 2006):49–79, 2006.

[70] K. Shibuya, H. Saito, F. Nishikido, M. Takahashi, and T. Yamaya. Oxygen sensing ability of positronium atom for tumor hypoxia imaging. *Commun. Phys.*, 3(1):173, Oct 2020.

[71] S. Lipschutz, R.G.T. Zegers, J. Hill, S.N. Liddick, S. Noji, C.J. Prokop, M. Scott, M. Solt, C. Sullivan, and J. Tompkins. Digital data acquisition for the low energy neutron detector array (LENDA). *Nucl. Instrum. Meth. A*, 815:1–6, 2016.

[72] C.J. Prokop, S.N. Liddick, B.L. Abromeit, A.T. Chemey, N.R. Larson, S. Suchyta, and J.R. Tompkins. Digital data acquisition system implementation at the National Superconducting Cyclotron Laboratory. *Nucl. Instrum. Meth. A*, 741:163–168, 2014.

[73] C.J. Prokop, S.N. Liddick, N.R. Larson, S. Suchyta, and J.R. Tompkins. Optimization of the National Superconducting Cyclotron Laboratory Digital Data Acquisition System for use with fast scintillator detectors. *Nucl. Instrum. Meth. A*, 792:81–88, 2015.

[74] L. Dick, L. Feuvrais, L. Madansky, and V.L. Telegdi. A novel efficient method for measuring the polarisation of positrons. *Phys. Lett.*, 3(7):326–329, 1963.

[75] D. Freytag and K. Ziock. Der einfluß eines magnetfeldes auf die lebensdauer von positronen in fester materie. *Z. Phys.*, 153(1):124–128, Feb 1958.

[76] https://eljentechnology.com/products/plastic-scintillators/ej-200-ej-204-ej-208-ej-212.

[77] X. Mougeot. Towards high-precision calculation of electron capture decays. *Appl. Radiat. Isot.*, 154:108884, 2019.

[78] X. Mougeot. Atomic exchange correction in forbidden unique beta transitions. *Appl. Radiat. Isot.*, 201:111018, 2023.

[79] H. W. Park, D. W. Jeong, J. Jegal, A. Khan, and H. J. Kim. A novel hermetic detection system of KAPAE for measuring multiphoton decays of positronium. *JINST*, 18(03):P03011, Mar 2023.

[80] C. Bartram and R. Henning. Caliope: a search for CPT-violation in o-ps. *JPCS*, 1342(1):012106, Jan 2020.

[81] S. Bass. QED and fundamental symmetries in positronium decays. *Acta. Phys. Pol. B*, 50, 2019.

[82] M. Diehl and O. Nachtmann. Optimal observables for the measurement of three gauge boson couplings in $e^+e^- \to W^+W^-$. *Z. Phys.C*, 62(3):397–411, Sep 1994.

[83] M. González-Alonso, O. Naviliat-Cuncic, and N. Severijns. New physics searches in nuclear and neutron β decay. *Prog. Part. Nucl. Phys,*, 104:165–223, 2019.

[84] V G Baryshevsky, O N Metelitsa, and V V Tikhomirov. Oscillations of the positronium decay γ-quantum angular distribution in a magnetic field. *J. Phys.B*, 22(17):2835, Sep 1989.

[85] V.G. Baryshevsky, O.N. Metelitsa, V.V. Tikhomirov, S.K. Andrukhovich, A.V. Berestov, B.A. Martsinkevich, and E.A. Rudak. Observation of time oscillation in 3γ-annihilation of positronium in a magnetic field. *Phys. Lett. A*, 136(7):428–432, 1989.

[86] E. Ivanov, I. Vata, D. Dudu, I. Rusen, and N. Stefan. Quantum beats in the 3γ annihilation decay of positronium observed by perturbed angular distribution. *Appl. Surf. Sci.*, 255(1):179–182, 2008.

[87] Y. Sasaki, A. Miyazaki, A. Ishida, T. Namba, S. Asai, T. Kobayashi, H. Saito, K. Tanaka, and A. Yamamoto. Measurement of positronium hyperfine splitting with quantum oscillation. *Phys. Lett. B*, 697(2):121–126, 2011.

[88] A. P. Mills. Line-shape effects in the measurement of the positronium hyperfine interval. *Phys. Rev. A*, 27:262–267, Jan 1983.

[89] A. Rich. Corrections to the measured $n = 1$ hyperfine interval of positronium due to annihilation effects. *Phys. Rev. A*, 23:2747–2750, May 1981.

[90] J. J. Sakurai and J. Napolitano. *Modern Quantum Mechanics*. Cambridge University Press, 3 edition, 2020.

[91] H. Wahl. First observation and precision measurement of direct CP violation: the experiments NA31 and NA48. *Phys. Rep.*, 403-404:19–25, 2004.

[92] C. Itzykson and J. B. Zuber. *Quantum Field Theory*. McGraw-Hill International Book Co, 1980.

[93] J. Pestieau and C. Smith. Soft photon spectrum in orthopositronium and vector quarkonium decays. *Phys. Lett. B*, 524(3–4):395–399, January 2002.

[94] P. D. Ruiz-Femenia. Orthopositronium decay spectrum using NRQED, 2004. arXiv, hep-ph/0410211.

APPENDIX A

FULL DESCRIPTION OF PS SPIN STATE FOR SPIN-0 AND SPIN-1

A.1 Density matrix

The density matrix is the most general description of a quantum state [40, 90], and is needed for a full description of an arbitrary positronium state [19]. A "pure" state $|a\rangle$ can be represented as,

$$\rho = |a\rangle \langle a| \tag{A.1}$$

The expectation value of an operator is then given as $\langle A\rangle_{\rho_a} = \langle a| A |a\rangle = \mathrm{Tr}(A\rho_a)$. A mixed state is a statistical mixture of states with weights p_i such that $\sum_i p_i = 1$. This warrants defining the density matrix,

$$\rho = \sum_i p_i |i\rangle \langle i| \tag{A.2}$$

where $|i\rangle$ does not need to be orthogonal to $|j\rangle$. This formal description of a state is minimal and complete. It allows a closer contact between a state and it's expectation value for observbales. A quantum state can be fully and uniquely described by all of its expectation values

Restrict to a finite dimensional system, for example spin-s with $2s + 1$ basis states in the Hilbert space. A general observable on this space is a $(2s + 1) \times (2s + 1)$ matrix. Shorten this to an n-dimensional Hilbert space, and $n \times n$ matrix. There is a complete set of operators, where completeness is defined with resepect to orthogonality in a trace, $\mathrm{Tr}(A_i A_j) = \delta_{ij}$. There are $n \times n$ such independent matrices including the unit element $1_{n\times n}$. This means all other observables must be traceless $\mathrm{Tr}(A_i 1_{n\times n}) = \mathrm{Tr}(A_i) = 0$. Any observable (or matrix on this $n \times n$ space) can be represented as a linear sum of these observables,

$$B = b_0 1_{n\times n} + \sum_i b_i A_i \tag{A.3}$$

The density matrix itself is a Hermitian $n \times n$ matrix defined on this Hilbert space, and can be represented as,

$$\rho = \rho_0 1_{n\times n} + \sum_i \rho_i A_i \tag{A.4}$$

A normalized state has $\mathrm{Tr}(\rho) = 1$ meaning $\rho_0 = 1/n$. Since $\mathrm{Tr}(A_i A_j) = \delta_{ij}$ the weights in the linear sum satsify $\rho_i = \langle A_i \rangle_\rho$. This shows that any state can be uniquely represented by its expectation values on a complete set of observables

$$\rho = \frac{1}{n} 1_{n\times n} + \sum_i \langle A_i \rangle_\rho A_i \tag{A.5}$$

A.1.1 Cartesian basis for spin-1 basis states

The calculations are presented in the "Cartesian basis" for spin-1. A spin-1 system has 3 degrees of freedom, meaning that the rotation matrices acting on the Hilbert space can take the same form as rotations acting on normal vectors. The relationship is the same as that between unit vectors and spherical harmonics. Start with the space of states that diagonalize the $\hat{S}_z$ operator, $\{|S=1, m=+1\rangle, |S=1, m=0\rangle, |S=1, m=-1\rangle\}$. Define the Cartesian basis kets as,

$$|S=1, x\rangle = \frac{1}{\sqrt{2}}(|S=1, m=+1\rangle + |S=1, m=-1\rangle) \tag{A.6}$$

$$|S=1, y\rangle = -i\frac{1}{\sqrt{2}}(|S=1, m=+1\rangle - |S=1, m=-1\rangle) \tag{A.7}$$

$$|S=1, z\rangle = |S=1, m=0\rangle$$

In this basis finite rotations act on the quantum state in the following manner,

$$\hat{U}(R_x(\theta)) = \begin{pmatrix} 1 & 0 & 0 \\ 0 & \cos(\theta) & -\sin(\theta) \\ 0 & \sin(\theta) & \cos(\theta) \end{pmatrix} \qquad \hat{S}_x = \begin{pmatrix} 0 & 0 & 0 \\ 0 & 0 & i \\ 0 & -i & 0 \end{pmatrix} \tag{A.8}$$

$$\hat{U}(R_y(\theta)) = \begin{pmatrix} \cos(\theta) & 0 & \sin(\theta) \\ 0 & 1 & 0 \\ -\sin(\theta) & 0 & \cos(\theta) \end{pmatrix} \qquad \hat{S}_y = \begin{pmatrix} 0 & 0 & -i \\ 0 & 0 & 0 \\ i & 0 & 0 \end{pmatrix} \tag{A.9}$$

$$\hat{U}(R_z(\theta)) = \begin{pmatrix} \cos(\theta) & -\sin(\theta) & 0 \\ \sin(\theta) & \cos(\theta) & 0 \\ 0 & 0 & 1 \end{pmatrix} \qquad \hat{S}_z = \begin{pmatrix} 0 & -i & 0 \\ i & 0 & 0 \\ 0 & 0 & 0 \end{pmatrix} \tag{A.10}$$

these have the same form as finite rotations acting on Cartesian spatial vectors. Further this gives the (j, k) component of the matrix representation of the angular momentum along the ith axis as, $(\hat{S}_i)_{jk} = i\epsilon_{ijk}$. This follows from spin-1 being the adjoint representation of SO(3).

A.1.2 A general observable defined on spin-1 basis states

A general observable acting on this space can be represented as a 3×3 Hermitian operator. There are exactly 9 independent numbers needed to specify a general observable.

Define the tensor polarization as the symmetric combination,

$$\hat{S}_{ij} = \frac{1}{2}(\hat{S}_i\hat{S}_j + \hat{S}_j\hat{S}_i) - \frac{1}{3}S^2\delta_{ij} \tag{A.11}$$

the trace of this tensor is zero in that $\hat{S}_{xx} + \hat{S}_{yy} + \hat{S}_{zz} = 0$ on every state. Each element represented as a matrix acting on a Hilbert space is also a traceless matrix, but strictly speaking these are two different traces that should not be confused.

The angular momentum operators satisfy $\mathrm{Tr}(S_i) = 0$, and $\mathrm{Tr}(S_iS_{jk}) = 0$. The elements of the tensor polarization are more complicated, there are 6 elements and one constraint ($\hat{S}_{xx}+\hat{S}_{yy}+\hat{S}_{zz} = 0$) giving 5 independent elements. Take these as $\hat{S}_{ij}$ where $i \neq j$, $\hat{S}_{zz}$, and finally $\hat{S}_\Delta = \hat{S}_{xx} - \hat{S}_{yy}$. These are five independent components with mutually vanishing traces.

A.1.3 Description of Ps state

The density matrix is a Hermitian operator defined on the Hilbert space and as such all the above machinery directly carries over. Taking the (normalized) density matrix as a combination of the independent operators gives,

$$\rho = \frac{1}{3}1_{3\times3} + \sum_i s_i\hat{S}_i + \sum_{ij} s_{ij}\hat{S}_{ij} \tag{A.12}$$

where $s_i = \langle\hat{S}_i\rangle_\rho$ and $s_{ij} = \langle\hat{S}_{ij}\rangle_\rho$. If we represent this as a matrix acting on the Hilbert space, choosing the Cartesian basis it takes the particularly simple form,

$$\rho_{ij} = \frac{1}{3}\delta_{ij} + \frac{1}{2i}\epsilon_{ijk}s_k - s_{ij} \tag{A.13}$$

where $i, j \in (x, y, z)$, and $s_{xx} + s_{yy} + s_{zz} = 0$.

A.2 Ps density matrix for combined spin-0 and spin-1

In the Cartesian basis the full density matrix is a 4×4 matrix and therefore needs $16-1$ components. The two block diagonal subspaces are the spin-0 and spin-1 spaces. These must correspond to operators with well defined angular momentum, $\mathbf{J}$ and J^2. There are still then 6 parameters as yet unidentified. Now consider that $\mathbf{J} = \mathbf{s}^e + \mathbf{s}^{\bar{e}}$, there are exactly 6 combinations of $\mathbf{s}^e$ and $\mathbf{s}^{\bar{e}}$ that do not correspond to $\mathbf{J}$, those being $\mathbf{s}^e - \mathbf{s}^{\bar{e}}$ and $\mathbf{s}^e \times \mathbf{s}^{\bar{e}}$.

The density matrix has he form,

$$\rho = \begin{pmatrix} \rho_{00} & \mathbf{u}^\dagger \\ \mathbf{u} & \rho_{ij} \end{pmatrix} \tag{A.14}$$

where ρ_{ij} corresponds to the 3×3 density matrix of spin-1 discussed above. Considering the combinations of the electron and positron spins gives exactly 15 independent combinations. These are largely determined by the rotational properties in the Cartesian basis. ρ_{00} is unchanged under rotations, ρ_{ij} rotates like a second rank tensor, and $\mathbf{u}$ has three components that rotate between each other (but do not correspond to definite angular momentum). Direct computation gives the following,

$$\rho_{00} = (\frac{1}{4} - \mathbf{s}^e \cdot \mathbf{s}^{\bar{e}}) \tag{A.15}$$

$$\mathbf{u}_i = \frac{1}{2}(\mathbf{s}^e_i - \mathbf{s}^{\bar{e}}{}_i) - i(\mathbf{s}^e \times \mathbf{s}^{\bar{e}})_i \tag{A.16}$$

$$\rho_{ij} = \left\{(\frac{1}{4} + \mathbf{s}^e \cdot \mathbf{s}^{\bar{e}})\delta_{ij} - (\mathbf{s}^e_i \mathbf{s}^{\bar{e}}_j + \mathbf{s}^e_j \mathbf{s}^{\bar{e}}_i) - \frac{i}{2}\epsilon_{ijk}(\mathbf{s}^e_k + \mathbf{s}^{\bar{e}}_k)\right\} \tag{A.17}$$

This encapsulates the earlier description in Equation A.12 by restoring the dependence on $\mathbf{J} = \mathbf{s}^e + \mathbf{s}^{\bar{e}}$. The two spin-1/2 operators individually satisfy $\mathbf{s}^e_i \mathbf{s}^e_j = \frac{1}{4}\delta_{ij} + i\frac{1}{2}\epsilon_{ijk}\mathbf{s}^e_k$. This means that $(\mathbf{s}^e_i \mathbf{s}^e_j + \mathbf{s}^e_j \mathbf{s}^e_i) = \frac{1}{2}(\mathbf{J}_i \mathbf{J}_j + \mathbf{J}_j \mathbf{J}_i) - \frac{1}{2}\delta_{ij}$. The terms corresponding to the spin-0 and spin-1 subspaces can be simplified to,

$$\rho_{00} = 1 - \frac{1}{2}J^2 \tag{A.18}$$

$$\rho_{ij} = \frac{1}{6}J^2\delta_{ij} - \left(\frac{1}{2}\left(\mathbf{J}_i \mathbf{J}_j + \mathbf{J}_j \mathbf{J}_i\right) - \frac{1}{3}J^2\delta_{ij}\right) - i\epsilon_{ijk}\mathbf{J}_k \tag{A.19}$$

which reproduces the expected behavior for $J^2 = 2$ and is zero for $J^2 = 0$. This shows that a tensor polarized positronium source cannot be made without both polarized positrons and electrons. The off-diagonal depending on $\mathbf{s}^e - \mathbf{s}^{\bar{e}}$ also agrees with the calculations of the Hamiltonian including a B-field, which is proportional to this term and generates an off-diagonal term between the $S = 0$ and $S = 1$ spaces.

A.3 Polarized positronium in a B-field

Now consider positrons that are partially polarized in the x-z plane, and unpolarized electrons. This is described by the density matrix,

$$\rho = \begin{pmatrix} \frac{1}{4} & -\frac{1}{2}\mathbf{s}^{\bar{e}}_x & 0 & -\frac{1}{2}\mathbf{s}^{\bar{e}}_z \\ -\frac{1}{2}\mathbf{s}^{\bar{e}}_x & \frac{1}{4} & -\frac{1}{2}i\mathbf{s}^{\bar{e}}_z & 0 \\ 0 & \frac{1}{2}i\mathbf{s}^{\bar{e}}_z & \frac{1}{4} & -\frac{1}{2}i\mathbf{s}^{\bar{e}}_x \\ -\frac{1}{2}\mathbf{s}^{\bar{e}}_z & 0 & \frac{1}{2}i\mathbf{s}^{\bar{e}}_x & \frac{1}{4} \end{pmatrix} \tag{A.20}$$

For a B-field in the $\hat{z}$ direction each component has time dependence. For the sake of studying the decay products we only need to consider the $\rho_{00}(t)$ and $\rho_{ij}(t)$, as the $\rho_{0i}(t)$ do not survive the trace with the decay matrix. Take the energy differences as $\omega_{pS} - \omega_T = \omega_1$, $\omega_{pS} - \omega_{pT} = \omega_2$, and $\omega_{pT} - \omega_T = \omega_3$, and similarly for the lifetimes, $\Gamma_{pS} + \Gamma_T = 2\Gamma_1$, $\Gamma_{pS} + \Gamma_{pT} = 2\Gamma_2$, and $\Gamma_{pT} + \Gamma_T = 2\Gamma_3$. The time dependence is given as,

$$\rho_{00}(t) = c^2(\frac{1}{4} + 2sc\mathbf{s}_z)e^{-t\Gamma_{pS}} + 2sc(s^2 - c^2)\mathbf{s}_z\cos(\Omega_2 t)e^{-t\Gamma_1} + s^2(\frac{1}{4} - 2sc\mathbf{s}_z)e^{-t\Gamma_{pT}} \tag{A.21}$$

$$\rho_{xx}(t) = \rho_{yy}(t) = \frac{1}{4}e^{-t\Gamma_T} \tag{A.22}$$

$$\rho_{xy}(t) = -i\mathbf{s}_z e^{-t\Gamma_T} \tag{A.23}$$

$$\rho_{xz}(t) = sc\mathbf{s}_x \left(e^{-it\omega_1}e^{-t\Gamma_1} - e^{+i\omega_3}e^{-t\Gamma_3}\right) \tag{A.24}$$

$$\rho_{yz}(t) = i\mathbf{s}_x \left(s^2 e^{-it\omega_1}e^{-t\Gamma_1} - c^2 e^{+i\omega_3}e^{-t\Gamma_3}\right) \tag{A.25}$$

$$\rho_{zz}(t) = -s^2(\frac{1}{4} + 2sc\mathbf{s}_z)e^{-t\Gamma_{pS}} - 2sc(s^2 - c^2)\mathbf{s}_z\cos(\omega_2 t)e^{-t\Gamma_1} + c^2(\frac{1}{4} - 2sc\mathbf{s}_z)e^{-t\Gamma_{pT}} \tag{A.26}$$

These are the components of a tensor, and therefore any arbitrary direction for $\hat{B}$ and $\hat{\mathbf{s}}$ can be described by the proper rotation of the above components.

This distribution is mapped into the final state photon distribution by,

$$\dot{N}(\mathbf{k}_1, \mathbf{k}_2, \mathbf{k}_3) = \sum_{ij} R_{ij}(\mathbf{k}_1, \mathbf{k}_2, \mathbf{k}_3)\rho_{ij}(t) \tag{A.27}$$

Restrict to times after 1 ns and take the energy and angle dependent terms, $a(\omega_1, \omega_2) = a$, $B_i(\mathbf{k}_1, \mathbf{k}_2, \mathbf{k}_3) = B_i$, and $C_{ij}(\mathbf{k}_1, \mathbf{k}_2, \mathbf{k}_3) = C_{ij}$.

$$\dot{N}_{2\gamma} = \Gamma_{2\gamma} s^2 (\frac{1}{4} + 2sc\mathbf{s}_z) e^{-t\Gamma_{pT}} \tag{A.28}$$

$$\begin{aligned}\dot{N}_{3\gamma}(\mathbf{k}_1, \mathbf{k}_2, \mathbf{k}_3) = \Gamma_{3\gamma}\{&\frac{1}{4}(A - C_{xx})e^{-t\Gamma_T} - B_z\mathbf{s}_z e^{-t\Gamma_T} - C_{xz}sc\mathbf{s}_x\cos(\omega_3 t)e^{-t\Gamma_3} \\ &+ B_y sc\mathbf{s}_x\sin(\omega_3 t)e^{-t\Gamma_3} + \frac{1}{4}(A - C_{yy})e^{-t\Gamma} \\ &+ C_{yz}c^2\mathbf{s}_x\sin(\omega_3 t)e^{-t\Gamma_3} + B_x c^2\mathbf{s}_x\cos(\omega_3 t)e^{-t\Gamma_3} \\ &+ (A - C_{zz})c^2(\frac{1}{4} - 2sc\mathbf{s}_z)e^{-t\Gamma_{pT}}\end{aligned} \tag{A.29}$$

Since C_{ij} is a traceless tensor, the components must satisfy $C_{xx} + C_{yy} + C_{zz} = 0$. This simplifies the "diagonal term",

$$\begin{aligned}\dot{N}_{3\gamma}(\mathbf{k}_1, \mathbf{k}_2, \mathbf{k}_3) = \Gamma_{3\gamma}\{&\frac{1}{4}A(2e^{-t\Gamma_T} + c^2(1 - 8sc\mathbf{s}_z)e^{-t\Gamma_{pT}}) + \frac{1}{4}C_{zz}(e^{-t\Gamma_T} - c^2(1 - 8sc\mathbf{s}_z)e^{-t\Gamma_{pT}}) \\ &- B_z\mathbf{s}_z e^{-t\Gamma_T} - C_{xz}sc\mathbf{s}_x\cos(\omega_3 t)e^{-t\Gamma_3} + B_y sc\mathbf{s}_x\sin(\omega_3 t)e^{-t\Gamma_3} \\ &+ C_{yz}c^2\mathbf{s}_x\sin(\omega_3 t)e^{-t\Gamma_3} + B_x c^2\mathbf{s}_x\cos(\omega_3 t)e^{-t\Gamma_3}\}\end{aligned} \tag{A.30}$$

This form does not currently agree with existing literature [85] and likely has both minus sign errors and missing factors of $1/2$. This can be quickly interpreted as follows, choose a term, like $B_z\mathbf{s}_z e^{-t\Gamma_T}$, this says that the correlations $\langle\kappa_{1z}\rangle$, $\langle\kappa_{2z}\rangle$, and $\langle n_z\rangle$ could be present for a source with polarization $\mathbf{s}_z$ in the z-direction, with time dependence $e^{-t\Gamma_T}$. For this term all three correlations correspond to new physics.

For $\mathcal{CP}$-violation from $1^3S_1 - 2^1P_1$ mixing the tensor term gets a contribution from $\mathrm{Re}(\delta_1)$, and the vector term (manifesting as oscillations in $\langle\hat{\mathbf{k}}_1\rangle$ and $\langle\hat{\mathbf{k}}_2\rangle$) get contributions from $\mathrm{Im}(\delta_1)$. To date there have been no searches for the vector correlations indicative of $\mathcal{CP}$-violation. Simple arguments might imply that such a correlation, $\langle\hat{\mathbf{s}}\cdot\hat{\mathbf{k}}_1\rangle$, would indicate $\mathcal{CPT}$-violation. The argument goes as, the spin and momentum change sign under $\mathcal{T}$ but only the momentum changes

sign under $\mathcal{P}$, therefore this correlation picks up a minus sign and would indicate $\mathcal{CPT}$. This argument is wrong, and the addition of new physics will generally induce both B_i and C_{ij} correlations at similar magnitudes. For the example above, both are proportional to the mixing coefficient, the imaginary and real parts respectively [19].

APPENDIX B

MATRIX ELEMENT AND 3-γ PHASE SPACE

Here we provide a more technical discussion of the phase space and the matrix element. We first discuss the non-trivial implications of photon indistinguishability that are hidden by imposing an energy ordering. Following this we give a discussion of the structure of direct versus indirect $\mathcal{CP}$-violation in ortho-positronium decay, ultimately showing where this prefactor of $1/775$ originates from.

B.1 Photon indistinguishability

The final state contains three indistinguishable particles. This manifests in multiple places, for example the structure of the matrix element as calculated from Feynman diagrams requires permutation of the interaction vertices as shown in Figure B.1. However it also manifests as the definition of the phase space, and it is this manifestation that we are primarily addressing here. Consider for example 2-γ decay, there are two photons each with 511 keV, restricted back to back momenta. Label the two photons a and b, the two photon phase space goes as,

$$\mathrm{d}f^{2\gamma} = \zeta \frac{\mathrm{d}k_a^3}{(2\pi)^3 2\omega_a} \frac{\mathrm{d}k_b^3}{(2\pi)^3 2\omega_b} \delta^{(3)}(\mathbf{k}_a - \mathbf{k}_b) \tag{B.1}$$

This can be integrated over $\mathbf{k}_b$, and we are left with integrating $\mathbf{k}_\alpha$ over all possible directions (with $\mathbf{k}_b = -\mathbf{k}_a$). The appropriate scaling for ζ is $1/2$ due to photon indistinguishability. The contribution from ($\hat{\mathbf{k}}_a = +\hat{z}$,$\hat{\mathbf{k}}_b = -\hat{z}$) is double counted by considering ($\hat{\mathbf{k}}_a = -\hat{z}$,$\hat{\mathbf{k}}_b = +\hat{z}$) as a distinct final state.

This is not as straightforward when the photons can have different energies. A photon with energy ω_1 can be distinguished from one with ω_2. In the definition of the phase space, as shown in

Figure B.1 Two of the six Feynman diagram for 3-γ decay of ortho-positronium in QED. The other 4 are generated by cyclic permutation of which photon couples to which vertex.

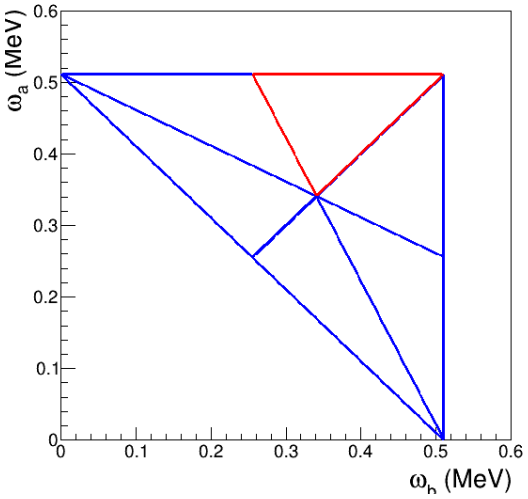

Figure B.2 The six-fold redundant full kinematically allowed phase space. We can restrict ourselves to considering any individual cell (in effect choosing an ordering for the photons). In principle we could consider the dynamics on the full space so long as we account for the redundancy.

Figure B.2, when we impose the ordering on the energies $\omega_a > \omega_b > 2m_e - \omega_a - \omega_b$, every event occurs in the red triangle. We only consider the matrix element defined on this triangle. This is however, a choice of coordinates for phase space and not something fundamental. We could instead just consider ω_a and ω_b as the energies of two of the photons, with no ordering. Then we would consider the full region of $\omega_a < m_e$, $\omega_b < m_e$, and $2m_e - \omega_a - \omega_b < m_e$ as the kinematically allowed phase space. In this case, the matrix element is defined over the entire region, but since there is no physical meaning to the labels a and b the matrix element must be symmetric under their interchange, $R_{ij}(\mathbf{k}_a, \mathbf{k}_b) = R_{ij}(\mathbf{k}_b, \mathbf{k}_a)$. This is why there are six redundant regions in the phase space that correspond to the six ordering of the photons. We could restrict our consideration to any one of the six, or consider the whole space and divide the final result by $1/6$.

The decay matrix and the irreducible tensors are unchanged except we replace the momentum and energy labels 1 and 2 with a and b,

$$R_{ij}(\mathbf{k}_a, \mathbf{k}_b) = a(\omega_a, \omega_b)\delta_{ij} + \epsilon_{ijk}B_k(\mathbf{k}_a, \mathbf{k}_b) + C_{ij}(\mathbf{k}_a, \mathbf{k}_b) \tag{B.2}$$

To recover the form factors as defined in Ref. [19] we must impose a partial ordering. They describe the decay plane as an oriented vector defined as $\hat{\mathbf{n}} = \hat{\mathbf{k}}_a \times \hat{\mathbf{k}}_b / |\sin(\psi_{ab})|$. This has defined an orientation to the 3-γ phase space. This orientation is flipped under the interchange of any

two labels, meaning $\hat{\mathbf{n}} \to -\hat{\mathbf{n}}$ under $a \leftrightarrow b$. If the labels are arbitrary then the dynamics must be unchanged under the switch of labels. Switching the labels for the scalar term,

$$a(\omega_a, \omega_b) \to a(\omega_b, \omega_a) \tag{B.3}$$

requires $a(\omega_a, \omega_b) = a(\omega_b, \omega_a)$. For the vector term,

$$\begin{aligned}\hat{\mathbf{k}}_a b_1(\omega_a, \omega_b) + \hat{\mathbf{k}}_b b_2(\omega_a, \omega_b) + \hat{\mathbf{n}} b_3(\omega_a, \omega_b) \\ \to \hat{\mathbf{k}}_b b_1(\omega_b, \omega_a) + \hat{\mathbf{k}}_a b_2(\omega_b, \omega_a) + (-\hat{\mathbf{n}}) b_3(\omega_b, \omega_a)\end{aligned} \tag{B.4}$$

this requires that $b_1(\omega_a, \omega_b) = b_2(\omega_b, \omega_a)$ and $b_3(\omega_a, \omega_b) = -b_3(\omega_b, \omega_a)$. The $\mathcal{CP}$-odd tensor terms behave as,

$$\begin{aligned}(\hat{\mathbf{k}}_{ai}\hat{\mathbf{n}}_j + \hat{\mathbf{n}}_i\hat{\mathbf{k}}_{aj}) c_4(\omega_a, \omega_b) + (\hat{\mathbf{k}}_{ai}\hat{\mathbf{n}}_j + \hat{\mathbf{n}}_i\hat{\mathbf{k}}_{aj}) c_5(\omega_a, \omega_b) \\ \to (\hat{\mathbf{k}}_{bi}(-\hat{\mathbf{n}}_j) + (-\hat{\mathbf{n}}_i)\hat{\mathbf{k}}_{bj}) c_4(\omega_b, \omega_a) + (\hat{\mathbf{k}}_{bi}(-\hat{\mathbf{n}}_j) + (-\hat{\mathbf{n}}_i)\hat{\mathbf{k}}_{bj}) c_5(\omega_b, \omega_a)\end{aligned} \tag{B.5}$$

which requires $c_4(\omega_a, \omega_b) = -c_5(\omega_b, \omega_a)$. This reproduces the properties quoted in Chapter 2. We can now choose the ordering of the photons and restrict the phase space to a single cell, but that does not change the properties of the matrix element, only the domain on which it is evaluated.

The reason for explicitly working this out is to derive that $c_4(\omega_1, \omega_2) = -c_5(\omega_2, \omega_1)$ quite generally, not just for the model provided in Ref. [19]. This means that it is inconsistent to consider a model where only one of these terms is zero, to do so is to assume that the photons are distinguishable. It is for this reason that we cannot consider separate contributions for a term like $\kappa_{1_z} n_z$ from a term like $\kappa_{2_z} n_z$, but instead we always get contributions from both. This further leads to why the analyzing powder cannot be factored into a purely energy dependent part factor multiplying a purely geometric factor, as the weighting of the two terms is energy dependent and model dependent. For a signal like $b_3(\omega_1, \omega_2)$ such a split is possible as it gets contributions from a single term.

B.2 Direct versus indirect $\mathcal{CP}$-violation in ortho-positronium decay

In exact analogy with neutral Kaon physics, $\mathcal{CP}$-violation can manifest through two different mechanisms in 3-γ decay of spin-1 positronium. The $\mathcal{CP}$ eigensvalues are determined by the

spin and orbital angular momentum of the positronium, and by the number of photons and their polarization/angular distribution of the final state photons. Direct $\mathcal{CP}$-violation means that an initial state with a definite $\mathcal{CP}$ eigenvalue transitions to a final state that does not have a matching $\mathcal{CP}$ eigenvalue, for example the spin-1 ground state positronium decaying to 3 photons with a parity odd angular distribution. There can also be indirect $\mathcal{CP}$-violation where the positronium states are mixed by $\mathcal{CP}$-violating physics, and therefore do not have a well defined $\mathcal{CP}$ eigenvalue before decaying.

Most likely if one is occuring the other occurs as well, however the two are not easily related and how much direct versus indirect is always dependent on the specific model and system being studied. $\mathcal{CP}$-violation was discovered in 1964 in neutral Kaons [9], but the relative magnitudes of the direct versus indirect $\mathcal{CP}$-violation was not determined until 1991 [91]. The difference is where the new physics manifests. If it is direct then it manifests in the Feynman diagram mapping ortho-positronium$\rightarrow 3\gamma$. If it is indirect then it manifests in the positronium Hamiltonian governing the time evolution of the positronium energy eigenstates before decay.

As argued in Ref. [19] direct $\mathcal{CP}$-violation would be dominated by a permanent electric dipole moment, which has been excluded to a high level of sensitivity [16]. They therefore considered exclusively indirect $\mathcal{CP}$-violation in the positronium Hamiltonian that induces mixing between the n^3S_1 and 2^1P_1 states, quantified by a mixing parameter δ_n. We are studying ground state positronium so we are sensitive to δ_1. They calculated the form factors $c_4(\omega_1, \omega_2)$ and $c_5(\omega_1, \omega_2)$ for this state mixing. For the purposes of this work that is all that is needed, we can now include those in our simulation and extract the sensitivity to this specific model.

It is worth commenting on the phenomenology of direct versus indirect $\mathcal{CP}$-violation in positronium. Firstly the decay of positronium is generally calculated at tree level by calculating the amplitude for free electron-positron annihilation, $\langle n\gamma|\,\mathcal{T}\,|e^-, \mathbf{p}, s; e^+, -\mathbf{p}, s'\rangle = \mathcal{M}(\mathbf{p})$. The initial momentum distribution is taken as the (Fourier transform of the) Hydrogen wavefunction with the reduced mass for positronium, $\tilde{\psi}_{nJLSm_J}(\mathbf{p}) = \tilde{\Psi}_I(\mathbf{p})$, where $I = \{n, J, L, S, m_J\}$ [92]. The kinetic energy is highly non-relativistic and it is very safe to take a low momentum approximation. Most

derivations of the S-wave annihilation only keep the first term, but for this discussion it is vital to consider the first two terms [1],

$$\langle n\gamma|\,\mathscr{T}\,|Ps,I\rangle = \int \mathrm{d}^3p\,\mathscr{M}(\mathbf{p})\tilde{\Psi}_I(\mathbf{p}) \tag{B.6}$$

$$= \int \mathrm{d}^3p\,\left(\mathcal{M}|_{\mathbf{p}=0} + \nabla_p\mathcal{M}|_{\mathbf{p}=0}\cdot\mathbf{p} + ...\right)\tilde{\Psi}_I(\mathbf{p}) \tag{B.7}$$

$$= \int \mathrm{d}^3p e^{-i\mathbf{p}\cdot\mathbf{0}}\mathcal{M}|_{\mathbf{p}=0}\tilde{\Psi}_I(\mathbf{p}) + \int \mathrm{d}^3p e^{-i\mathbf{p}\cdot\mathbf{0}}\nabla_p\mathcal{M}|_{\mathbf{p}=0}\cdot\mathbf{p}\tilde{\Psi}_I(\mathbf{p}) + ... \tag{B.8}$$

$$= \mathcal{M}|_{\mathbf{p}=0}\Psi_I(\mathbf{x}=0) + (\nabla_p\mathcal{M}|_{\mathbf{p}=0})\cdot(\nabla_x\Psi_I(\mathbf{x}=0)) + ... \tag{B.9}$$

The lowest order goes as the value of the wavefunction at the origin, this is reasonable as this is where the electron and positron could be considered "in contact". The second order term goes as the derivative of the wavefunction at the origin. Now inspecting the wavefunctions, the S-wave is the only wavefunction that does not vanish at the origin, but its derivative is zero, and the P-wave has vanishing value at the origin, but non-vanishing derivative. Generally the structure of the radial wavefunctions go as $\Psi(r) \propto R(r/a_{Ps})e^{-r/2a_{Ps}}$ where $R(x)$ is some polynomial in x, and a_{Ps} is the Bohr radius for Positronium. Each derivative carries a factor of $1/a_{Ps}$, and the Bohr radius carries a fine structure constant, $a_{Ps} \propto 1/\alpha$. Each higher order term in the low momentum expansion carries an extra suppression by the fine-structure constant. Therefore 2^1P_1 decay is suppressed by a factor of α relative to 1^3S_1 purely from the atomic structure of positronium. This suppression is unavoidable and will suppress any sensitivity that angular correlations in 3-γ decay have to state.

If the asymmetry gets a numerator with contributions from new physics and a denominator from QED then indirect $\mathcal{CP}$-violation would give a contribution of the form $A \propto -\mathrm{Re}(\delta_1)\alpha/(2\sqrt{8}) * f(\omega_1,\omega_2)$ where δ_1 is the mixing parameter, $\alpha/(2\sqrt{8})$ is the combination of prefactors arising from the atomic physics, and $f(\omega_1,\omega_2)$ is the quotient of two polynomials of energies defined on the phase space (that also depends on the normal vectors for the momenta). All-in-all this gives a contribution that is suppressed by a factor of $\alpha/(2\sqrt{8}) \approx 1/775$.

Compare this with the general structure of direct $\mathcal{CP}$-violation. ortho-positronium to 3 photon decay has 3 QED vertices and therefore carries $e^6 = \alpha^3$ from the diagram squared, then includes the wavefunction effects (which brings in more factors of α). Direct $\mathcal{CP}$-violation (at the tree

level) means replacing one or more QED vertices by the "new physics" vertices. But as we are not considering state mixing the atomic structure effects are the same. This means that an asymmetry where the new physics contribution is in the numerator and QED contribution is in the denominator would go as, $(\chi e^{6-n})/(e^6)$, where χ is the "new physics parameter", and $0 \leq n \leq 3$ is the number of QED vertices replaced by the new vertex. Consider an electric dipole interaction, this replaces one QED vertex by d/e (if measuring d in $e$cm), meaning the asymmetry goes as d/α, and we see an enhancement to the sensitivity. This is just to illustrate that the system in general has enhanced sensitivity for direct $\mathcal{CP}$-violation and suppressed sensitivity for indirect. Nevertheless, the model provided in Ref. [19] is for indirect violation through state mixing, on the grounds that there could be cancellations or enhancements in the positronium physics that allow $\mathcal{CP}$-violation to manifest as state mixing without inducing a permanent electron electric dipole moment. They carefully worked through general parameter space, and a few specific models and do find that a high level of fine tuning is needed for this to occur.

B.3 Translating matrix element into probability distribution function

One difficulty is that the calculated amplitude for annihilation of P-wave positronium generically diverges as the energies approach 511 keV [19]. This is due to neglecting the binding energy of the positronium. For the purpose of Monte Carlo simulation we need to turn this into a probability distribution function to sample events from. To handle the divergence we do not consider any 3-γ events where any photon has energy greater than m_e - 6.8 eV. This is a rough solution, but none of the predictions can be trusted in this energy range, and it is an experimentally inaccessible range (since we cannot distinguish it from back-to-back 2-γ decay). It is well known that the 3-γ distribution calculated in the method outlined above does not correctly reproduce the low energy soft-photon physics described by Low's Theorem [2, 93], and that more involved methods utilizing nonrelativistic QED are required [94]. For our purposes this region of phase space is completely negligible.

B.4 Form factors

Here we recite the explicit energy dependence of the form factors as given in Ref. [19]. We follow their notation by using,

$$x = \omega_1/m_e$$

$$y = \omega_2/m_e$$

$$z = \omega_3/m_e = 2 - x - y$$

The angle between $\hat{\mathbf{k}}_1$ and $\hat{\mathbf{k}}_2$ is determined by energy and momentum conservation. It is given as,

$$\hat{\mathbf{k}}_1 \cdot \hat{\mathbf{k}}_2 = \cos(\psi_{12}) = 1 - 2\frac{x+y-1}{xy} \tag{B.10}$$

this is denoted as $g(x, y)$ in Ref. [19].

The QED form factors are scaled to be unitless, $\hat{f} = \Gamma_{o-Ps} f / \mathcal{N}_{1S}^2$, where $\mathcal{N}_{1S} = -e^3\psi_{1S}(0)/(\sqrt{2}m_e^2)$, and $\psi_{1S}(0) = (\pi r_0^3)^{-1/2}$, and $r_0 = 2(m_e\alpha)^{-1/2}$ is the Bohr radius for positronium:

$$\begin{aligned}\hat{a}(x,y) =& \frac{64}{3}\frac{1}{x^2y^2z^2}\big(x^4 + 2x^3y - 4x^3 + 3x^2y^2 - 9x^2y + 7x^2 + 2xy^3 - 9xy^2 \\ &+ 13xy - 6x + y^4 - 4y^3 + 7y^2 - 6y + 2\big)\end{aligned} \tag{B.11}$$

$$\hat{c}_1(x,y) = 16\frac{1}{y^2z^2}\big(2x^2 + 2xy - 4x + y^2 - 2y + 2\big) \tag{B.12}$$

$$\hat{c}_2(x,y) = c_2(y,x) \tag{B.13}$$

$$\hat{c}_3(x,y) = 16\frac{1}{xyz^2}\big(x^2 + 2xy - 2x + y^2 - y + 1\big) \tag{B.14}$$

For models of $\mathcal{CP}$-Violation, they scale by $\hat{f} = -f m_e \Gamma_{o-Ps}/(\mathcal{N}_{1S}\mathcal{N}_{2P}\mathrm{Re}(\delta_1))$, where $\mathcal{N}_{2P} = -\sqrt{6}e^3 R'_{2P}(0)/(\sqrt{4\pi}m_e^2)$, and $R'_{2P}(0) = (24r_0^5)^{-1/2}$,

$$\begin{aligned}\hat{b}_1^{mix}(x,y) =& \frac{8}{x^2y^2z^3}(4 - 18y - 16x + 32y^2 + 44xy + 26x^2 - 28y^3 - 55xy^2 \\ &- 45x^2y - 22x^3 + 12y^4 + 32xy^3 + 36x^2y^2 + 24x^3y + 10x^4 - 2y^5 \\ &- 7xy^4 - 10x^2y^3 - 10x^3y^2 - 5x^4y - 2x^5\end{aligned} \tag{B.15}$$

$$\hat{b}_2^{mix}(x,y) = \hat{b}_1^{mix}(y,x) \tag{B.16}$$

$$\hat{c}_4^{mix}(x,y) = 8\frac{\sin(\psi_{12})}{xyz^3}\big(2 - 6x - 7y + 7x^2 + 13xy + 9y^2 - 4x^3 - 9x^2y - 9xy^2 - 5y^3 + x^4 + 2x^3y + 3x^2y^2 + 2xy^3 + y^4\big) \tag{B.17}$$

$$\hat{c}_5^{mix}(x,y) = -\hat{c}_4^{mix}(y,x) \tag{B.18}$$

Note that this gets,

$$\frac{c_4^{mix}(x,y)}{a(x,y)} = \frac{\mathcal{N}_{1S}\mathcal{N}_{2P}\mathrm{Re}(\delta_1)}{-m_e\Gamma_{o-Ps}}\frac{\Gamma_{o-Ps}}{\mathcal{N}_{1S}^2}\frac{\hat{c}_4^{mix}(x,y)}{\hat{a}(x,y)} \tag{B.19}$$

$$= -\mathrm{Re}(\delta_1)\frac{-\sqrt{6}e^3}{\sqrt{24r_0^5}\sqrt{4\pi}m_e^3}\frac{\sqrt{2}m_e^2\sqrt{\pi r_0^3}}{-e^3}\frac{\hat{c}_4^{mix}(x,y)}{\hat{a}(x,y)} \tag{B.20}$$

$$= -\mathrm{Re}(\delta_1)\frac{\alpha}{2\sqrt{8}}\frac{\hat{c}_4^{mix}(x,y)}{\hat{a}(x,y)} \tag{B.21}$$